universität wien

MASTERARBEIT / MASTER'S THESIS

Titel der Masterarbeit / Title of the Master's Thesis

„Structural evolution of the metamorphic rocks on Kalymnos (Greece)"

verfasst von / submitted by

ELEFTHERIA CHATZIIOANNOU

angestrebter akademischer Grad / in partial fulfilment of the requirements for the degree of

Master of Science (MSc)

Wien, 2020 / Vienna, 2020

Studienkennzahl lt. Studienblatt / degree programme code as it appears on the student record sheet:	UA 066 815
Studienrichtung lt. Studienblatt/ degree programme as it appears on the student record sheet:	Masterstudium Erdwissenschaften
Betreut von / Supervisor::	Univ. Prof. Mag. Dr. Bernhard Grasemann

Acknowledgement

I would like to thank my supervisor Bernhard Grasemann for the frequent and detailed discussions on geology that opened my mind for this wonderful subject. I am very thankful to Konstantinos Soukis for his supervision and discussions on tricky geologic questions. They supported me during the fieldwork with all their knowledge and experience, which helped me to become better in this scientific field.

I very much enjoyed the cooperation with Ivanka Mitrovic, Lukas Plan and Ivo Baron in the field. The laboratory analysis of David Schneider and Bernhard Hubmann provided me with the necessary insight into the characteristics of my data.

A very big thank you to Hugh N. Rice, Gerlinde Habler, Tom Griffiths, Theo Ntaflos, Konstantinos Petrakakis and Anna Rogowitz for showing me how to handle the SEM and EBSD equipment at the University and how to analyze the data in specialized software.

All my tasks would have been very difficult to accomplish without the support and discussions during coffee drinking with Evaggelia Prentouli, Katerina Tsevairidou, Ingrid Gjerazi and Martina Salomon.

The biggest thank you I owe to my mother Vasiliki Chatziioannou and my father Anastasios Chatziioannou for the encouragement and the support in all of these years, without them I could not have succeeded. I would also like to thank my Brother Dimitrios Chatziioannou and my grandmother Evaggelia for being there when I most needed them.

Last but not least, I would like to thank for the best support, discussions, encouragement and most frequent reminders by Andras Zamolyi and his family including Isabel, Eva and Marci!

Abstract

Kalymnos Island represents a key link between the Eastern Aegean and the Menderes region both geographically and regarding the metamorphic evolution of the Variscan basement. Very little attention was paid to the outcrops on Kalymnos Island and they were not studied extensively. The most detailed description dates back to Desio's work in 1925 and a more modern study by Triantafillis et al. (1994).

During 10 days of fieldwork the geologic mapping of the study area, the Kefala and Rachi areas, containing Variscan outcrops was conducted. The lithostratigraphy encountered reflects the complexity of the tectono-metamorphic evolution of the area. The main units can generally be recognized and with some degree of uncertainty even be correlated to units located on neighboring islands, such as Leros and Kos. A correlation and link to events in the Menderes, however, is still very vague and needs more investigation in the field and with laboratory methods.

After a detailed mapping of the units in the field, selected samples were taken for further investigation. The focus of the laboratory analyses was on paleontology and geochronology to be able to identify distinct units and to reconstruct the lithostratigraphic succession of the units. As a next step, the tectono-metamorphic evolution was described with the help of structural geologic methods, such as microscopy and EBSD.

The lithostratigraphic succession starts with the Interlayered Marble Unit, is subdivided by two thrust faults and one probable normal fault, and ends with Mesozoic limestones. Above the Interlayered Marble Unit, the Permian and Devonian Marble Units are located juxtaposed to each other by strike-slip faults and a possible depositional hiatus. The next units to follow are the Metaconglomerate and the Quartz-Mica Schist Units. On the map, the Interlayered Marble Unit is located to the Southwest of the study area on the Kefala peninsula, and the overlying Metaconglomerate and the Quartz-Mica Schist Units crop out towards NE in Rachi.

Additionally, to the nappe structure, multiple folding phases can be observed within the tectonic units and also affecting several units at the same time. An example for the intra-unit folding phases are the three folding events in the Quartz-Mica Schist Unit. Folding of several units at the same time can be seen at Kefala peninsula, where also a folded thrust was identified. A reconstruction of the possible geodynamic evolution is attempted, starting with the Early Devonian deposition of sediments at the NE Gondwana margin and concluding with their northward journey as Minoan Terranes. A peak in tectonic events occurs in the Carboniferous marked by a depositional hiatus and probably in the Early to Middle Triassic indicated by the folding of the thrust in Kefala and the three folding events in Rachi. The metamorphic evolution of the units resembles a low pressure/medium-temperature path with a probable amphibolite facies peak at around 500°C and 3 kbar and a greenschist facies peak at around 300°C and 3 kbar. An Alpine greenschist facies overprint affected all the Variscan units on Kalymnos that indicates a position at the margin of the Variscan and Alpine orogenic events.

The correlation of the units mapped on Kalymnos with units on neighboring islands and in the South Anatolide Block supports the existence of one, formerly continuous Variscan basement complex as also mentioned in literature (e.g. Franz et al., 2005). The pre-Alpine basement rocks on Kalymnos are regarded to be correlatable with units from the Menderes Cover. This would indicate a north- and westward thrusting of the Lycian Nappes onto the Menderes Massif and the Dodecanese Islands.

Zusammenfassung

Die Insel Kalymnos stellt sowohl geographisch, als auch durch die metamorphe Entwicklung des prä-variszischen Basements die Verbindung zwischen der östlichen Ägäis und dem Menderes Massiv dar. Die Aufschlüsse auf Kalymnos wurden nicht sehr viel beachtet und auch nicht im Detail untersucht. Die detaillierteste Beschreibung ist eine Arbeit von Desio (1925). Eine modernere Publikation stammt von Triantafillis et al. (1994).

Die Gebiete der Insel mit variszischen Aufschlüssen, die Halbinsel Kefala und das weiter landwärts gelegene Gebiet Rachi wurden in zehn Tagen Geländearbeit geologisch kartiert. Die dabei angetroffene Lithostratigraphie spiegelt die Komplexität der tektono-metamorphen Entwicklung des Gebietes wieder. Die Haupteinheiten können generell gut kartiert und mit einiger Unsicherheit sogar mit Einheiten auf den Nachbarinseln (z.B. Leros und Kos) korreliert werden. Eine Korrelation und die Verbindung zu Einheiten im Menderes Massiv ist jedoch noch immer sehr schwierig und benötigt mehr Zeit für Untersuchungen im Gelände und im Labor.

Nach einer detaillierten Kartierung der Einheiten im Gelände wurden ausgesuchte Proben für weitere Untersuchungen genommen. Die Untersuchungen im Labor hatten die Klärung des Fossilinhaltes der Proben, sowie deren Datierung als Hauptziel, um die einzelnen Einheiten identifizieren zu können. Mit Hilfe dieser Untersuchungen konnte die lithostratigraphische Abfolge rekonstruiert werden. Im nächsten Schritt wird die tektono-metamorphe Entwicklungsgeschichte mit Hilfe strukturgeologischer Methoden, Dünnschliff-Analysen und dem EBSD Verfahren beschrieben.

Die lithostratigraphische Abfolge beginnt mit der Zwischengeschichteten Marmor Einheit, wird durch zwei Überschiebungen und eine vermutete Abschiebung gegliedert und endet mit mesozoischen Kalksteinen. Über der Zwischengeschichteten Marmor Einheit liegen die Permischen und Devonischen Marmor Einheiten, die entlang von Seitenverschiebungen und wahrscheinlich einem sedimentären Hiatus in direkte Nachbarschaft gebracht wurden. Die nächsthöheren Einheiten sind die Metakonglomerat- und Quarzglimmerschiefer Einheiten. Auf der Karte liegt die Zwischengeschichtete Marmor Einheit im südwesten des Arbeitsgebietes auf der Kefala-Halbinsel und die darüberliegenden Einheiten sind weiter im Nordosten, in Rachi aufgeschlossen.

Zusätzlich zur Stapelung der Einheiten können mehrfache Faltungsphasen innerhalb der Einheiten und auch über mehrere Einheiten übergreifend beobachtet werden. Ein Beispiel für die Faltung innerhalb der Einheiten sind 3 Faltungsphasen in der Quarzglimmerschiefer Einheit. Die Faltung, die mehrere Einheiten betrifft, sieht man auf der Kefala Halbinsel durch eine gefaltete Überschiebung. Die Rekonstruktion der möglichen geodynamischen Entwicklung wird versucht. Diese beginnt mit der Ablagerung der Sedimente am NE-Rand von Gondwana im frühen Devon und setzt sich im Nordwärtsdriften der Einheiten als Minoische Terrane fort. Hauptphasen der tektonischen Aktivität liegen im Karbon (gekennzeichnet durch den sedimentären Hiatus) und wahrscheinlich in der frühen-mittleren Trias (gefaltete Überschiebung auf Kefala und 3 Faltungsphasen in Rachi). Die metamorphe Entwicklungsgeschichte der Einheiten gleicht eher niedrigdruck/mitteltemperatur – Pfaden mit einem höchstgrad der Metamorphose um wahrscheinlich 500°C und 3 kbar und einem grünschieferfaziellem höchstgrad bei ~300°C und 3 kbar. Eine alpine grünschieferfazielle Überprägung erfasste alle variszischen Einheiten auf Kalymnos, das auf eine randliche Position im Verhältnis zum Variszischen- und Alpinen Orogen hinweist.

Die Korrelation der Einheiten auf Kalymnos mit den Einheiten auf den benachbarten Inseln und im Süd-anatolischen Block weist auf einen früher existierenden, durchgehenden variszischen basement-complex hin, der auch bereits in der Literatur erwähnt wird (z.B. Franz et al., 2005). Die prä-alpidischen Gesteine aud Kalymnos sind am ehesten mit Deck-Einheiten des Menderes Massivs korrelierbar. Die würde auf eine nord- und westgerichtete Überschiebung der lyzischen Decken auf das Menderes Massiv und den Dodekanes hinweisen.

Περίληψη

Το νησί της Καλύμνου αποτελεί το κλειδί μεταξύ της γεωλογίας του Ανατολικού Αιγαίου και της περιοχής Μεντερές κυρίως όσον αφορά τη μεταμορφική εξέλιξη του Βαρίσκιου υποβάθρου. Η περιοχή δεν έχει μελετηθεί εκτενέστερα κατά το παρελθόν. Η πιο αναλυτική εργασία χρονολογείται το 1925 από τον Desio και η πιο μοντέρνα από τον Τριανταφύλη et al. 1994.

Κατά τη διάρκεια δέκα (10) ημερών στην ύπαιθρο χαρτογραφήθηκε η περιοχή Κεφάλα και Ράχη, όπου το Βαρίσκιο υπόβαθρο εμφανίζεται. Η λιθοστρωματογραφία της περιοχής μας πληροφορεί για την τεκτονοστρωματογραφική εξέλιξη των βαρίσκιων ενοτήτων. Οι κύριες ενότητες που χαρτογραφήθηκαν εμφανίζονται μερικώς στα γειτονικά νησία Λέρος και Κως. Η συχέτιση όμως των ενοτήτων της Καλύμνου με τις ενότητες του καλύμματος του Μεντέρες είναι ακόμα δύσκολη.

Ύστερα από μια λεπτομερή χαρτογράφηση της περιοχής, συλλέχθηκαν δείγματα για περεταίρω ανάλυση. Πιο συγκεκριμένα ορισμένα δείγματα ραδιοχρονολογήθηκαν με τη μέθοδο $^{40}Ar/^{39}Ar$ και U(Th)/He και σε άλλα διεξήχθει παλαιοντολογική ανάλυση. Σε ένα επόμενο βήμα, η τεκτονομεταμορφική εξέλιξη της περιοχής περιγράφθηκε με τη βοήθεια τεκτονικών, γεωλογικών μεθόδων καθώς και την βοήθεια του ηλεκτρονικού μικροσκοπίου και του ηλεκτρονικού μικροσκοπίου σάρωσης.

Στην βάση την κολώνας συναντάμε την κατώτερη ενότητα μαρμάρου και στην κορυφή της κολώνας μας συναντάμε τους Μεσοζωικούς ασβεστολίθους. Στην κατώτερη ενότητα Μαρμάρου επωθούνται τα ελαφρώς μεταμορφωμένα μάρμαρα ηλικίας Περμίου και Δεβονίου. Τα οποία μεταξύ τους έρχονται σε επαφή με την βοήθεια αριστερόστροφων ρηγμάτων, οριζόντιας ολίσθησης. Εν συνεχεία, συναντάμε το μεταμορφωμένο λατυποπαγές και τους Φυλλίτες – Χαλαζίτες.

Επιπλέον, πέρα από την καλυμματική τεκτονική που παρατηρούμε στην περιοχή, συναντάμε 3 διαφορετικές γεννεές πτυχώσεων κυρίως στην ενότητα των Φυλλιτών-Χαλαζιτών. Το κατώτερο Μαρμαρο που συναντάται στην περιοχή της Κεφάλας είναι επίσης πτυχωμένο συγχρόνως με τις εποθιμένες ενότητες.
Στην εργασία αυτή παρουσιάζεται ένα πιθανό σενάριο της γεωδυναμικής εξέλιξης στην περιοχή καθώς και η σχηματική απεικόνιση της συσχέτισης των ενοτήτων της Καλύμνου με τις γειτονικές περιοχές του Αιγαίου και της Τουρκίας.

Το κύριο συμπέρασμα της εργασίας αυτής αποτελεί, η ύπαρξη ενός συνεχούς, μεταμορφωμένου, Βαρίσκιου υποβάθρου, όπως υποστηρίζεται και από τον Franz et al., 2005. Το προαλπικό υπόβαθρο της Καλύμνου παρουσιάζει ομοιότητες με αυτό του καλύμματος του Μεντερές στην Τουρκία. Η έρευνα μας υποστηρίζει την επώθηση των Καλυμμάτων της Λυσίας προς τα ΒΔ πάνω στην Μάζα του Μεντερές και τις ενότητες των Δωδεκανήσων.

1. Introduction

1.1 Motivation and aim of the study

The aim of this study is to reveal the structural and metamorphic evolution of the pre-Alpidic basement rocks on Kalymnos Island (Dodecanese Islands - Greece) (Fig. 1), which were not in the focus of researchers up to now. The pre-Alpidic basement units in the Dodecanese are of key importance to link the geological history between the basement rocks of Eastern Crete and the Lycian Nappes in southwest Turkey, as revealed by the lithological similarities in the Variscan metamorphic history (Franz et al., 2005). This and the fact that the various lithological units were not studied in detail up to now, are the main reasons for mapping the basement in Kalymnos and to investigate its metamorphic evolution in more detail. The study area was mapped on 1:5 000 scale military topographic map sheets resulting in a 1:10 000 scale map, and it is located at the northwestern part of Kalymnos, in an area where the crystalline rocks crop out. For this research, a multidisciplinary approach was essential in order to understand the tectonometamorphic evolution. Hence, additionally to the geologic mapping of the study area at Kefala and Rachi, also sampling of the rocks for geochronological, petrographical and (micro)-structural analysis was carried out.

1.2 Geographic Overview

Kalymnos is located in the southeastern Aegean Sea and is part of the Dodecanese islands, also referred to as Southern Sporades (Fig. 1). The Aegean Sea is an extended archipelago of the Mediterranean Sea between the Greek and Anatolian peninsulas and is connected to the NE to the Marmara Sea through the Dardanelles. Philippson (1959) refers with the term "Aegean region" to the entire Greek and Anatolian peninsula as well as to the Aegean Sea. The Aegean islands are divided into: 1) Northeastern Aegean islands, 2) Euboea, 3) Northern Sporades, 4) Cyclades, 5) Dodecanese and 6) Crete.

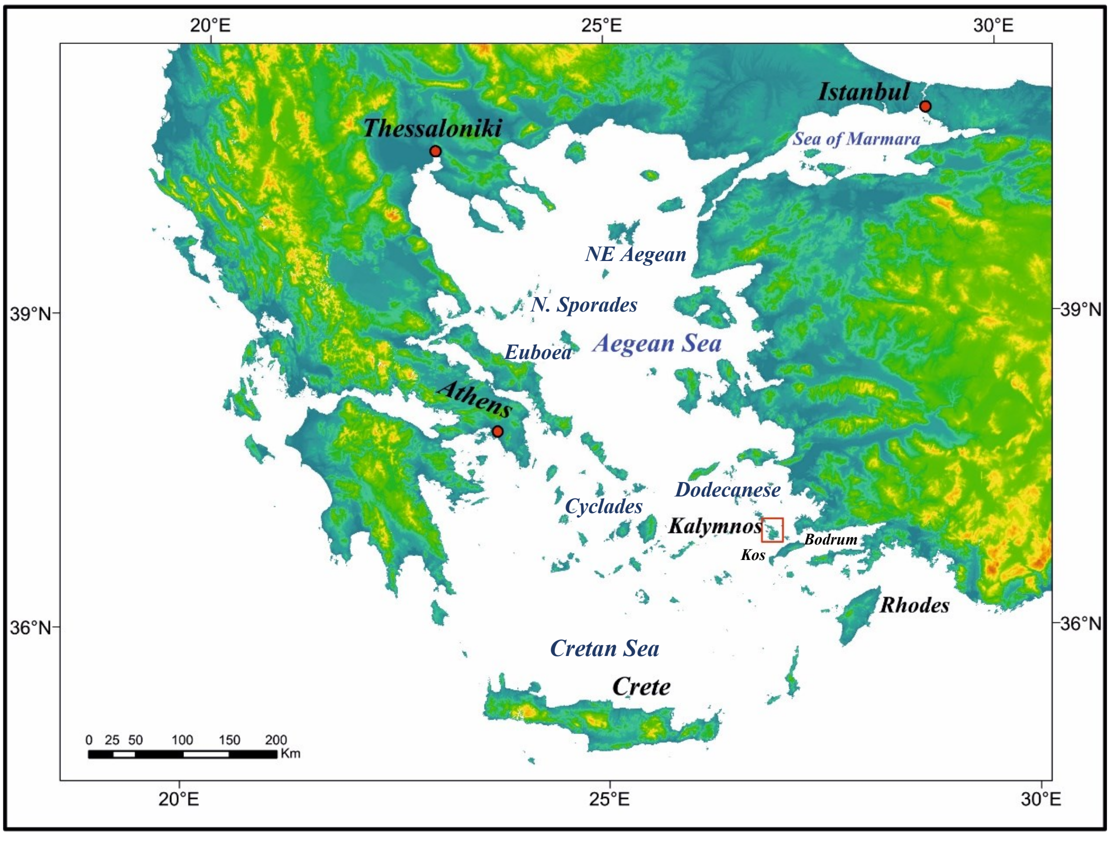

Fig. 1: Topographic overview map of Greece and the Aegean region. The red square shows the subject of this study: Kalymnos Island in the Dodecanese Islands. Topography based on SRTM data (Jarvis et al., 2008. available from http://srtm.csi.cgiar.org)

The Dodecanese (meaning the twelve Islands) are a group of 14 main (Rhodos, Kos, Agathonisi, Kalymnos, Symi, Leros, Patmos, Astypalaia, Nisyros, Chalki, Tilos, Karpathos, Kasos and Kastellorizo) and 150 smaller Greek islands in the SE Aegean Sea, of which 26 are inhabited. These islands are located at the easternmost part of the Cretan Sea. The name first appears during the Byzantine age. Although it was not used for the current group of islands, but to the twelve Cycladic islands which surround Delos, a smaller island with great history. The change of the name to this group has its roots in the Ottoman period. The two largest islands Rhodos and Kos came under direct Ottoman rule, while the other twelve enjoyed privileges to taxation and self-government (Giannopoulos, 2006). Neighboring Kalymnos, the Island of Kos is located (Fig. 1), which is and was one of the most important islands historically and also one of the well-known islands. Kalymnos is located in a central position: to the east there is the Bodrum peninsula (ancient Alicarnassos), to the north, at a distance of less than 2 km Leros Island is located, and to the south at a distance of 12 km lies Kos Island (Fig. 1). Expressed in geographic coordinates, Kalymnos is located 36°59´ N and 26°59´ E (WGS 1984) and its area is 109 km^2. The capital of the island bears the same name as the island and the main settlements are located along the southeastern shoreline including Myrties and Masouri (Fig. 2). The shape of the island is elongated in NW-SE direction with a length of 21 km and a width of 13 km. On the northwestern side the peninsula of Kefala and Rachi stretches in a SW direction with Kefala showing a peculiar plume-like shape on topographic maps. The main lithology that can be observed is karstic limestone, which offers the perfect geomorphology for rock climbing and bouldering during the entire year. Moreover, valleys can be observed close to compact banks of volcanic tuff, the relic of an ancient volcano near the village of Kantouni (Fig. 2). Around Kalymnos, some smaller islands can be found, which belong to the municipality of Kalymnos. These are Pserimos, Telendos, Kalavros, Kalolimnos and Plati. Of these, Kalavros and Telendos lie close to the peninsula of Kefala and Rachi (Fig. 2). At the southern point, where the peninsula meets the main island, Emporio, the northernmost village of Kalymnos is located (Fig. 2).

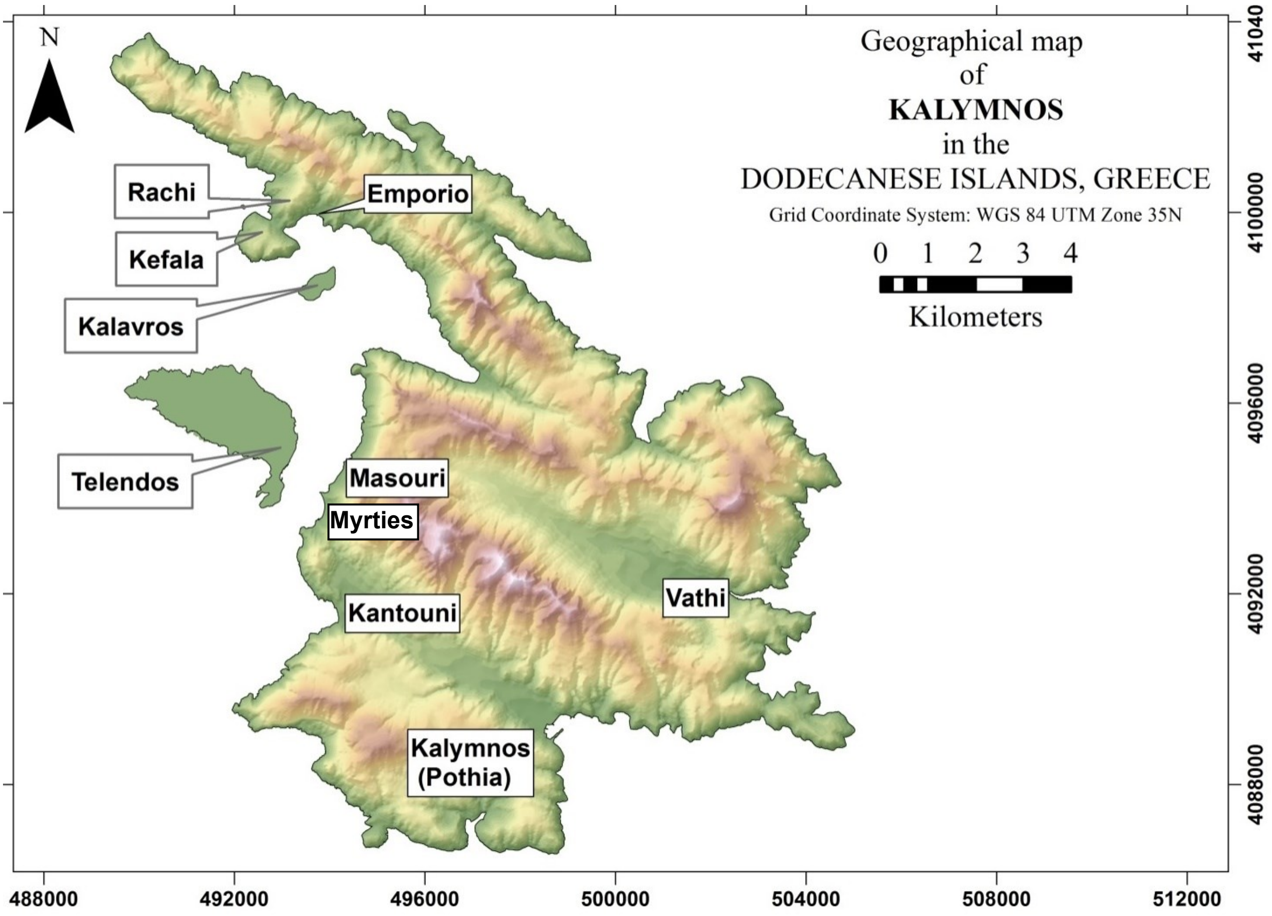

Fig. 2: Topographic map of Kalymnos Island showing the most relevant settlement and location names. The DEM is derived from digital contours lines (ANAVASI, 2014).

1.3 Thesis Outline

The thesis is divided into six chapters. The first chapter is the introduction, which includes the motivation, the geographical overview and the outline of the thesis. The second chapter introduces the reader to the geological setting of Greece, the Dodecanese Islands and Kalymnos Island. In the third chapter, a detailed description of the lithostratigraphy of the study area is given accompanied by the overview geological map, which was the result of 10 days of fieldwork in the studied area. The fourth chapter includes the Geo- and thermochronological results of two methods, $^{40}Ar/^{39}Ar$ and (U-Th)/He that were used to determine the main metamorphic events affecting the basement rocks. The fifth chapter comprises the structural and microstructural analysis of the studied rocks. The sixth chapter is a discussion/conclusions chapter on the presented results and a synthesis focusing on an attempted reconstruction of the geologic evolution of the study area and the relationship with the neighboring areas. The geological map at scale 1:10 000 along with the lithostratigraphic column and the type cross section is presented in the appendix 7.1. The appendices 7.2 and 7.3 contain the geo- and thermochronological datasheets.

2 Geologic setting of Greece and the Aegean area

2.1 Present-day geologic configuration

The present state tectonic framework of the Aegean area is a result of the movement of the Eurasian, African, Anatolian and Arabian plates. At 25 Ma, the Red Sea started rifting causing the separation of the Arabian plate from the African plate (McClusky et al., 2003; Garfunkel, 1998). As a result, the collision and movement of the Arabian plate towards the north causes the escape of the Anatolian block to the West along the North Anatolian Fault and East Anatolian Fault. At the same time the convergence between Africa and Eurasia resulted in the subduction of the African Plate beneath the Eurasian continent forming the Hellenic Arc at around 10-25 Ma together with the tectonic elements preserved until today (Fig. 3). Several scientists, e.g. Banga (1982) and Angelier et al. (1982) proposed a North-South extension of the basins of the Aegean area around the Miocene, with the low angle normal faults (extensional detachments) as the main structural features. These faults largely formed the metamorphic core complexes like those on Ios Island (Banga, 1982) and on Naxos (Lister et al., 1984) and exhumed the middle crust. The extension probably started at 30 Ma linked to a migration of the subduction zone to the South as a result of the slab roll back of the cold subducted plate (Royden, 1993; Wortel & Spakman, 2000; Jolivet & Brun, 2010).
Another important feature, the South Aegean Volcanic arc is situated to the South of this back-arc Extension zone, including Sousaki, Aegina, Methana, Milos, Santorini, Kolumbo, Kos, Nisyros and Yali. The steep subduction angle of the slab and the slab roll-back are the two main reasons of this magmatic zone along the arc (Dilek, 2006). As a next step, the southern margin of the Aegean microplate forms the Hellenic Arc (Ionian Islands, Peloponnese, Crete, Carpathos and Rhodes), where also most of the seismic activity is taking place (Fig. 4). The Hellenic trench with depths of up to 5 km develops almost parallel to the Hellenic Arc, together with the accretionary wedge from the deformed nappes of sediments (Jacobshagen, 1986). The sketch in figure 5 shows a cross-section of the area.

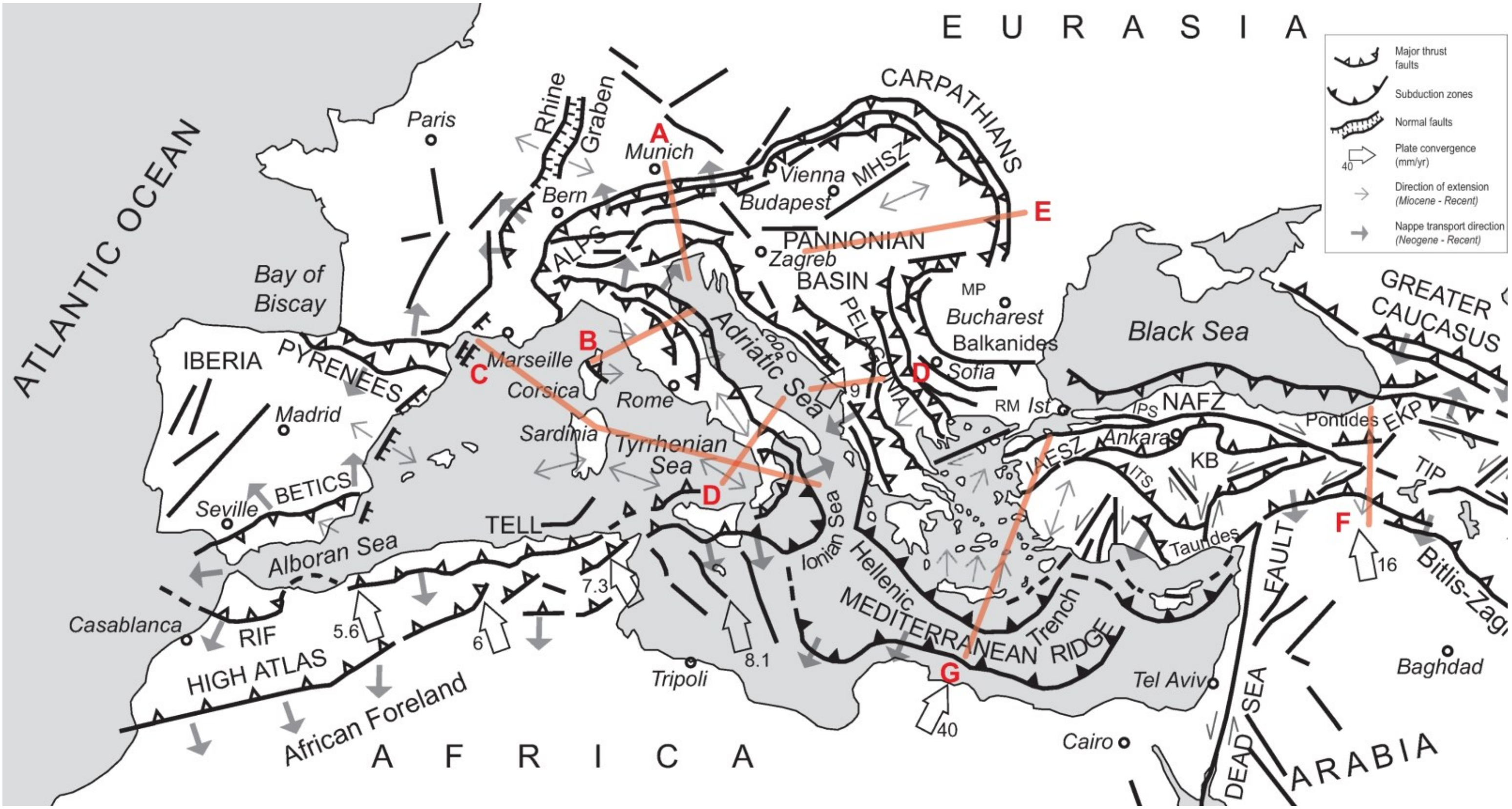

Fig. 3: Simplified tectonic map of the Mediterranean area presenting the major thrust faults, the subduction zones, the normal faults, the plate convergence zones, the directions of extension and the nappe transport directions. This map shows some profile lines where the profile G is presented in the next figure. MHSZ–mid-Hungarian-shear-zone; MP–Moesian-platform; RM–Rhodope-massif; IAESZ–Izmir-Ankara-Erzincan-structure-zone; IPS–Intra-Pontide-suture-zone; ITS-inner-Tauride-suture-zone; NAFZ–north-Anatolian-Fault-zone; KB–Kireshir-block; EKP–Erzurum-Kars-plateau; TIP–Trukish-Iranian-plateau (Dilek, 2006).

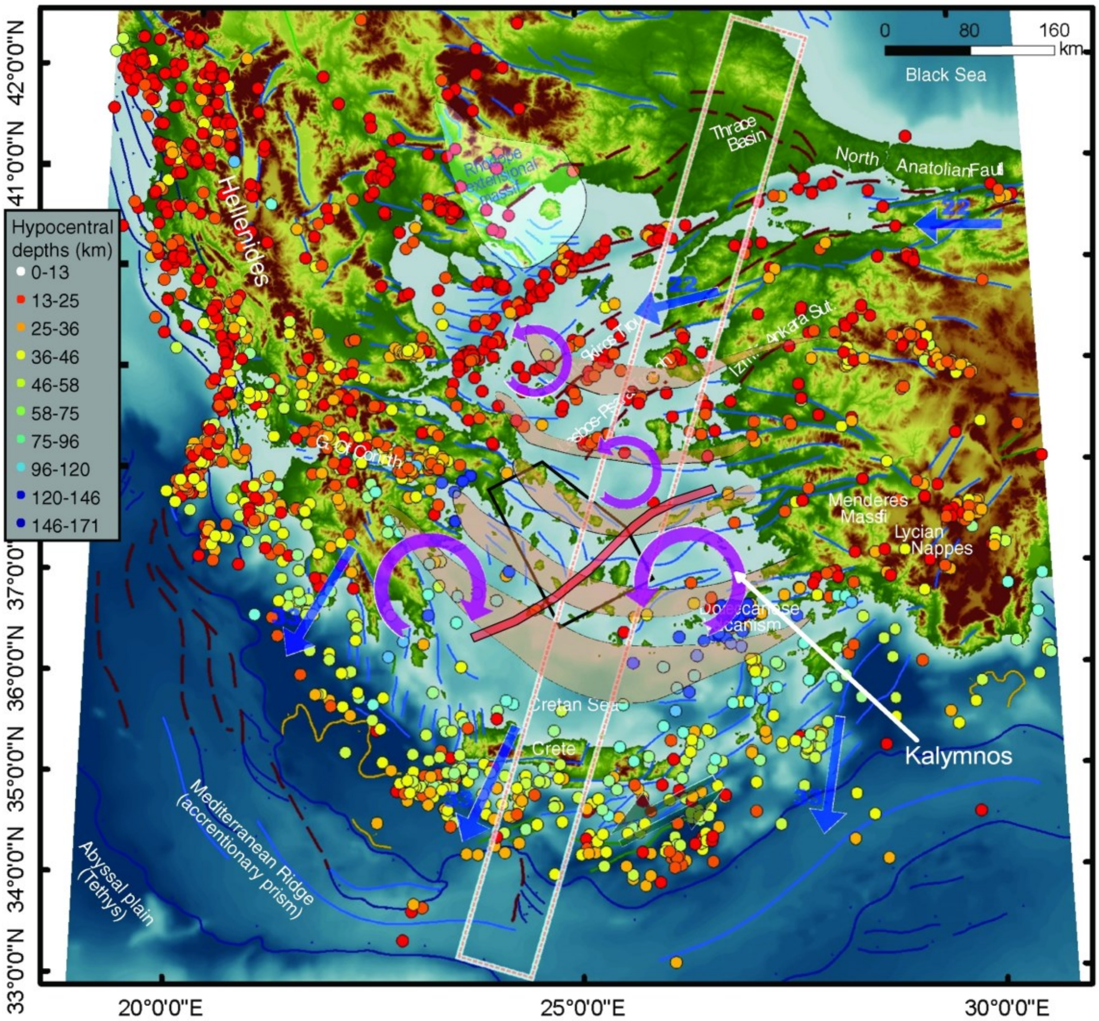

Fig. 4: Map of seismicity (presenting the hypocenters) in the eastern Mediterranean region, with the arrow pointing to the location of Kalymnos Island (modified after Edwards & Grasemann, 2009, confined by National Earthquakes Information Center, USGS).

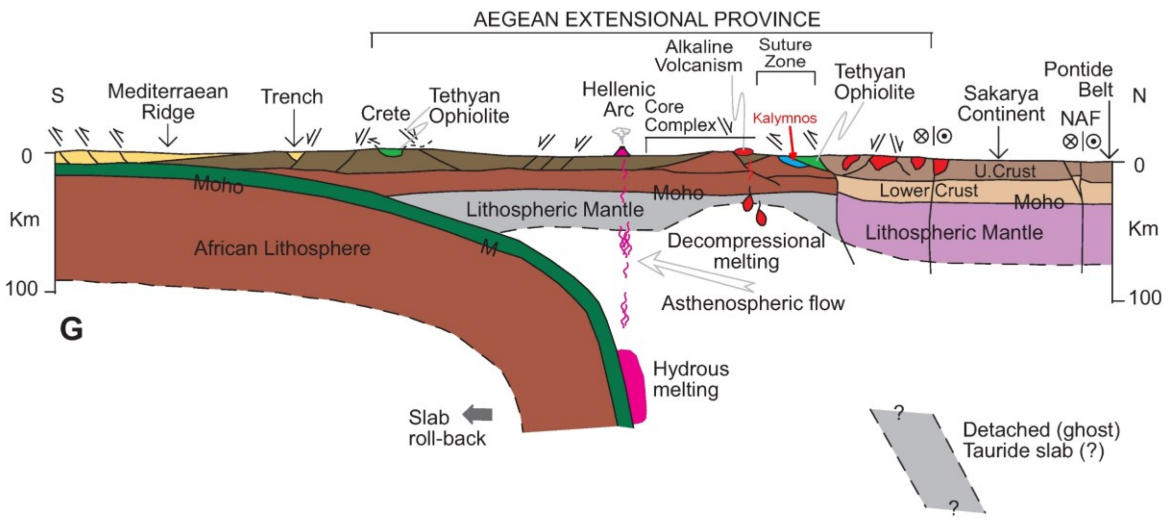

Fig. 5: Simplified tectonic cross-section (profile G in Fig. 3) showing the subduction of the African lithosphere underneath the Eurasian plate (Dilek, 2006).

2.2 Geologic evolution

For the description of the pre-Variscan and early Alpine geologic history, a bigger geographic area is taken into consideration. Examples from wider Europe are mentioned.

The pre-Variscan geodynamic evolution of Variscan basement areas reflects an origin from the peri-Gondwana terranes (Stampfli & Kozur, 2006). Within this phase an important event is related to the slab roll-back of the Rheic ocean and is a first mid-Devonian Variscan orogenic event with HP-LT metamorphism. This event occurred due to a collision between Eurasian and Gondwanan terranes and arcs from the Asiatic ocean (Stampfli et al., 2002). The second Variscan orogenic event between 350 and 330 Ma (Visean) included lateral escape processes, convergence and build-up of a Variscan Cordillera (Stampfli & Kozur, 2006). It is noteworthy that the Alleghenian orogeny starting in the Late Carboniferous did not affect the Eastern Alpine and Mediterranean part of the Variscan Cordillera, which was active until earliest Permian (e.g. Vavassis et al., 2000). In this part, we see plutonic activity and in the Early Permian, this area was focus of extensional deformation (Stampfli & Kozur, 2006). Between Late Carboniferous and Early Permian flexural basins developed with pelagic sedimentation occurring until earliest Kungurian (~283 – 273; Fokin et al., 2001).

The post-Variscan evolution begins with a major plate boundary reorganization including subduction progradation and detachment of terranes such as the Cimmerian composite terrane (Stampfli & Kozur, 2006). During the collapse of the Variscan Cordillera and consolidation of the Alleghenian orogeny, magmatic and tectonic activity decreased from Iberia to the Tornquist line. In the Late Permian the Neotethys rift system propagated westward (Ziegler & Stampfli, 2001) and marginal basins along the Eurasian margin opened (e.g. Meliata system). In the Early-Middle Triassic, the opening of the Pindos ocean close to the southern margin of Eurasia started (Robertson, 2006). During the following Eocimmerian (Late Triassic) and Cimmerian (Late Jurassic) collision of terranes with the Palaeotethys arc-trench system, these basins were closed (Stampfli & Kozur, 2006 and citation therein). The Eocimmerian collision extends from Apulia to Thailand without the formation of a major orogeny, only with terrane docking (Sengör & Hsü, 1984).

According to Jacobshagen (1986), the Hellenides were formed from Mesozoic to the Tertiary during four orogenic phases (Cycles) that are associated to the episodic closure of the Tethys Ocean, presented in the following paragraphs:

Cimmerian Cycle:

This cycle is known from the innermost areas of the Vardar-zone and the Circum-Rhodope Belt. A major hiatus is observed in the Triassic, followed by an unconformity in the Liassic. In the Aegean Sea this evolution is reflected in the stratigraphic column of the allochthonous unit of Chios Island (Fig. 6), that was overthrusted on the autochthonous unit (Robertson & Pickett, 2000; Papanikolaou, 2015). In Eastern Crete, clastic beds of metaconglomerates and violet slates can be found at the base of the Lower Anisian Tripokefala beds (Zulauf et al., 2008).

Eohellenic Stage:

This cycle begins at the Mid -to Late Jurassic and continues until the early Cretaceous. During this period the Vardar-Axios Ocean, that stretched between the Pelagonian block (present day southwest) and the Rhodope belt (present day northeast), subducted first beneath the Paikon island arc and at a later stage below the Rhodope belt. The closing of the Vardar-Axios Ocean is documented by the position of the ophiolites in the Pelagonian unit (Piper & Pe-Piper, 2002; Jacobshagen, 1986).

Mesohellenic Cycle:

At this phase the Pindos Ocean and the remaining part of Axios –Vardar, which was not obducted during the previous stage, are consumed in the Late Cretaceous - early Tertiary and the continental blocks of Apulia, Pelagonia and the Rhodope massif collided (Piper & Pe-Piper, 2002).

Neohellenic Period:

The peak of this period is regarded to be in the late Oligocene to early Miocene times. The Apulian plate collided with the Eurasian margin and formed the Alpine Hellenic Orogen. A post-orogenic extension followed the previous event and terrestrial sedimentary basins are formed (Jacobshagen, 1986).

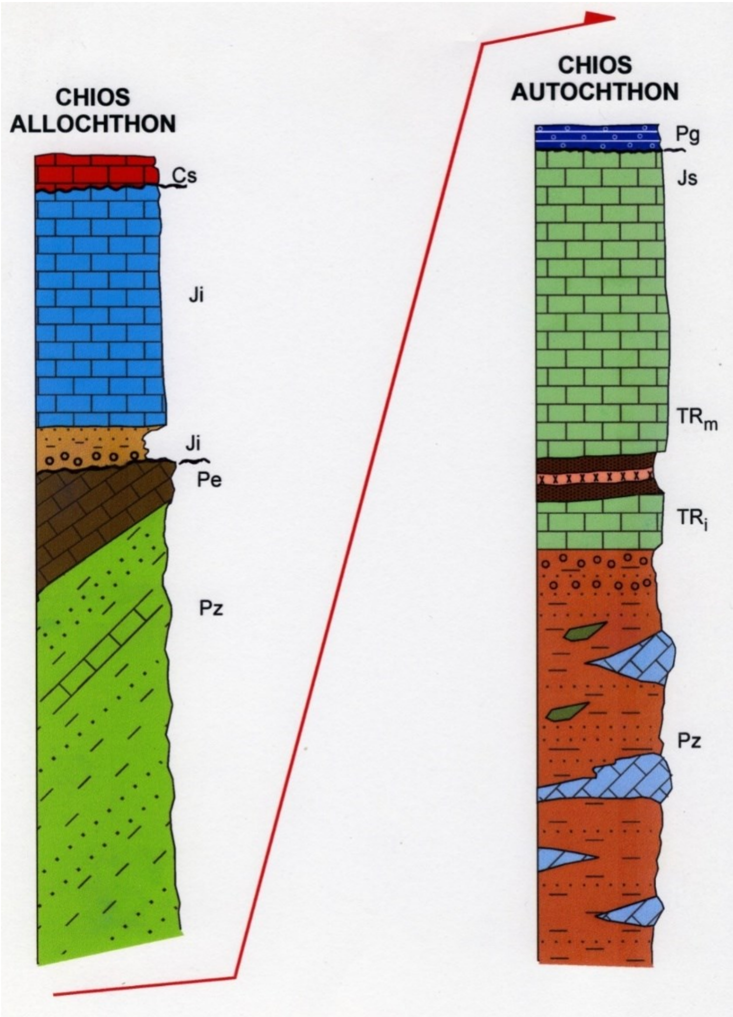

Fig. 6: The two stratigraphic columns present the allochthonous and autochthonous unit of Chios Island (from Papanikolaou, 2015). Pz = Palaeozoic, Tri = Lower Triassic, Trm = Middle Triassic, Js = Late Jurassic, Pg = Paleogene, Pe = Permian, Ji = Early Jurassic, Cs = Cenozoic.

During the late Paleozoic to early Mesozoic and before the opening and subsequent closure of the Tethys Ocean, the Aegean area is part of the Paleotethys. The Palaeotethys was subducted at an Andean-type margin at 300 Ma (Variscan orogeny) and NE Gondwana rifted during Carboniferous, Permian and Triassic age creating the late Triassic to Jurassic small ocean basins (Pe-Piper, 1998; Finger & Steyrer, 1990). The most important rifting events (Robertson et al., 1991) are documented in the two ophiolitic belts stretching along the Dinarides to the Hellenides (Robertson, 1997). The ophiolite complexes of the outer belt indicate subduction related, Late Jurassic events. The inner belt is more variegated. According to Robertson (1997), the existence of a Jurassic Andean type margin is evident.

The limestones of the Tripolitza and Pelagonian zone, which are of Mid Triassic age, lie above volcanic rocks of upper Skythian and lower Anisian age. Moreover, these lavas are accompanied sometimes by red limestones and cherts. In Sicily and Crete, a marine, deep water sedimentary facies of Late Permian age can be observed, representing the earlier rifting of Apulia (Stampfli & Pillevuit, 1993).

Figure 7 shows the two ocean basins, Pindos and Vardar, which were developed during Triassic and separated Pelagonia from Apulia, as well as Pelagonia from the Serbo-Macedonian and Sakarya (Rhodope) microcontinents respectively (Pe-Piper, 1998). The exact relative positions of these small continental blocks and their Mesozoic evolution is unknown, but the researchers (Sengör et al., 1984; Dercourt et al., 1986; Robertson et al., 1991; Dercourt et al., 1993) placed them in their paleogeography reconstructions at the northern margin of Gondwana based on stratigraphic and paleomagnetic data (Pe-Piper, 1998; Robertson et al., 1996). The convergence of these blocks continued during the Mesozoic and Cenozoic, resulting in the present nappe structure of the Hellenide Orogen. The Vardar ocean, for instance, closed subsequently from N to S in the Late Jurassic (Robertson, 1997). However, the exact tectonic phases during the closure and the amount of the sediments filling up the Pindos and Vardar oceans cannot be reconstructed, but most of the researchers believe that no large-scale displacement took place (Robertson et al., 1991; Wooler et al., 1992).

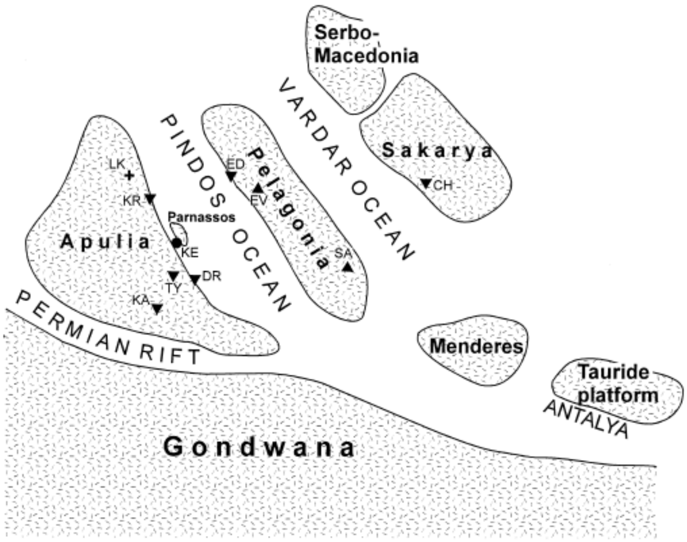

Fig. 7: Scheme modified from Robertson et al. (1991) presenting the early Jurassic microplate reconstruction.

2.3 Tectonostratigraphic overview

The Hellenides can be divided into three groups according to Aubouin (1959) and Jacobshagen (1986). Each of these groups include a number of tectono-stratigraphic units, which are presented from west to east in table 1. Next to this orogeny, the Menderes Massive and the Lycian Nappes are located in the area of Turkey (Renz, 1940, Aubouin, 1959, and Jacobshagen, 1986).

Foreland	External Hellenides	Central Hellenides: Median Crystalline Belt	Internal Hellenides
Pre- Apulian (Paxos) zone (Renz, 1940)	Plattenkalk unit (PS)	Beotian zone (BZ)	Pelagonian zone (PEZ)
	Phyllite- Quartzite unit (PQS)	Attic- Cycladic crystalline (ACC)	Vardar- Axios zone (VAZ)
	Ionian zone (IZ)	Tectonic window at Olympus	Circum – Rhodope belt (CRB)
	Gavrovo- Tripolitza zone (GTZ)	Tectonic window at Ossa	Serbo – Macedonian massive (SMM)
	Pindos zone (PZ)	Tectonic window at Almyropotamos (Evvia)	Rhodope crystalline (RC)
	Parnassus – Giona zone (PGZ)		
	Tripali Unit		

Tab. 1: Tectonostratigraphic units (zones) of the Hellenides area according to Auboin (1959) and Jacobshagen (1986).

For the understanding of this thesis some detailed information on the tectono-stratigraphic units of the External Hellenides are important to mention. The external Hellenides consist of (1) the Plattenkalk unit, (2) the Phyllite – Quartzite unit, (3) the Ionian unit, (4) the Gavrovo – Tripolitsa unit, (5) the Pindos zone, and (6) the Parnassos – Giona unit. In the following the mentioned units are described:

Plattenkalk unit (Fassoulas et al., 2004)
This unit has been low-grade metamorphosed, (HP/LT, 7-10 kbar/~350°C). The lithologies of this unit from the base to the top are: Marbles and phyllites of Upper Carboniferous- Upper Triassic age; thick layered dolomitic marbles of Upper Triassic – Lower Jurassic; a sequence of marbles alternating with nodular cherts of Lower Jurassic – Eocene; and the Middle Oligocene metaflysch consisting of fine-grained metaclastic sediments (Chatzaras et al., 2006; Bonneau, 1973; Bonneau, 1984; Bizon et al., 1976; Kopp & Ott, 1977 and Krahl et al., 1988).

Phyllite-Quartzite unit
This unit consists of quartzites and metaconglomerates with marble intercalations of Upper Carboniferous – Triassic age and is metamorphosed under HP/LT conditions (10±3 kbar/ 400±50°C) (e.g. Chatzaras et al., 2006).

Ionian unit
The Ionian unit can be regarded as an inverted sub-basin of the Tethyan margin. A representative stratigraphic column was presented by Karakitsios (1995). At the base of the succession, Early to Middle Triassic evaporites were deposited and are overlain by a unit of heterogeneous carbonates that contain cherty limestone layers, clastic material and shales of different colors (from Jurassic up to the late Eocene). On top of these rocks, pelites and sandstones of the Oligocene flysch were deposited.

Gavrovo- Tripolitsa unit
This unit begins with Tyros beds, a volcanoclastic sequence of early to mid-Triassic age, which is overlain by late Triassic – Eocene shallow water carbonate rocks and ends at the top with flysch deposits of Upper Eocene – Oligocene age according to Bonneau (1973,1984); Bizon et al., (1976), Kopp & Ott (1977) and Krahl et al., (1988) quoted in Chatzaras et al., (2006).

Pindos unit
The deposition of the deep-water carbonate lithologies of the Pindos zone begins in the early to mid-Triassic and lasts until the late Cretaceous to Paleocene times. The topmost formation of this unit is the Paleocene-late Eocene flysch (Chatzaras et al., 2006 and citations therein).

Parnassos – Giona unit
This unit is located in central Greece north of the Gulf of Corinth and consists mainly of a neritic carbonate platform that formed from Upper Triassic to Upper Cretaceous including three interlayered bauxite horizons (b1 from Middle Jurassic to Upper Jurassic, b2 from Upper Jurassic to Lower Cretaceous, and b3 from Cenomanian to Turonian).

2.4 Geological Setting of the Dodecanese

In this chapter, the geological setting of the Dodecanese is described with the focus on Variscan Units and related topics. Desio (1931) was the first to describe in detail the geology of the Dodecanese Islands. For Kalymnos Island, he reported the existence of Cretaceous limestones and schists along the coast of Emborio.
In Kalymnos and Leros Islands, a metamorphic basement of medium grade and a group of low-grade metamorphic rocks of Upper Paleozoic age are present (Desio, 1931; Christodoulou, 1966, 1969; Dounas et al., 1972 and Dürr et al., 1978). For the areal distribution of these metamorphic basement rocks see figure 8.

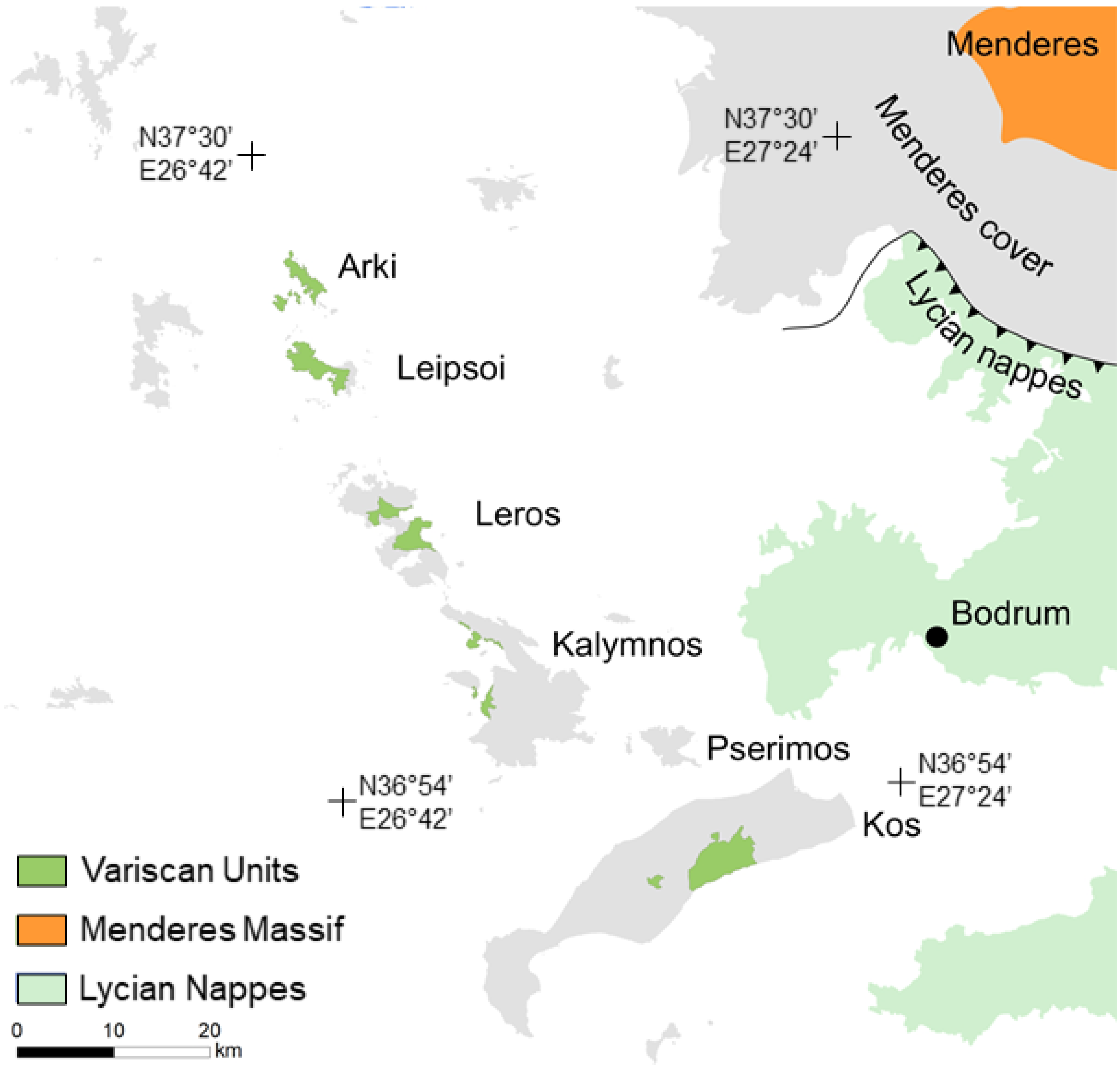

Fig. 8: Overview of the Variscan units in the Dodecanese Islands and western parts of Menderes Massif (compiled from Franz et al., 2005; Jolivet et al., 2004 and geologic maps of IGME).

Dounas et al. (1972) suggest that this Upper Paleozoic unit is covered transgressively by Upper Mesozoic limestones. These carbonate rocks are overthrusted by carbonate rocks of similar lithology and age.
Brinkmann (1971) proposed that Leros, Kalymnos, and the neighboring islands Lipsi and Arki can be considered as the border area of the Menderes Crystalline Complex. According to Dürr et al. (1978) Agathonisi Island, which geographically is west of the Büyük Menderes, belongs to the marble envelope of the Menderes Massif.
Dürr et al. (1978) suggested a new tectonic subdivision with specific unit names based on their investigations (Fig. 9). The basal unit, which is called "Temenia Unit", comprises three formations, which show signs of lower greenschist metamorphic overprint according to Katagas & Sapountzis (1977b). From bottom to the top these three formations are: first, a schistose sequence with thin heterogeneous, interlayered limestones, with the presence of fossils that provide an Upper Paleozoic age as proposed by Christodoulou (1966, 1969) and Dounas et al. (1972). Secondly, come marbles with a well-preserved metamorphic layering and last but not least, a quartzitic formation. Dürr et al. (1978) suggested that the Temenia Unit is reversed on Leros and consists of lithologies very similar to the Kara Dag Unit of the Lycian nappes (Brunn et al., 1971; de Graciansky, 1972). Also, blueschist blocks have been found in Leros according to Katagas and Sapountzis (1977b).
The unit above Temenia is called Marina unit. At the base consists of amphibolites, kyanite-staurolite micaschists (Katagas & Sapountzis, 1977a) and some interlayered marbles. This basal sequence is

transgressively covered by a probably Permo- Triassic formation with the name Val-Camere (Dürr et al., 1978). This is followed by dark dolomites and fossiliferous limestones of Upper Triassic – Liassic age. A sequence of layered cherty limestones is cited by Dürr et al. (1978). Alternative age dates are ?Upper Jurassic (Christodoulou, 1969) to ?to Lower Cretaceous. According to Brinkmann (1967) and Bernoulli et al. (1974) these three subunits correspond to specific formations of the Lycian nappes (Karaova, Gereme and Cal Dag).

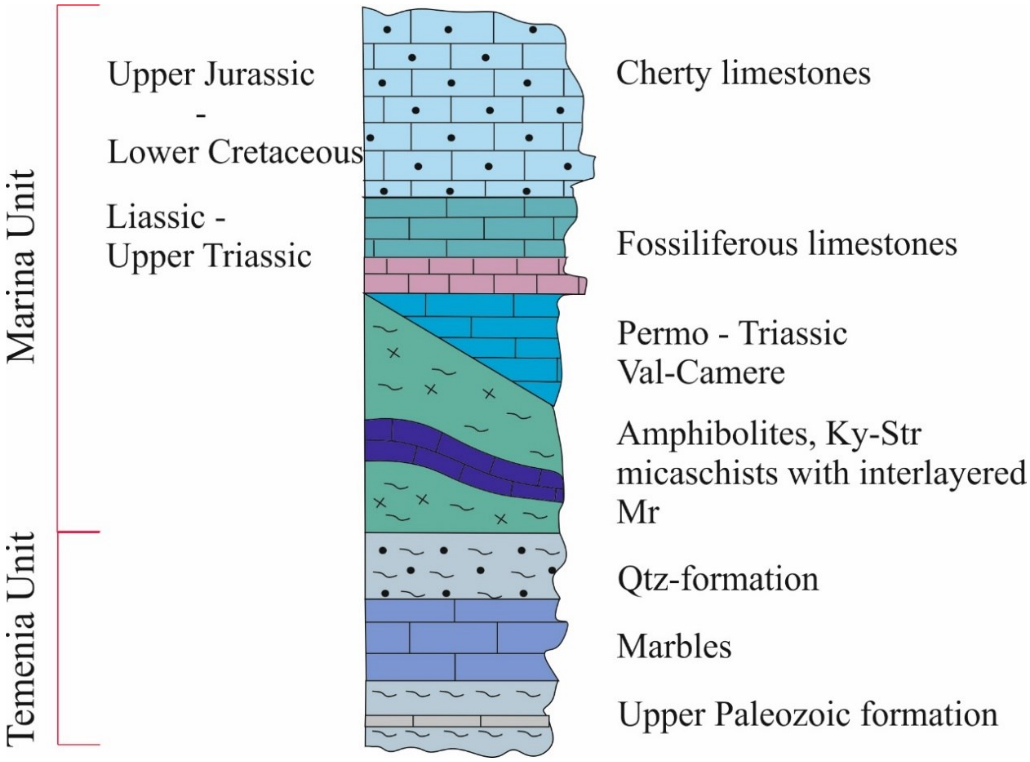

Fig. 9: Schematic stratigraphic column based on Dürr et al. (1978), descriptions for the Crystalline Belts in Kalymnos island (Dodecanese, Greece).

Parts of the island of Kos host a quartz-bearing monzonite intruding into the existing units in three events:

- A first sequence that is equivalent with the Temenia Unit of Leros and Kalymnos, which have been described above. This means that the formations (phyllites, marls and limestones) have a Paleozoic age. This unit has undergone contact metamorphosis by the plutonic intrusion and the mineral assemblages indicate a maximum temperature of 800 °C and pressures between 4-6 kbar, pointing to 13 km minimum intrusion depth. The temperature in the surrounding rocks was around 400 °C according to Altherr et al. (1976).

- A thrust brings in contact Mesozoic – Eocene limestones with the above described sequence. These limestones were not influenced by the intrusion and according to Dürr et al. (1978) and Altherr et al. (1976), the emplacement took place after the intrusion and the erosion of the plutonite.

- Neogene Sediments of lacustrine and fluvial origin cover all the previous units, mixed with ignimbrite rocks.

Dürr et al. (1978), Besang et al. (1976) and Altherr et al. (1976) mentioned that K-Ar dating on hornblendes of the monzonite gave cooling ages of 11.9 ± 0.4 Ma. The main conclusion of Dürr et al. (1978) is that the northern Dodecanese islands Arki, Lipsi, Leros and Kalymnos are part of the Lycian Nappes.

2.5 Geological mapping

The geological mapping was carried out in September and in this month, the conditions are favorable due to less vegetation and no rain. During the scouting trip, the Myrties area was visited first. After documenting the findings there, the focus shifted to the Kefala/Rachi areas to the north. In both areas, Variscan basement rocks were observed. However, the lithostratigraphic succession showed different units, which is described in more detail in the lithostratigraphy chapter. In between Myrties and Kefala/Rachi, the outcrop at Emporio was studied briefly.

The final decision was to focus on the Kefala/Rachi areas, because it is an area of a suitable size with very good outcrop conditions and favorable topography. 10 days of fieldwork in the Kefala/Rachi areas had as a result the creation of a geological map of the studied area in scale 1:10 000. It is presented in figure 10 and the complete geological map with the structural geologic measurements can be found in the attachment. The geologic map is draped over the hillshade model of the island. The DEM of Kalymnos used for the hillshade was created from line data digitized in ArcGIS 10.1.

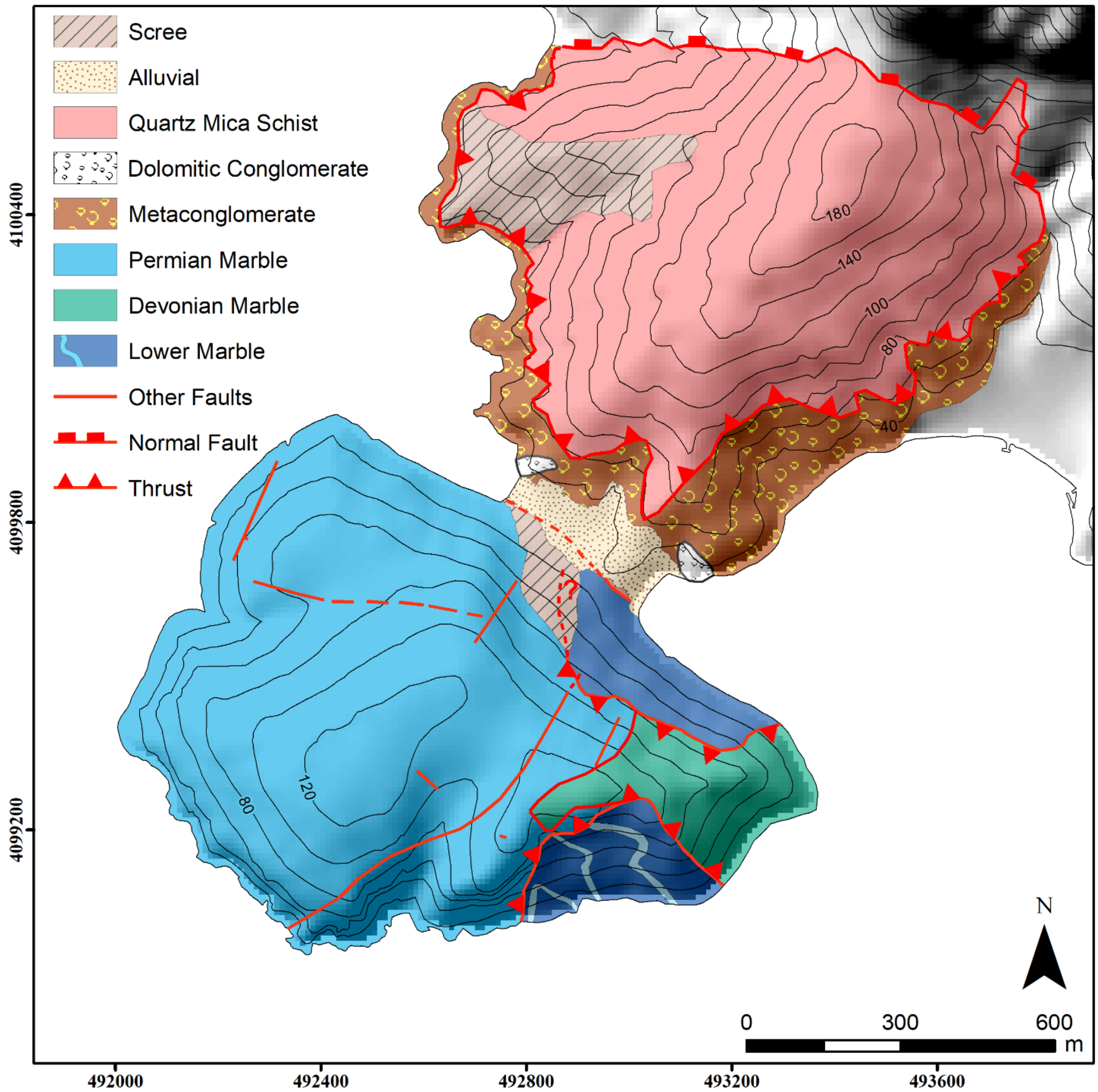

Fig. 10: Geological map of Kefala/Rachi areas with major faults draped over the hillshade model of Kalymnos Island.

3 Lithostratigraphy

In this chapter, a synthesized lithostratigraphic column of the study area in the NW part of the Island of Kalymnos is presented (Fig. 11). The main and most complete lithostratigraphic column covers the Kefala peninsula. At the area of Myrties a different unit was observed in the position of the Quartz-Mica schist – this difference is shown in the small column in figure 11. Also, a detailed description of the units and lithologies that have been observed and mapped is given, based on the 1:10 000 scale geologic map and supported by geochronological and paleontological data.

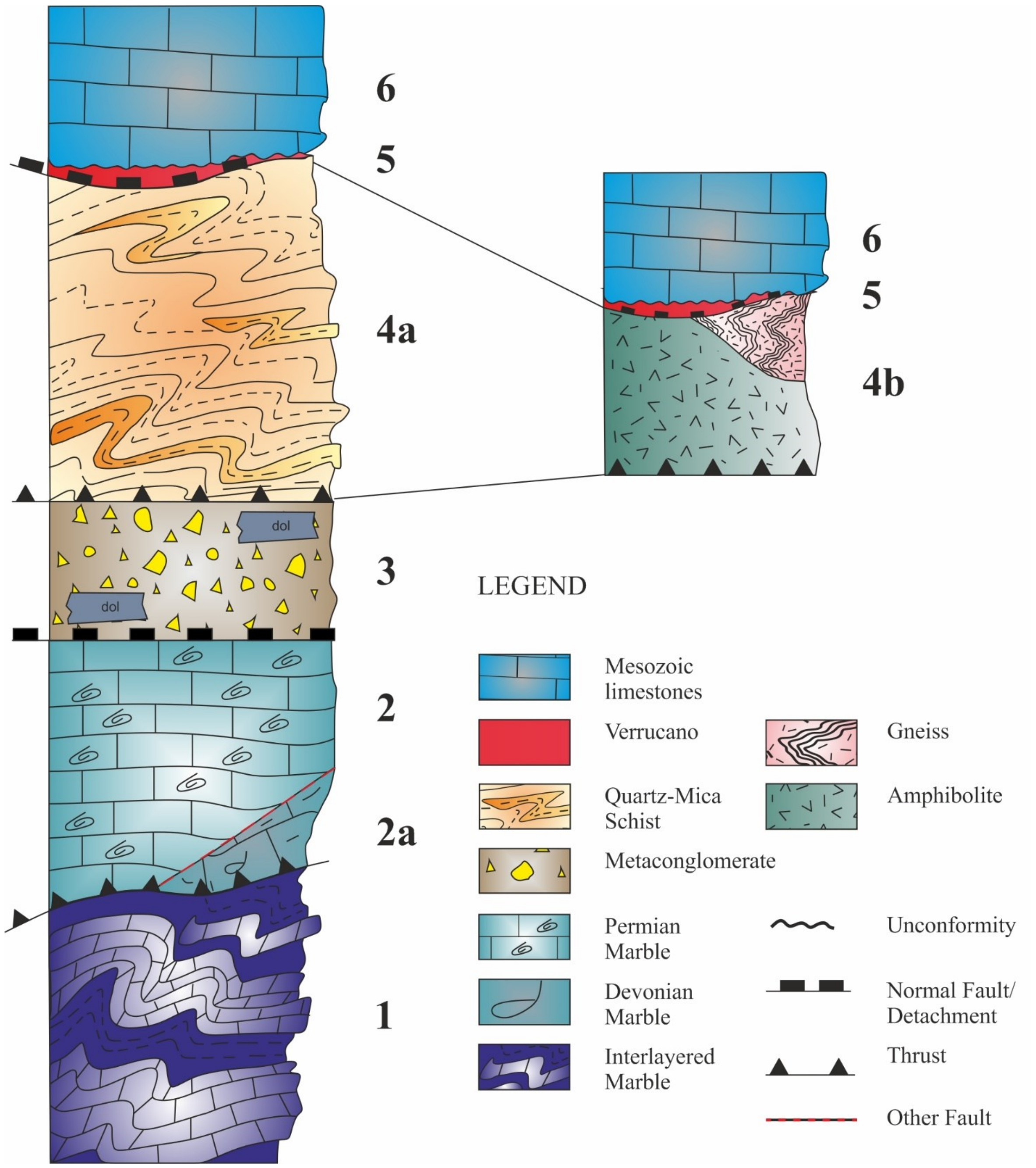

Fig. 11: Tectonostratigraphic column of the study area in the NW part of Kalymnos Island. The numbers refer to the following units: 1) Interlayered Marble Unit 2a) Devonian Marble Unit 2) Permian Marble 3) Metaconglomerate 4a) Quartz Mica Schist Unit 4b) Amphibolite-Gneiss Unit 5) Verrucano 6) Mesozoic Limestone Unit.

Lower greenschist facies metamorphic overprint due to a series of tectonic events affected the limestones of Kefala peninsula. Therefore, further in the text, they are referred to as marbles. The focus of investigations was the deformation and on the dating of the rocks and not on the stratigraphy and the depositional environment. Consequently, only a small proportion of a variety of samples was useful for further investigation. Furthermore, due to the lack of a continuous section, samples could not be taken in the best fitting locations, thus limiting temporal- spatial characterization of the deposition area.

3.1 The Interlayered Marble Unit (1)

The Interlayered Marble Unit forms a small part of Kefala peninsula with two areas of outcrops and a stratigraphic thickness of 75 to 30 m. The two areas of outcrops are located in the SE and the NE part of the peninsula (Fig. 12 and 13). This unit has a dome shape and is exposed underneath a folded thrust, which has been observed and mapped during the fieldwork, so this lower unit can be characterized as a tectonic window. Two dominant lithologies have been observed: marbles and metapelites. The marbles are dark blue-grey colored with some thin white veins with calcitic composition (Fig. 14). In the NE part of the Kefala peninsula, a dark brown metapelite crops out in the core of an anticline, which shows actinolite overgrowth (Fig. 15).

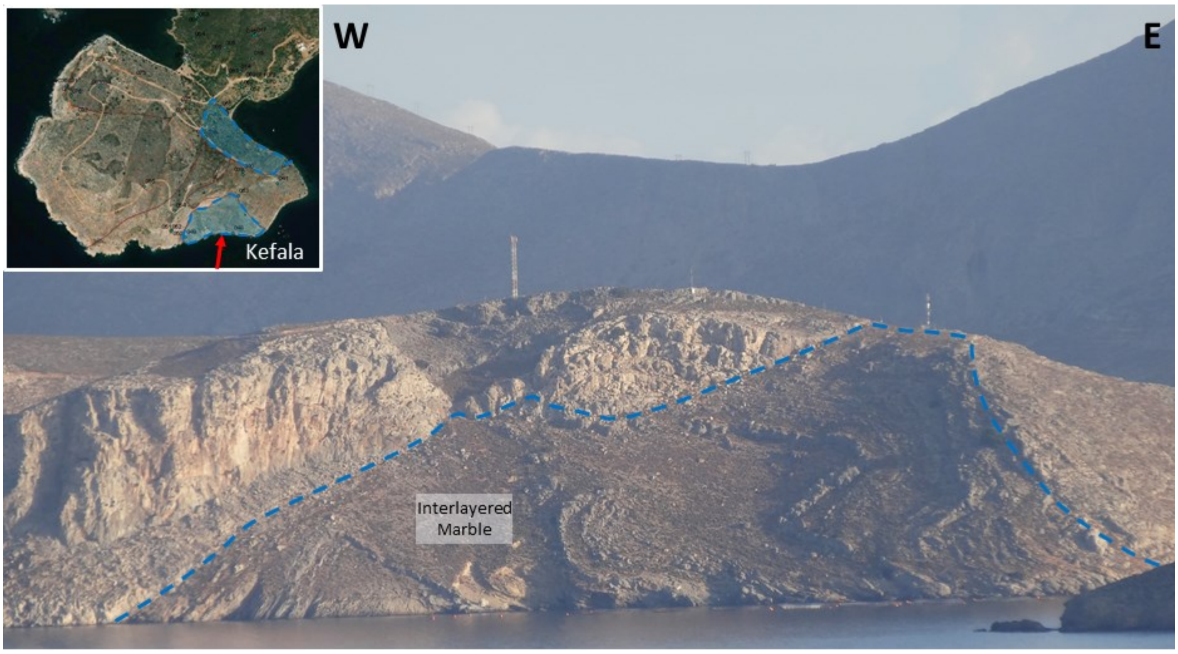

Fig. 12: View from the sea onto the SE outcrop of the Interlayered Marble Unit showing large-scale folding.

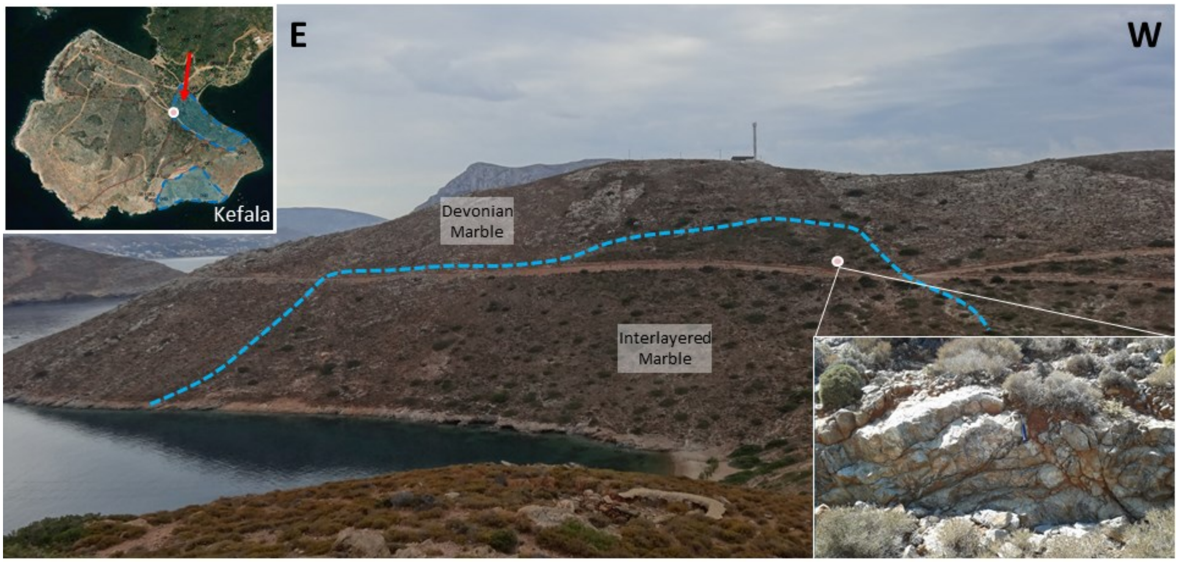

Fig. 13: Overview of the southern tip of Kefala peninsula showing the NE-outcrop of the Interlayered Marble Unit and its contact to the Devonian Marble. In the Inset image at the lower right corner, we can see the core of the antiform in the Interlayered Marble Unit that consists of Metapelite/ Quartzite.

Crinoids are also present, but rarely and only in the NE outcrop of the Kefala peninsula, thus the depositional age of the unit could not be determined. Also, no sample for geochronological analysis could be taken, as these lithologies are exposed along a steep topographic slope. The marbles are folded into large-scale upright folds, but are better exposed at the SE area of the peninsula (Fig. 12). Thin quartzitic layers (5 to 30 cm) are frequently seen within the metapelites, especially when the layers are folded and have their maximum thickness in the hinge. The interlayering is shown in figure 14 for the NE and the SE area.

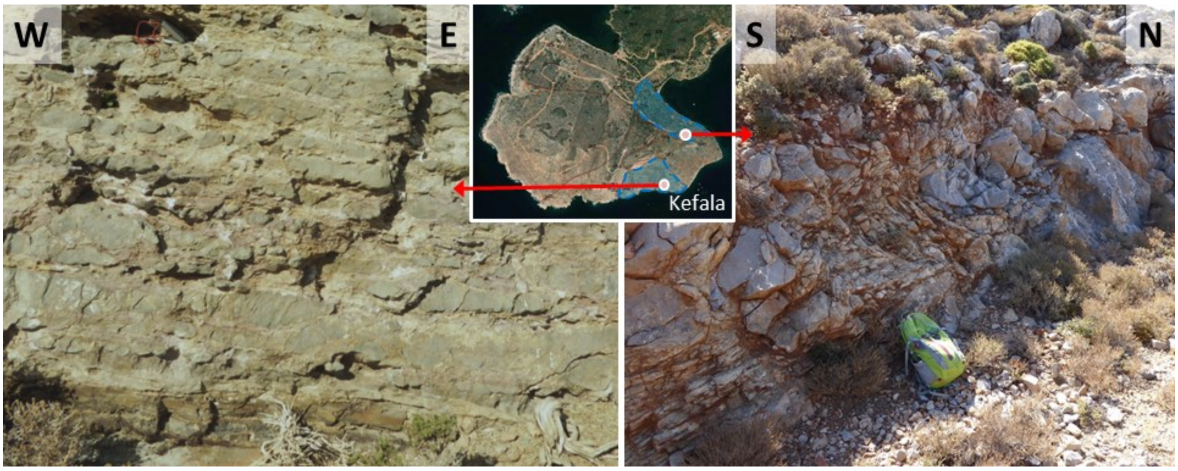

Fig. 14: Detail view of the marble-metapelite intercalation in the SE area (left image). Note the geologic compass for scale at the top-left. Right image: Overview photograph of the marble and metapelite interlayering in the NE-area. The dark blue-grey marbles contain calcite veins at an irregular spacing.

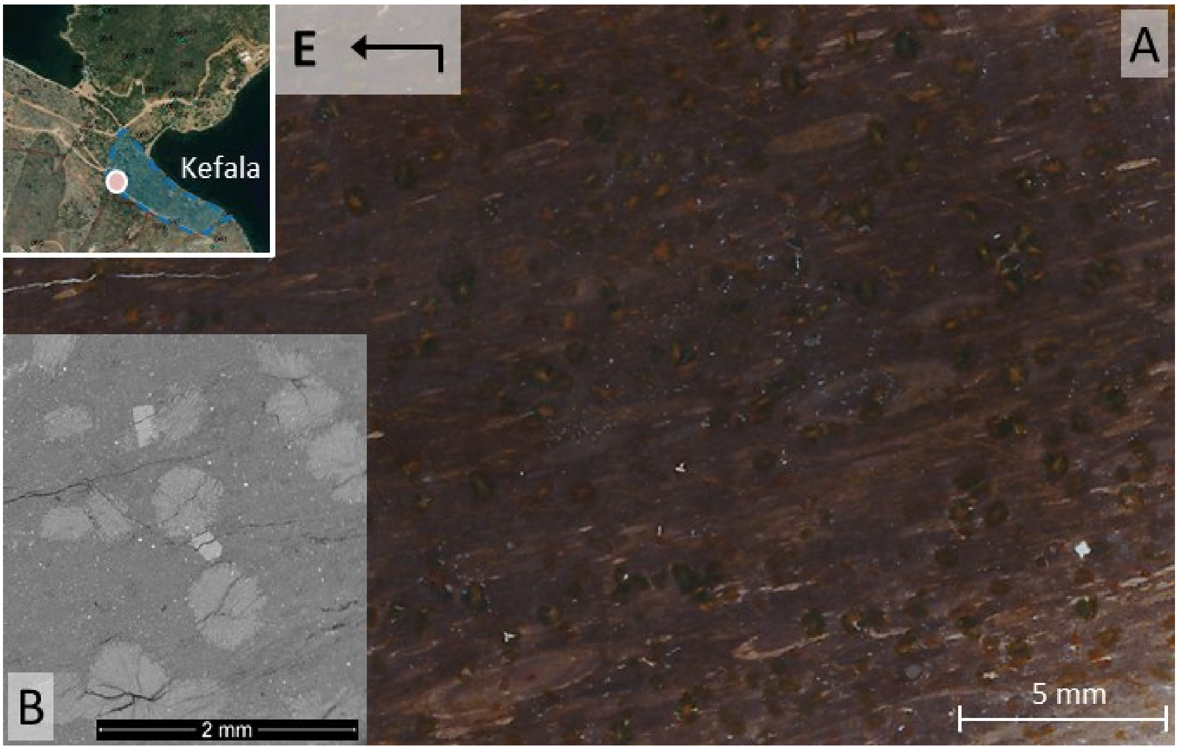

Fig. 15: In the white marble lithology in the NE-area, a soft, brown lithology can be observed. It contains green actinolite in radiating spots distributed all over the lithology and growing on an older, pervasive foliation. This foliation is created by elongated and arranged minerals. A) Overview thin section photograph of sample KA014010 in linear polarized light showing the older foliation and the actinolite overgrowth. B) Detail SEM image with actinolite spots that contain also stilpnomelane and rectangular apatite.

3.2 Devonian Marble Unit (2a)

At the western side of the peninsula, a massive white – blue marble crops out, above the interlayered marble-phyllite sequence (Fig. 16). It is very fossiliferous, and it contains brachiopods, ammonoid cephalopods (Goniatids?) and crinoids based on which a Devonian age is probable (Fig. 17 and 18). Thus, it is regarded as the Devonian Marble Unit that is thrusted onto the Interlayered Marble Unit. The fossils are slightly deformed and elongated, but still well recognizable. The marble is folded and contains dolomitic veins that are also folded, but at a higher frequency.

Fig. 16: View from Rachi on the Devonian Marble Unit located above the Interlayered Marble Unit and next to the Permian Marble Unit on Kefala Peninsula.

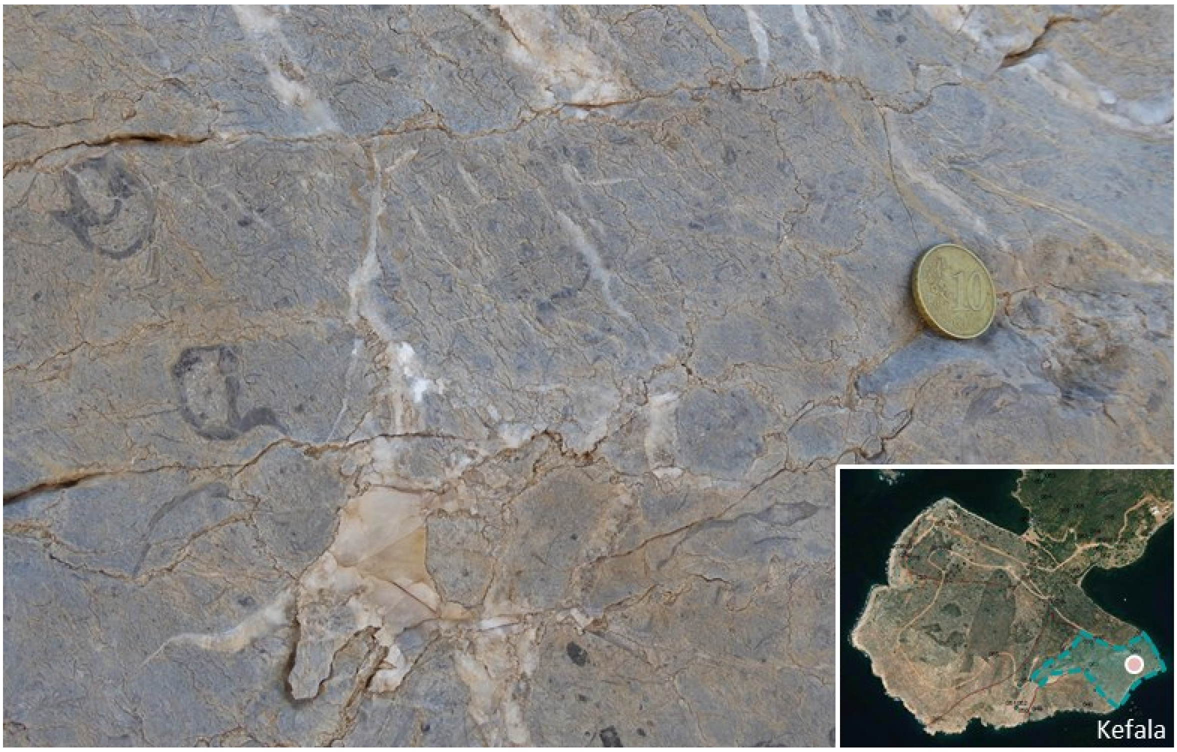

Fig. 17: View of parts of the fossil content of the Devonian Marble Unit containing brachiopods, ammonoid cephalopods (Goniatids? – middle-left) and crinoids (center-bottom). The fossils are slightly deformed, but well recognizable.

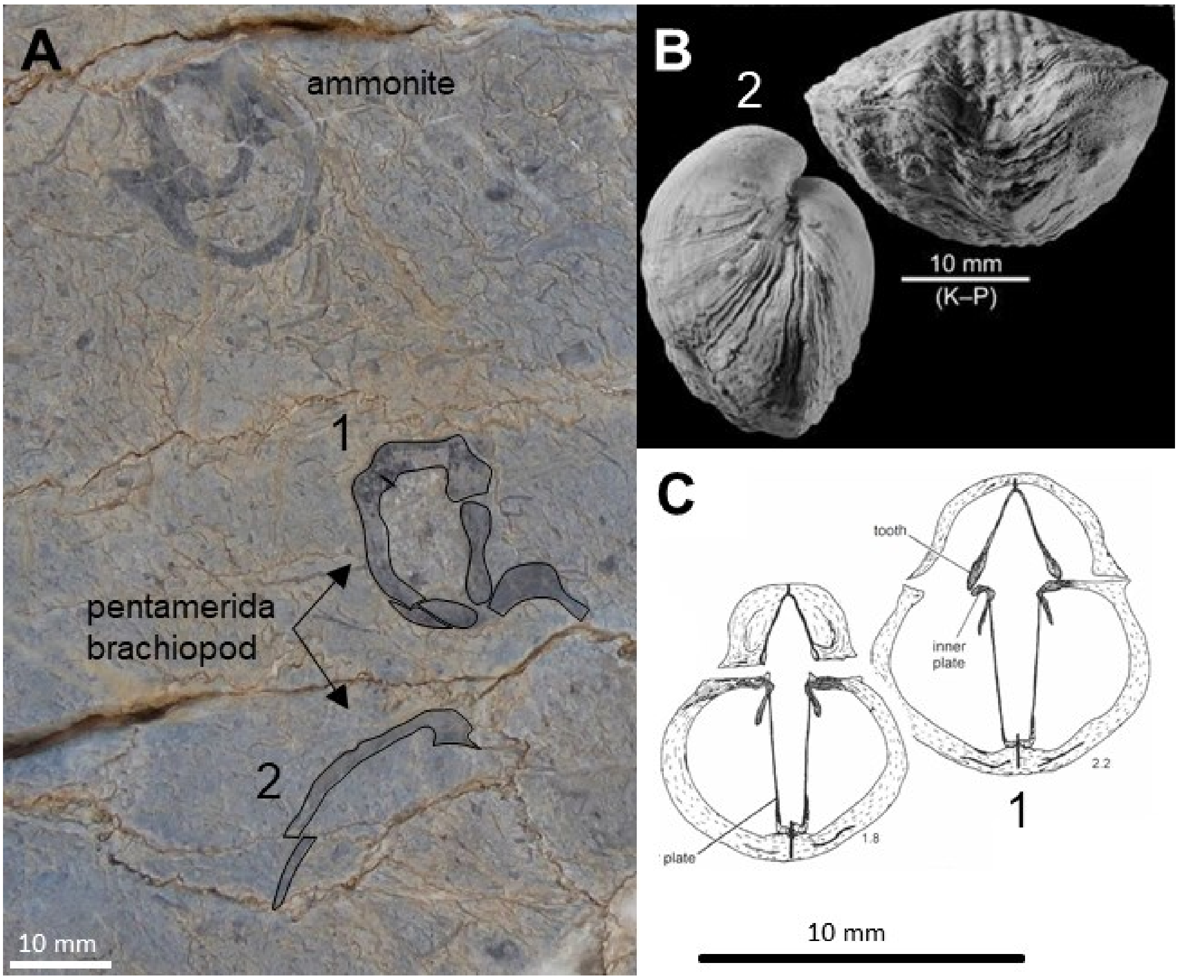

Fig. 18: Detail view of the Devonian Marble Unit from Fig. 17 showing the interpreted fossil content. The focus is on the brachiopod of the order of Pentamerida, genus Parastophinella reversa (Schuchert & Cooper, 1931). The order Pentamerida the only order to become extinct during the Late Devonian (Gould & Calloway, 1980; Mottequin et al., 2014 and citations therein). Fig. 18a: interpreted outcrop photograph. Fig. 18b: Middle Devonian Pentamerida from the eastern Anti-Atlas, Morocco (Halamski & Baliński). Fig. 18c: Serial section of Parastophinella reversa (Jin & Copper, 2000). The numbers in the figures indicate the links between the outcrop photograph and the type-fossil details from literature.

3.3 Permian Marble Unit (2)

The Permian Marble forms the main lithology of Kefala peninsula since it occupies 75% of the area (Fig. 19). This marble consists of dark grey and white marbles. Both marbles are very low grade metamorphosed as they contain really well preserved and just slightly deformed fossils (Fig. 20 to 22). The white marbles are rich with fossils like corals (Fig. 23), echinoderm fragments, brachiopods and fusulinidae, endothyrid and schwagerinidae foraminifera. The marble contains a dark grey colored zone that is mylonitic (Fig. 24) with a lot of kinematic indicators such as δ- and σ- clasts.

Fig. 19: View on the Kefala peninsula and the Permian Marble Unit. Note the darker areas of vegetation that occur only in this unit.

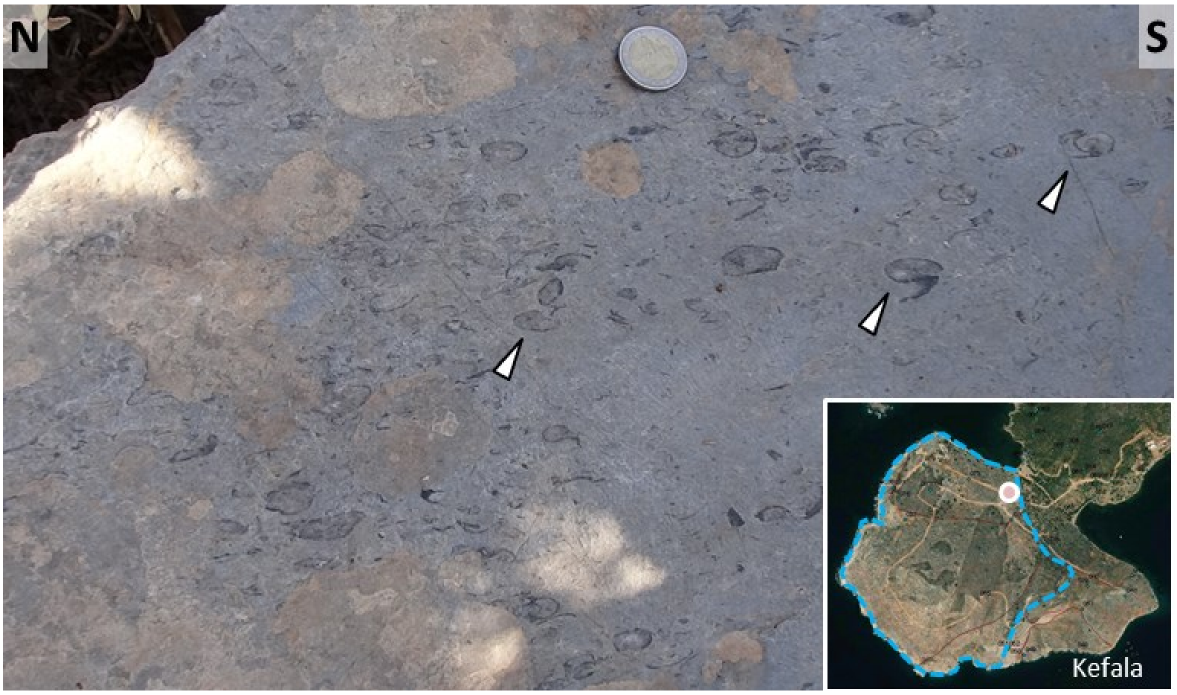

Fig. 20: Slightly deformed fossils (white arrows) in the light grey zone of the Permian Marble at the border of the mylonitic shear zone.

Fig. 21: Outcrop photo of Permian Marble Unit with the white, undeformed fossil-bearing zone containing echinoderm fragments, brachiopods and foraminifera (white arrows).

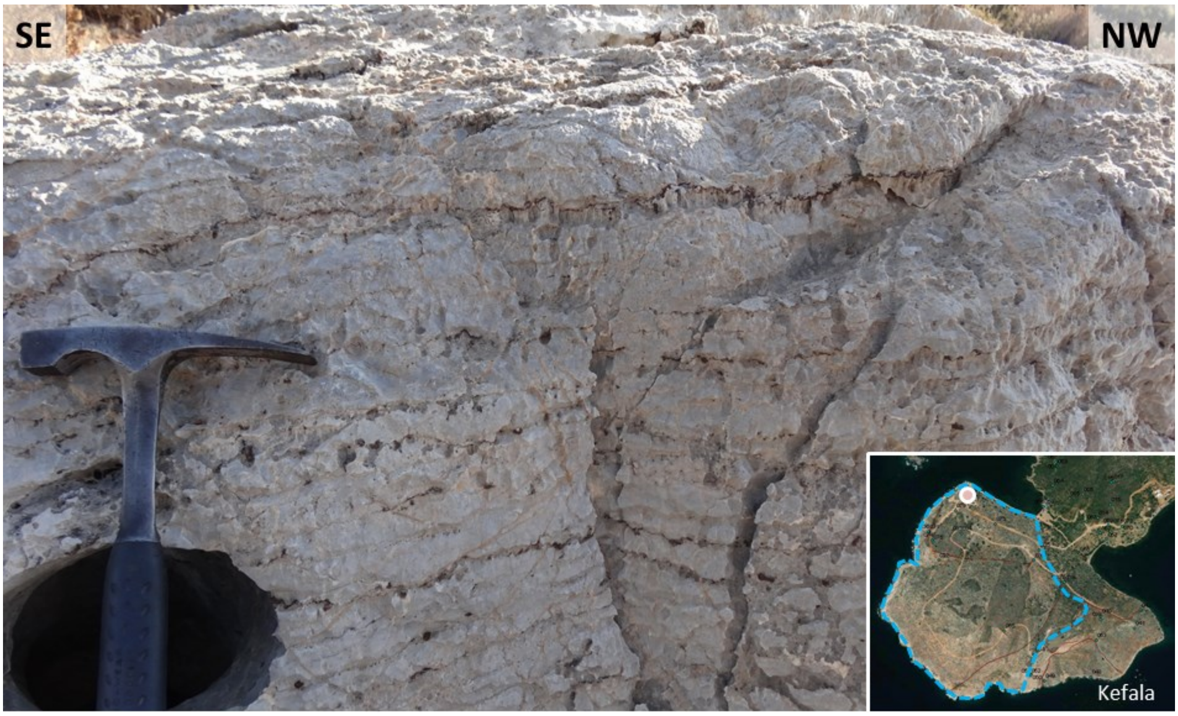

Fig. 22: Light grey colored marble of the Permian Marble Unit that is slightly deformed and fossil bearing.

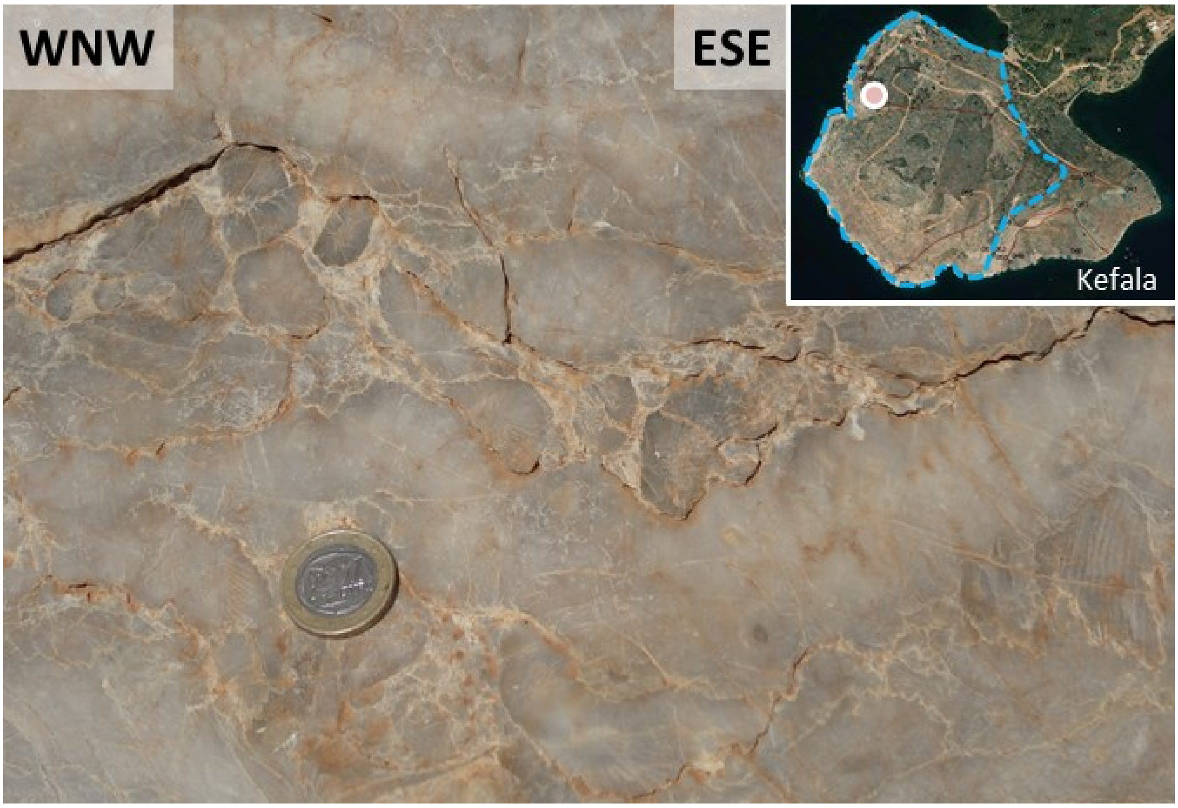

Fig. 23: Corals in the Permian Marble Unit belonging to the organic build-up part of the reef core.

Fig. 24: View of the dark grey marble of the mylonitic zone with abundant kinematic indicators. The white arrows indicate SC' structures with rotated clasts.

Within this unit, a mosaic of several lithofacies-types is distinguishable. They are referred to with their names from the facies nomenclature of Wilson (1975), see also figure 25. The fossils were identified by Bernhard Hubmann and the lithofacies-types developed are as follows:

(a) Foraminiferal wackestone

Contrasting inconsistent micritic matrix contains in nests non-fusulinid foraminifera. Individual sizes of the endothyrid foraminifera (Globivalvulina) vary between 600 and 730 µm.

(b) Peloids grainstone

Peloids are elongated and parallel arranged due to the tectonic overprint but originally were rounded to sub-rounded in shape. The majority of peloids shows microstructures in their central parts. This suggests that they originate from micritised bioclasts rather than fecal pellets (Plate 1, E). Original micritic matrix appears to have been washed out by wave motion.

(c) Oncoid rudstone

Elongated spherical oncoids reveal indications of originally layered structures. In some cases, nuclei of brachiopod (?) shells (Plate 1, B) or skeletal grains (Plate 1, H & I) form centres of biogenous cortices. Oncoid cortices show apparitional concentric laminations formed by thin calcified filaments of most probably cyanobacteria and spongiostromate sediments.

(d) Fusulinid pack- to rudstone

Fusulinids occur either in loose accumulations (Plate 1, A) or even intergranular (sutured with stylolites; Plate 1, D) contacts. Fusulinids are generally accompanied by fragments of echinoderms (Plate 1, A & D) but in matrix- rich sediments, they may also be associated with calcareous gymnocodiacean algae (Plate 1, D) and bryozoans (Plate 1, G).

These different types of lithofacies point to a structured shallow water depositional environment on a carbonate shelf under low and temperately high to high energy conditions. Low wave energy areas are documented by mud- to wackestones containing the stationary semi-infaunal foraminifera Globivalvulina. Peloidal grainstones indicate a deposition in high to moderate energy environment, presumably above fair-weather wave base. Initially mineralized organic hard parts (e.g. mollusc and brachiopod shells) were totally fragmented due to reworking by wave or tidal processes in a relatively shallow–water environment. Extensive bioerosion by endolithic organisms caused micritic envelops of bioclasts.
Moreover, the oncoids (lithofacies-type c) suggest typically shallow marine, temperate to high wave energy conditions. A depositional area within a shallow platform interior (corresponding to SMF 13) is proposed since the oncoids lack abrasion and therefore long-distance transport can be excluded. Fusulinids were bottom-dwelling forms confined to tropical-subtropical shallow water (e.g., Ross et al. 1977). However, shells are often abraded to various degrees indicating allochthonous deposition by wave and current action. The presence of Pseudofusulinoides and Robustoschwagerina allows a time classification into the Sakmarian/Artinskian time span. A lower Permian age (i.e. “middle Rattendorf stage” to “lower Trogkofel stage”) was already proposed by Kahler (1987) for the “Fusulinid limestones” at Kefala peninsula, which were first mentioned by Thorbecke (1987).

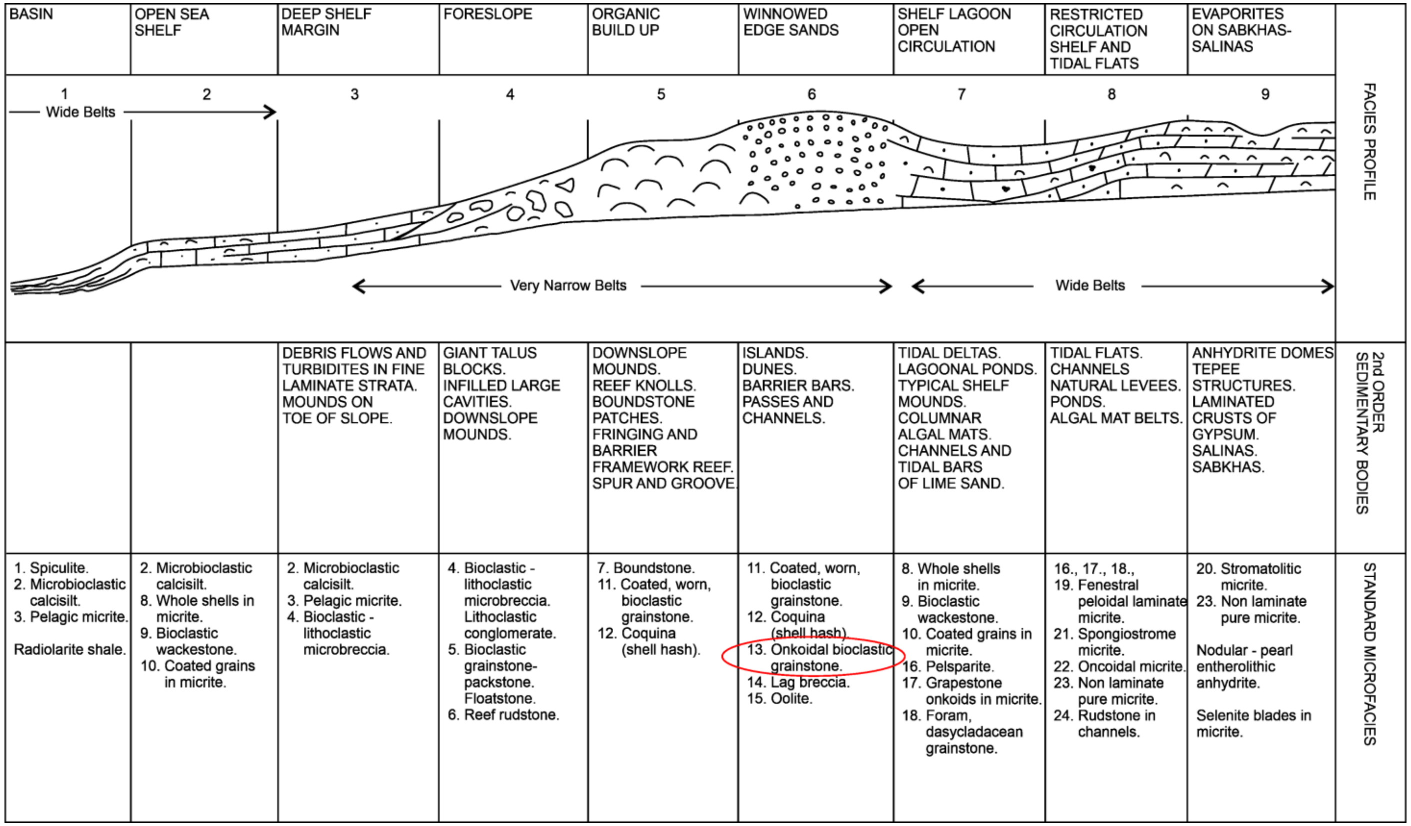

Fig. 25: Nomenclature of facies profiles after Wilson (1975). The red circle indicates the dominant facies in the Permian Marble Unit.

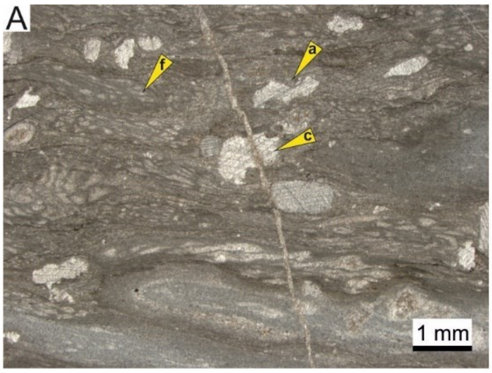

Plate 1, A.: KA014008, Densely packed echinoderm-fusulinid rudstone with strong signs of deformation. The fusulinid shells are elongated along the shear direction (f) and show tangential contacts. Echinoderm fragments (e) are more resistant to shear influence but may be antithetically sliced (a). Most of the echinoderms are presumably crinoids: (c) shows a crinoid columnar in cross-section exhibiting the axial canal.

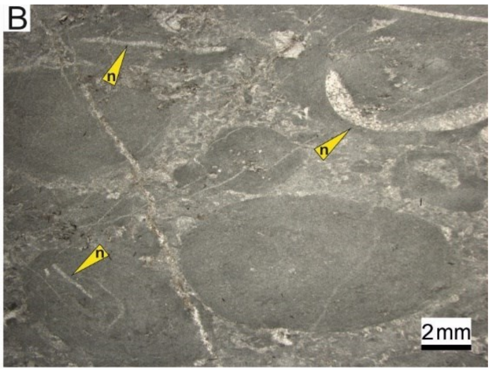

Plate 1, B.: KA014009, Moderately-sorted elongated oncoids in peletoidal grainstone matrix. In some oncoids, ‘ghost structures’ of primary lamination are recognizable. Brachiopod or bivalve shell fragments (n) forming nuclei of biofilm-generated cortices.

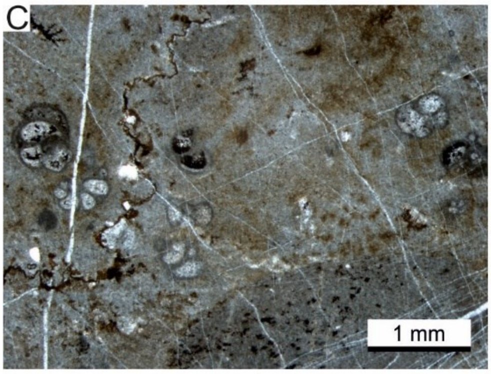

Plate 1, C.: KA014012, Cluster of endothyrid foraminifera (Globivalvulina sp.) in blotched micritic matrix

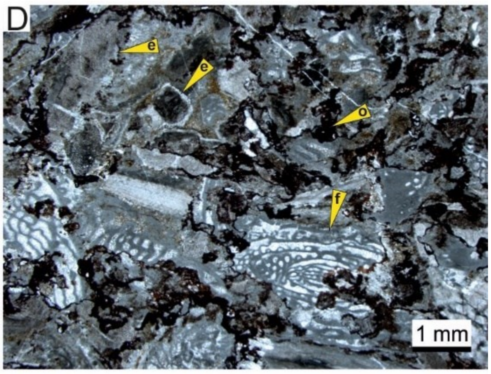

Plate 1, D.: KA014024, Densely packed bioclastic packstone (stylobreccia) dominated by fractured components of fusulinids (f) and echinoderms (e) which are bounded by stylolites. Opaque residuals (o) are concentrated along dissolution seams

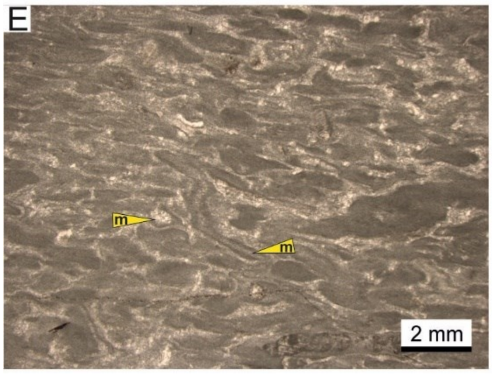

Plate 1, E.: KA014022, Peloidal grainstone with small and irregularly shaped peloidal grains. The irregular/elongate shape may suggest that they are micritized skeletal grains deriving from mollusk or brachiopod shells (m)

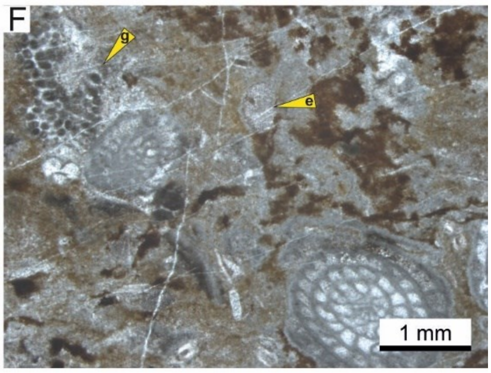

Plate 1, F.: KA014024, Fusulinid float- to rudstone containing fragment of gymnocodiacean thallus (Gymnocodium ?) in oblique section (g) and echinoid spine (e). Brownish patches are due to the partial enrichment of carbonate-insoluble substances during pressure solution

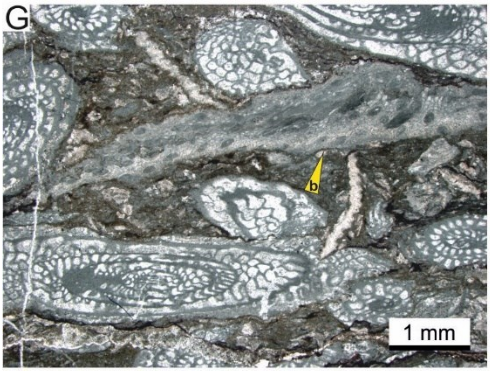

Plate 1, G.: KA014025, Fusulinid rudstone with Pseudofusulinoides in various sections and a cystoporate bryozoan colony (b) In this sample less fracturing can be observed than the (D) thin section.

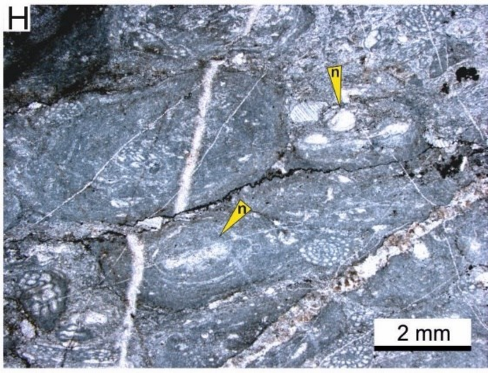

Plate 1, H.: KA014008, Fusulinid foraminifers bearing oncoid rudstone with fine grained peletoidal/bioclastic matrix. Cortices of oncoids grew around different bioclastic nuclei (n) and show considerable lamination which were probably caused by trichomous calcareous cyanobacteria

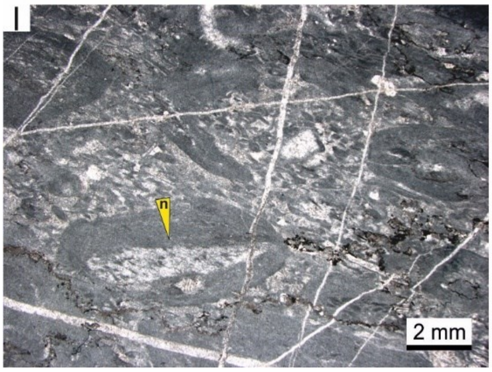

Plate 1, I.: KA014009, Oncoids in peloidal grainstone matrix.

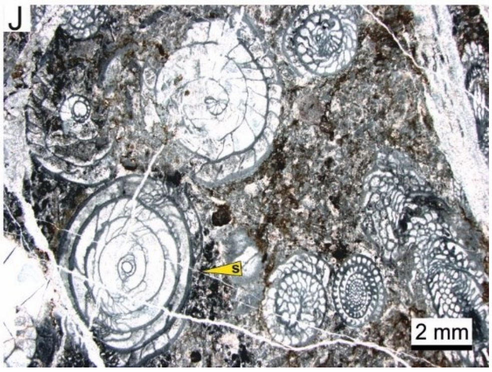

Plate 1, J.: KA014025, Fusulinid rudstone with differently heavily corroded shells. Schwagerinid foraminifera (Robustoschwagerina; s) in axial section

3.4 Metaconglomerate Unit (3)

This lithology shows signs of low-grade recrystallization similar to the units mentioned before. The meta-conglomerate lies between the Quartz-Mica Schist Unit and the marble dominated succession on Kefala (Fig. 26). The matrix of the meta-conglomerate is difficult to identify, since it is strongly weathered in the outcrops and only soft sediment or soil can be observed. In this strongly weathered matrix, two big blocks with recrystallized calcitic matrix and dolomitic clasts are embedded (Fig. 27 and 28). Also, at the SE side of the Rachi area, two large mafic blocks are embedded within the metaconglomerate.

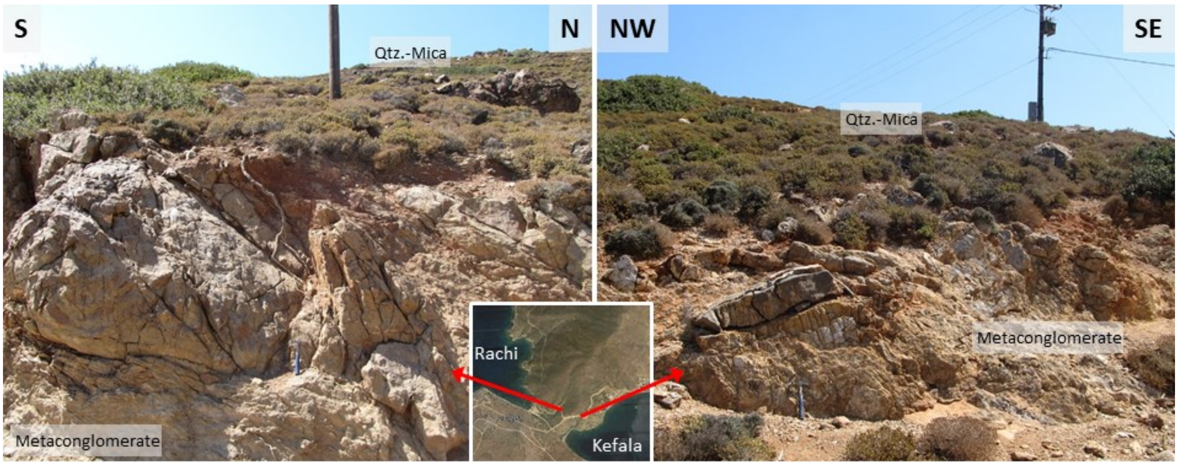

Fig. 26: Example outcrops of the Metaconglomerate Unit beneath the Quartz-Mica Schist Unit at the SW-part of Rachi. Just above the Metconglomerate, the Quartz-Mica Schists start outcropping. In several spots larger blocks of harder, cemented metaconglomerate are visible. Sometimes, a dolomite coating is present.

Fig. 27: View on the metaconglomerate at Rachi. Note that there are two subfacies of this lithology: A darker, more weathered and a lighter colored, more cemented facies. In this view, the western block with recrystallized, more cemented matrix can be seen.

Fig. 28: The Metaconglomerate Unit in the outcrop at Rachi showing various components including marble clasts and dolomitic fragments.

3.5 Quartz-Mica Schist Unit (4a)

The Quartz-Mica Schist is the dominant lithology of Rachi area (Fig. 29). This unit is thrusted on top of the Metaconglomerate Unit. On top of the Quartz-Mica Schist Unit, a low angle normal fault juxtaposes the Mesozoic limestones against the Quartz-Mica Schist Unit. Other outcrops occur along the western coast of Kalymnos and one outcrop at Emporio was sampled for the Quartz-Mica Schist lithology (Fig. 30). Since the sample was used for geochronology, it is described here as well along with examples from Rachi.

The Quartz-Mica Schists show a specific mineral assemblage consisting of quartz, white micas, some small plagioclase grains and secondary calcite crystals (Fig. 31 and 32). This mineral assemblage including calcite and recrystallized feldspar is characteristic of upper greenschist to amphibolite facies. Macroscopically, the schist has a red brownish color because of oxidation. The rock is strongly layered with white mica and prominent quartz zones, which were highly deformed. A further detailed description of the structural elements in this rock type can be found at the structural geology chapter.

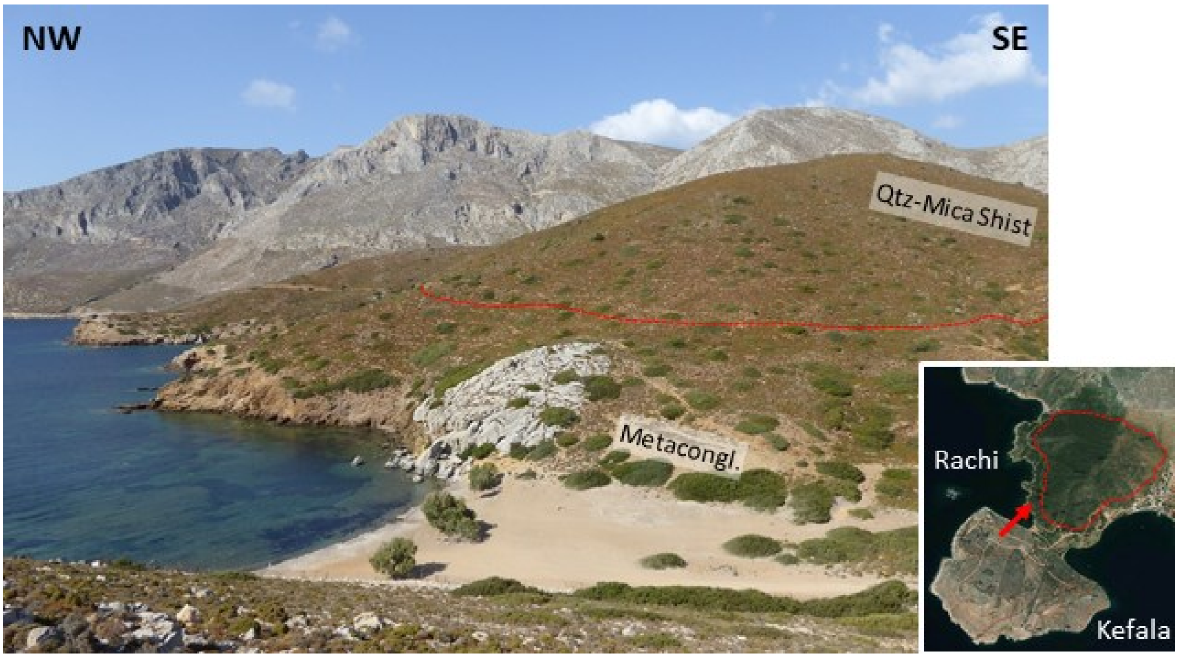

Fig. 29: View from Kefala towards Rachi onto the Quartz-Mica Schist Unit thrusted onto the Meta-conglomerate Unit. In the background, the light-grey colored Mesozoic limestones can be seen.

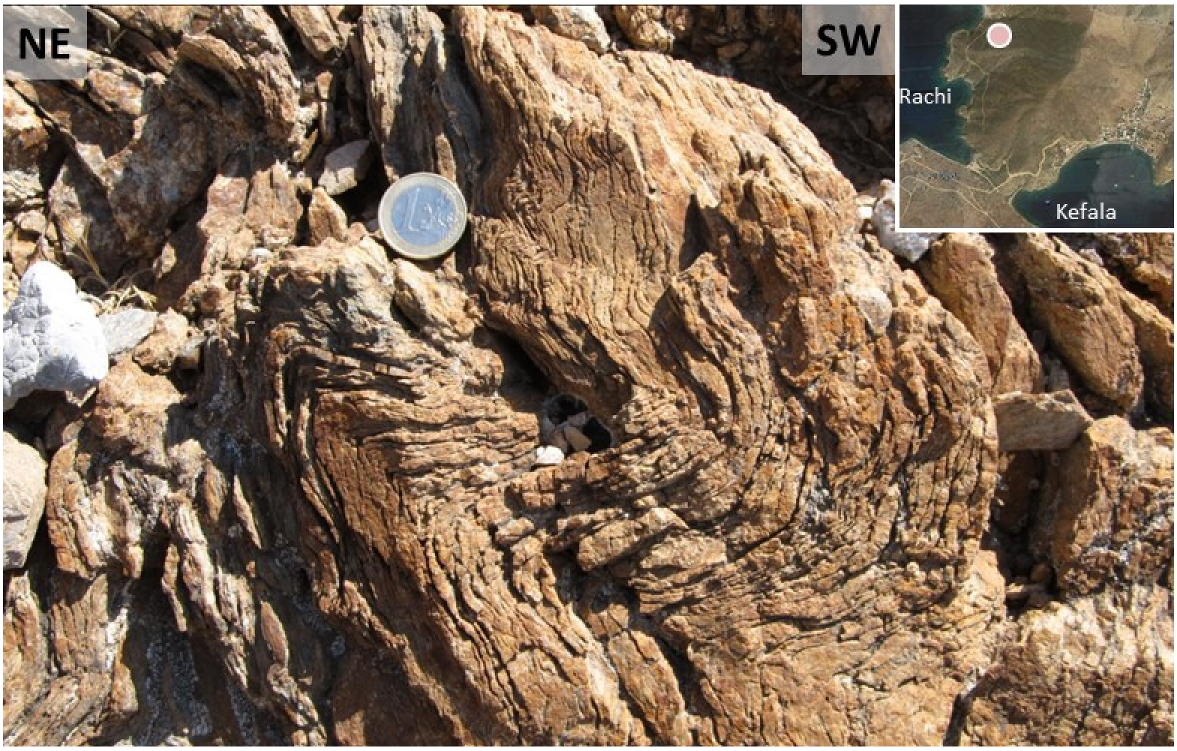

Fig. 30: Outcrop photograph of the Quartz-Mica Schist from Rachi area.

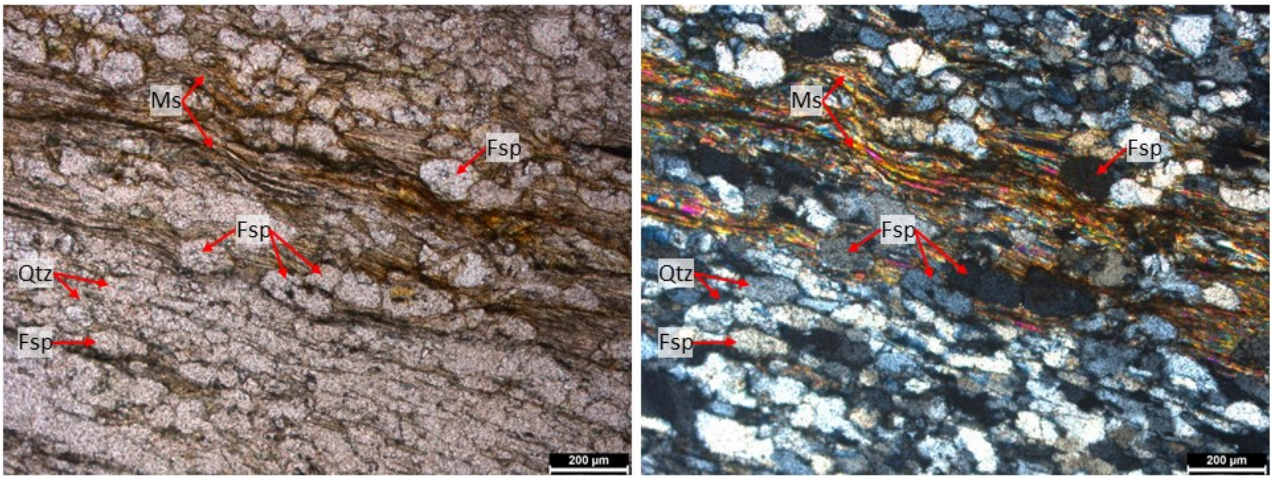

Fig. 31: KA014003 from Rachi in plane polarized light (left side) and with crossed nicols (right side). The white mica are aligned to an undulous, wavy foliation and also the quartz components follow this foliation. The quartz grains have all a very similar grain size and have a slight shape preferred orientation.

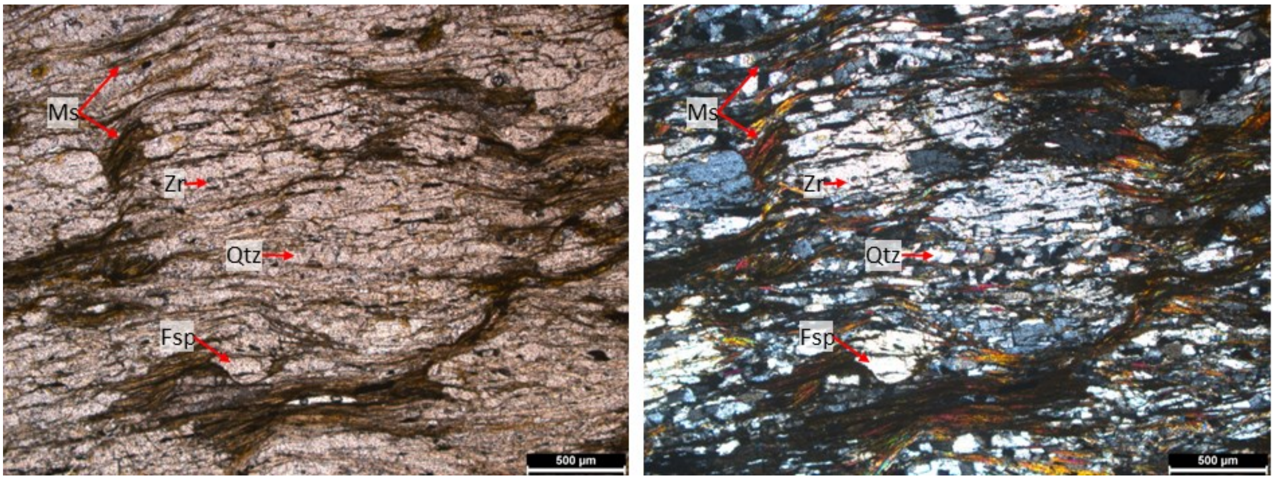

Fig. 32: KA014026 from Emporio area. Note the remnant feldspars that are arranged in an augen-like structure. The white micas are defining the foliation that often bends around the feldspar augen. In between and parallel to the foliation, abundant quartz grains line up along in ribbons. Left side in plane polarized light, right side with crossed nicols.

3.6 Amphibolite-Gneiss Unit (4b)

The Amphibolite-Gneiss Unit was observed in the Masouri area, at the Myrties village and at Telendos Island to the west of Kalymnos (Fig. 33). This dark green schistose basic to ultrabasic, fine-grained body is defined by a weak lineation of aligned amphiboles (Fig. 34). The thickness of this formation is around 100 meters and is overlain by a light-colored gneiss. The lithologies are separated by a cataclastic zone. The minerals that form this rock are Epidote, Actinolite and Albite. The Epidote grains are rounded and strongly weathered. Also, they have high relief and a weak pleochroism from yellow to green (Fig. 35).

The EDAX measurements show that the actinolite is surrounded by a matrix of muscovite and small biotite minerals. There are two generations of Actinolite. The first one has rounded and bulging edges with a weathered appearance. It is overprinted by the second generation at a high angle. This second generation of Actinolite is oriented into a penetrative foliation and the grains are very elongated with well-defined edges (green to dark green pleochroism). Occasionally, isolated, idiomorphic Actinolite occurs. Very small grains of Albite were observed in the microscope, but no Garnet at all. Isolated Apatite minerals were identified through EDAX measurements.

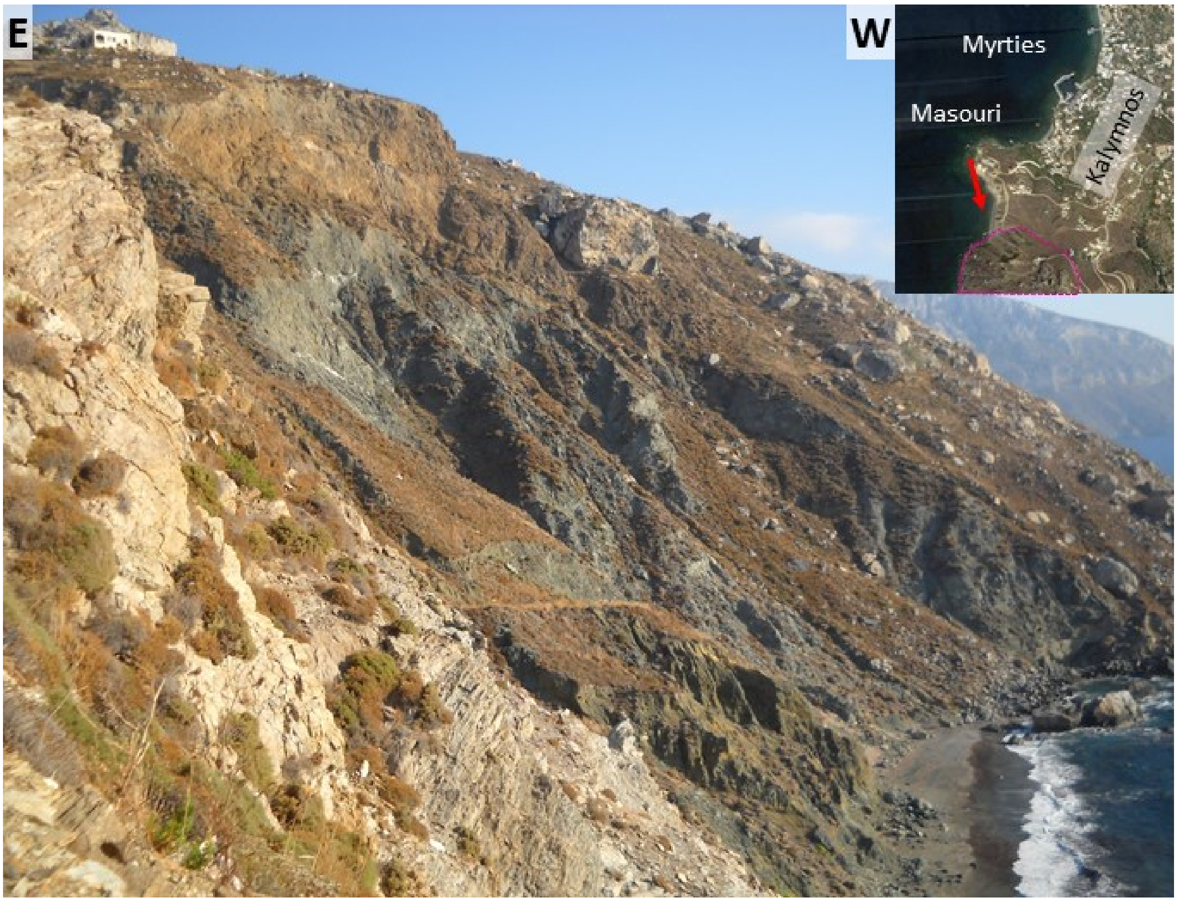

Fig. 33: Photo of Amphibolite Gneiss Unit at Myrties. The dark green amphibolite is well visible in the background. In the foreground, the Conglomerate Unit can be seen. The amphibolite is overlain by the gneiss. The two lithologies are separated by a fault zone.

Fig. 34: The amphibolite lithology in the outcrop at Myrties.

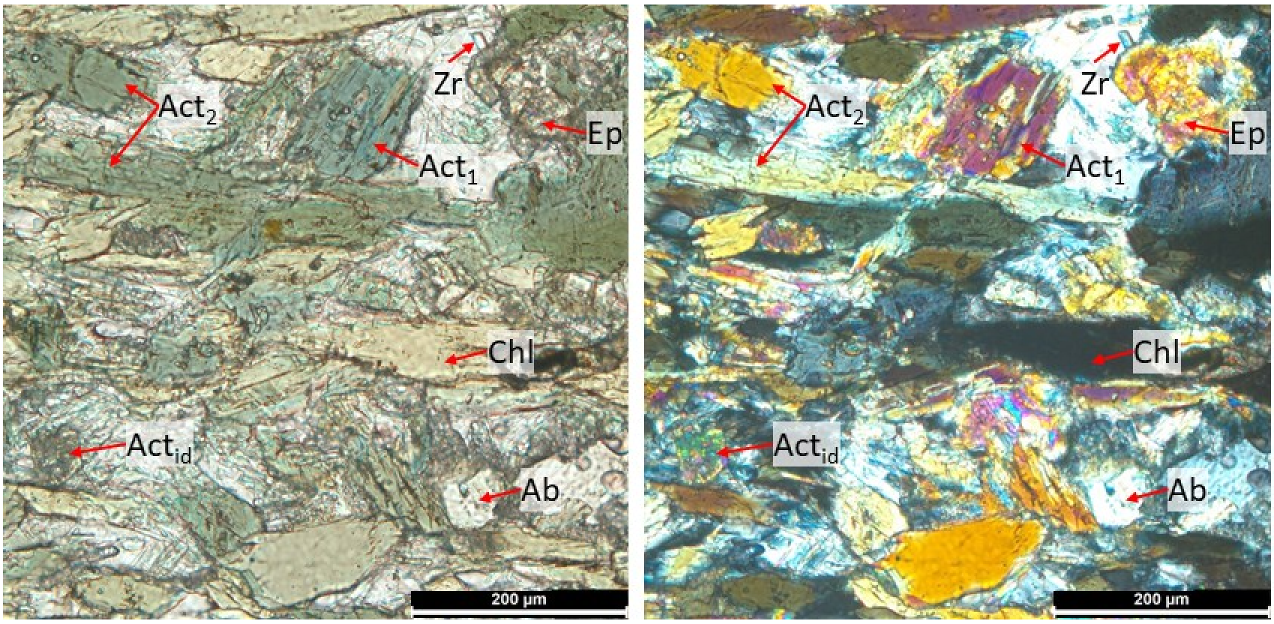

Fig. 35: Thin section photographs of the amphibolite with plane polarized light on the left-hand side and cross-polarized light on the right-hand side. Generally, the Actinolites are well oriented along the foliation, but rarely, unoriented and idiomorphic specimen can be observed (Act_{id}). The well-oriented actinolite grains (Act_2) overgrow an earlier generation of actinolite (Act_1). Act= Actinolite, Ep= Epidote, Chl= Chlorite, Zr= Zircon

A thick zone of gneiss can be distinguished above the amphibolite in Myrties village (Fig. 33) with a foliated cataclastic zone in-between the gneiss and the amphibolite. This tectonic contact is visible only in this special outcrop. Further gneiss outcrops were also found at Emporio area.

The gneiss is folded into large-scale open folds (Fig. 36) with a cleavage and a stretching lineation similar to the amphibolites. The mineralogic composition of the gneiss contains predominantly Quartz, Muscovite, Feldspar along with Biotite, Chlorite and Chloritoid and Zircon as accessory mineral (Fig. 37).
In the microscopic image (Fig. 37 and 38) coarse-grained quartz is present. The grains are arranged in zones with undulose boundaries that originate from the grain boundary migration mechanism of dynamic recrystallization. An initial phase of ribbon quartz formation can be observed. Very thin zones of micas run between the quartz grains. Rarely, interstitial growth of big calcite grains occurs. Parallel to the quartz and mica zones, Actinolite grows in bigger and larger crystals than quartz.

Fig. 36: Open folds in the gneiss of the Amphibolite Gneiss Unit at Myrties.

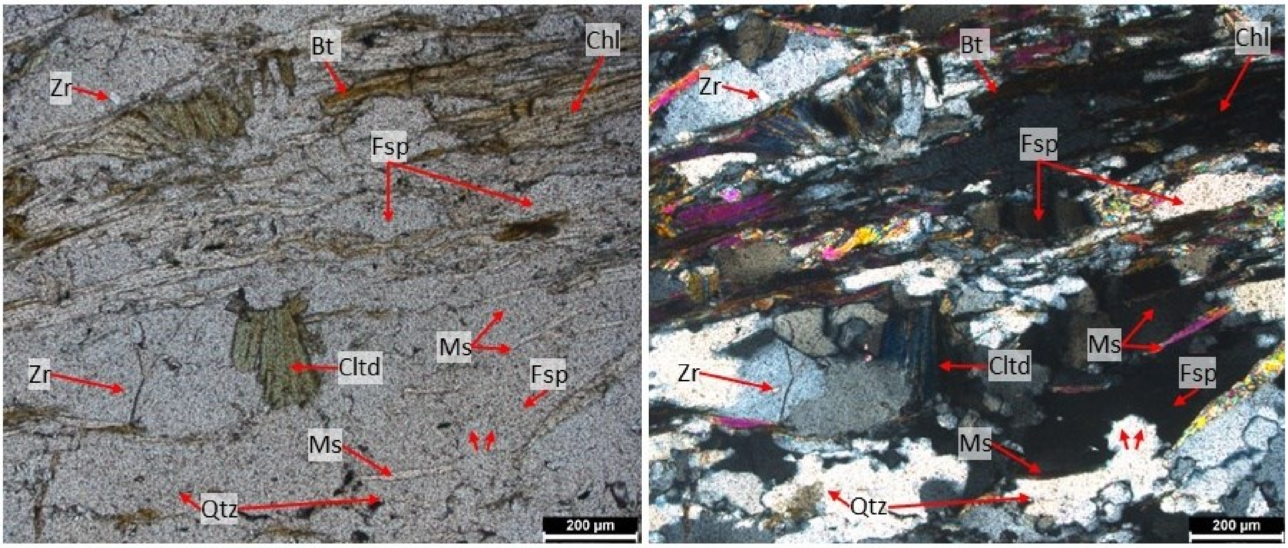

Fig. 37: Thin section view of the gneiss sample KA14002. Same view on the left hand side in plane polarized light and on the right hand side with crossed nicols. The foliation is defined by the white mica and aligned smaller quartz grains. Larger quartz and feldspar crystals form islands with white mica bending around. Chloritoide grows across the original fabric. Note the lobate grain boundaries, especially between quartz and feldspar in the lower right section of the image (two small red arrows). Here, a quartz crystal is pinned down by two white mica, but bulges in between them into the feldspar.

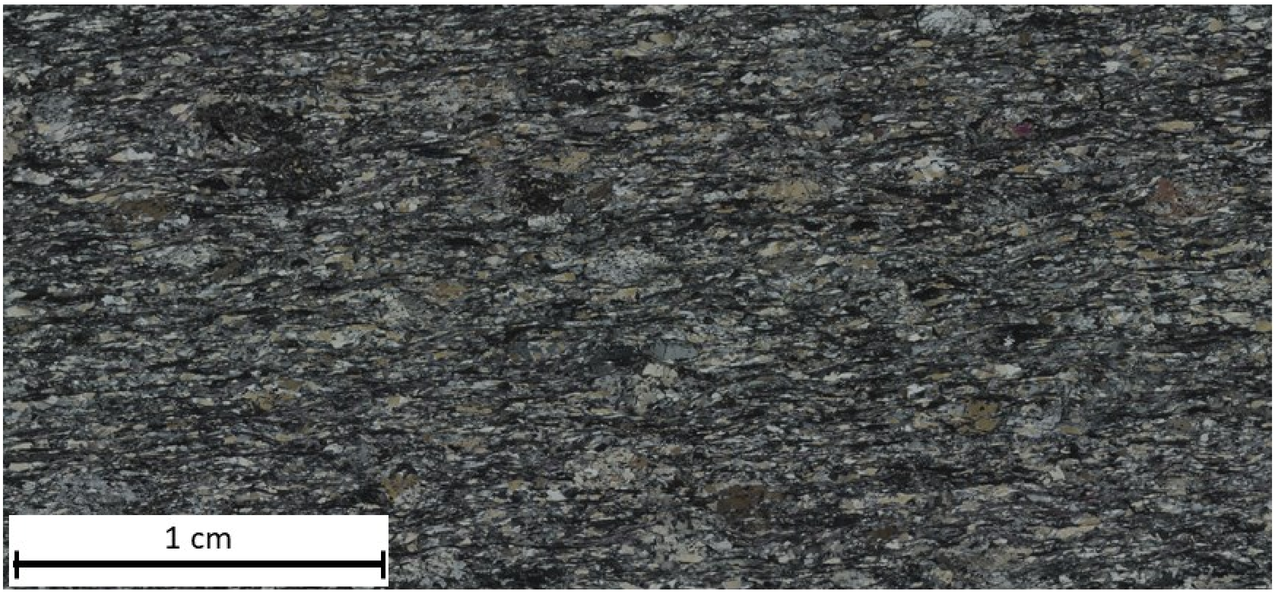

Fig. 38: Thin section view of the gneiss sample KA14002 with relic feldspar-augen structure, which is defined by homogenous, sharp-edged grains and also by larger grains showing inclusions and weathering.

3.7 Verrucano (5)

The Verrucano is a siliciclastic formation with colors ranging from dark red (pelites) to orange (sandstones) and grey (lenses of limestones). This lithology originates from the fill of intramontane basins in the western Mediterranean (Murawski & Meyer, 2004). On Kalymnos, it was found in outcrops along the road between Myrties and Rachi (Fig. 39). The thickness of the unit is almost 20 m. The age of this formation is believed to be Upper Permian to Triassic (Triantafillis et al., 1994; Franz et al., 2005) based on stratigraphic observations. As it is referred to in the paper by Triantafillis et al. (1994), the Verrucano comprises the main unit at the base of the Ionian Unit. Desio (1931) characterized this stratigraphic unit as Val Camere strata. Dounas et al. (1983) believe that the unit belongs to the upper horizons of Neopaleozoic strata. Franz (1991) states that this unit follows on top of the Marina Unit but is separated from the latter by an unconformity. Triantafillis et al. (1994) regards this contact as tectonic with a tectonic breccia of 5 to 40 cm thickness in-between. This, however, contradicts with the observations of Gerolimatos et al. (1993) for Leros Island.

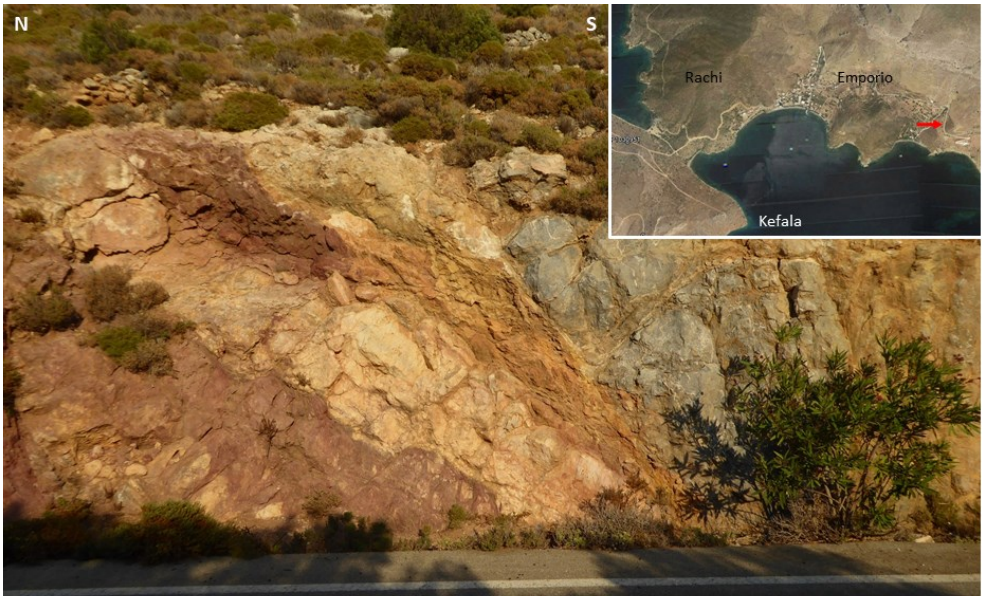

Fig. 39: Roadside outcrop of Verrucano close to Emporio.

3.8 Mesozoic Limestones (6)

The Mesozoic limestones were not investigated in detail, since this was not the main aim of this study. Because they represent the structurally overlying lithologies to the main units that occupy the Kefala peninsula some observations were made. The main observations are: (a) The limestones form prominent cliffs that have a vertical thickness of over 350 m. (b) Different types of karstic forms of all scales can be seen including caves of various sizes. (c) The contact between the Mesozoic limestones and the Variscan basement is also tectonic as the presence of a thin (~10 m) cataclastic zone indicates. Figure 40 shows a typical appearance of these limestones. Christodoulou (1969) refers to these limestones as one calcareous nappe of Mesozoic age. The sedimentary sequence that Christodoulou (1969) has described consists of massive, thick-bedded limestones with a color ranging from dark brown to black. It contains horizons of cherts and nodules and white to brown massive, thick-bedded limestones of Upper Jurassic and Tithonian age respectively. The contact, which brings these two different lithologies next to each other, represents an unconformity according to Christodoulou (1969). Triantafillis et al. (1994) provides a more detailed description by dividing the above-mentioned limestones into different units and subunits, which are comparable to Ionian unit and Gavrovo unit. However, it is not clear, how the ages for each of the layers were derived. The Ionian unit on Kalymnos Island corresponds to these lithologies from the base to the top: (a) Verrucano ?Permian-Lower Triassic, (b) Dolomites – Dolomitic limestones with black color, bituminous content and a thickness of 100-400 m, (c) Limestones with white to black color, and a thickness around 400 m. At the base, the rocks are black and consist of dolomitic particles. At the upper beds chert laminae, lenses and nodules occur more frequently, (d) Limestones with chertlayers (black color, thin bedded, chert laminae of 15 cm thickness and nodules with a maximum thickness of 350 m and Upper Jurassic to Cretaceous age).

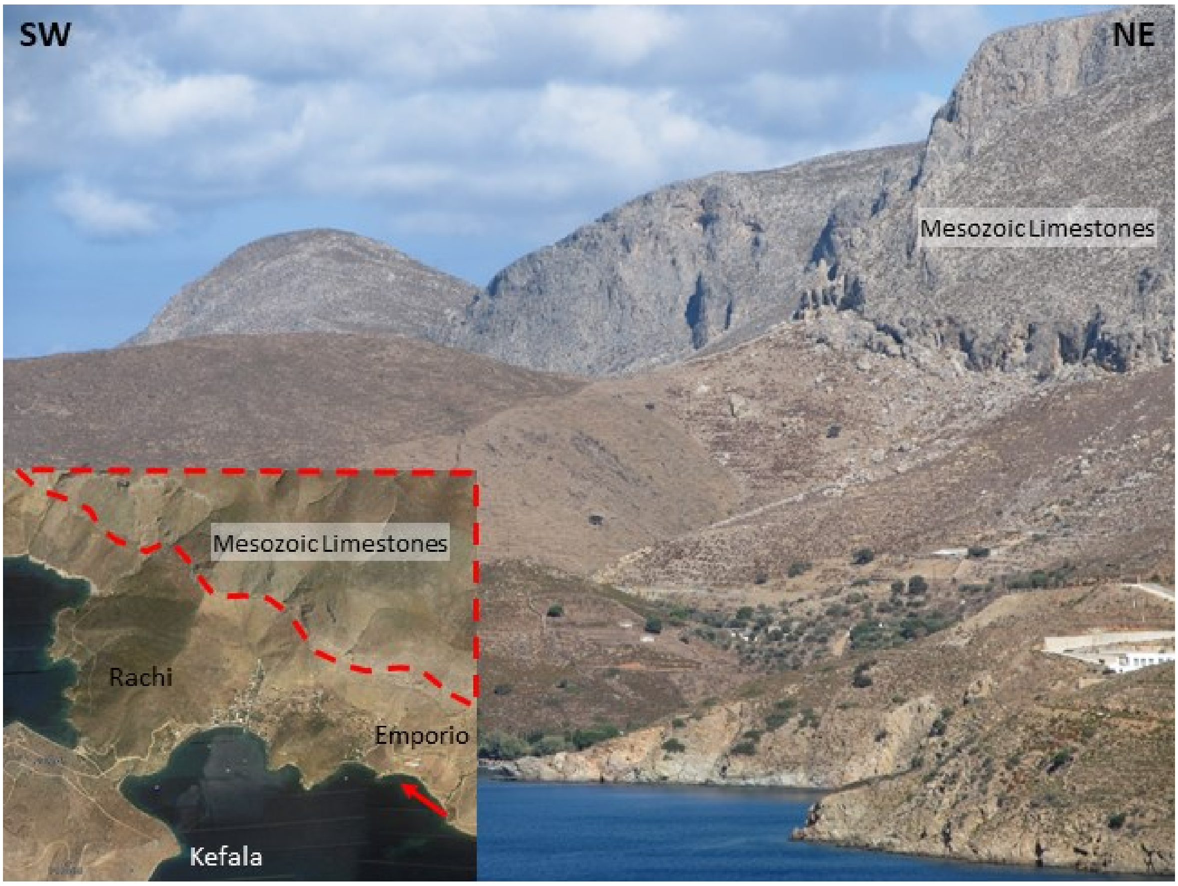

Fig. 40: View on the Mesozoic limestone cliffs on Kalymnos. According to Triantafillis et al. (1994), these limestones with its units and subunits are comparable to Ionian and Gavrovo Units.

4 Geochronology

Representative samples of the Quartz-Mica Schist Unit in Rachi area, as well as from the gneisses that have been observed, but not mapped in detail near of Emporio village and further south at Myrties village (Fig. 41), were collected for $^{40}Ar/^{39}Ar$ and (U-Th)/He analysis. These geochronological methods were applied in order to clarify the timing of moderate to low temperature deformation of the basement rocks of Kalymnos Island. Progressively step-heated $^{40}Ar/^{39}Ar$ geochronology was performed on hand-picked mica samples with a Photon Machines CO_2 laser coupled to a Nu Instruments Limited Noblesse magnetic sector multicollector noble gas mass spectrometer at the Geological Survey of Canada in Ottawa.

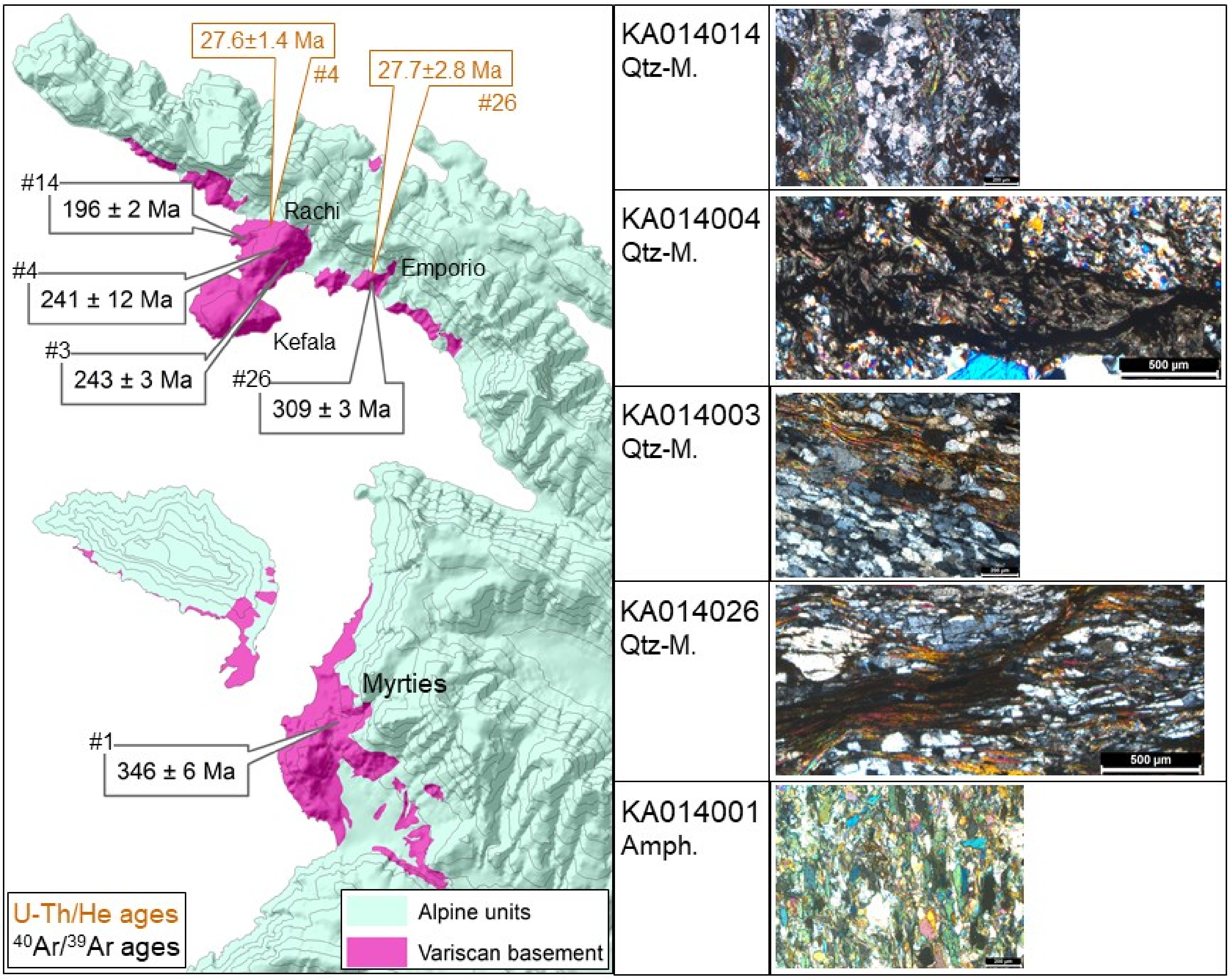

Fig. 41: Map of sample locations for geochronology and sample numbers with lithology/ thin section example images in cross-polarized light.

Furthermore, following standard mineral separation procedures, eight individual zircon crystals from each of two separate basement samples were hand-picked for (U-Th)/He analysis at the Thermochronology Research and Instrumentation Laboratory (U-Th)/He facility at the University of Colorado in Boulder, USA, using an ASI Alphachron He extraction line connected to a Balzers PrismaPlus QME 220 quadrupole mass spectrometer. A Thermo Element 2 magnetic sector mass spectrometer was used for the U and Th analyses.

4.1 $^{40}Ar/^{39}Ar$ sample preparation

To achieve 99% purity, the samples were separated mechanically from the host rocks to isolate white mica with a grain size between 106 and 250 µm. Three samples were selected: KA014003, KA014004 and KA014014. The mica were picked under a binocular microscope and washed with dilute HCl. Individual mineral separates were loaded into 2-3 mm-deep aluminum foil packets, which were subsequently stacked vertically into 35 mm long foil tubes and placed into the tubular holes of an aluminum cylinder. Respectively number of flux monitor grains of Fish Canyon tuff sanidine (FCT-SAN) (28.02 ± 0.16 1σ Ma; Renne et al., 1998, ^{40}K decay = 5.543e-10/a, Steiger & Jäger, 1977) were loaded into each sample package. Every packet underwent a 160 MWH irradiation in medium flux position 8A at the research nuclear reactor of McMaster University in Hamilton, Canada. The neutron flux was approximately 1.08 x 1013 neutrons/cm2 operating at a 2.5 MW power level. Typical nucleogenic interference corrections were ($^{40}Ar/^{39}ArK$): 0.058, ($^{39}Ar/^{37}ArCa$): 0.000743 and ($^{36}Ar/^{37}ArCa$): 0.000258.

In the samples KA014003 and KA014004 the white mica are oriented parallel to the foliation, are folded and show the same grain sizes (Fig. 42). In the sample KA014014, however, there are also grains within the quartz matrix and not only in well-defined bands along the foliation as in KA014003 and KA014004 (Fig. 42). Generally, the observed white mica grains are regarded as diagenetically formed – no neoblastic mica grains could be observed.

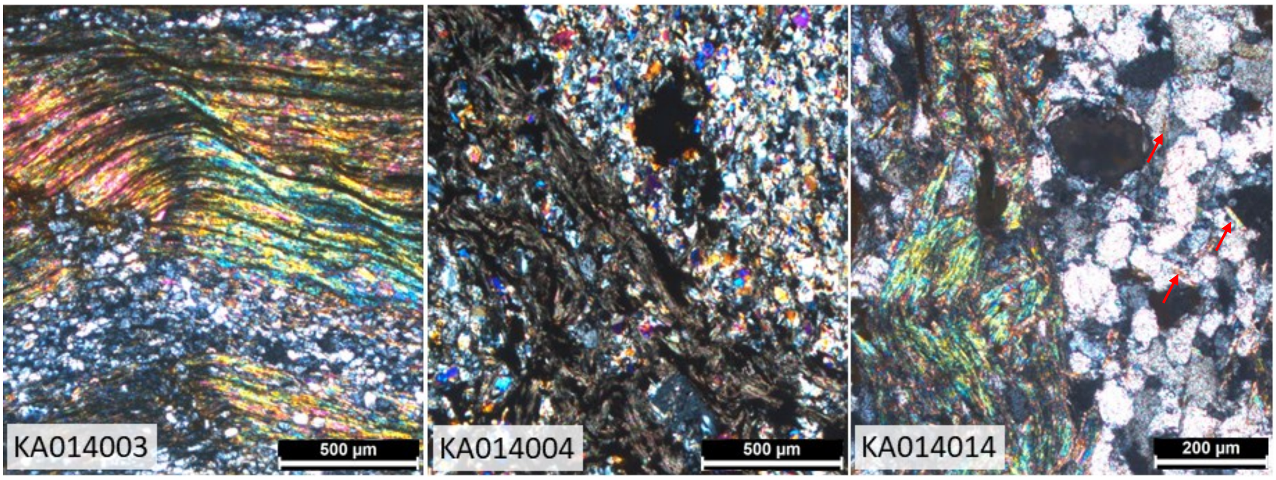

Fig. 42: Thin section images of the samples KA014003, KA014004 and KA014014 with crossed nicols. The red arrows in sample KA014014 indicate the white mica within the matrix.

4.2 $^{40}Ar/^{39}Ar$ analyses

The protocols of Kellet & Joyce (2014) were followed for the analyses of the grain sizes between 106-250 µm. Duplicate single grain aliquots were used (except for sample KA014004) via 15-17 heating increments. These single grain aliquots and monitors were arranged into separate 1.5 mm diameter cavities in a copper planchet and placed under vacuum. A Photon Machines Ltd. Fusion 10.6 55W CO_2 laser was used to heat and analyze singular grains in progressive steps. This machine was coupled to the all-metal extraction line and a Nu Instruments Noblesse multicollector mass spectrometer operated at the Geological Survey of Canada in Ottawa. Laser heating was homogenized over a beam radius of 2 mm for a total of 40s, after which the released gas was exposed to SAESTM NP-10 (~400°C) and HY-STOR® 201 (25°C) getters in the extraction line for three minutes. After this step, the sample gas was expanded into the mass spectrometer. The Nu Noblesse can be described as a single focusing, Nier-source, magnetic sector multicollector noble gas spectrometer equipped with two quadrupole lens arrays. A fixed array of three ETP® discrete dynode ion-counting multipliers (IC0, IC1, IC2) was used for measuring the argon ions. Data collection occurred in two multicollection cycles; more specifically, cycle 1 = $^{40}ArIC0$, $^{38}ArIC1$ and cycle 2 = $^{39}ArIC0$, $^{37}ArIC1$, $^{36}ArIC2$. Blanks were run for every five analyses in an identical manner to unknowns. Air shots were analyzed every 10 analyses to monitor efficiency and mass fractionation. The $^{40}ArIC0/^{36}ArIC1$ and $^{40}ArIC0/^{36}ArIC2$ measurements of air have been used to correct for the relative collector efficiency and mass bias of IC1 and IC2 collectors relative to IC0. No correction was applied for mass bias in IC0 due to cancelling out in the age calculation (e.g. Brumm et al., 2010). The error in the irradiation-related parameter J is conservatively estimated at ± 0.6% (2σ) and the sensitivity of the Nu Noblesse at the time of analyses was 7.1-7.5 Amps/mol. All errors are quoted at the 2σ level of uncertainty in the calculations. The software MassSpec (version 7.93; Deino, 2001) was used for the calculations like data collection, reduction, error propagation, age calculation and plotting.

Analytical results of this study are presented in table 2. In figure 43, the data are presented also as spectra where the width of each bar (thermal increment) shows the proportion of evolved gas, and the height represents the uncertainty associated with the apparent age. The average age for the sample consists of the sum of the isotopic measurements of all steps with an uncertainty calculated by quadratically combining errors of isotopic measurements of all steps. This can also be referred to as the integrated (or total gas: Tg) age. Plateau ages are generally defined as the portion of an age spectrum that consists of contiguous increments representing >70% of gas released which results in concordant ages (Mahon, 1996). On the contrary, a preferred age (Tp) is calculated as the weighted mean of a selection of mostly contiguous increments which correspond to a released gas of >50% of ^{39}Ar and result in concordant ages. The analytical precision in the age of each heating step is high, concluding that the calculated age uncertainties are relatively small.

4.3 (U-Th)/He geochronology

(U-Th)/He geochronology was conducted at the Thermochronology Research and Instrumentation Laboratory (U-Th)/He facility at the University of Colorado in Boulder (USA). In this study, eight zircon grains were analyzed for each sample. Moreover, a Leica M165 binocular microscope equipped with a calibrated digital camera and capable of both reflected and transmitted, polarized light was used to choose the individual mineral grains. All the grains were screened for quality including crystal size, shape and presence of inclusions, and were characterized. After this process, grains were placed into small Nb tubes that were then crimped on both ends. The Nb packet is then loaded into an ASI Alphachron He extraction and measurement line. The packet is placed in the UHV extraction line (~3x10-8 torr) and heated with a diode laser to ~800-1100°C for 5 to 10 m to extract the radiogenic 4He. The degassed 4He is then picked with approximately 13 ncc of pure 3He, cleaned via interaction with two SAES getters, and analyzed on a Balzers PrismaPlus QME 220 quadrupole mass spectrometer. Degassed grains are then extracted from the line and input to a Class 10 clean lab for dissolution. A multi-step acid-vapor dissolution process was applied to the zircons, which have been placed in Parr large-capacity's vessels. Grains (including the Nb tube) are located in Ludwig-style Savillex vials, spiked with a ^{235}U-^{230}Th tracer and mixed with 200 μl of Optima grade HF. The phials are then covered, stacked in a 125 mL Teflon liner, placed in a Parr dissolution vessel and baked at 220 °C for 72 hours. After the cooling process, the vials are uncapped and dried down on a 90 °C hot plate until dry. After this process followed a second round of acid-vapor dissolution, this time with the help of 200 μl of Optima grade HCl in each phial that is baked at 200 °C for 24 h. Phials then were located in a hot plate to dry down for a second time. Once the samples were dry, 200 μl of a 7:1 HNO_3: HF mixture is added to each vial, then the vial is capped and cooked on the hot plate at 90 °C for 4 h. The minerals at the end of the processes are dissolved, regardless of the dissolution process they are diluted with 1 to 3 mL of doubly deionized water. As next step, the samples were analyzed in the ICP-MS lab. To ensure data integrity, mineral standards of Durango Apatite (31.5 Ma) and Finish Canyon Tuff Zircon (28.2 Ma) were routinely analyzed in conjunction with the samples. A Thermo Element 2 magnetic sector mass spectrometer was used to analyze sample solutions, standards and blanks for U, Th and Sm. Once the element contents were measured, He dates and all connected data are calculated in a custom spreadsheet made by CU TRaIL staff.

4.4 Results

The results from the conducted $^{40}Ar/^{39}Ar$ geochronological analysis, gave disturbed $^{40}Ar/^{39}Ar$ age spectra with some well-defined plateaus (Fig. 43). Also, a significant ^{39}Ar gas release (>50%) was observed that gave Carboniferous deformation ages at Emporios and Myrties area and Triassic deformation ages at Rachi area. In general, the spectra show a stair-step shape for the early increments, and at least three samples have stair-step shapes for the entire analysis.

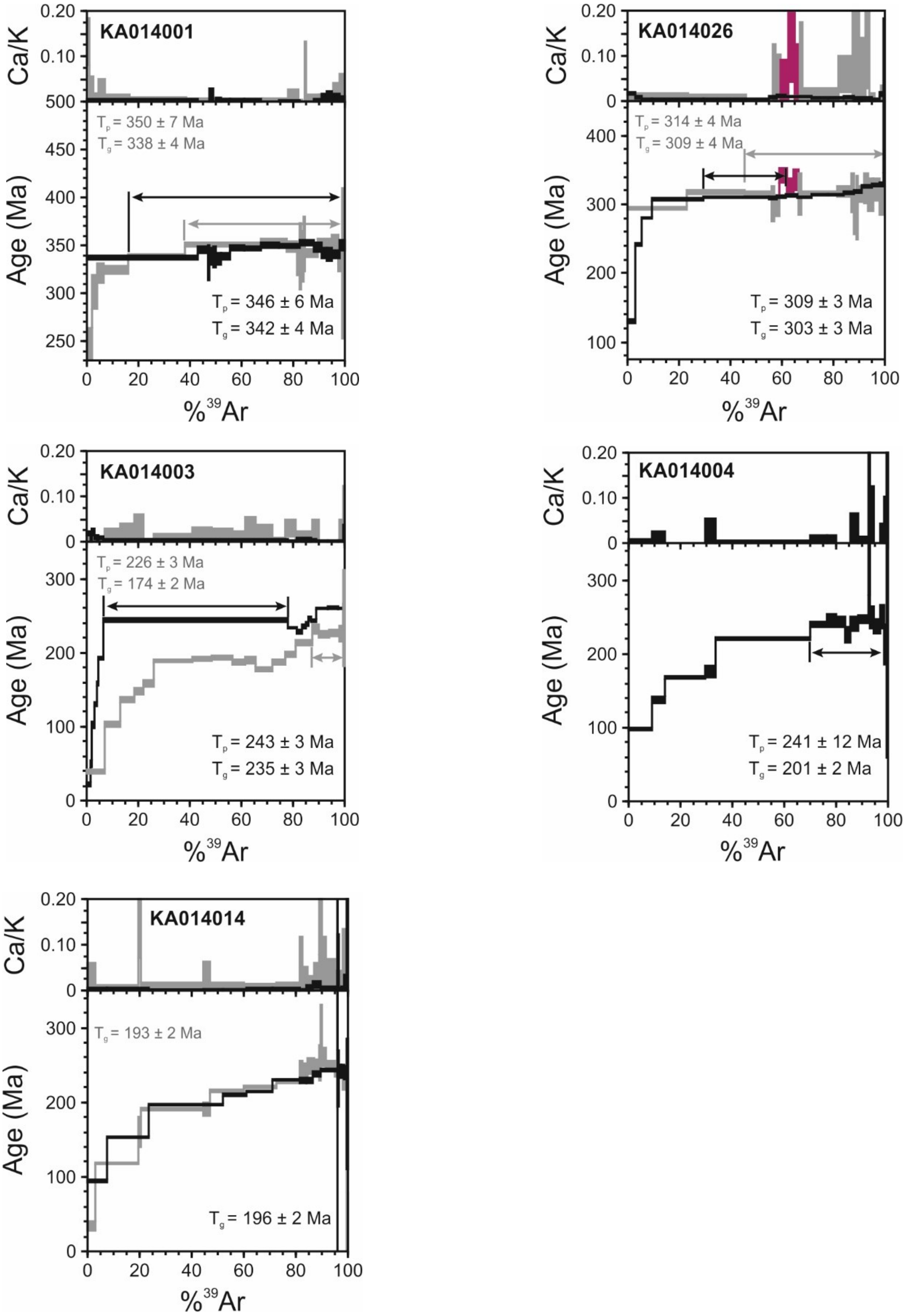
KA014001
Tp = 350 ± 7 Ma
Tg = 338 ± 4 Ma
Tp = 346 ± 6 Ma
Tg = 342 ± 4 Ma
KA014026
Tp = 314 ± 4 Ma
Tg = 309 ± 4 Ma
Tp = 309 ± 3 Ma
Tg = 303 ± 3 Ma
KA014003
Tp = 226 ± 3 Ma
Tg = 174 ± 2 Ma
Tp = 243 ± 3 Ma
Tg = 235 ± 3 Ma
KA014004
Tp = 241 ± 12 Ma
Tg = 201 ± 2 Ma
KA014014
Tg = 193 ± 2 Ma
Tg = 196 ± 2 Ma
Ca/K
Age (Ma)
%39Ar

Fig. 43: $^{40}Ar/^{39}Ar$ age spectra of samples from the Kalymnos Island. Results from white mica: (i) from Qtz-mica Schist /Rachi unit (Samples: KA014003, KA014004, KA014014), (ii) from the Gneiss in Myrties area (Sample KA014001) and (iii) from the Gneiss in Emporio area. The width of each bar (thermal increment) represents the proportion of evolved gas, and the height represents the uncertainty associated with the apparent age. Tg: total-gas integrated age. Tp: preferred age. The apparent age scale changes between figures. Analytical data tables are included in the appendix 7.2 and 7.3.

(U-Th)/He analyses could be performed only in two samples, KA014004 and KA014026. The weighted average of eight zircons from the first sample is 27.6 ± 1.4 Ma (MSWD: 0.54), with a ~400 ppm range of effective uranium (eU) values. The second sample, KA014026, yielded single grain date dispersion from 387 Ma to 26 Ma that revealed a moderately negative date- eU trend. A weighted average of the two youngest and least retentive (high eU) grains gave an age 27.7 ± 2.8 Ma (MSWD: 0.48), concordant with the other sample. All ages for (U-Th)/He, were corrected for the effects of α-ejection and are reported with a ~8% (2σ) analytical uncertainty (Tab. 2).

Sample	**Location**	**Lithotype/Unit**	**(U-Th)/He (Ma)**	**$^{40}Ar/^{39}Ar$ age (Ma)**
KA014014	Rachi	Qtz-mica schist / Quartz-Mica Schist Unit	-	196 ± 2
KA014004			27.6 ± 1.4	241 ± 12
KA014003			-	243 ± 3
KA014026	Emporio		27.7 ± 2.8	309 ± 3
KA014001	Myrties	Amphibolite / Amphibolite-Gneiss Unit	-	346 ± 6

Tab. 2: Summary of samples and geochronologic results of this study from the Kalymnos area, sorted geographically from North to South. Note the southwards increasing ^{40}Ar-^{39}Ar age derived from muscovites. The (U-Th)/He ages were measured on zircons.

5 Structural Geology

In this chapter the different structural elements that were investigated during the fieldwork are described in macro/-mesoscale and then in microscale. The description of the structures starts from the lowermost lithology according to the schematic lithostratigraphic column of Kalymnos Island (Fig. 11), which is shown in the Lithostratigraphy chapter (3). The focus is on the documentation of key features and cross-cutting relationships that should help to determine the succession of folding, faulting and ductile deformation.

5.1 Macro/-mesoscale structural observations

Interlayered Marble Unit

In the Kefala area, the lowermost tectonic unit is the Interlayered Marble Unit and it crops out in a tectonic window, as mentioned in lithostratigraphy chapter (3.1). The most striking feature of this formation are the large-scale folds of the SE-outcrop area that are well visible from the sea (F1a, F1b, and F2). The poles to the fold limbs of these folds align along a best-fit great circle indicating NE-dipping fold axis (Fig. 44). There is one fold that has a fold axis oblique to this main system: F2. A geomorphologically well distinguishable thrust is running along the top of the folds, close to the top of the topographic high of the Kefala peninsula.

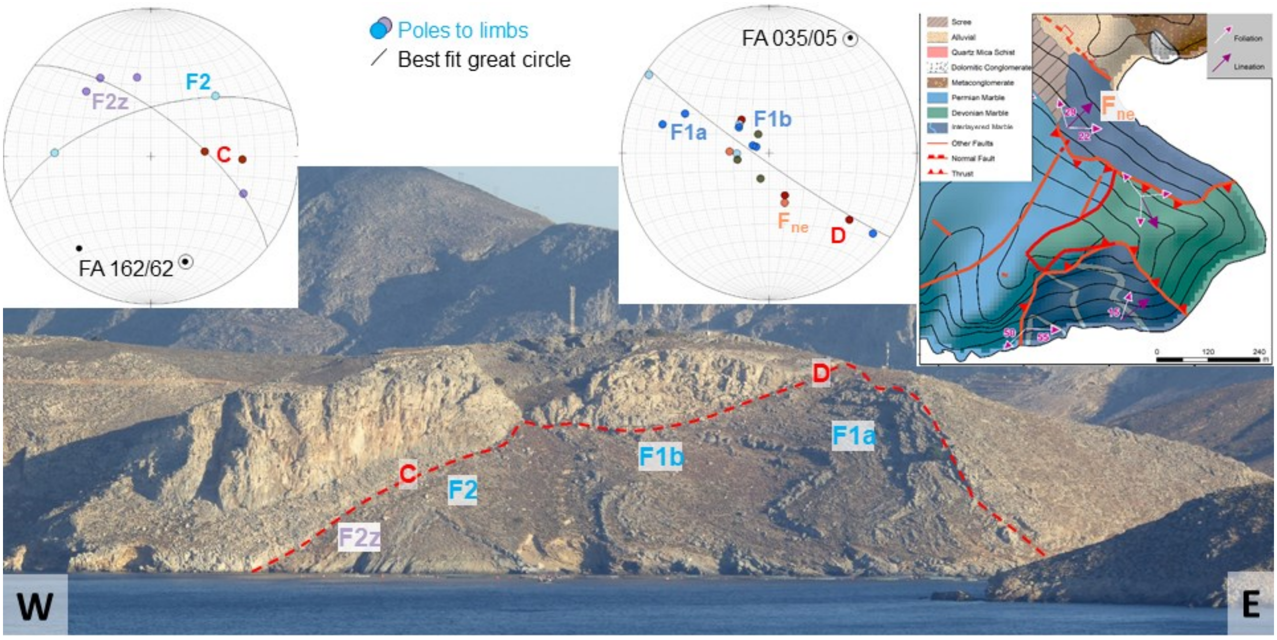

Fig. 44: View from the sea onto the large-scale folds of the Interlayered Marble Unit. Most of the folds in the SE outcrop and in the NE outcrop fit into a single system with a fold axis of around 035/05. Measurements of the fold limbs, the thrust fault plane and the foliation are shown in the PI-plots on the stereoplot. F1a, F1b, F2, F2z, F_{ne} = poles to planes of fold limbs, C,D = poles to planes of thrust. The resulting fold axes are indicated on the plots. Note that the fold F2 has an oblique fold axes to the main system.

Foliation/Lineation:
Distinct layers of marble are clearly visible in a matrix of Quartzite and Metapelites (Fig. 45). The foliation is folded parallel to the large-scale folds. Only an intersection lineation could be observed.

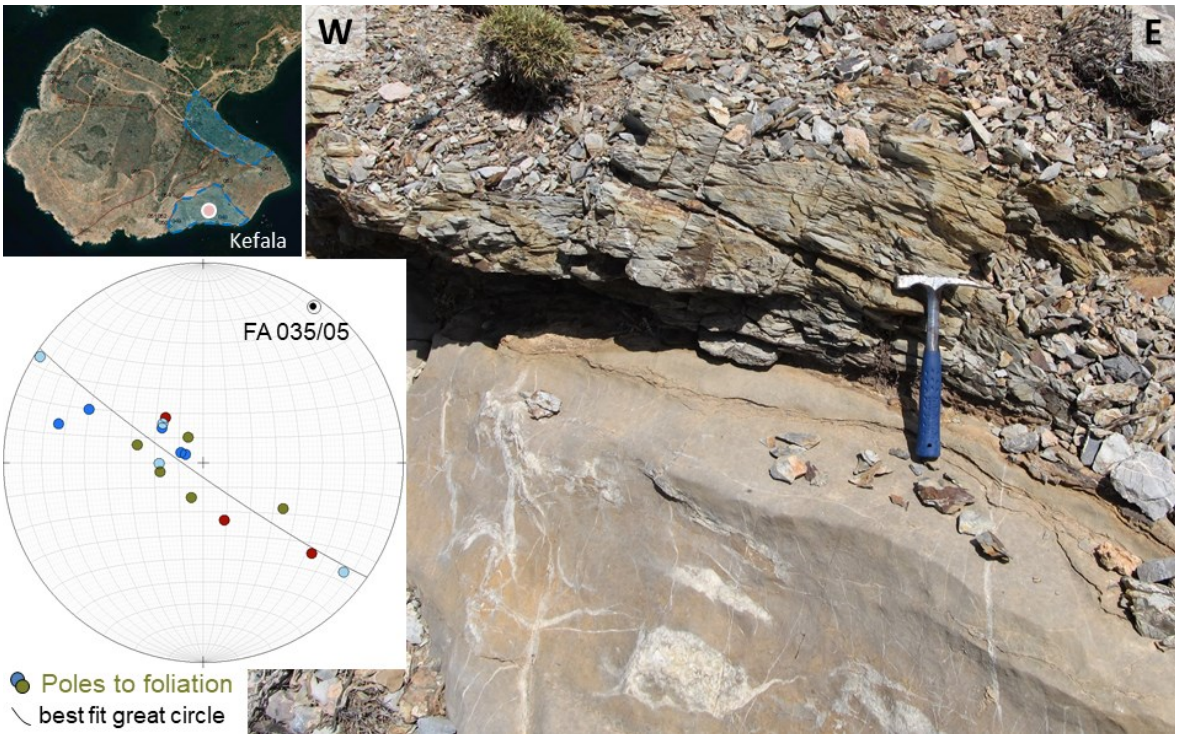

Fig. 45: A close-up view of the contact between the marble and the metapelite layers in the SE area with well visible foliation (shown in the stereonet as pi-plot along with the resulting fold axis).

Folds:
Gently plunging upright antiforms can be detected throughout the area. The classification of Fleuty (1964) based on the plunge of the hinge line and the dip of the axial surface was used (Fig. 46). The shape of the folds is sharp and angular, so they can also be characterized as chevron folds.

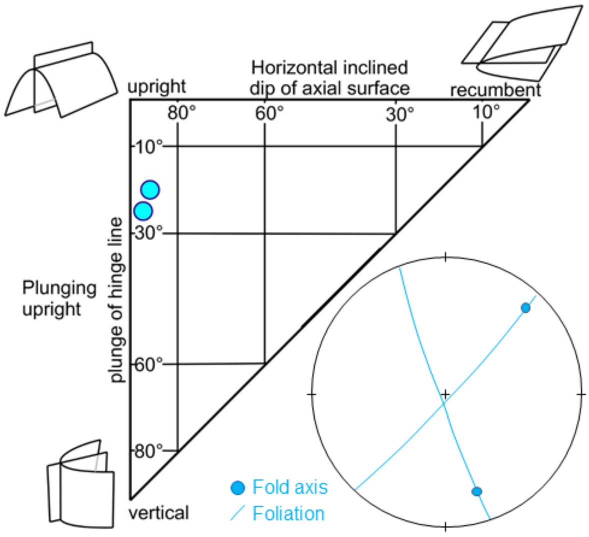

Fig. 46: Fleuty classification of folds (modified after Fleuty, 1964).

Distinct layers of marble that are clearly visible in a matrix of Quartzite and Marble are folded into the higher-order folds of a bigger antiform with the larger scale fold axis dipping to the SE. It can be well observed that the poles are aligned along a NW-SE trend. The intersection lineation is parallel to the fold axis (Fig. 44). The Interlayered Marble Unit contains four well-expressed folds: F1A, F1B and F2. At the SW limb of the F2 fold a smaller scale higher-order Z-fold verging to the SE, is observed (Fig. 47). The Pi-Plots of the foliations of the higher-order folds are shown in the same figure.

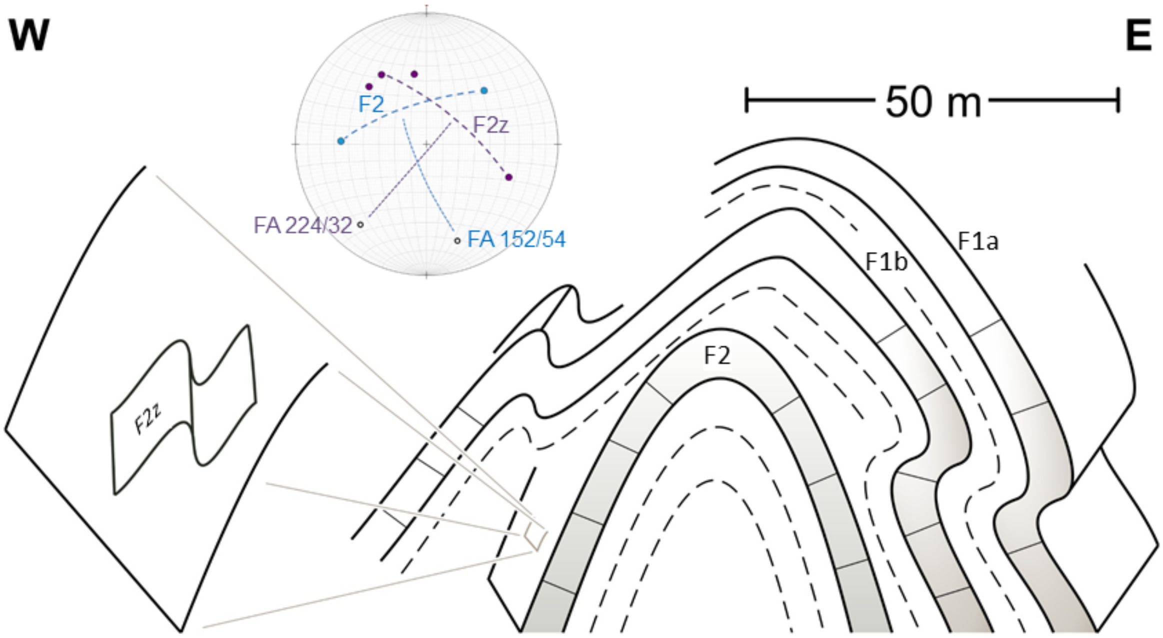

Fig. 47: Folds in the SE-outcrop area in the Interlayered Marble Unit with measured higher-order fold F2z. The stereonet shows the poles to the limbs, the best-fit great circles and the related fold axes.

In the NE outcrop area, an antiform can be found with a quartzite core (Fig. 48). The western limb of the fold is cross-cut by a fault.

Fig. 48: At the core of the antiform in the interlayered Marble unit, a quartzite can be found. Sample KA014011 is taken for microscopic description in the lithostratigraphy chapter (3.1).

Faults:
The Interlayered Marble Unit has been overthrusted by the Devonian Marble and the Permian Marble Units. The thrust plane is also folded with the same SE vergence as the higher-order F2z fold. The thrust fault contains an additional strike-slip component, indicated by a C-type and a C´-type shear band cleavage at the thrust contact between the Interlayered Marble unit and the Permian Marble (Fig. 49). The C´-type shear band cleavage is oblique to the shear zone boundaries with an angle of 15° to 35° between the shear band and the shear zone margin (Passchier & Trouw, 2005; Dennis & Secor, 1987; Passchier, 1991; Blenkinsop & Treloar 1995).

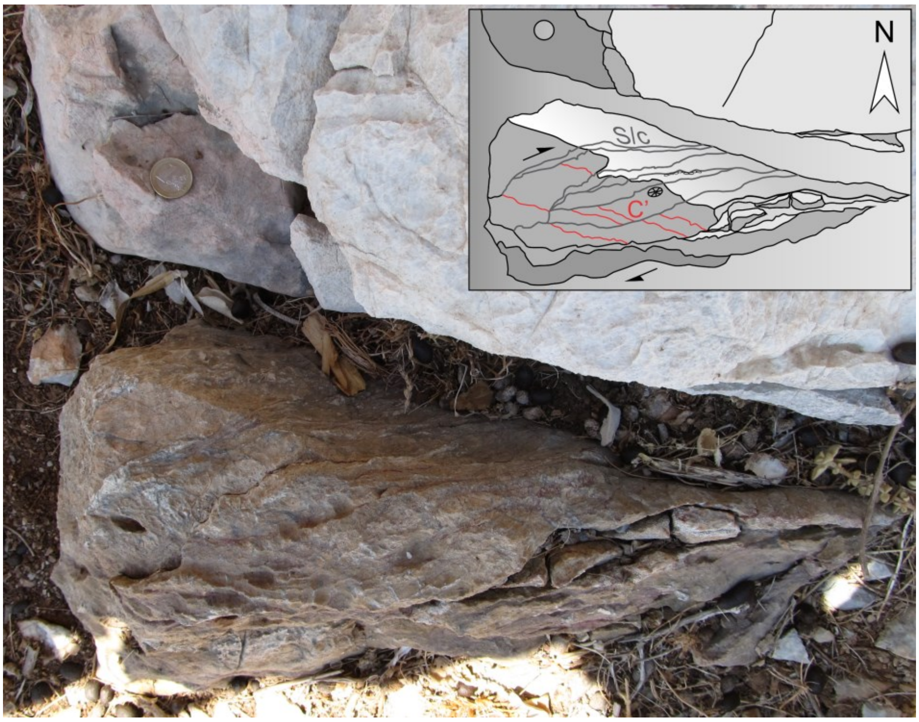

Fig. 49: Detail of the thrust zone between Interlayered Marble Unit and the overlying Permian Marble Unit. The dark grey specimen shows an SCC'-Structure.

At another outcrop, the contact between the Interlayered Marble Unit and the Permian Marble Unit is exposed and shows a cemented cataclastic zone (Fig. 50).

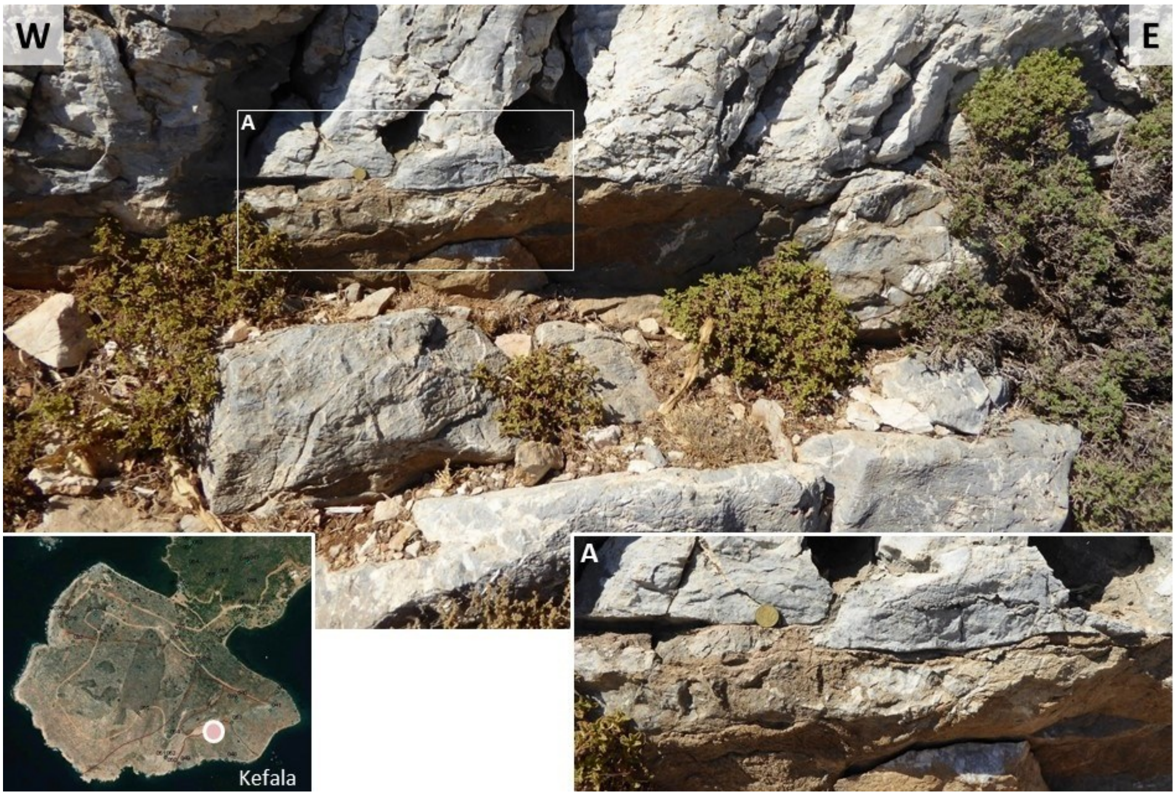

Fig. 50: Contact between the Interlayered Marble Unit and the Permian Marble Unit

Devonian Marble Unit

A sequence of Devonian Marble is thrusted onto the Interlayered Marble Unit. In the area in which it is exposed, little variation without major facies zones can be observed. Generally, it is a grey to light grey marble with slightly deformed fossil content. Abundant calcite and dolomitic veins cross the lithology, along with stylolithes (Fig. 51). The two structural elements of veins and stylolithes cross-cut each other in a probably coeval pure-shear system. The Devonian Marble Unit is in contact with the Permian Marble Unit probably along a sedimentary hiatus that is re-used by fault systems. These are very broad, contain a foliation and show a high degree of weathering of the components (Fig. 52). Sub-vertical faults with minor offsets cross cut these fault zones.

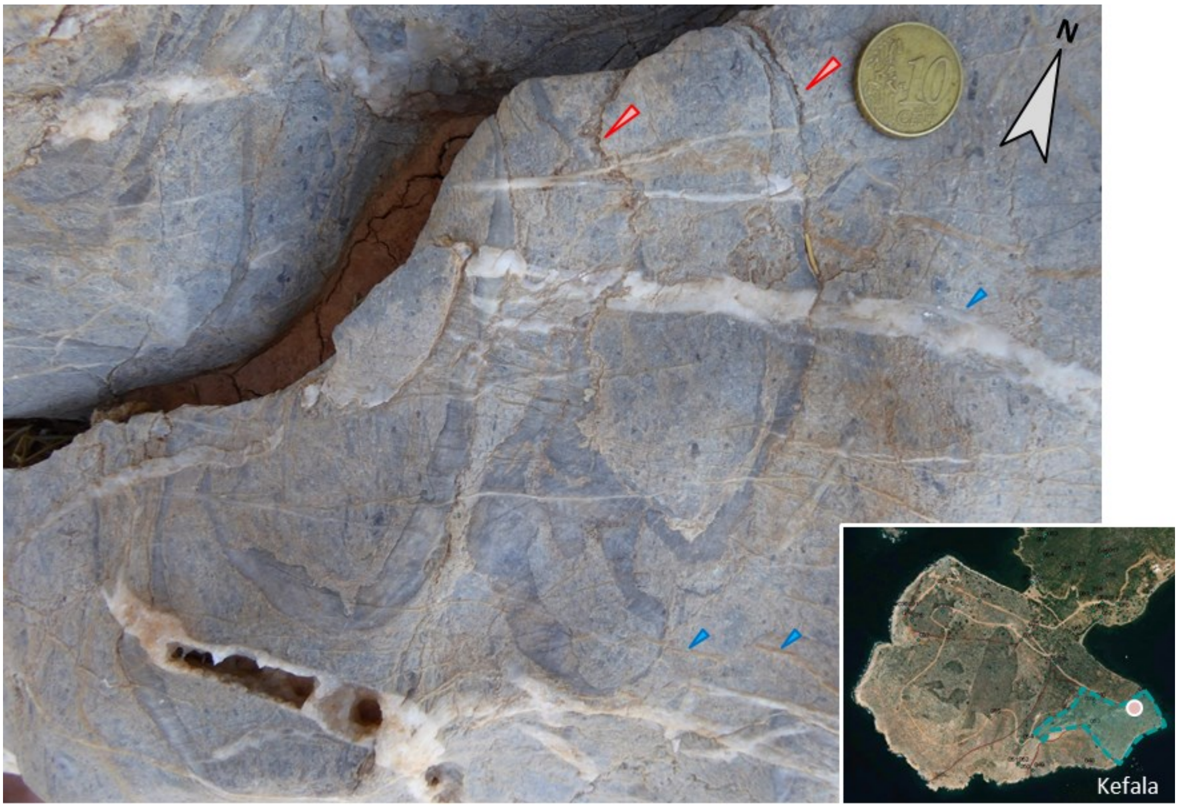

Fig. 51: Example photograph (map view) of the Devonian Marble Unit with stylolithes of ~N-S orientation (red arrows) and tensile joints filled with calcite that are oriented ~E-W. The sequence of the two structures is not entirely clear; they probably form a coeval pure-shear system.

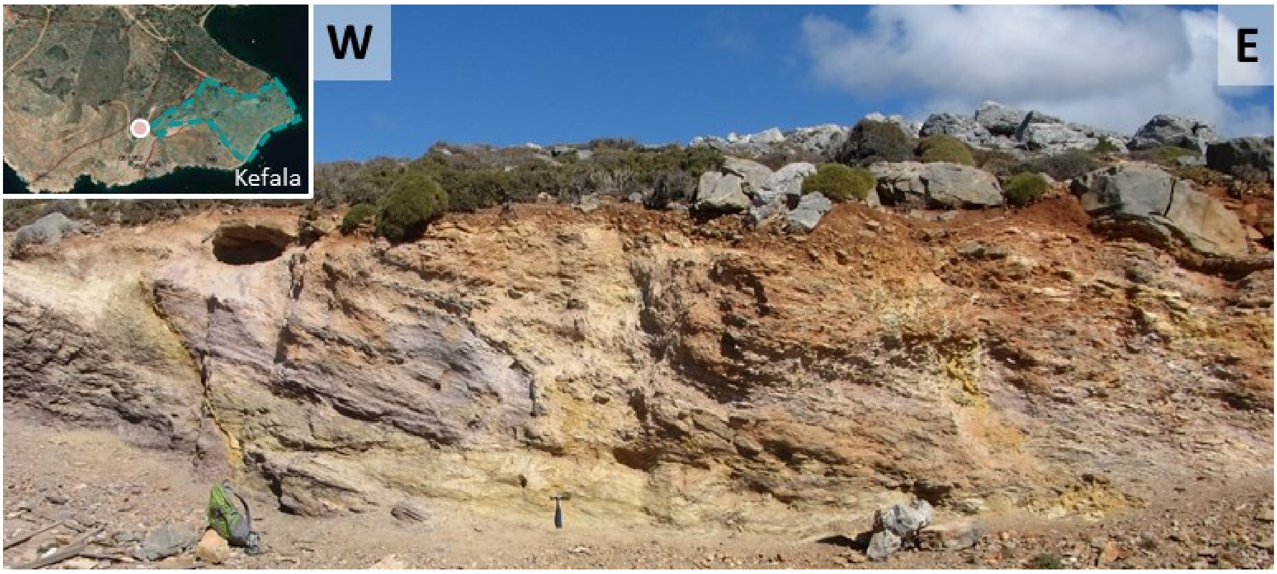

Fig. 52: Alpine fault zone along the boundary of the Devonian Marble to the Permian Marble Unit. The fault zone is up to 10 m wide with a still visible foliation, which is cross-cut by sub-vertical faults. The offset along these faults is very minor. The rock is strongly weathered and broken.

Foliation/Lineation:
The foliation in the central part of the area covered by the Devonian Marble (N4099370 E0493075) indicates an open fold (Fig. 53a). Further to the East, planar and parallel, SE-dipping foliation can be observed, which fits well to the open fold system (Fig. 53a). The intersection lineation is oriented in two main directions, one to the NNE and a second to the SSE. Both lineation systems best fit to the observed foliation of 084/07 (Fig. 53b).

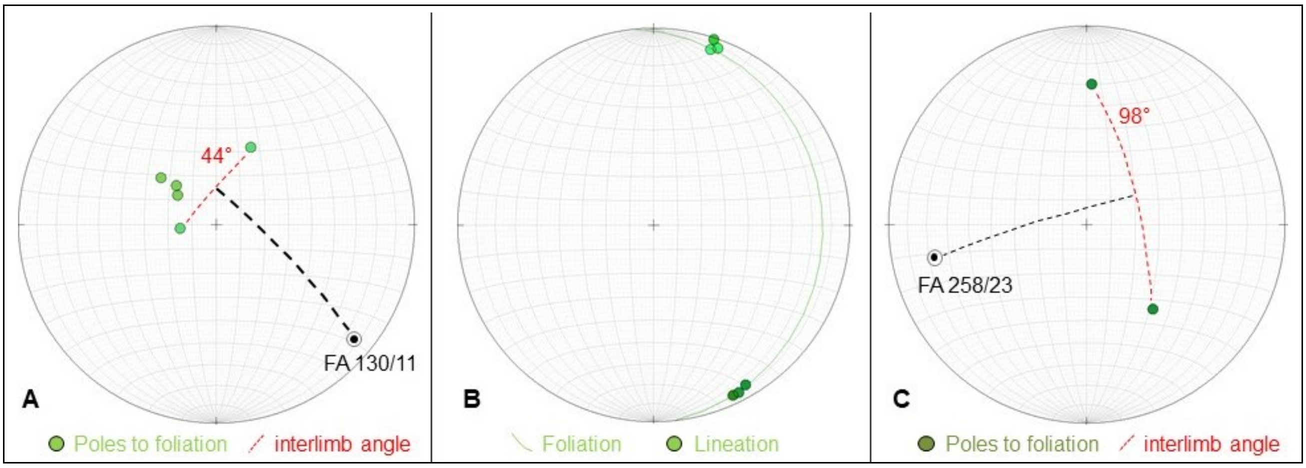

Fig. 53: Foliation and lineation measurements in the Devonian Marble Unit. In A) an upright fold at WP39 at the central part of the Devonian Marble Unit can be observed with foliation from WP41 (eastern part of unit) that fits to the NE-limb of the fold. B) shows lineations that seem to be oriented in two clusters forming a conjugate system. The NNE-plunging cluster was observed at WP41 at the eastern part of the unit and the SSE plunging cluster is from WP39 in the central part. In C) a very differently oriented fold system is shown from WP40 (central part of unit, close to WP39). This upright fold system with a much wider interlimb angle probably shows a disharmonic fold system.

Permian Marble Unit

The Permian Marble comes in contact with the Devonian Marble along the previously mentioned hiatus and the alpine faults. The exact order of succession is not clear: The Permian and the Devonian Marbles lie next to each other without observable orientation of faulting. The contact of the Permian Marble with the Interlayered Marble Unit is formed by the same thrust that separates the Devonian Marble from the Interlayered Marble Unit below.

Foliation/lineation:

In this lithology, a low-grade foliation accompanied by a stretching lineation was observed and measured. The poles to the foliation show an alignment along a distinct best-fit great circle with a WNW –ESE and a NW-SE trend (Fig. 54).

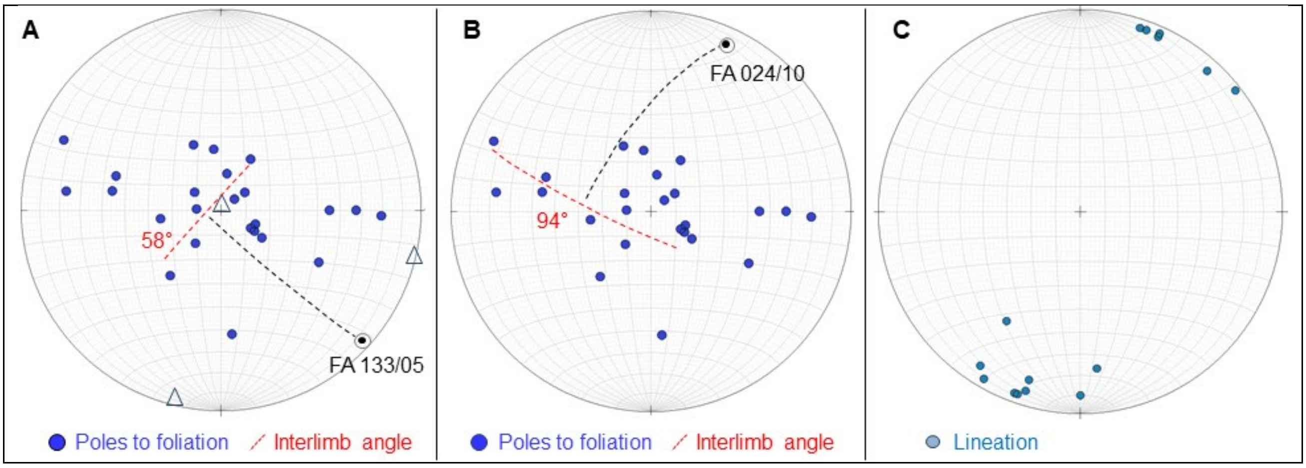

Fig. 54: Structural plots of measurements in the Permian Marble Unit. A) and B) demonstrate the type I fold interference pattern observed. The fold in A) also fits to the folding in the Devonian Marble (Fig. 53a). The fold in B) fits very well to the folded thrust and folding in the Interlayered Marble (Fig. 44). C) The very consistent direction of lineation throughout the dome and basin structure plunging NE-SW.

Folds:

The two orientation trends of the foliation that are perpendicular to each other indicates a dome and basin structure and thus a Type 1 refold structure (Fusseis & Grasemann, 2002). This refold structure is also visible in the satellite image showing that in Kefala peninsula characteristic features of saddles and domes dominate the landscape (Fig. 55).

Fig. 55: The type I refold structure observed in the outcrops can be interpreted on the satellite image of Kefala: The darker areas probably represent softer layers in-between the white marble that are then eroded and form deeper areas. The inset shows a text-book outcrop example from Ramsay (1950).

Besides the Type I interference pattern, cylindrical folds can be observed locally. The outcrop at WP 30 is an example. Here, a part of a locally cylindrical fold is exposed with a cleavage-bedding intersection lineation (Fig. 56). The top part of the fold is eroded and covered by soil.

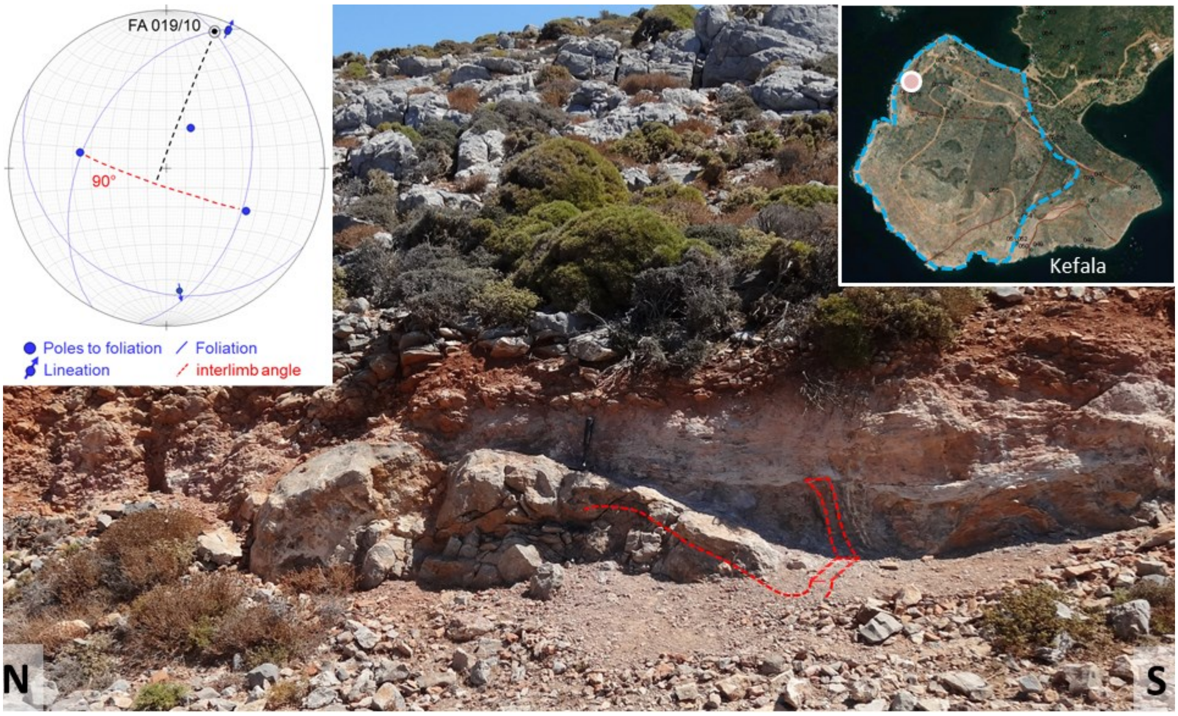

Fig. 56: Eroded fold that is locally cylindrical in the western part of the Permian Marble Unit. Note the fold axis at 019/10. Red lines on the outcrop image indicate the outline of the fold.

The Permian Marble Unit contains an ultramylonitic shear zone with boudinaged veins filled secondarily with iron-rich calcite. These boudinaged veins have pure calcite crystals in the necks and are ptygmatically folded.

The stretch of the folded boudinage layers was calculated for layers of different orientation. The highest amount of shortening is recorded in the layer oriented. These results and the strain estimations from the ptygmatic folds presented in the Mohr circle are shown in figure 57.

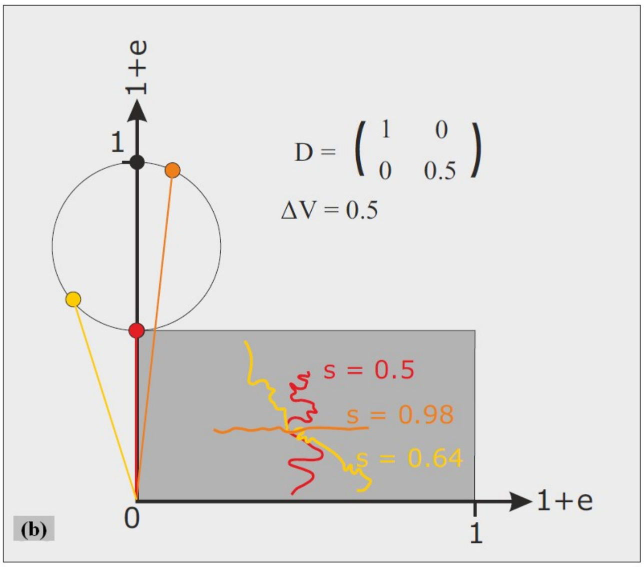

Fig. 57: Ptygmatic folds in the outcrop on the left-hand side (a, view towards W). The diagram on the right-hand side (b) shows the strain estimation from the ptygmatic folds presented on the Mohr circle in the Z-Y section (D finite deformation tensor and ΔV area change).

The stretch (s) is calculated according to the equation:

$$s = \frac{l}{lo}$$

Where l is the elongation after the deformation and lo is the elongation before the event of deformation. The result in stretch estimation is 1.64 which means that we have extension of 64%. At the same time, the strain value is estimated from the ptygmatic folds and are presented as Mohr circle for the zy section. The Deformation Matrix (D) or Strain was calculated for pure shear. Therefore, the equation is

$$D = \begin{bmatrix} k_x & 0 \\ 0 & k_y \end{bmatrix}$$

I this equation k_x and k_y are the stretch and shortening along the x and y coordinate axes, respectively (Fossen, 2010). The result of this equation is:

$$detD = \begin{bmatrix} 0.98 & 0 \\ 0 & 0.5 \end{bmatrix}$$

$$detD = 0.98 * 0.5 = 0.49$$

$$\Delta area = (0.49 - 1) * 100 = -51\%$$

This area change implies a volume change, which can be calculated by taking into consideration the stretch along the third axis (sz=kz=0.64).

$$\Delta volume = (1 - 0.64) * 0.51 = 0.184$$

Thus, the recorded volume loss during deformation is approximately 18%.

Faults:
In this unit at the northeastern part of Kefala peninsula a shear zone with a blue–grey ultramylonitic marble is located. It has a top to SSW shear sense. The mylonitic shear zone contains 1-20 mm thick iron-rich calcite veins (boudinaged and then ptygmatically folded, as mentioned above). The lineation dips very gently towards SSW (average orientation: 200/05). Numerous structures such as the boudinaged veins, ptygmatic folds with boudinaged limbs and shear sense indicators e.g. δ-clasts (Fig. 58), sigmoids, winged inclusions (Fig. 59) and rotated boudins (Fig. 59) indicate a minor top-to-the-SSW shear component. Additionally kinematic indicators such as: δ-clasts, tension gashes (Fig. 60 and 61) and asymmetric folds show a top to SSW shear-sense.
The observed tension gashes indicate that simple shear took place during the formation of the mylonitic zone. The tension gashes are aligned in two conjugated zones with their intersection shown in (Fig. 61). The instantaneous stretching axis has a direction of 330°-150° degrees and the instantaneous compression axis oriented along 60°-240° degrees. The tension gashes are also boudinaged in certain cases (Fig. 60 and 61).

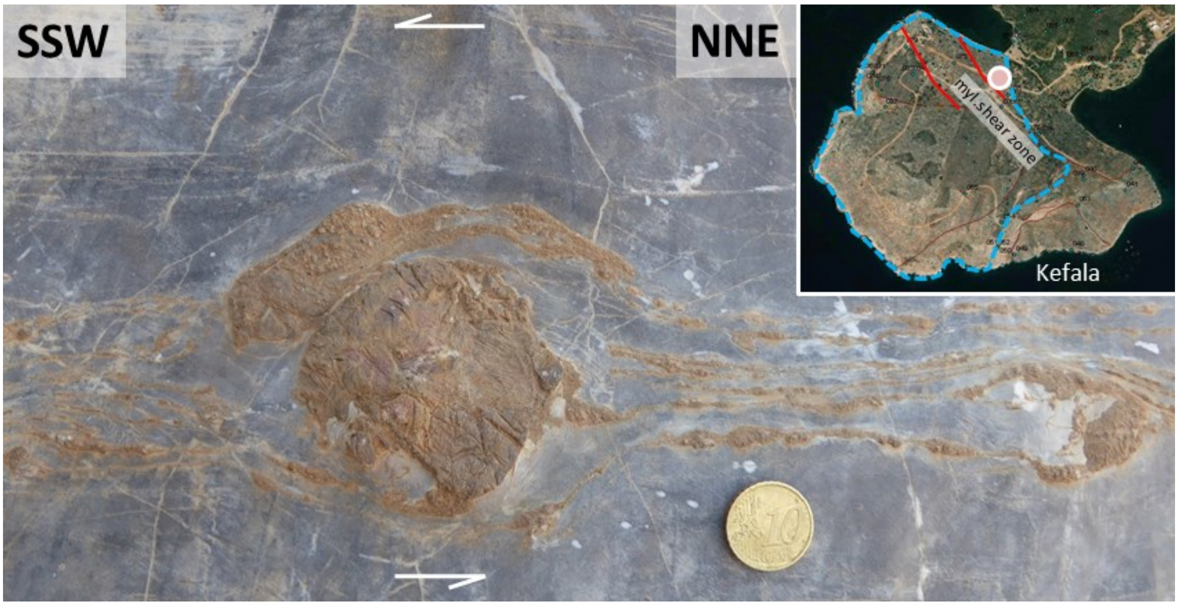

Fig. 58: Example of a rotated clast (δ-clast) in the shear zone in the Permian Marble Unit indicating top to the SSW shear component.

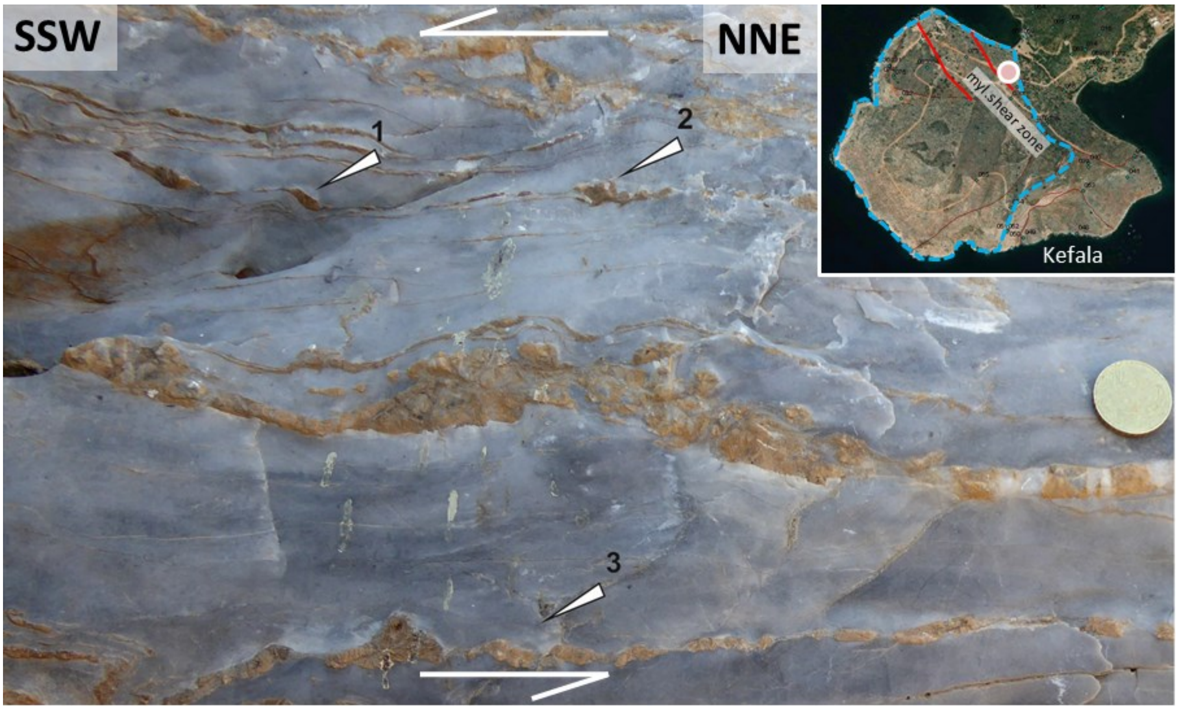

Fig. 59: Shear sense indicators in the ultramylonitic shear zone in the Permian Marble Unit.
1) sigmoid, 2) winged inclusion, 3) asymmetric boudinaged segments

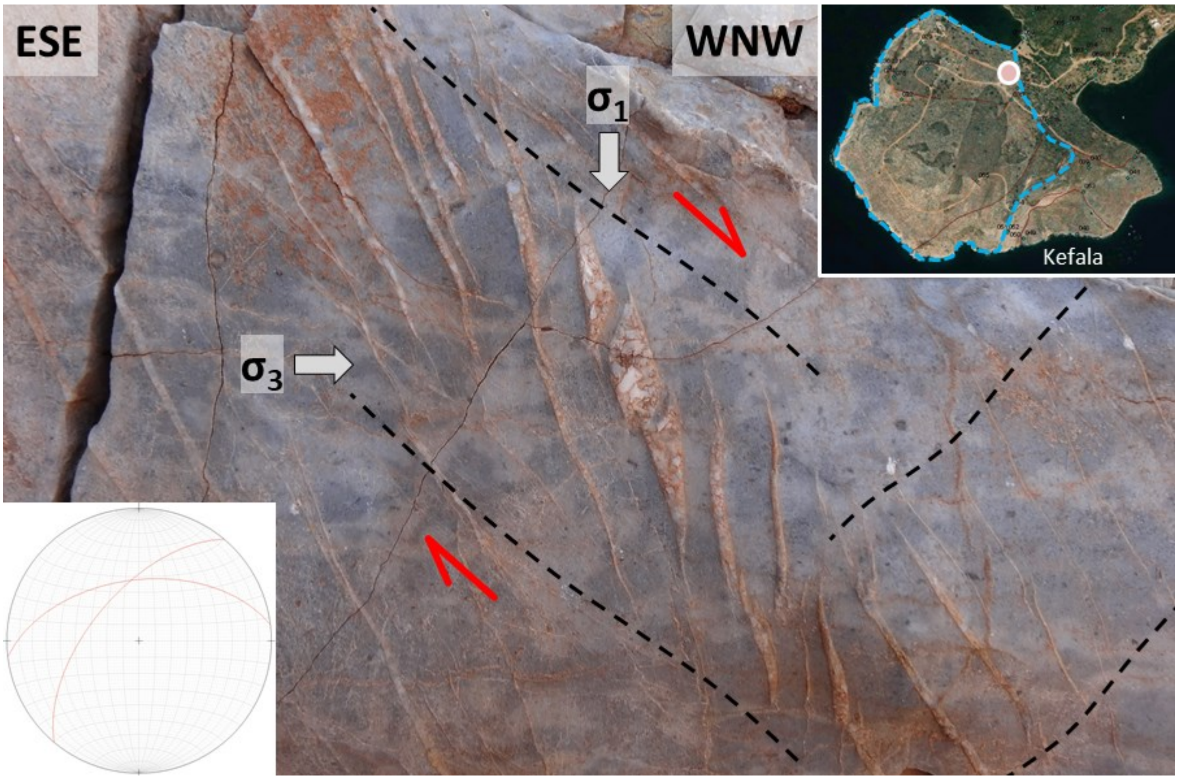

Fig. 60: Tension gashes from the mylonitic shear zone in the Permian Marble Unit. Larger-scale tension gashes contain broken-up components. Note that the tension gash in the center of the image is boudinaged. There is a conjugate, second set of tension gashes visible at the right side of the image.

Fig. 61: 3D view on the tension gashes showing the cylindrical character of the deformation zone.

Outside of the mylonitic shear zone, no significant deformation could be observed. Fig. 62 shows an outcrop right at the SW margin of the mylonitic shear zone with circular, undeformed crinoid stems and other fossils. Within the mylonitic shear zone, deformation of the crinoids is evident and is documented in Fig. 63.

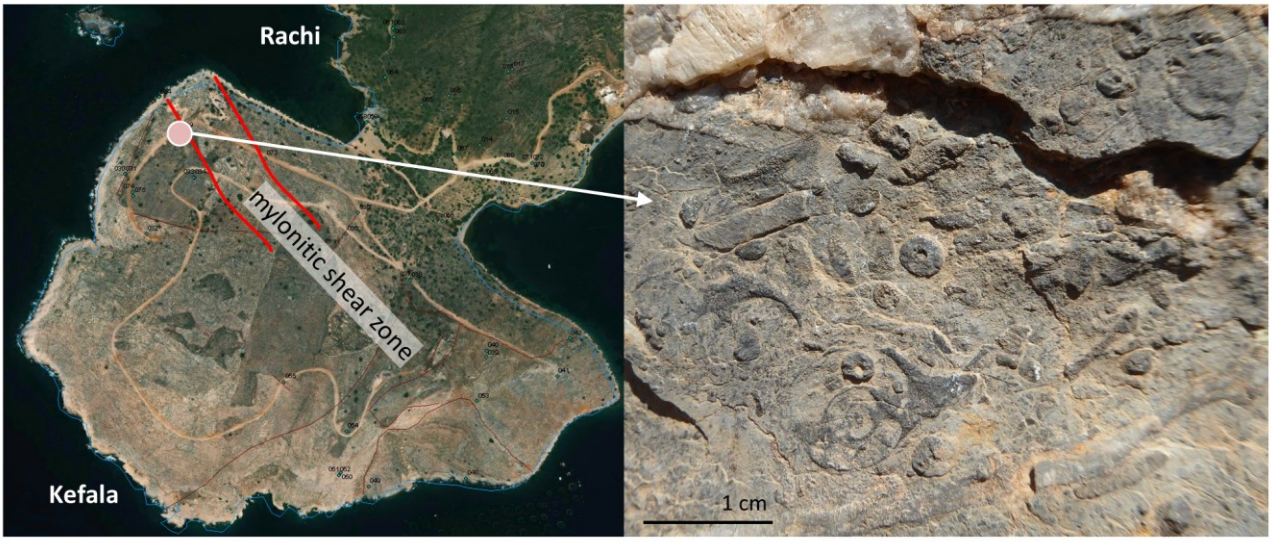

Fig. 62: Outcrop at the SW margin of the mylonitic shear zone with undeformed fossils.

Fig. 63: Deformed crinoid stem in the marginal zone of the mylonitic shear zone.

Also at the SW-margin of the mylonitic shear zone, unfolded boudinaged dolomitic layers can be observed in the white micritic marble zone of the Permian Marble Unit (Fig. 64).

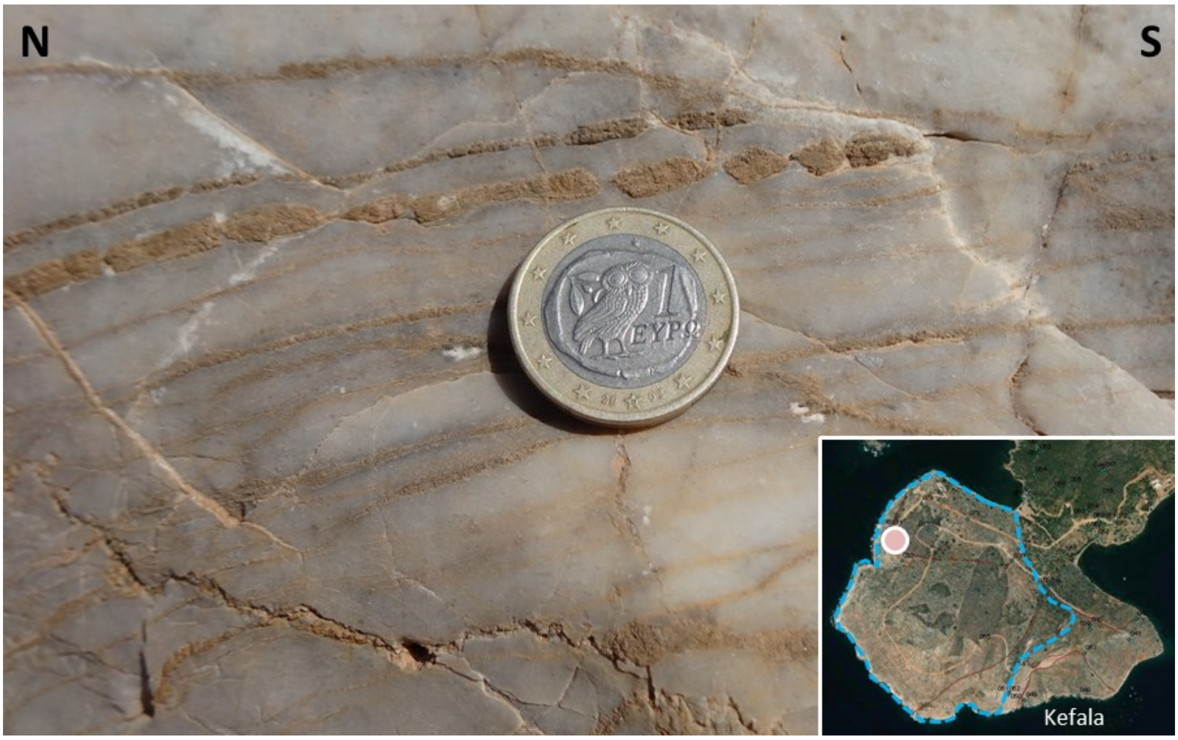

Fig. 64: The dolomitic layers within the white micritic marble litho-type of the Permian Marble unit are boudinaged when reaching a certain thickness. Note the stylolite that is perpendicular to the extension direction of the boudinage.

Additional alpine fault zones are also present in the Kefala area mainly within the Permian Marble trending NE-SW and WNW-ESE (Fig. 65).

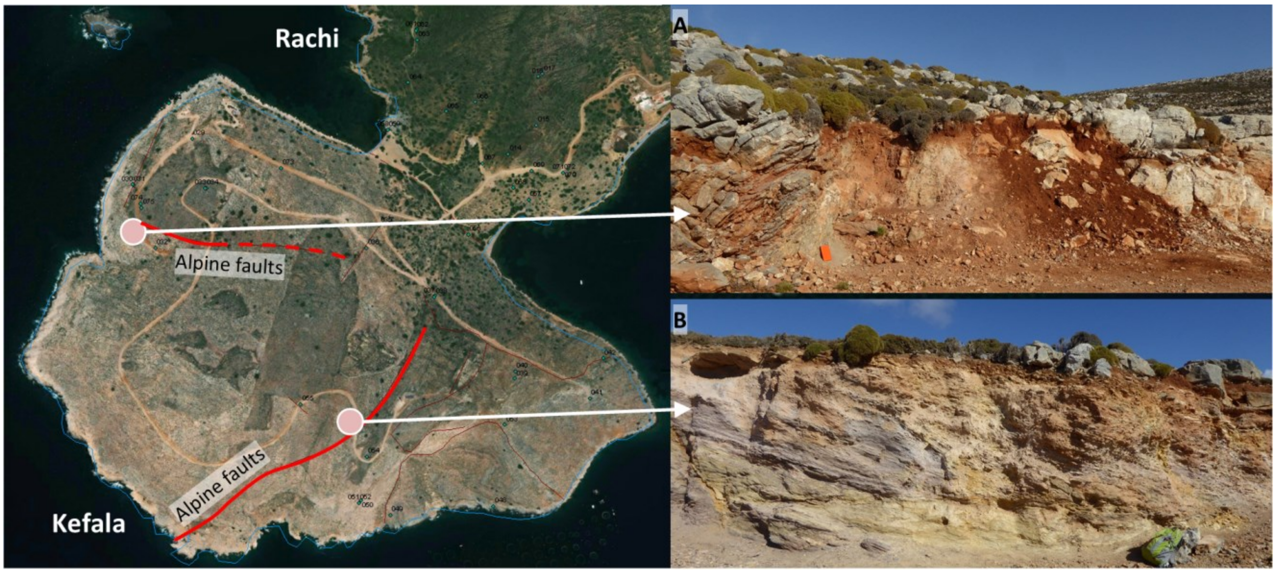

Fig. 65: Location and internal structure of younger, alpine fault zones within and at the border of the Permian Marble Unit. A) Highly brecciated sub-vertical fault zone that shows drag structures at the margins in the E of Kefala. B) Fault zone with remnant foliation, highly weathered and broken rocks in the fault core close to the boundary with the Devonian Marble Unit in the SW-part of Kefala.

Metaconglomerate Unit

At the transition from the Kefala area to the Rachi area, a low grade recrystallized metaconglomerate can be found. The contact between the Metaconglomerate Unit and the units on the Kefala peninsula is not obvious because of the cover of scree and alluvial sediments. The metaconglomerate sediments are separated from the higher grade metamorphosed Quartz-Mica Schist Unit by a horizontal thrust. No systematic internal deformation features could be observed.

Quartz-Mica Schist Unit

The Quartz-Mica Schist Unit is located in the topmost position of the lithostratigraphy and is separated from the metaconglomerates by a horizontal thrust.

Foliation/lineation

The original sedimentary layering (S0) of the Quartz–Mica Schist Unit is isoclinally folded and a new, penetrative, metamorphic foliation (S1) is developed. A crenulation cleavage starts to form by folding the S1 foliation by NW-SE trending fold axes (Fig. 66). The stretching/intersection lineation is not well defined, since the unit was folded and refolded three times. The measurements are shown in figure 67.

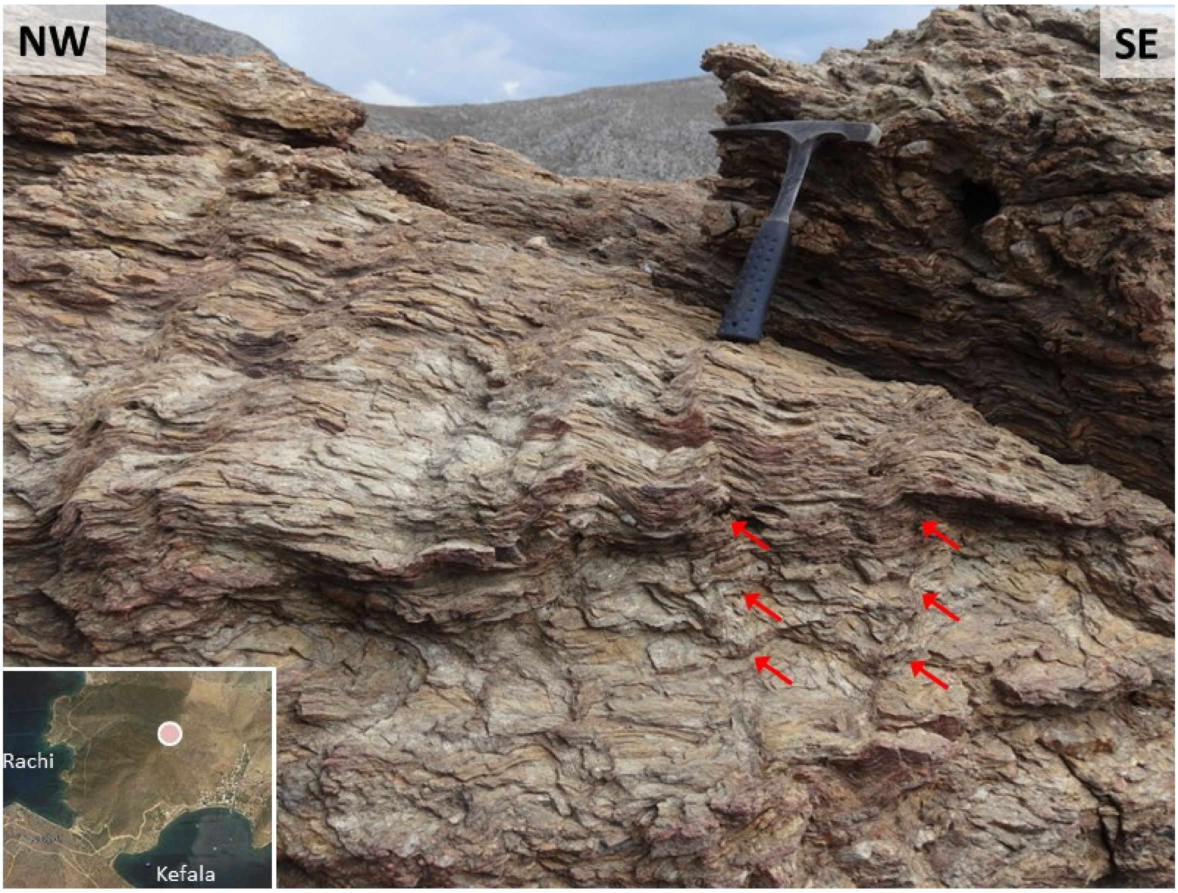

Fig. 66: Quartz-Mica Schist at outcrop in WP20. The original sedimentary layering (S0) is isoclinally folded and a metamorphic foliation (S1) develops. S1 is then folded by tight folds and a crenulation cleavage (S2) is starting to form (indicated by red arrows).

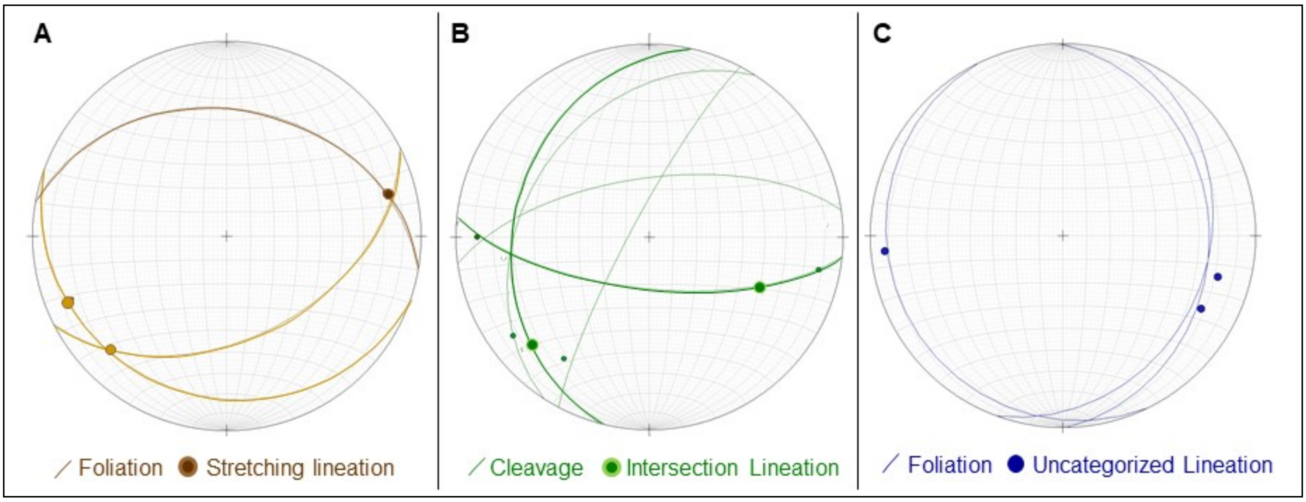

Fig. 67: Lower hemisphere stereonet plots for A) metamorphic foliation with stretching lineation, B) cleavage developed during folding with the intersection lineation, and C) uncategorized foliation/lineation pairs. Note that the stretching lineation is clockwise oblique to the foliation and the intersection lineation is counterclockwise oblique. The uncategorized lineation is almost parallel to the foliation dip direction.

Folds:
There are three different generations of folds. The first generation consists of isoclinal folds (F1) developed in the sedimentary layering (S0) with fold axes mostly striking NE-SW. The second folding event has tightly folded fold limbs creating a crenulation cleavage with fold axes around NW-SE. The F1 and the F2 is a roughly orthogonal system that changes direction across the Rachi area due to the oblique refolding by the "open-folds" (F3) with axes dipping to the SW (Fig. 68 and 69). The F3 open folding folds the crenulation cleavage. The F3 fold axes cluster very well defined around the SW plunge direction and are therefore regarded as the youngest event.

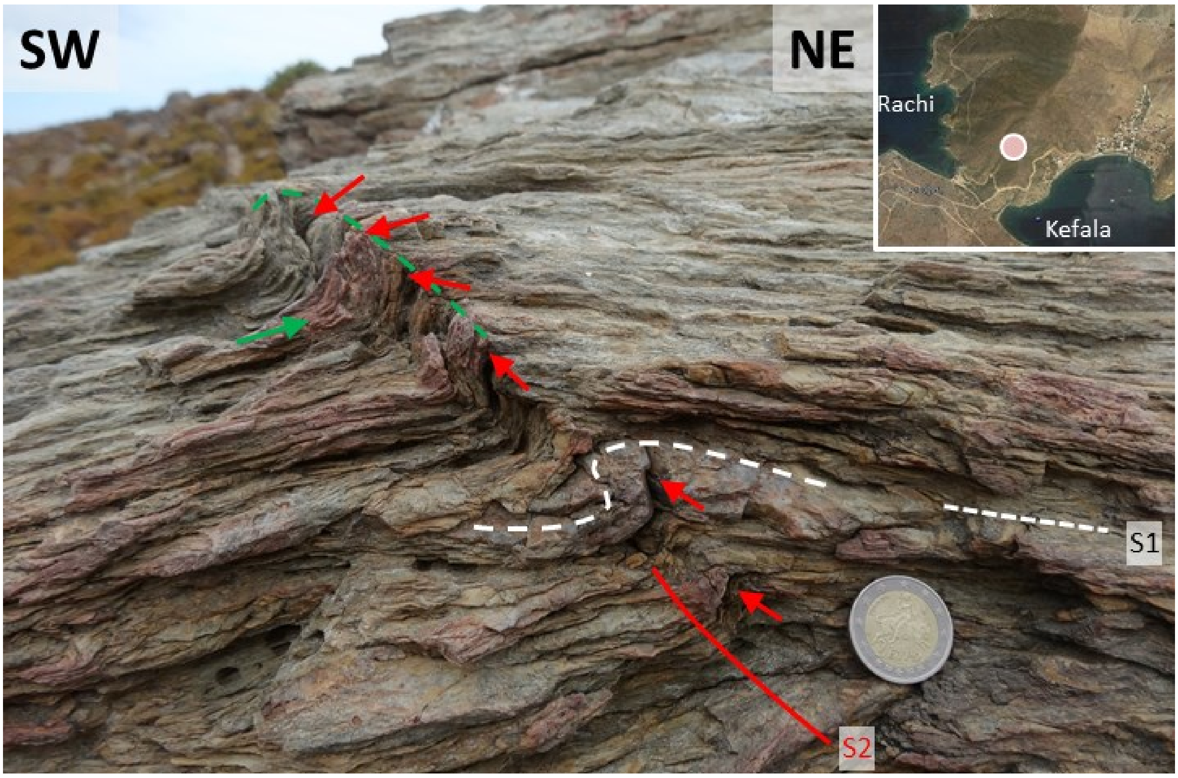

Fig. 68: Quartz-Mica Schist outcrop at WP16 showing two folding phases. Red arrows: F2 fold axes creating S2 crenulation cleavage (~114/40). Green arrow: F3 fold axis folding the crenulation cleavage (234/20).

The same sequence of folding can be observed in the outcrop at WP20 in the center of the Rachi area (Fig. 69). However, here the fold axes are a bit more oblique relative to the entire folding system. In the following, examples are shown for each folding phase. Fig. 69 represents an example for the isoclinal folds (F1) that can vary in size from very small, intra-bedding folds to larger, 1 cm thick folds.

The tight, cleavage-forming F2 folds usually have a wavelength of around 3 cm. The example photographs in Fig. 70 and 71 show the dimensions of the folds and also details of their geometry.

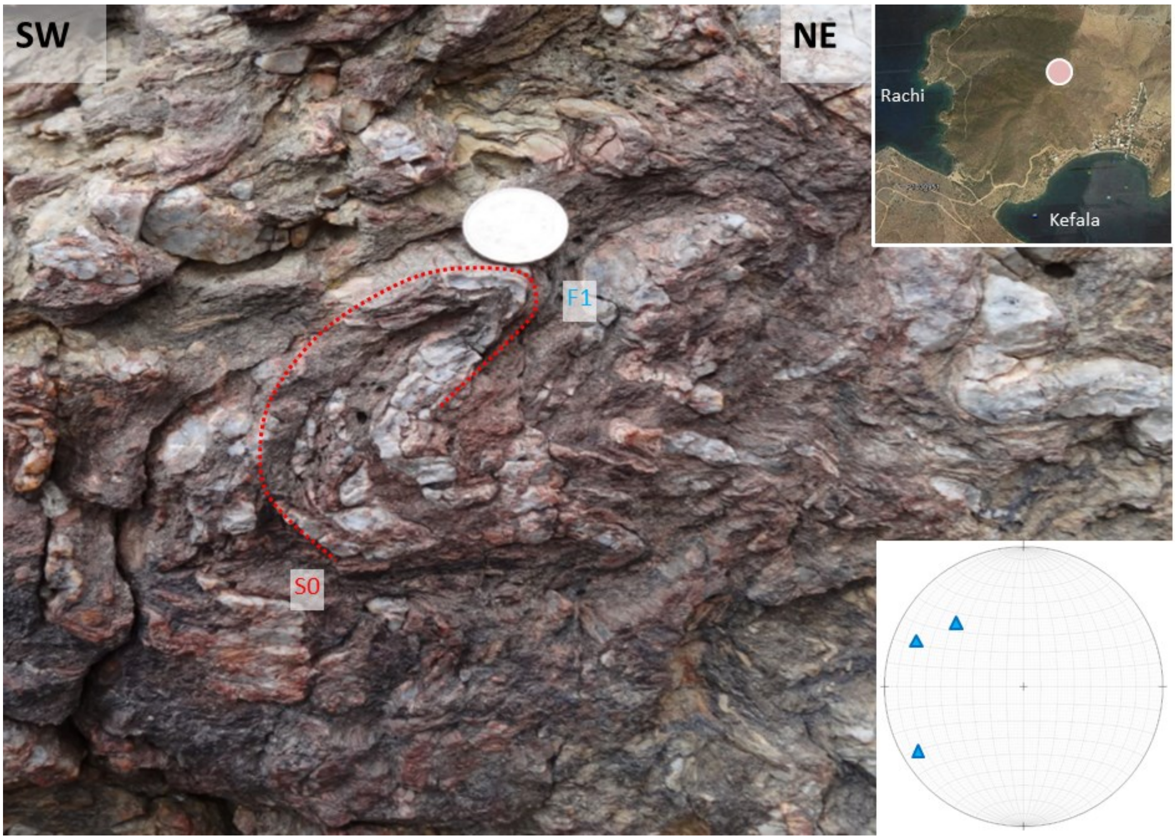

Fig. 69: Example of a folded F1 isoclinal fold in outcrop at WP20 with the most prominent fold axes of 312/35 and 292/18.

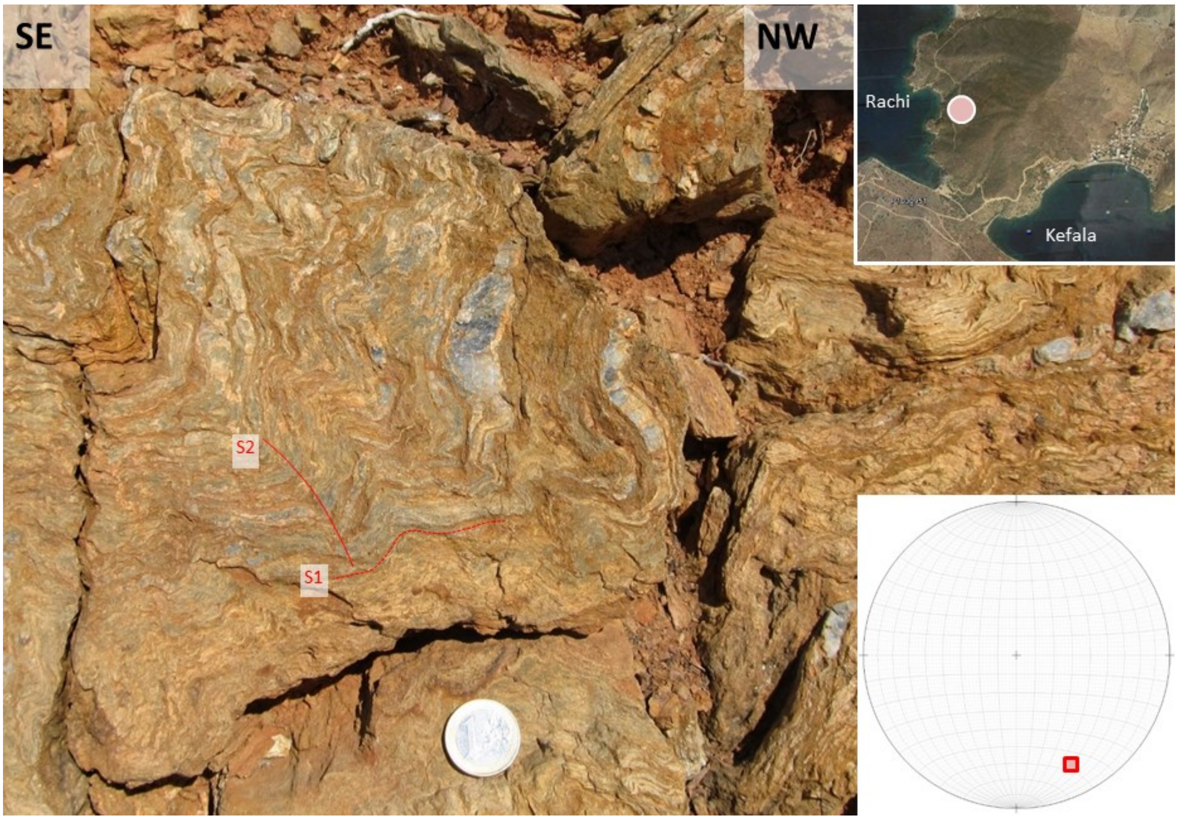

Fig. 70: F2 tight fold creating the S2 crenulation cleavage (upper left). These folds sometimes show a bulbous hinge collapse. Note that the crenulation cleavage is bending in a concave way from the top left of the photographs to the lower right.

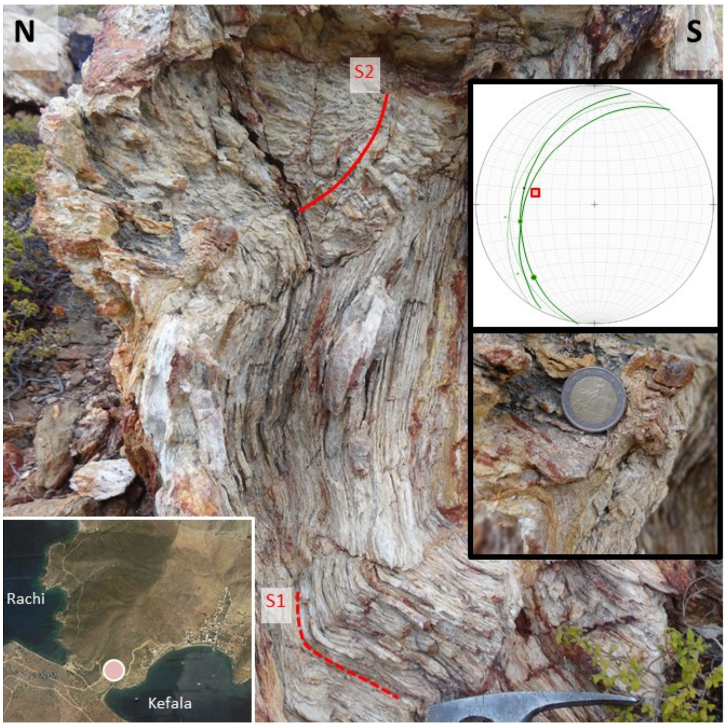

Fig. 71: F2 tight fold at WP14 with a clearly developed bulbous hinge collapse. The F2 fold axis in this outcrop is mainly 283/39.

During the F3 phase, the crenulation cleavage is folded around a ~ SW plunging fold axis. In the field, this relationship can be best observed in the outcrops at WP16 (Fig. 68) and WP46 (Fig. 70). The measured fold axes and lineations are summarized in Fig. 72 and 73. The three folding phases can be explained as follows: First, F1 isoclinal folds develop that are plunging gently towards ~NE. The second F2 phase consists of fold axes plunging steeper ~NW-SE and during this phase, the F1 fold axes are tilted, spreading between N and E, but remaining with a gentle plunge due to the steep F2 axes. The gently ~SW plunging F3 fold axes make the F2 fold axes plunge gentler, but still in a ~NW-SE orientation. At the same time, the F1 fold axes are folded for a second time and the fold axes spread even more in N-E direction, as well as across the compass directions due to the gentle dip of the F3 axes.

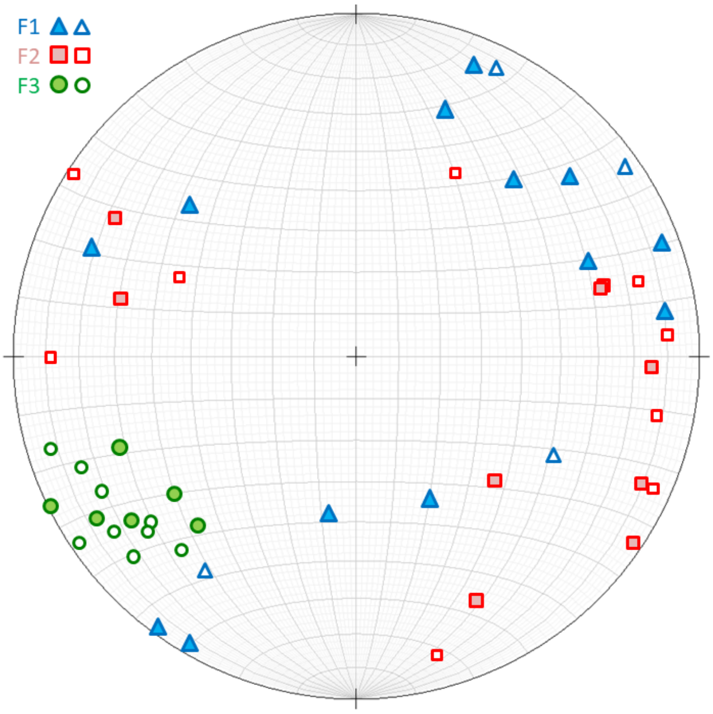

Fig. 72: Lower hemisphere stereo-net showing the fold axes of all three folding phases, along with associated lineation measurements. The fold axes are shown with filled symbols and the associated lineations are represented by symbols without filling.

The stereoplots in Fig. 73 were constructed by back-rotating the folding of each phase. First, the average interlimb angle of each folding phase was estimated. This estimate is 80° interlimb angle for the F2 tight fold phase and 150° interlimb angle for the F3 open fold phase. Thus, the limbs of the F2 phase were rotated by 50° and the limbs of the F3 phase were rotated by 15°. In the next step, an eigenvector calculation was applied to determine the mean rotation axis of the F3 fold axes. The calculation resulted in a mean F3 fold axis of 237/18, which was used as the first rotation axis. The fold axes of the tight F2 folds were separated according to their location in one of the two F3 fold limbs with respect to the mean F3 fold axis. The F2 fold axes located in the NW F3 fold limb were rotated clock-wise by 15° and the F2 fold axes located in the SE F3 fold limb were rotated counter-clockwise by 15° to "flatten out" the F3 folding. Now, an eigenvector calculation on the newly derived F2 fold axes was carried out. It resulted in a mean F2 fold axis of 111/01. The F1 fold axes were sorted into the fold axes of the SW and NE F2 fold limbs. The F1 fold axes of the SW fold limb were rotated by 50° counter-clockwise and the F1 fold axes of the NE fold limb were rotated by 50° clock-wise. As a result, each back-rotated phase shows the possible orientations of the fold axes prior to folding in the respective stereoplot of Fig. 73.

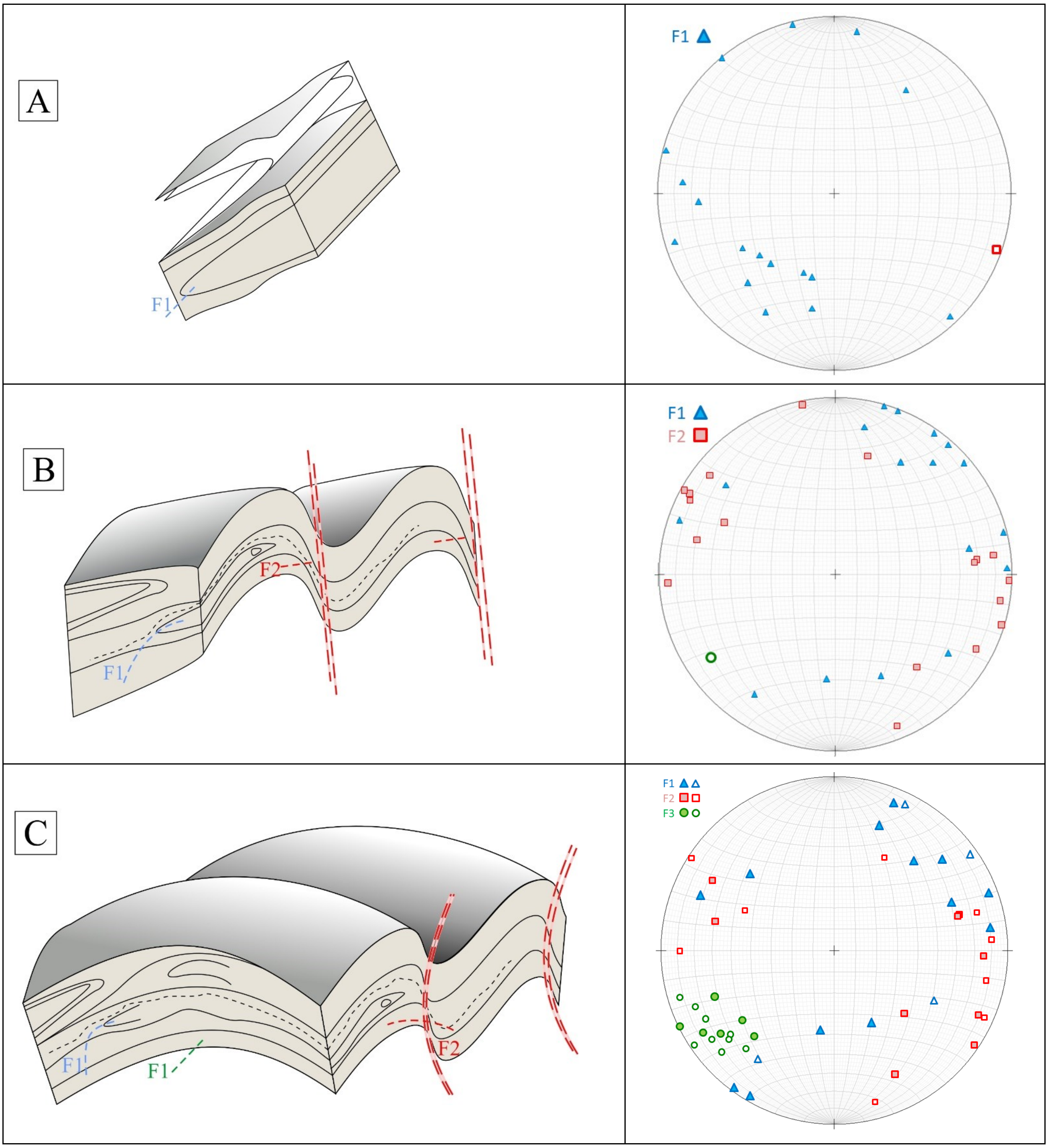

Fig. 73: Schematic diagrams of each folding phase next to stereoplots showing the back-rotated fold axes of the respective folding phase that affected the Quartz-Mica Schist Unit. A) First, isoclinal folds develop mostly within the bedding. B) The second, tight folding with an almost perpendicular fold axis creates a crenulation cleavage. C) The last phase has a fold axis oriented very consistently to the SW and refolds the crenulation cleavage. The method of stereoplot construction is explained in the text on the previous page.

Faults:

The majority of the observed structural features in the Quartz-Mica Schist is brittle-ductile layer parallel stretching of the quartz mobilisates (Fig. 74), or ductile shear zones parallel to the foliation creating sigma clasts (Fig. 75). Brittle faulting is limited to fractures developing along the weak zones of the foliation or related to features using planes that were formed during F2 or F3 folding. Brittle activation of the crenulation cleavage occurs, but offsets are very small - the mode of these fractures is tensile (Fig. 76).

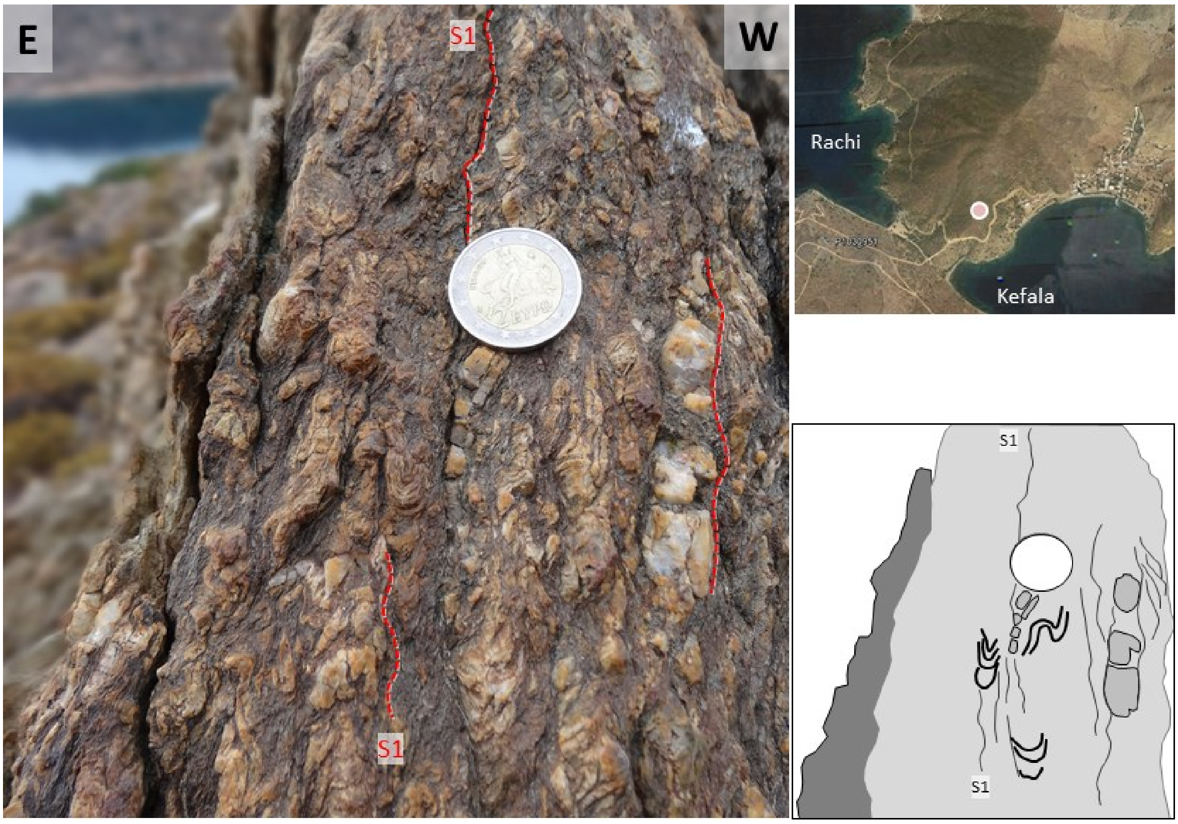

Fig. 74: Ribbons of quartz mobilisates arranged parallel to the S1 metamorphic foliation and along the limbs of the isoclinal folds at the outcrop at WP15 in Rachi area. The S1 possibly derives from the crenulation cleavage of the F1 isoclinal folds. In the microlithons the sedimentary bedding S0 can be observed. The quartz ribbons are boudinaged into angular blocks indicating layer-parallel stretching.

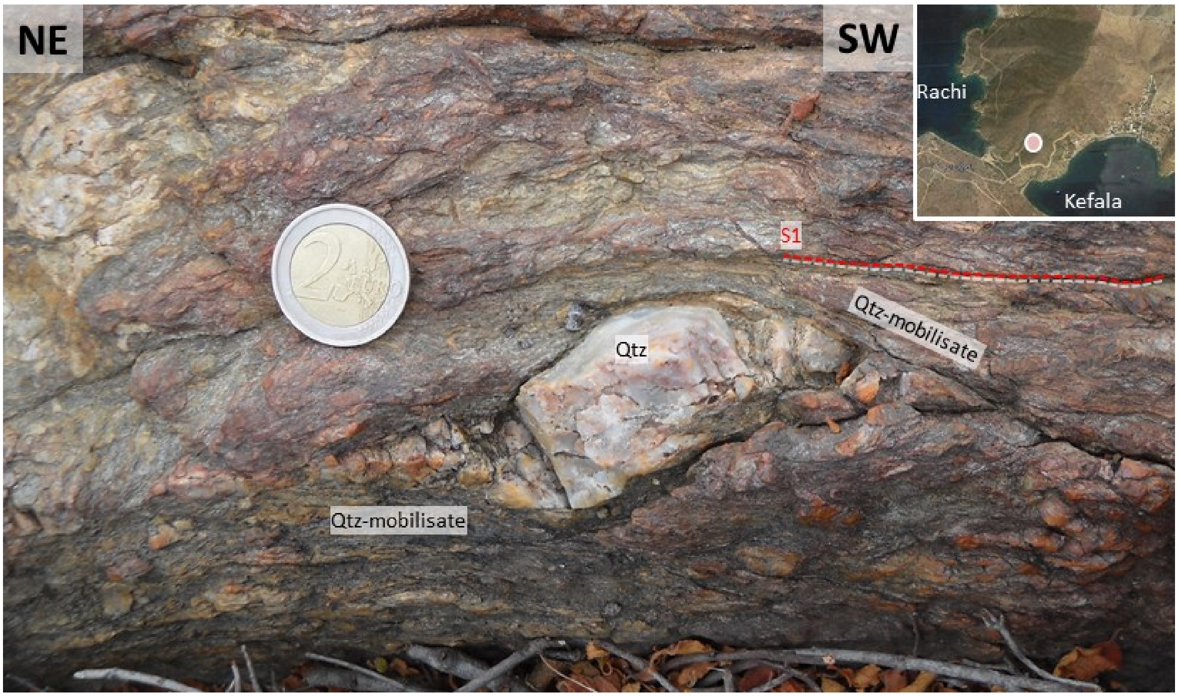

Fig. 75: Deformed quartz mobilisate in the Quartz-Mica Schist close to WP17. A dense, central part of the mobilisate can be seen with symmetrically thinning outer parts indicating a pinch and swell structure sub-parallel to the S1 foliation.

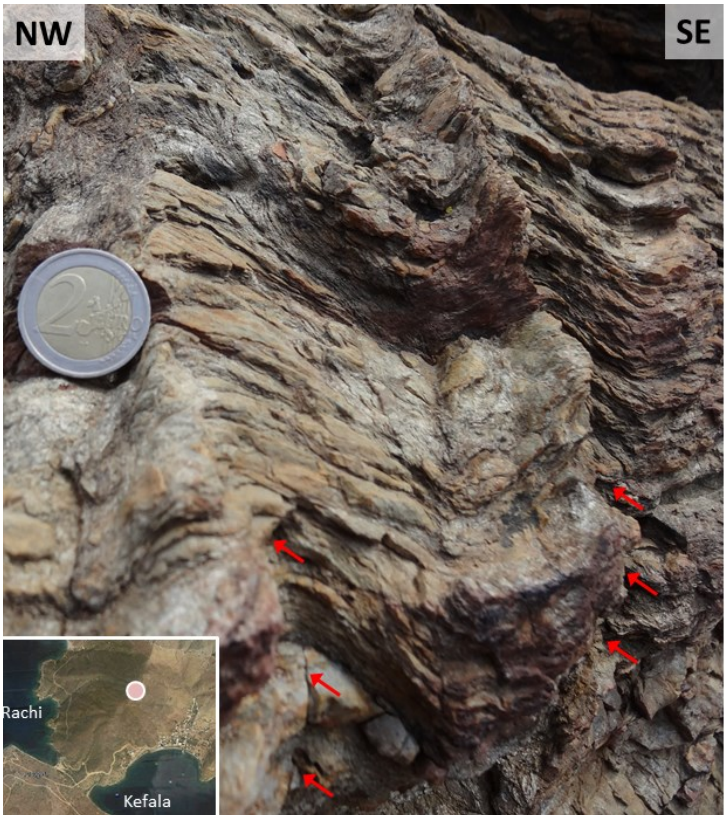

Fig. 76: Tensile fractures using the crenulation cleavage as initiation plane. These fractures occur very late in the geologic history and are not filled.

5.2 Microstructural observations

In this chapter, microstructural observations from the study of thin sections of the Variscan units, as well as the techniques for the preparation of the samples are summarized. The methods include optical microscopy and EBSD. The description of the samples starts from the tectonically lower to the tectonically upper unit. Not all units have thin sections – the lowest unit with thin section samples is the Interlayered Marble Unit.

Interlayered Marble Unit

In the NE outcrop of the Interlayered Marble Unit, the crinoid stem shown in figure 77 was found. It is slightly deformed and cracked. The strain ellipse could not exactly be reconstructed, since the original diameter of the undeformed crinoid stem is not known.

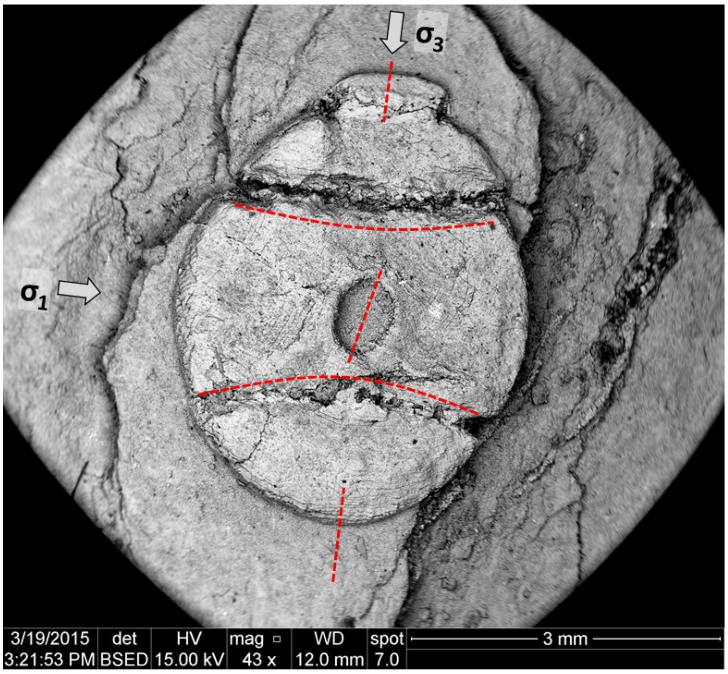

Fig. 77: SEM image of brittle-ductile deformation of a crinoid stem from the Interlayered Marble Unit. Two veins formed in the extensional field perpendicular to the main compressive stress axis. Note that the ellipse of the inner cavity of the stem has slightly oblique stress axes indicating a two-phase deformation: an initial ductile phase overprinted by dissolution precipitation creep.

<u>Devonian Marble Unit</u>

From the Devonian Marble Unit no thin sections were produced. Structural observations are only available in macro- to mesoscale.

<u>Permian Marble Unit</u>

In these next paragraphs an ultramylonitic zone in the low-grade recrystallized Permian Marbles is investigated, which is cut by 1-20 mm thick iron-rich calcite veins. The researched outcrop is located at the N part of Kefala peninsula. The composition of the marble matrix is fine to coarse-grained pure calcite as determined from EDAX measurements. In the ultramylonitic zone iron-rich calcite veins are boudinaged and then ptygmatically folded, which can be seen from bent and rotated boudins with asymmetric and newly formed calcite wings (Fig. 78). The ptygmatically folded boudins in the mylonitic shear zone consist of iron-rich calcite, while in the necks of the boudins, pure calcite crystals form. The calcite in the necks of the boudins shows thin twins of type I and type II, which indicates a temperature of deformation at around 170°C to 200°C and higher (Ferrill et al., 2004). Two examples are shown in figure 79. The presence of two different twining types might show a heterogenous distribution of temperature-rise.

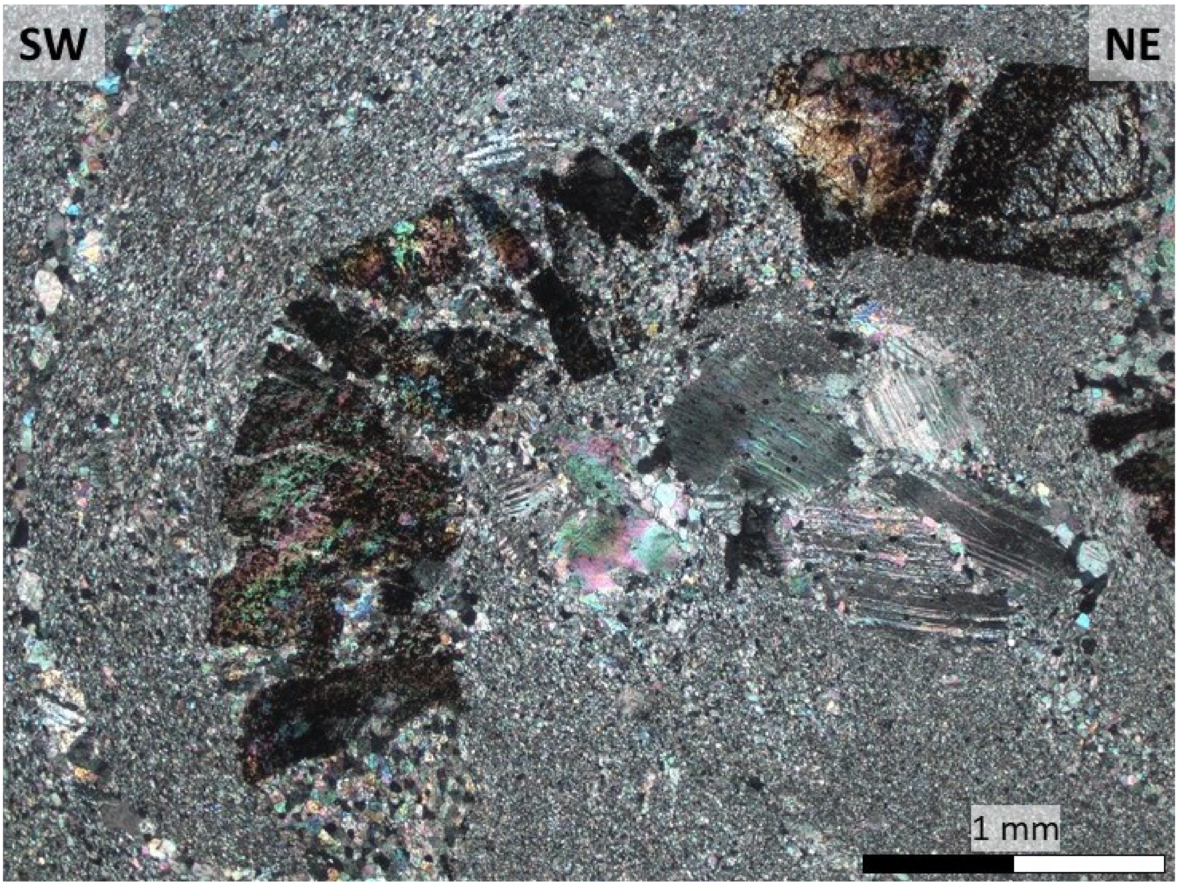

Fig. 78: Detail view of ptygmatically folded boudin of iron-rich calcite material (KA014006). This example shows that the iron-rich calcite veins were first boudinaged and then ptygmatically folded. Around the outer rim of the boudin, the grains show a shape preferred orientation aligned with the folding.

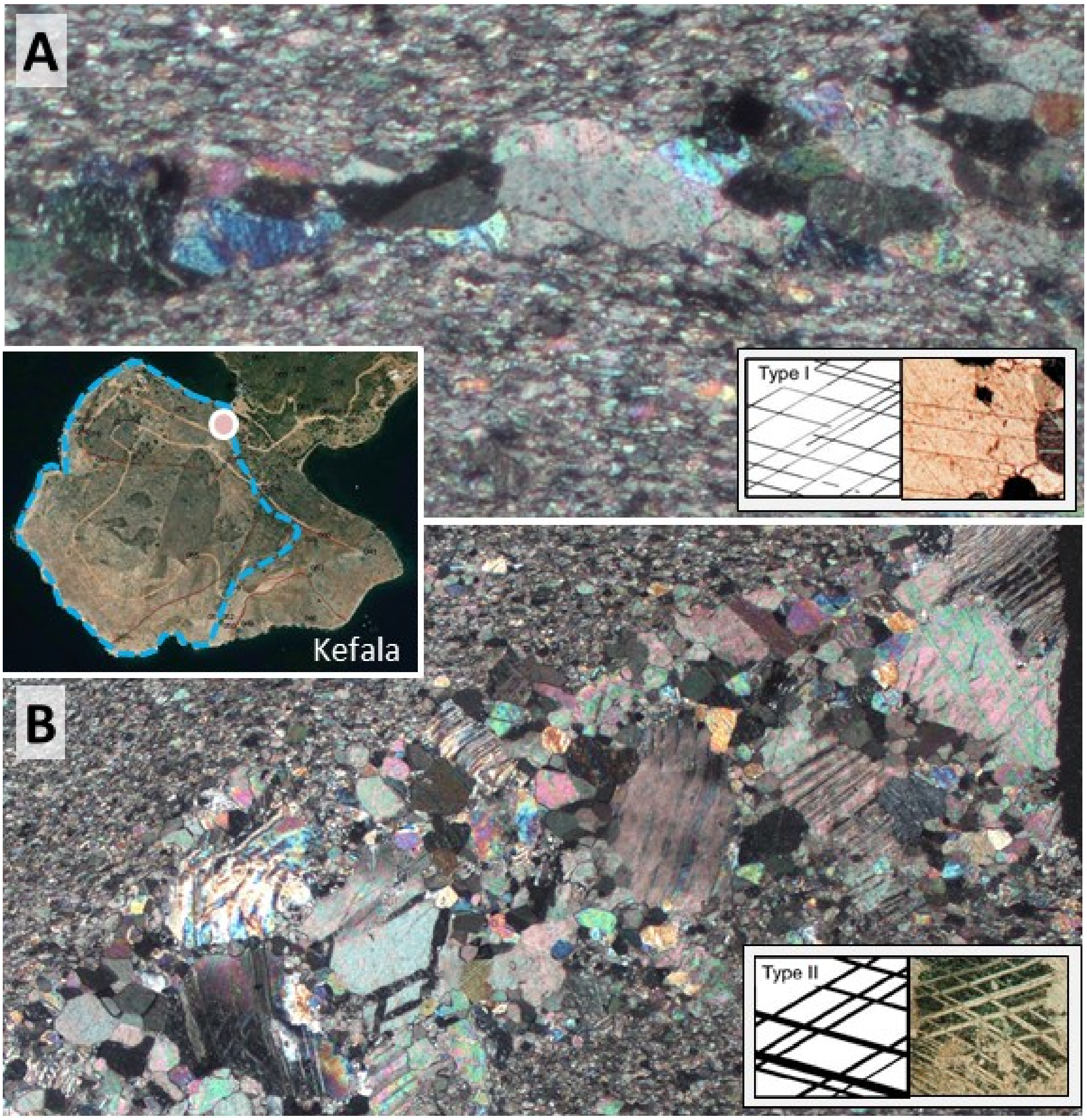

Fig. 79: A) Calcite twinning in the boudin neck in the Permian Marble (KA014006) indicating type I twinning at 170°C to 200°C. B) Another position in the Permian Marble sample KA014006. Here the calcite of the boudin neck closely resembles type II twinning (Ferrill et al., 2004) with two sets of twins present.

EBSD measurements:

The EBSD investigation focused on the ptygmatically folded boudinage that can be seen in the thin section of sample KA014006 (Fig. 80). It is a detail of a mylonitic zone, in which the strain localization along the micro-boudinage was calculated.

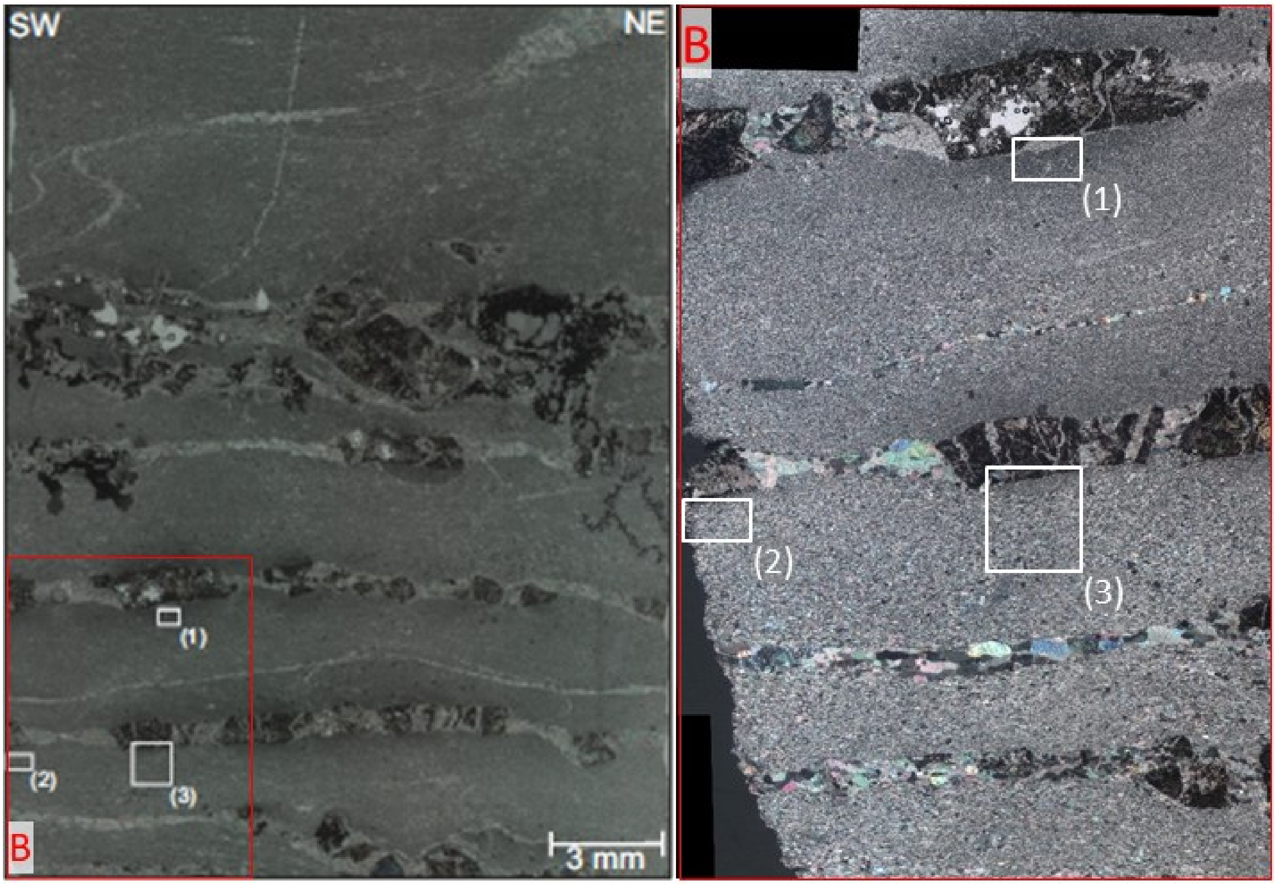

Fig. 80: KA014006, thin section cut parallel to the lineation, with the white boxes showing the locations of the EBSD scans: (1) fine grained area, (2) coarse grained area and (3) region with increased shear from the boudinage segment towards the coarse-grained matrix. B shows a zoomed-in area.

Methodology:

The sample KA014006 from the described thin section (Fig. 80) was cut from the oriented outcrop sample parallel to the stretching lineation and in the YZ plane of finite strain. After that, the thin section was polished with diamond paste and also with Köstrosol 3530, an alkaline colloidal silica suspension. As a last preparation step for EBSD, the sample was coated with a thin carbon film for electric conductivity.

The selection of the areas of interest was conducted after the thin-section analysis on micro-photographs taken on a Leica DM4500 P microscope. Three regions were selected for further EBSD analysis (Fig. 80), which was carried out on a FEI Quanta 3D FEG instrument. The focus of the measurements was on crystallographic preferred orientations, grade of intra-crystalline deformation and the creation of misorientation maps.

For each of the three regions of interest (fine-grained area, coarse-grained area, and shear region) the instrument was calibrated separately, as well as the parameters were selected individually (Tab. 3). The definition of step sizes occurred depending on the grain size.

Parameters		*Scan 1*	*Scan 2*	*Scan 3*
Scanning settings	Fixed step size	*0.7 microns*	*1.00 microns*	*1.40 microns*
	Scan Mode	*hexagonal grid*	*hexagonal grid*	*square grid*
Hough space	Resolution binned pattern size	*120*		
	Theta step size	*1°*		
	Rho fraction (to avoid edge artefact detection)	*85%*		
	Convolution mask	*9x9*		
	Minimum peak distance	*10 pixels*		
	Minimum peak magnitude	*200*		
	Peak counts	*3-12*	*3-15*	*3-15*
Indexing rates		*16.7 points/sec*		
Camera settings	Exposure time	*58.78 ms*		
	Binning	*4x4 (348x260)*		

Tab. 3: Parameters for the EBSD scanning of the three selected regions.

The measured data were post-processed and cleaned in the OIM Data Collection and Analysis software according to standard procedures using a confidence index ci of >0.1 and the neighbor orientation correlation of 3 and 5. The clean-up cycle was repeated three times.

The detection of grain boundaries and the misorientation analysis was conducted in MATLAB with MTEX toolbox (https://code.google.com/archive/p/mtex/, https://mtex-toolbox.github.io/). A misorientation angle of 10° degrees was chosen to define the grain boundaries between adjacent points. Orientation distribution functions (ODFs) were calculated and visualized in pole figure plots (Bunge, 1982) with an orientation of (0001), for –a <11-20> axes and m {10-10}, e {01-10}, r {10-14} planes of calcite. The correlated and uncorrelated misorientation-angles were detected by OIM Data Analysis software. A correlated misorientation angle is measured between adjacent points of two grains and the uncorrelated misorientation angle is measured between two randomly chosen grains that are not necessarily adjacent. Also, the theoretical curve for a random misorientation distribution was calculated (Fig. 81).

Results:

The uncorrelated misorientation angle distributions are very close to the theoretical curve for a random misorientation – distribution due to the weak crystallographic preferred orientation in both fine and coarse-grained areas (Fig. 81). The peaks at 75°- 80° in both correlated and uncorrelated misorientation distributions for fine and coarse-grained areas are related to the twinning system in calcite (Bestmann et al., 2003). The distributions of misorientation angles measured for the fine-grained area and the coarse-grained area are both left skewed. The distribution of the fine-grained map has a characteristic tail of outliers at low values (0°-40°). However, for both scans the correlated, uncorrelated and the theoretical distribution curves have a broad peak, or plateau from 60° to 85° degrees (Fig. 81).

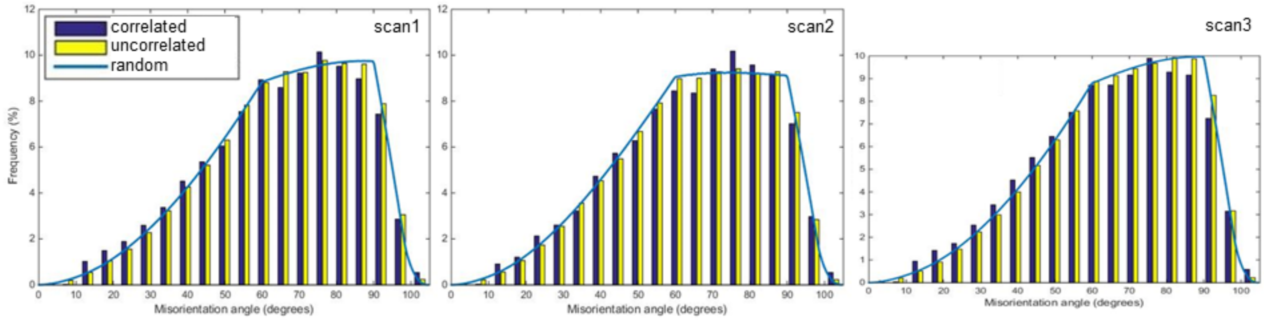

Fig. 81: Correlated, uncorrelated and expected random misorientation angle distributions for the selected three scanning areas. From left to right: Scan 1 (fine-grained area), scan 2 (coarse-grained area) and scan 3 (area with increased shear).

Orientation distribution functions (ODFs) can be visualized with pole figure plots, inverse pole figure plots, ODF sections and fibre sections (https://mtex-toolbox.github.io/files/doc/ODFPlot.html). The stereographic, equal area upper hemisphere projections of the ODF data are presented for fine -and coarse-grained maps, as well as for the increased shear region (Fig. 82 to 84). Figure 85 shows the orientation of the respective HKL projection planes in space. The texture of the grains is weaker in the coarse-grained area than in the fine-grained map with indexes 1.38 and 1.81 and ODFmax 2.1 and 2 respectively. Histograms represent the distribution of the grain size that is calculated with the help of the equivalent diameter $d = 2\sqrt{\frac{A}{\pi}}$.

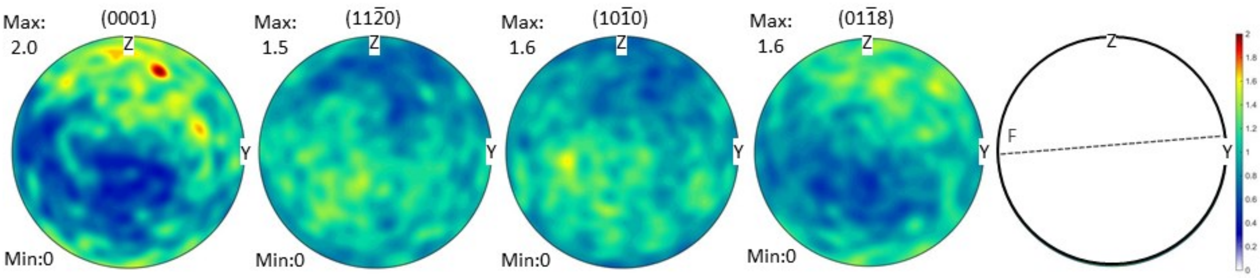

Fig. 82: ODF pole plots of scan 1 (fine grained area). The calcite c-axes show aligned weak maxima along a great circle in the (0001) plane. Y, Z are the sample axes. The foliation is horizontal (indicated in right-most plot).

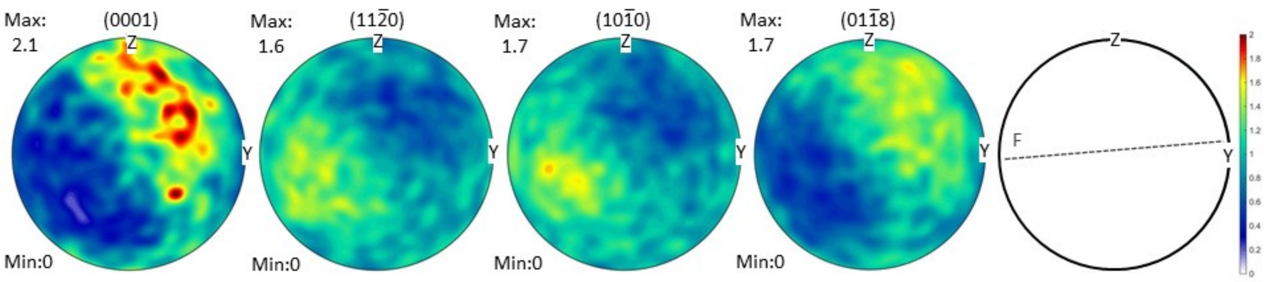

Fig. 83: ODF pole plots of scan 2 (coarse-grained area). C-axes show strong, broader maxima along a similar great circle as scan 1 in the (0001 plane, but no striking pattern in the other planes. Y, Z are the sample axes. The foliation is horizontal (indicated in right-most plot).

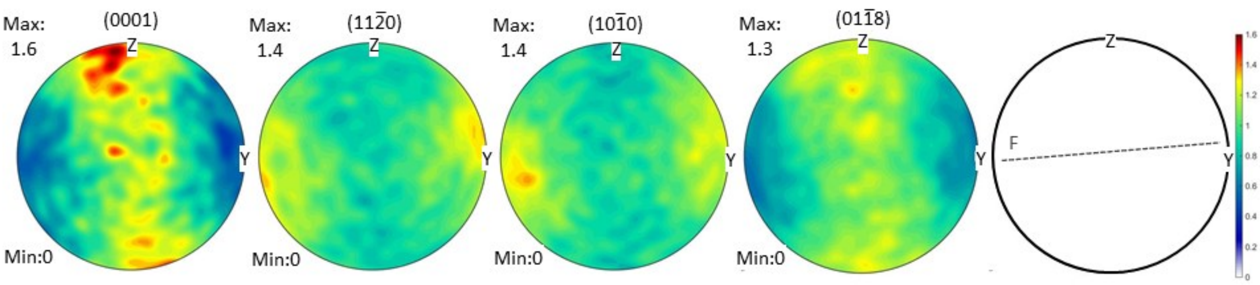

Fig. 84: ODF pole plots of scan 3 (area with increased shear). The c-axes show a marked girdle in the (0001) plane as the possible indication for simple shear. The girdle pattern is visible in all the other planes as well. Y, Z are the sample axes. The foliation is horizontal (indicated in right-most plot).

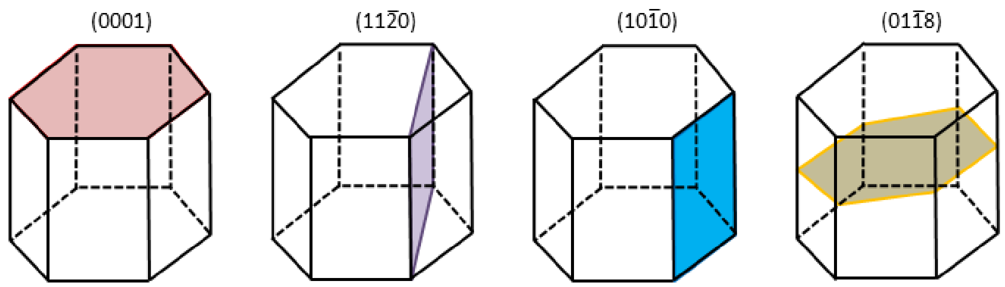

Fig. 85: Orientation of the respective HKL projection planes in space (modified after Kleber et al. 2010).

Additionally, the total number of analyzed grains, the mean grain sizes and the standard deviation values were calculated as well (Fig. 86). The histogram of the fine-grained area shows the peak in the grain size ranges between 5 and 10 µm. The range between 0 and 5 µm has also a very high count, broadening the peak. The histogram of the coarse-grained area presents a peak between 5 and 10 µm with a continuous slope to the range of 25 and 30 µm. After this range it shows a tail until 40 and 45 µm. The average grain size of the fine-grained area is 7 µm and the average grain size of the coarse-grained area is 10 µm. So, a clear difference between the two grain size histograms can be observed (Fig. 86).

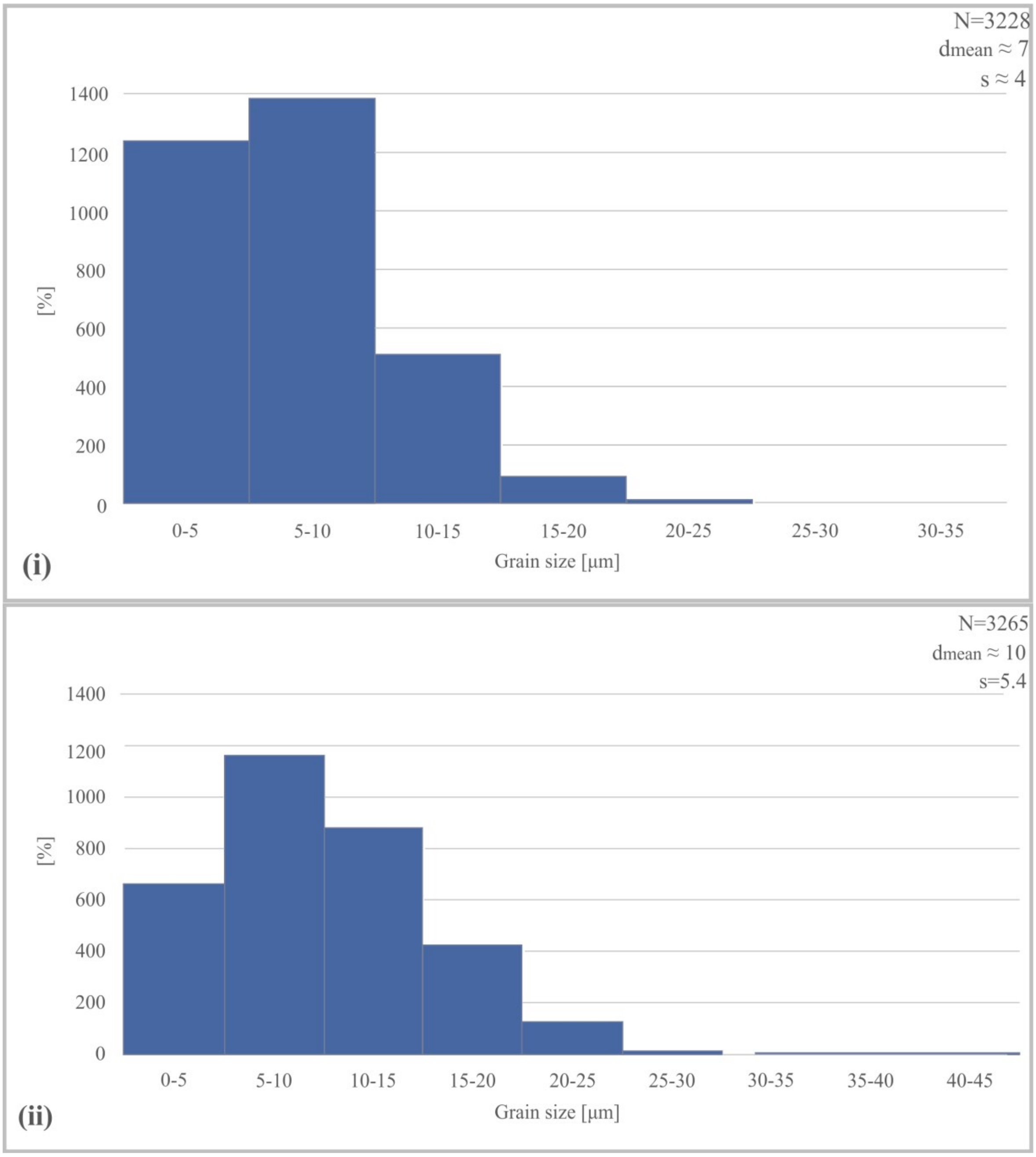

Fig. 86: (i) Grain-size histogram of the fine-grained area (scan 1), (ii) Grain-size histogram of the coarse-grained area (scan 2). N=total number of analyzed grains, dmean=mean grain size, s=standard deviation.

A detailed EBSD grain boundaries map of the third scan area that was mapped, and a diagram of the average grain size with respect to the distance from the veins are shown in figure 87. The average grain size increases from 8 µm at 100 µm distance to 12 µm at a distance of 500 µm and then stays roughly constant until 1400 µm with one negative exception at 1100 µm. Close to the necks of the boudins, micro-shear zones nucleate (Fig. 88).

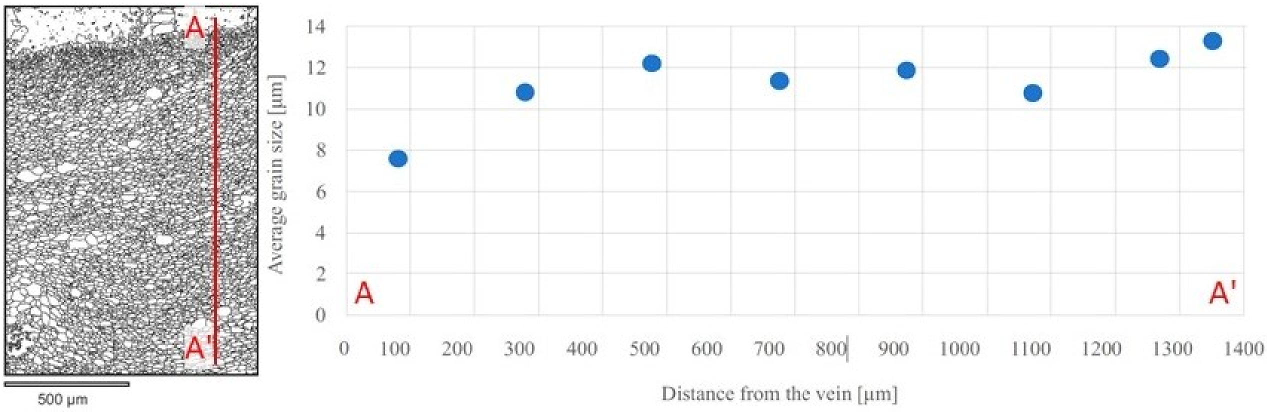

Fig. 87: Cross-section showing the average grain-size with distance from the vein shown on the EBSD grain boundary map 3.

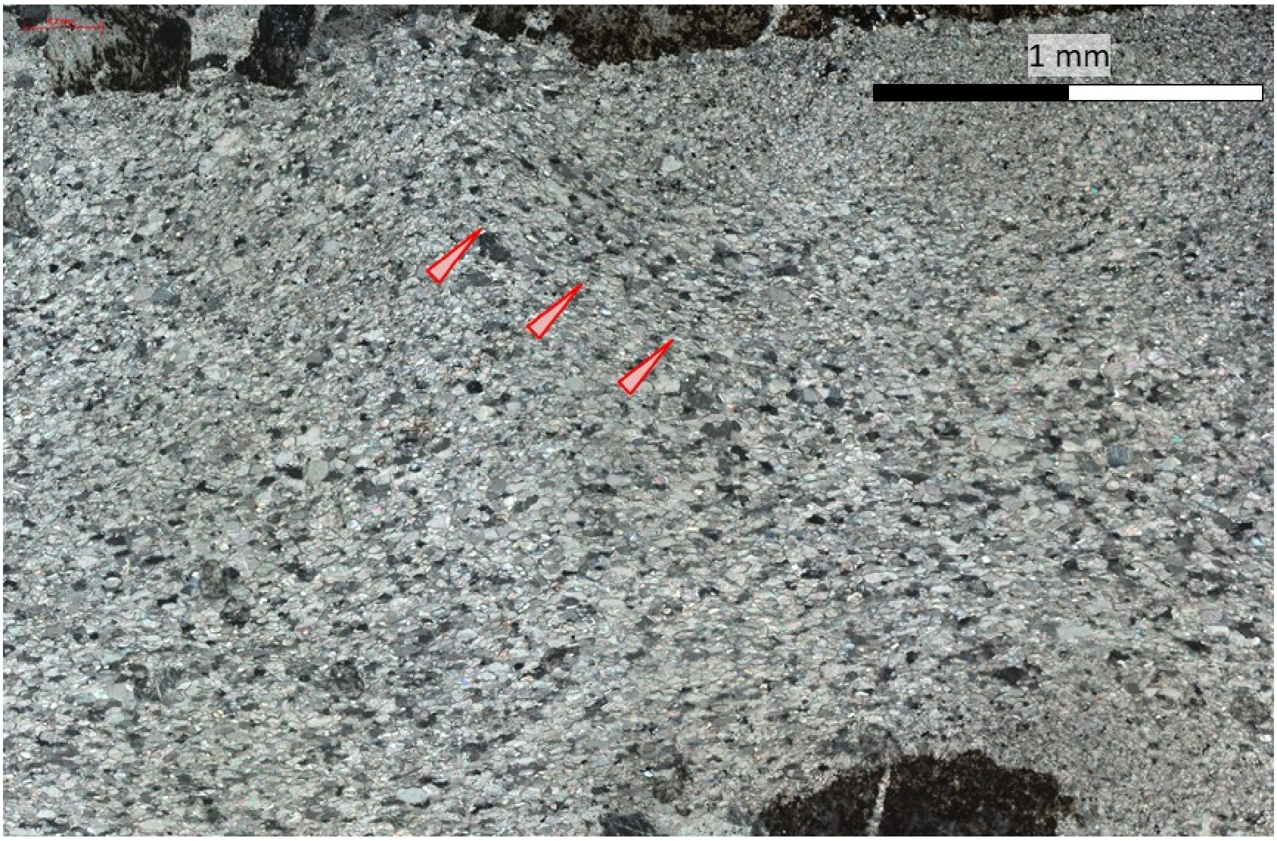

Fig. 88: Micro shear zones which nucleate in the necks of rotated boudin segments. Note the strong shape preferred orientation of coarse-grained marble while the fine-grained marble next to the vein shows a random orientation.

Interpretation:

The three scan areas were chosen based on their different textures and with the aim to derive information on the microstructural evolution stages of the mylonite. The ptygmatically folded, boudinaged and twinned calcite layers are regarded as part of the protolith. The high twin density and undulose extinction in the protolithic boudinaged layers points to a high initial stress, temperatures at ~ 200°C and intracrystalline slip (Bestmann et al., 2000). The probable evolution starts from the boudinaged calcite layers proceeding to the coarser grained areas that then are transformed into finer grained areas due to grain size reduction and dynamic recrystallization (scan areas 1 and 2). Dynamic recrystallization is linked to grain size and temperature and can start at temperatures lower than 250°C (Ferrill et al., 2004). The final stage would be the development of micro-shear zones initiating in the boudin necks due to the progressing transpressional deformation (scan area 3). In this scenario, inheritance from older microstructures should be more visible in the coarse-grained scan area (scan area 2), because that would be a remnant protomylonite area.

In the misorientation angle distribution plots (Fig. 81), however, there is no significant difference between the uncorrelated and correlated misorientation distributions. This means that there is no difference in the orientation of grains farther apart from each other and between grains next to each other. Additionally, both uncorrelated and correlated misorientation angle distributions show no significant deviation from the expected random misorientation angle distribution. Thus, no indication of inherited microstructures is given in the observed scan areas (Wheeler et al., 2001). Only a slight difference between the misorientation angle distributions in the range between 10° and 30° (scan area 1 and 2) and 10° to 50° (scan area 3) can be observed. This difference at small angles points together with the small grain sizes to grain boundary sliding as predominant deformation mechanism (Lloyd et al., 1997; Passchier & Trouw, 2005).

The ODF plots show clearly visible girdle arrangements of c-axes in the 0001 hkl plane. The girdles of the fine- and coarse-grained scan areas (scan area 1 and 2), follow a great circle on the pole plot, whereas the girdle of the sheared scan area (scan area 3) is a straight zone (Figs. 82 to 84). These facts, together with the overall similar misorientation angle distributions indicate a homogenous, simple shear environment and an incipient state of the mylonitic shear zone.

<u>Amphibolite – Gneiss Unit (Myrties)</u>

The Amphibolite lithology in the Amphibolite-Gneiss Unit does not display significant deformation features. A thin section image is shown in the lithostratigraphy chapter in figure 35. A major feature that can be observed is the two dominant directions of foliation. The gently dipping pervasive foliation overprints an older, steeper foliation.

The Gneiss lithology displays relic augen structure with the white mica forming the foliation (see chapter 3.6, Fig. 37 and 38). The Quartz grains display pinning structures against the Muscovite and also have an undulose extinction (Fig. 89).

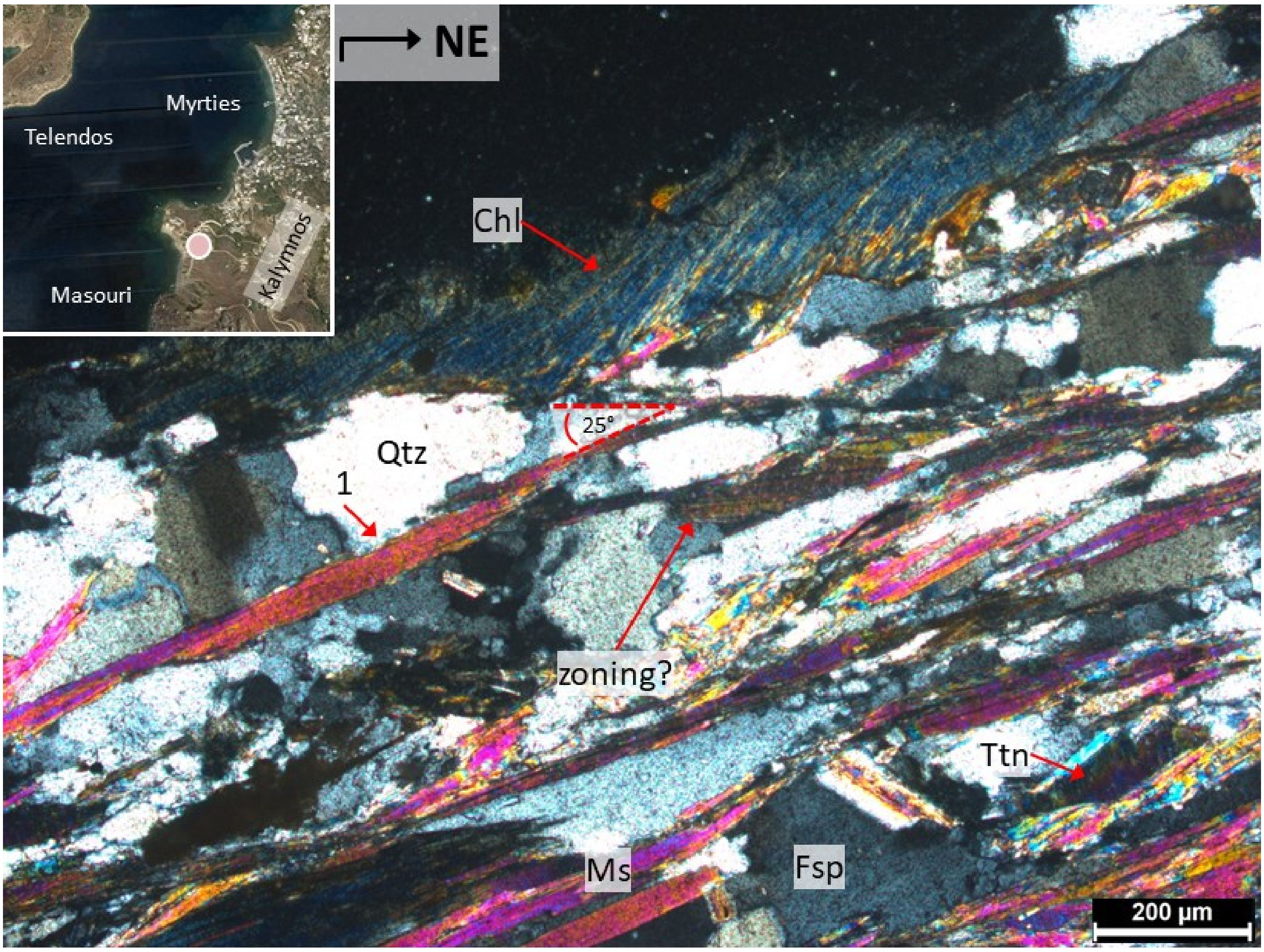

Fig. 89: The thin section example from the Gneiss in Myrties (KA014002) shows preferred orientation of the muscovite flakes (Ms) with a second, weakly developed orientation at an angle of 25° to the main foliation. The quartz grains (Qtz) show bulging recrystallization with pinning structures on mica (point No.1). Feldspars (Fsp) are partly elongated. On top of the cross, polarized image bookshelves of chloride minerals (Chl) can be observed. In the lower right corner, an idiomorphic titanite grain (Ttn) can be seen.

<u>Quartz-Mica Schist Unit</u>

The three different folding phases described in chapter 5.1 can be seen in the thin section samples. Quartz and feldspar layers alternate with layers formed mainly by muscovite. The developing crenulation cleavage is very well visible in the muscovite-rich layers (Fig. 90). At certain locations, the crenulation cleavage follows a curved trace, which might be indicating the F3 folding. In this thin section example, a hinge collapse can be observed, similar to the outcrop scale (Fig. 90 compare to Fig. 71), which is typical for the F2 folding phase. In this case, we see relatively thick quartz-feldspar layers at the boundary of the hinge collapse and muscovite within the hinge collapse zone. The muscovite layers form a wavy foliation with kinking observed in the southern area of Rachi, close to the Kefala Unit. Here, brittle deformation zones are more abundant in the Quartz-Mica Schist (Fig. 92), probably indicating the near-by fault zone separating the Units on the Kefala peninsula from the Units in Rachi.

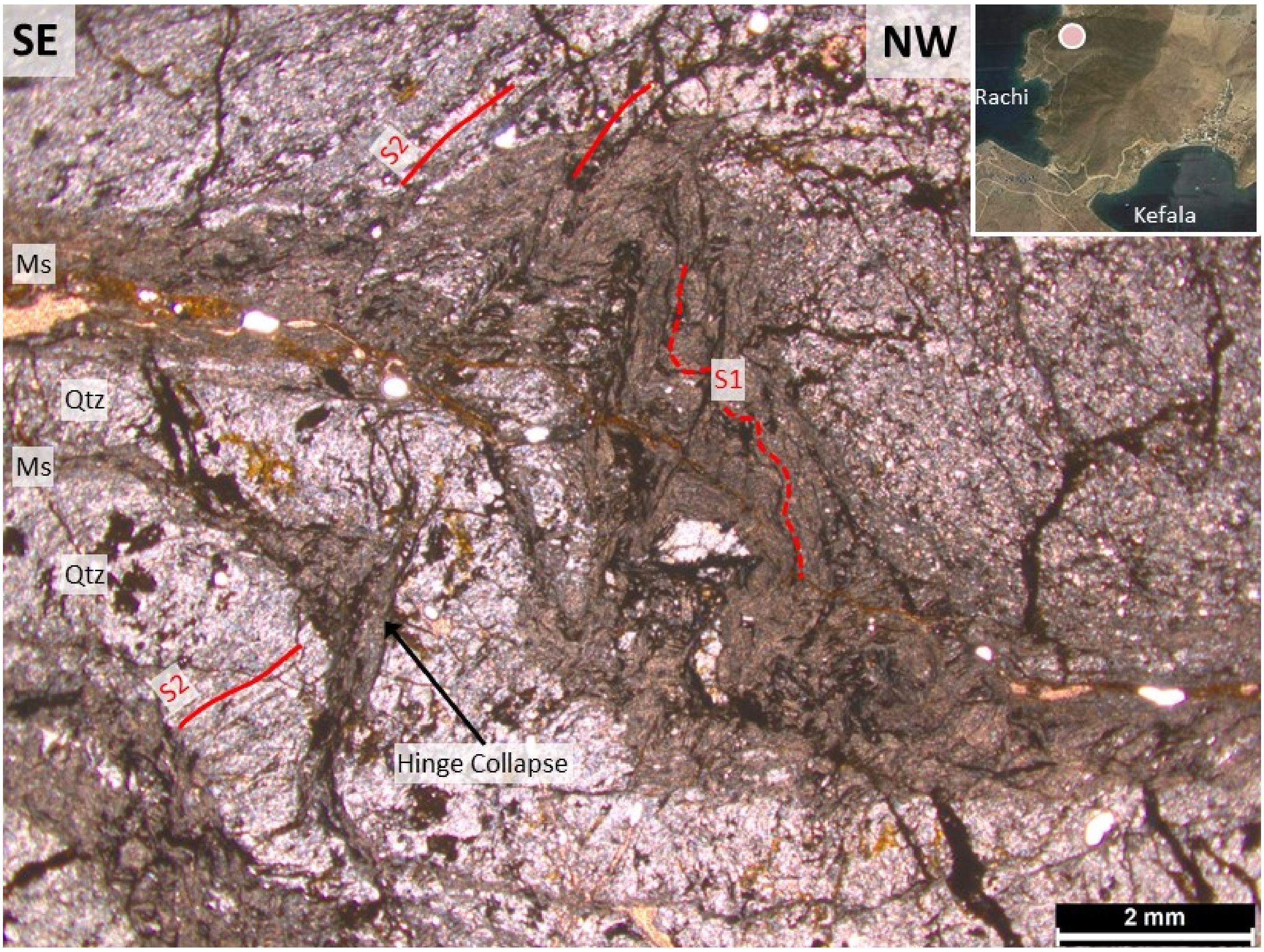

Fig. 90: Thin section sample KA014014 (WP46) in linear polarized light showing the developing crenulation cleavage (S2) created by F2. The white mica are folded by F2. S2 is curved due to the F3 folding. At the lower left part of the image, a hinge collapse can be seen. S1 = metamorphic foliation, S2 = crenulation cleavage.

In figure 91 the F1 isoclinal folding can be seen. The coarse-grained quartz of the isoclinally folded layer and also neighboring grains with lobate grain boundaries show grain boundary migration recrystallization (Passchier & Trouw, 2005). This process requires high temperature and corresponds to the regime 3 of Hirth & Tullis (1992). The white micas are concentrated in thin folded zones in between the quartz grains.

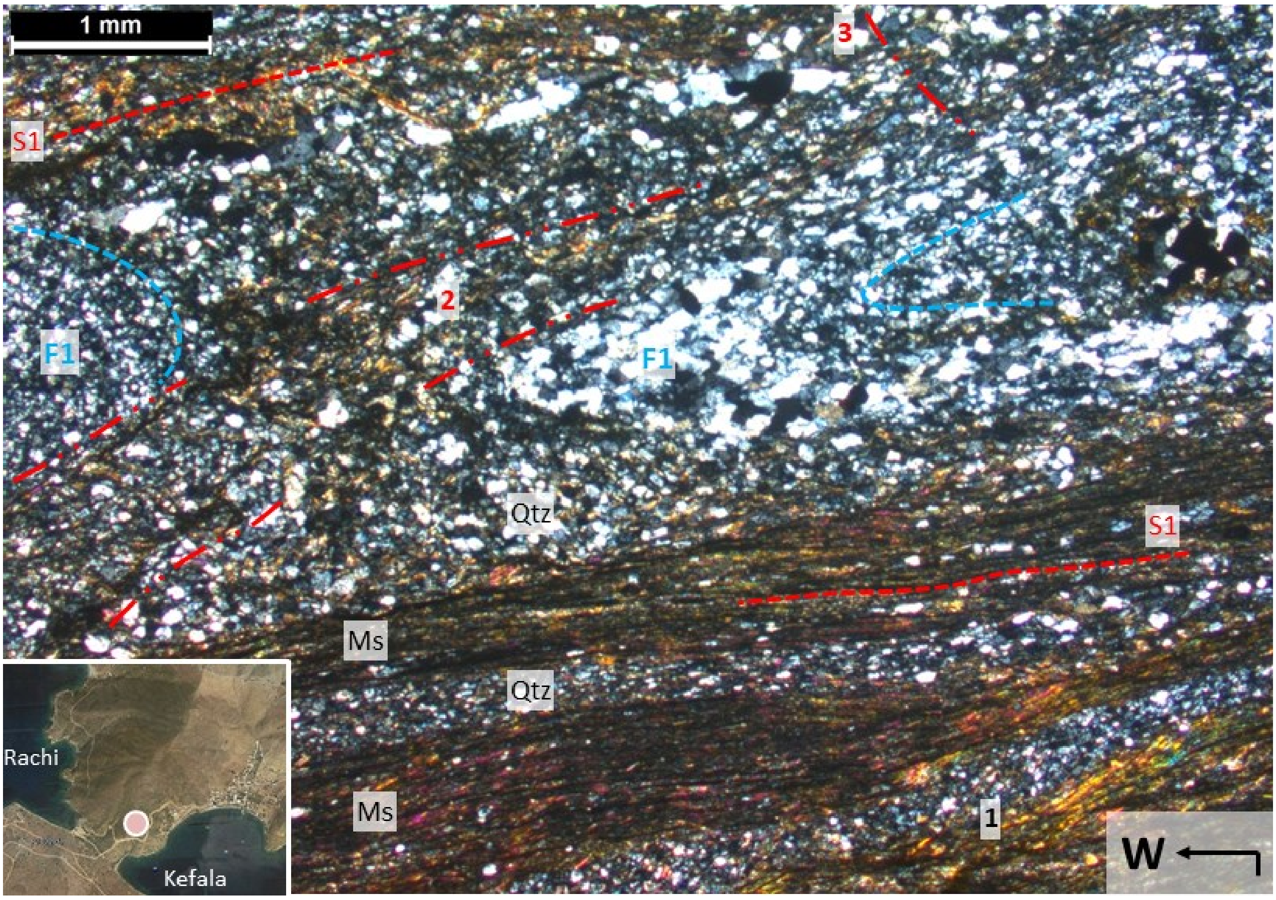

Fig. 91: Example thin section of the Quartz-Mica Schist KA014003 at WP17 in Rachi. In the center of the image, the F1 isoclinal and mostly intra-bedding fold can be seen. The layering consists of muscovite and quartz-feldspar dominated zones. Note the increased grain size of quartz in the F1 fold. 1) Kinking of the muscovite layer. 2) Zone of reduced quartz grain size probably indicating a shear zone between the two F1 fold hinges. 3) Later-stage brittle deformation zone offsetting the number 2 shear zone. This brittle deformation zone has similar orientation to the kinked muscovite zone in 1). Quartz shows weak shape preferred orientation with lobate grain boundaries and grain boundary mobility structures that indicate grain boundary migration (Passchier & Trouw, 2005). Cross-polarized light with enhanced contrast for structural features.

Closer to the Metaconglomerate Unit the Quartz-Mica Schist Unit is more deformed, the quartz grains have a higher variety in the grain size and brittle-ductile faulting of the muscovite grains occurs (Fig. 92). The layer-parallel stretching of the quartz mobilisates can be seen in figure 93 along with the F1 folding.

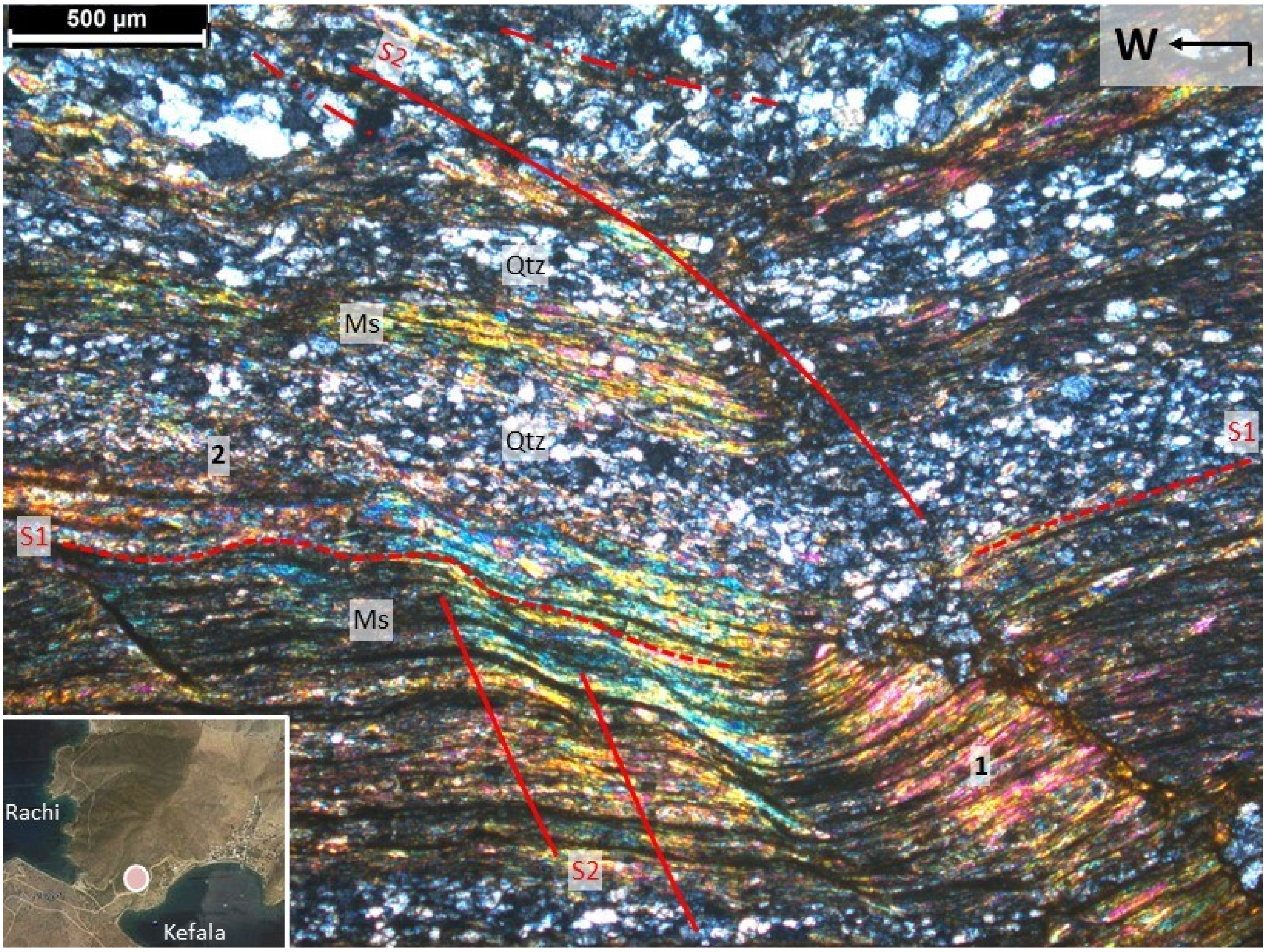

Fig. 92: Quartz-Mica Schist (KA014003) showing oblique view on the crenulation cleavage (S2). 1) The mica are kinked sub-parallel to the crenulation cleavage indicating that they are syntectonic to F2. 2) The quartz shows different grain sizes. In certain parts, smaller Quartz grains are arranged along the foliation. Sometimes also a shape-preferred orientation can be seen (middle-right part of image).

Figures 94 and 95 show changes in the Quartz-Mica Schist structure. The Sample from Rachi (Fig. 94) is not a typical Quartz-Mica Schist: It has much thicker quartz mobilisate zones that show undulose extinction and porous apatite grains. It is located close to the Metaconglomerate Unit. At Emporios, closer to Myrties - closer to the Amphibolite-Gneiss Unit - the Quartz-Mica Schist develops a relic augen structure with larger feldspar grains (Fig. 95).

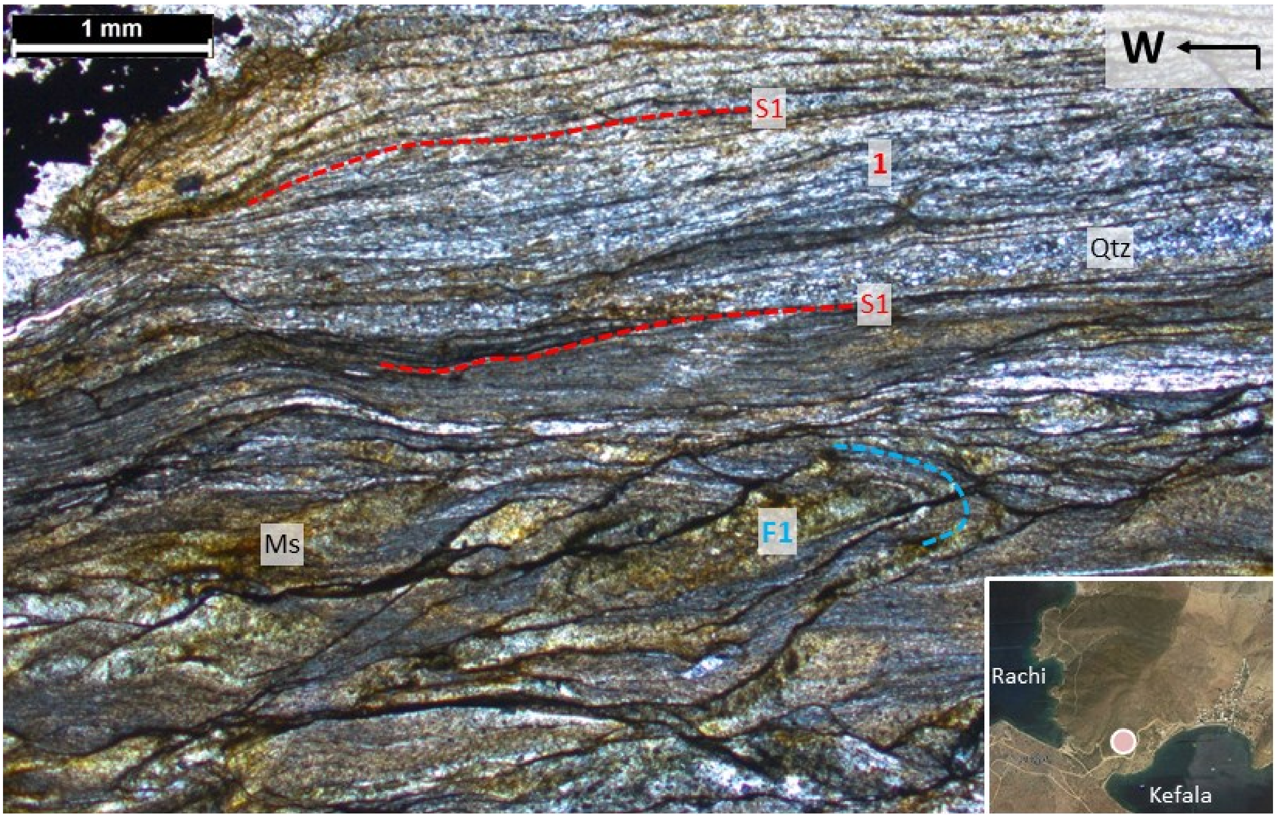

Fig. 93: Quartz-Mica Schist Rachi (KA014003, WP59). The interlayering of quartz and muscovite layers is well observable. The Quartz grains partly show shape preferred orientation along the foliation or pinch & swell structures (#1). In the Ms layer at the center-bottom, a refolded F1 isoclinal fold is located.

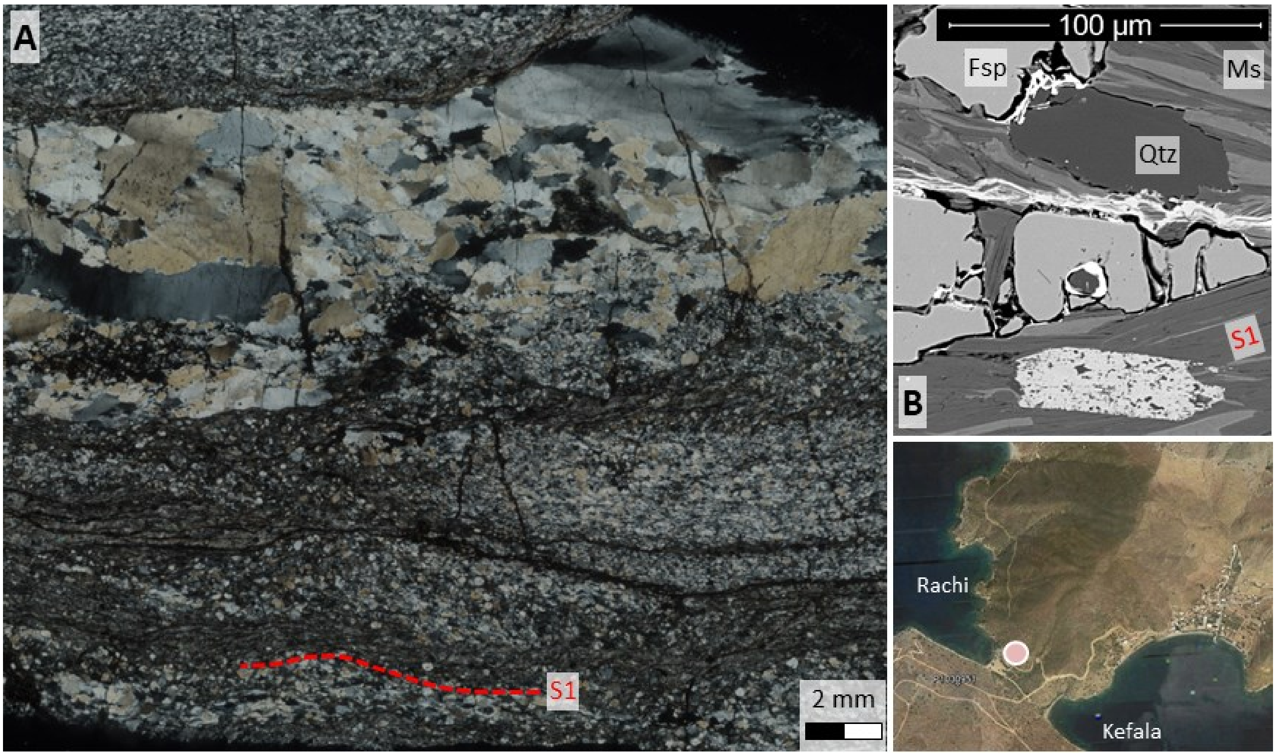

Fig. 94: A) Overview thin section image of Quartz-Mica Schist sample KA014020 (WP59) in cross-polarized light. The thick recrystallized Quartz ribbon with undulous extinction is special to this sample. B) Apart from Quartz, Feldspar and Mica, a porous Apatite grain occurs (center bottom of the EDAX image).

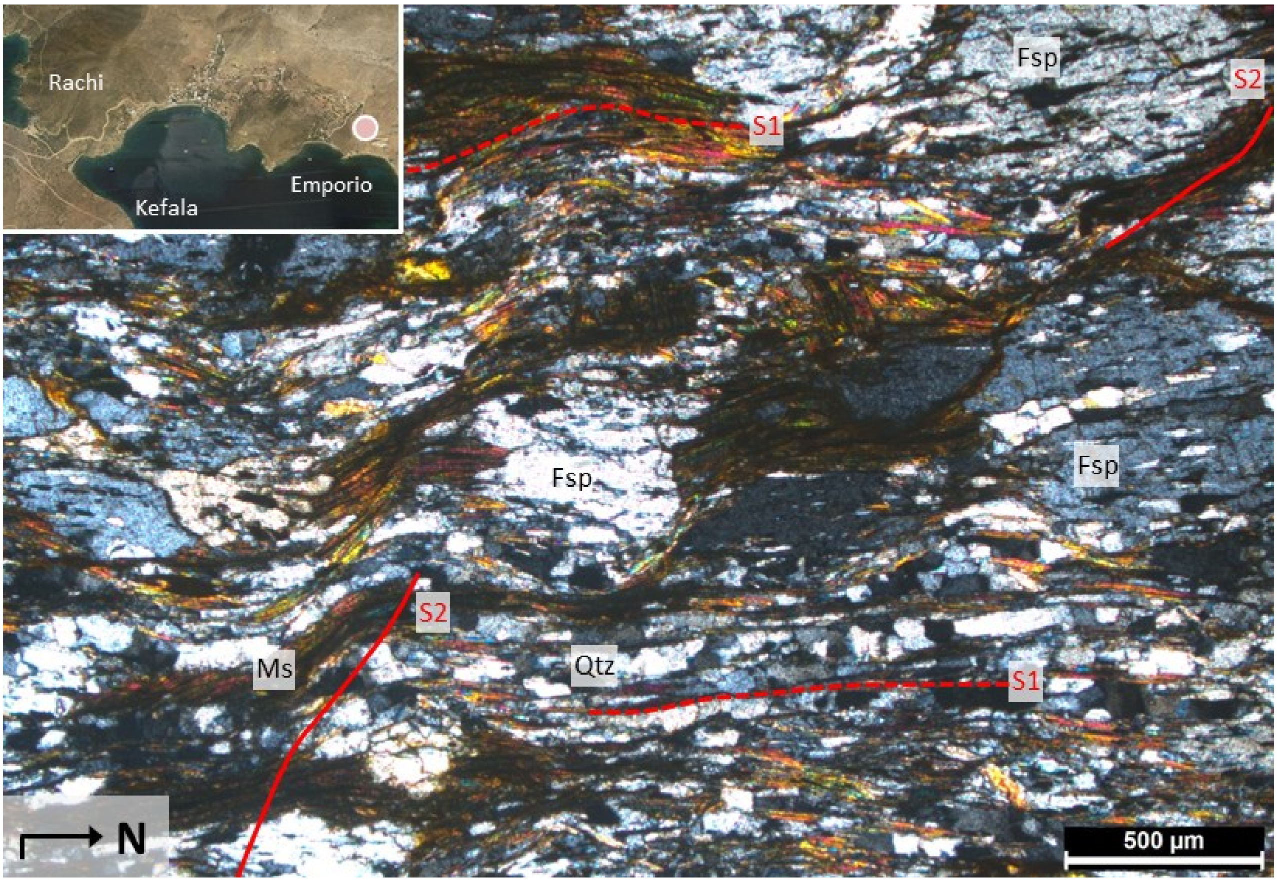

Fig. 95: Sample of the Quartz-Mica Schist from Emporios (KA014026, WP76) in cross-polarized light. The Feldspars are arranged in relic augen structures and overprinted or preserve the foliation (middle-right part of image). These remnant augen structures seem to be crossed by quartz ribbons. The quartz grains form recrystallized zones bounded my mica. The mica (Muscovites) are sometimes folded, syntectonic to F2, forming the early stages of a crenulation cleavage.

6 Discussion

During the ten days of fieldwork, the pre-Alpidic Units of Kalymnos could be mapped on the Kefala peninsula, in Rachi and in the area close to Myrties. The pre-Alpidic Units form a nappe-stack of five units, separated by thrusts/normal faults and intersected by faults and mylonitic zones: (1) Interlayered Marble Unit, (2) Devonian Marble Unit, (3) Permian Marble Unit, (4) Metaconglomerate Unit and (5) Quartz-Mica Schist Unit. The unit at Myrties is a sixth unit (Amphibolite-Gneiss Unit) that can be correlated to the Quartz-Mica Schist Unit at Kefala peninsula.

The sampling and geochronologic investigation in the Quartz-Mica Schist and the Amphibolite-Gneiss Units resulted in white-mica Ar-Ar geochronologic data that are interpreted as cooling ages - at these dates the siliciclastic units cooled below 400°C (Forster & Lister, 2016; Schneider et al., 2019). The zircon (U-Th)/He ages from the Quartz-Mica Schist are also interpreted as cooling ages with a closure temperature of 183°C (Reiners, 2005). Detailed mapping, combined with paleontological and geochronological data revealed that the pre-Alpidic rocks were deformed under amphibolite facies conditions during the Variscan orogeny and experienced a greenschist facies overprint.

The following discussion focuses on two main topics: The geologic / metamorphic evolution history of the mapped units and their relation to similar units on neighboring islands.

6.1 Paleogeographic framework and geodynamic evolution

The Variscan outcrops at the study area on Kalymnos Island can be roughly separated into two regions: (1) the greenschist facies marbles on the Kefala peninsula, originating from shallow-water reef limestones that are transgressed by the Metaconglomerates, and (2) the greenschist facies Quartz-Mica Schist Unit in the Rachi area and the Amphibolite-Gneiss Unit in the Myrties area deriving from siliciclastic sediments. This separation is done due to structural geologic reasons: The thrust in the Rachi region, between the Metaconglomerate and the Quartz-Mica Schist Unit is horizontal and not folded. On the other hand, the thrust in the Kefala region between the Interlayered Marble Unit and the Devonian/Permian Marble Units is folded. If the two regions would have been next to each other at the time the thrusts were active, then traces of this activity should be visible in any of the two regions. However, both regions display different and independent large-scale structural features.

The probable location of the original formation of the limestones region (today Devonian, Permian and Interlayered Marble) and the deposition of the siliciclastics (today Quartz-Mica Schists) is the NE-margin of Gondwana, just to the West of the Menderes and Taurus terranes (Stampfli & Kozur, 2006). Their deposition occurred at a distance from each other and at different times, due to the higher metamorphic grade of the Quartz Mica Schists. Both regions were then probably parts of peri-Gondwana terranes that drifted from Gondwana towards Laurussia from ~420 Ma onwards. Zulauf et al. (2007) also mentions these terranes as “Minoan Terranes”. Franz et al. (2005) suggests that the pre-Alpine basement rocks of Crete and the Dodecanese Islands belong to the Apulian Microplate. It is important to note that the Gondwanan Anatolide-Tauride block was not affected by the Late Paleozoic Variscan deformation (Eren, 2001; Zanchi et al., 2003 and citations therein) and its accretion to Laurasia occurred during the late Cretaceous – Palaeogene (Okay & Tuysuz, 1999).

In the following, a probable origin and evolution history of the metamorphosed sediments is described in several points.

Point 1
The deposition of the Devonian Marble Unit cannot be constrained accurately. The Middle-Devonian continental shelf development at the NE-margin of Gondwana, which can be observed today in the central Taurides (Mackintosh & Robertson, 2012), is taken as an example. Thus, the origin of the Devonian Marble Unit is assumed to be in the period from Lower to Middle Devonian (~420 – 382 Ma).

Point 2
The second Variscan orogenic event in the Visean from ~347-331 Ma (Stampfli et al., 2002) and the increasing glaciation lead to more terrestric and subaerial exposure of areas in Gondwana (Spaletti et al., 2010). The Carboniferous is eroded from the top of the Devonian Marble and is not present at Kalymnos any more. Carboniferous sediments and turbidites can be found on Chios, which thus forms the foreland of the second Variscan orogenic event (Zanchi et al. 2003).

Point 3
During the Permian shallow marine reef limestones were deposited very close to - or on the NE-margin of Gondwana. The Neotethys just began to form and no oceanic crust was present yet (Stampfli & Kozur, 2006). The Kungurian (~270 Ma) is marked by another cycle of transgression that affects the marginal low-lying areas of Gondwana (Acharyya, 2018). The limestones later becoming the Permian Marble were deposited on top of the Devonian limestones with a depositional hiatus due to the missing Carboniferous. The present arrangement of Permian Marble next to Devonian Marble can thus be explained without extensive tectonics. Later, maybe during the Alpine orogenic phases, the boundary between the Permian Marble and Devonian Marble is re-used by Alpine faults. The deposition of the Permian limestones on top of the Devonian limestones is feasible, since in the field a continuous deposition sequence could be seen.

Point 4
The deposition of the sediments later forming the Interlayered Marble Unit occurred probably in the late Permian. A possible time would be ~260 Ma, during the Late Permian transgression-regression cycles (Gradstein et al., 2012), which would favor the intercalation of terrestric/fluviatile sediments (metapelites) and limestones (marble). The location of the terrane was at that time almost halfway between Gondwana and Laurasia. The oceanic crust of the Neotethys between the terrane and Gondwana has now already formed (Stampfli & Kozur, 2006).

Point 5
The Devonian Marble/Permian Marble Units are thrusted onto the Interlayered Marble Unit. The entire carbonate sequence was then folded together with the thrust plane along ~N-S oriented fold axes. The timing and direction of thrusting and folding is not fully clear, but it must have occurred prior to the emplacement next to the Quartz-Mica Schist and Metaconglomerate Units.

Point 6
The deposition of the Quartz-Mica Schist Unit and the Amphibolite-Gneiss Unit probably occurred at the NE-margin of Gondwana as well. The time is unknown, but it took place before deposition of the Devonian limestones, since the ^{40}Ar-^{39}Ar cooling ages to below 400°C of these units are around 243 Ma and 346 Ma. In general, the units at Kefala, Rachi and Myrties are interpreted as a ?Silurian to Late Permian passive margin succession.

Point 7
The first folding phase of the Quartz-Mica Schist is regarded as next event. The time and location of the folding/refolding of the Quartz-Mica Schist Unit is very difficult to constrain with the current data. Peak metamorphic conditions are probably at Amphibolite facies conditions at around 500°C and 3 kbar, as observed from the mineral parageneses. A key observation is the recrystallization of quartz along the F1 isoclinal fold shape (see chapter 5.2, Fig. 91). The increase in quartz grain size and the geometry of the grain boundaries is interpreted as grain boundary migration recrystallization (Passchier & Trouw, 2005) that corresponds to the regime 3 of Hirth & Tullis (1992). The temperature for the regime 3 ranges from 500°C to 1200°C and strain rates of 10^{-8} to 10^{-5} per second (Hirth & Tullis, 1992). The F1 isoclinal fold is regarded to form close to peak metamorphic conditions. Another indicator is the F2 kinking/folding of muscovite and thus the formation of a crenulation cleavage (see chapter 5.2, Fig. 90). Mariani et al. (2006) show that deformation in muscovite is not very sensitive to temperature up to 700°C. Above this temperature blocks of schistose, metapelitic rocks in the mid- to lower crust are probably weak, supporting shear stresses of only 1-10 MPa. So, for the F2 formation

along NW-SE oriented sub-horizontal fold axes a considerable stress is needed, which could be provided by a setting of NE-SW compression, probably related to collision of terranes in the Middle Triassic (see also Stampfli & Kozur, 2006).

Point 8

The Quartz-Mica Schist Unit was thrusted onto the Metaconglomerate Unit along a sub-horizontal thrust, which could be the flat part of a ramp-flat thrusting geometry (Fig. 96). During the 10 days of fieldwork, no clear indication regarding the kinematics of the thrust could be observed. The only observation that might be linked to the kinematics are the very consistently SW-plunging F3 open fold axes. If the F3 folding is a result of the thrusting, the thrust direction possibly could be directed to the SE. After thrusting, the metamorphosed siliciclastic sequence was emplacement of next to the meta-carbonate sequence.

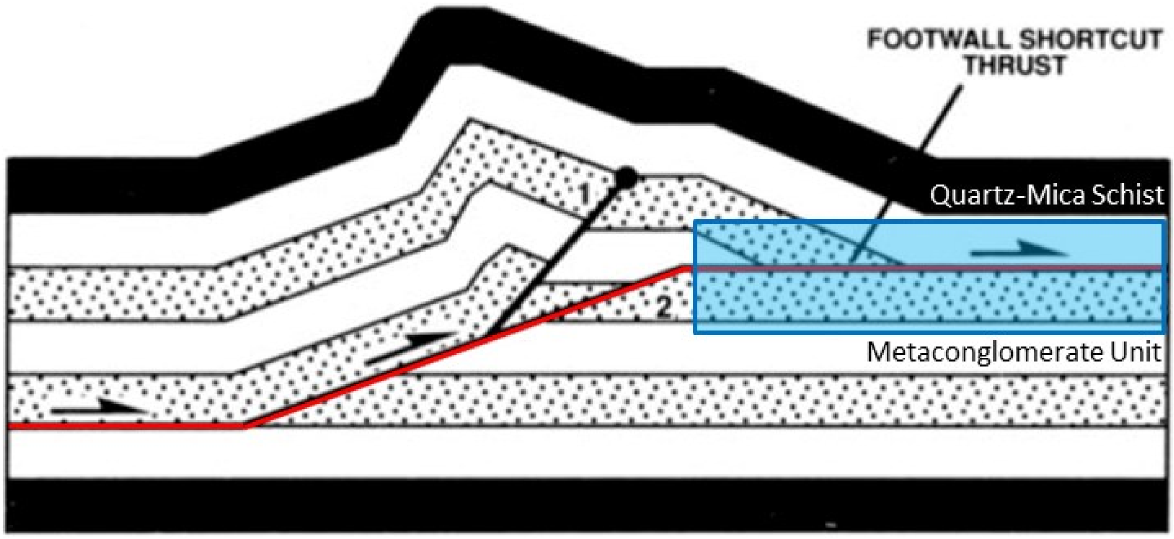

Fig. 96: Ramp-flat staircase thrust geometry with a fault propagation fold. The blue box indicates the possible positions of the units along the horizontal thrust. Modified after McClay (1991).

Point 9

The burial and metamorphic history of the Variscan Units is constrained by the mineral paragenesis and deformation structures observed in the field and in thin sections (Fig. 97). The peak metamorphic conditions were most probably Epidote-Amphibolite facies (~500°C and 3 kbar) for the siliciclastic unit at Myrties as shown by the coexistence of Epidote and Albite, and the occurrence of up to 1 cm large garnets in the S of Kalymnos outside the study area (pers. comm. Grasemann). Similar peak metamorphic conditions can be assumed for the siliciclastic unit at Rachi but with a strong greenschist facies overprint (~400°C and 3 kbar) as indicated by the presence of chlorite and no major neoblastic mineral phases. The carbonate units at Kefala had peak metamorphic conditions in the lower greenschist facies (Calcite dominates, no phase-changes could be observed, fossils are very well preserved). The metapelite/quartzite in the marble fold core at Kefala shows growth of abundant, radiating Actinolite bundles with Stilpnomelane (see chapter 3.1, Fig. 15), which indicates a later greenschist facies overprint. The Ar-Ar cooling ages indicate a decreasing trend from Myrties (~346 Ma) towards north, towards Rachi (~196 Ma). The cooling ages from Rachi of around 241 Ma and 243 Ma fit well to Mid-Triassic flexural uplift due to rift reactivation as a precursor to the opening of the Pindos Ocean (Robertson, 2006). The older cooling ages at Emporio (~309 Ma) and Myrties (~346 Ma) are probably related to Variscan orogenic phases in the Middle and Late Carboniferous (Stampfli et al., 2002; Spaletti et al., 2010).

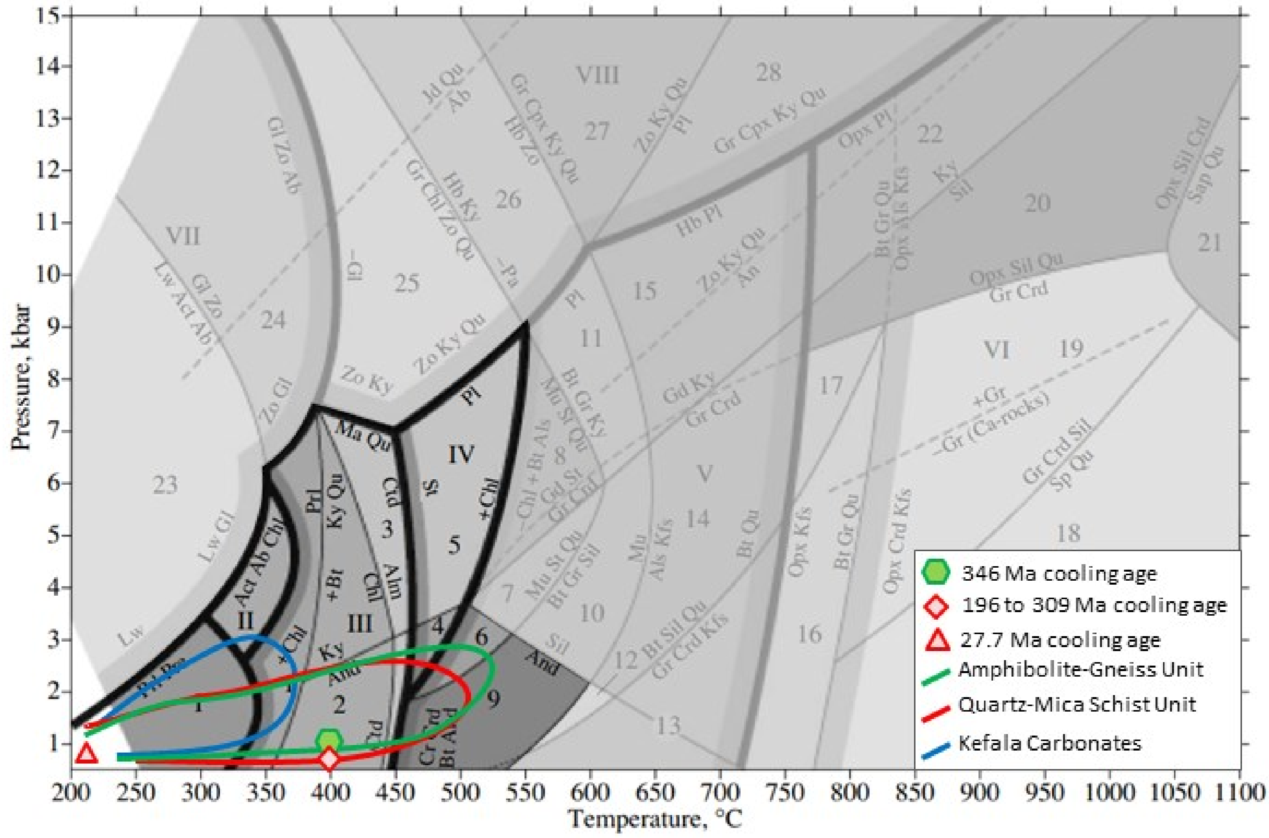

Fig. 97: Proposed P-T path for the pre-Alpidic Units on Kalymnos. The PT grid in the background is modified after Bushmin & Glebovitsky (2008). Only the close-by facies fields are listed in this caption: (**I**) zeolite and prehnite–pumpellyite; (**II**) pumpellyite–actinolite; (**III**) greenschist: (1) muscovite–stilpnomelane–chlorite, (2) muscovite–chlorite–biotite, (3) chlorite–chloritoid–garnet; (**IV**) epidote-amphibolite: (4) andalusite–chlorite–staurolite, (5) kyanite–chlorite–staurolite; (**V**) amphibolite: (6) andalusite–muscovite–biotite–staurolite, (7) sillimanite– muscovite–biotite–staurolite, (8) kyanite– muscovite–biotite–staurolite, (9) cordierite–andalusite–biotite–muscovite, (10) garnet–sillimanite–biotite–muscovite, (11) garnet–kyanite–biotite–muscovite, (12) cordierite–biotite–andalusite–orthoclase, (**VII**) glaucophane-schist: (23) lawsonite–glaucophane, (24) zoisite–glaucophane. The carbonates are projected onto the siliciclastic system for overview purposes.

Point 10

The formation of the mylonitic shear zone in the Permian Marble Unit occurred probably during further cooling to around 300°C. The calcite grains in the boudin necks show twinning that indicates temperatures of 170°C to 200°C. The mylonitic shear zone is a top to SSW transpressional shear zone probably active from the Jurassic onwards. Extension observable through boudinage in the mylonitic shear zone and also at its margins precedes the last, transpressional phase. The (U-Th)/He cooling ages of ~27 Ma mark the termination of any major ductile deformation in the study area. The strong shape preferred orientation of coarse-grained marble, together with the weak crystallographic preferred orientation, indicates that dynamic recrystallization was active at an early stage. The EBSD data, in combination with the quantitative strain data, show that the main deformation mechanism in the Permian ultramylonitic marble was dissolution with minor precipitation, associated with grain boundary sliding. This is supported by the minor differences between the correlated, uncorrelated and the expected random misorientation angle distributions. The early stage of the development of the ultramylonitic zone in a homogenous stress field is further indicated by EBSD data, especially by the overall similar misorientation angle distributions.

The discussion points are summarized in the figure 98 showing also paleogeographic sketches.

Paleogeographic sketch	**Geodynamic history**		**Discussion/conclusions point**
	Carbonate region (Kefala)	**Siliciclastic region (Rachi)**	
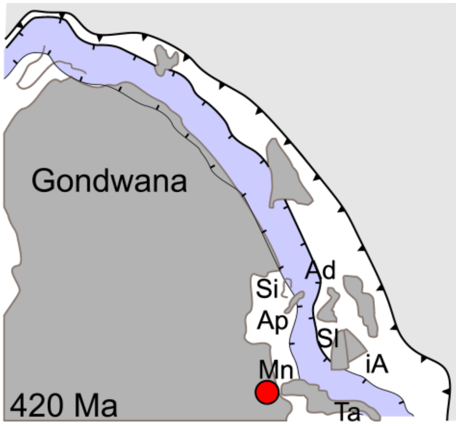		Latest time of deposition of sediments of Quartz-Mica Schist Unit and the Amphibolite-Gneiss Unit (these units can potentially be of older origin, as old as Late Ordovician).	Point 6
	Deposition of the reef limestones of Devonian Marble Unit.	Cooling of units below 400°C starting from 346 Ma on.	Point 1, Point 6
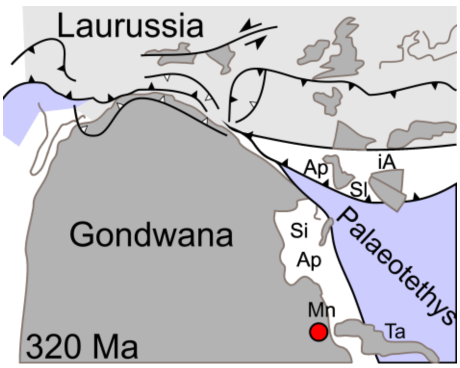	Erosion/non-deposition of Carboniferous sediments on Kalymnos due to the second Variscan orogenic event.		Point 2

Fig. 98A: Palaeogeographic map for Point 1 modified after Stampfli & Kozur (2006). Ad = Adria s.s., Ap = Apulia, Ct = Cantabria-Asturia, iA = intra-alpine terrane, Mn = Menderes, Si = Sicanian, Sl = Slavonia, Ta = Taurus.

<table>
<tr><th rowspan="2">Paleogeographic sketch</th><th colspan="2">Geodynamic history</th><th rowspan="2">Discussion/conclusions point</th></tr>
<tr><th>Carbonate region (Kefala)</th><th>Siliciclastic region (Rachi)</th></tr>
<tr><td>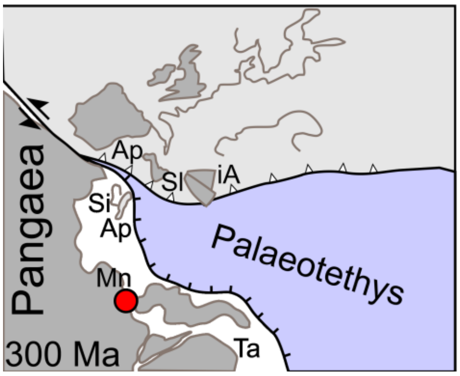
</td><td>Permian shallow marine reef limestones are deposited. These limestones will later form the Permian Marble Unit and the Interlayered Marble Unit.</td><td></td><td>Point 3, Point 4, Point 7</td></tr>
<tr><td rowspan="2">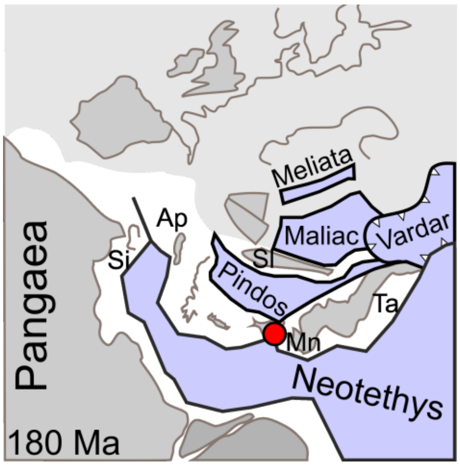
</td><td>Thrusting of the Permian/Devonian Marble Units onto the Interlayered Marble Unit and folding of the thrust.</td><td>Folding events in the Quartz-Mica Schist Unit probably in the Middle Triassic.</td><td>Point 5, Point 8

(Representative sketch from Early Jurassic times)</td></tr>
<tr><td colspan="2">Emplacement of siliciclastic units on Rachi next to the carbonatic sequences on Kefala.

Development of the mylonitic shear zone in the Permian Marble Unit.</td><td>

Point 10</td></tr>
<tr><td>27.7 Ma</td><td colspan="2">Cooling of Units below 200°C as documented by geochronologic data from Rachi/Emporios.</td><td></td></tr>
</table>

Fig. 98B: Palaeogeographic map for Point 1 modified after Stampfli & Kozur (2006). Ad = Adria s.s., Ap = Apulia, Ct = Cantabria-Asturia, iA = intra-alpine terrane, Mn = Menderes, Si = Sicanian, Sl = Slavonia, Ta = Taurus.

6.2 Correlation of lithostratigraphic column with neighboring areas

The lithostratigraphic column of the study area, compiled from the field observations is shown in this chapter next to lithostratigraphic columns from literature of the neighboring islands. The correlation is attempted based on the lithology, metamorphic grade and structural position of the outlined units. Data on stratigraphic thickness is scarce and not easy to obtain. Thus, the lithostratigraphic columns are displayed not exactly to scale (Fig. 99).

Several authors provide a description of the lithostratigraphic succession of the Dodecanese (Dürr, 1975; Dürr et al. 1978; Katagas, 1980; Franz, 1992; Franz & Okrusch 1992; Franz et al., 2005, Roche et al., 2018), which is very consistent for the islands of Arki, Lipsos, Leros and Kalymnos. The succession starts with the lowermost

Temenia Unit that consists of interlayered micaschists and marbles. A late Palaeozoic age is probable according to Christodoulou (1970) and Wachendorf & Gralla (1983). On Arki, the lower parts of the Temenia Unit show HP/LT rocks – blueschists – within a succession of greenschists and micaschists (Franz & Okrusch, 1992). This HP/LT metamorphism is also observed on Leros; the HP-metabasites contain epidote and blue amphiboles (Roche et al., 2018). In the upper part of the Temenia Unit shallow-marine carbonates of Triassic to Cretaceous age are located. The top of the Temenia Unit consists of a basal conglomerate that lies between the marbles and micritic Sarmatian limestones already belonging to another nappe (Franz & Okrusch, 1992).

As a next nappe sheet, Franz & Okrusch (1992) mention pre-Alpidic basement rocks that underwent upper greenschist to lower amphibolite facies Variscan metamorphosis. This unit is divided into the Panormos and Emporios Units (Franz et al., 2005). The lower part of the Panormos Unit is described as a massive amphibolite of about 100 m, followed in the upper part by a sequence of marble, plagioclase gneiss and kyanite-staurolite-garnet mica schist interbedded with banded epidote and garnet amphibolite. Above the Panormos Unit, the greenschist facies Emporios Unit follows after a tectonic contact. It contains albite gneiss and chloritoid-biotite schist (Franz et al., 2005). It is important to note that the pre-Alpidic rocks were not affected by high-pressure metamorphism (Franz et al., 2005). The outcrops of Panormos and Emporios Units have a highly variable thickness and are limited on Leros. The Temenia Unit is in some places in direct contact with the Marina Unit, which is located on top of the Emporios Unit (Roche et al., 2018).

The sequence closes with the previously mentioned Marina Unit that consists of Verrucano-type, weakly metamorphosed violet schists, conglomerates and sandstones that transition into a Mesozoic carbonatic succession at the top (Dürr et al., 1978; Franz & Okrusch, 1992).

Looking at the wider Aegean region, further correlations are possible. The lithologies of the Panormos and Emporios Units are correlated with the Myrsini Crystalline Complex and Chamezi Crystalline Complex on Crete by Franz et al. (2005). The pre-Alpine crystalline basement is located in the Myrsini syncline in Eastern Crete (Zulauf et al., 2008). It consist of three complexes: (1) Kalavros Crystalline Complex, which was subject to Permian (~ 270 Ma) amphibolite facies metamorphism related to top-to-the NE shearing. (2) Myrsini Crystalline Complex showing Carboniferous (~ 330 Ma) amphibolite facies metamorphism and top-to-the N shearing. Here, a slow cooling is documented by Jurassic fission track ages. Also, an Alpine metamorphic overprint is documented by Zulauf et al. (2008) (3) Chamezí Crystalline Complex at the top with upper greenschist facies metamorphism (Franz, 1992).

Rocks similar to the Emporios Unit can be found on Santorini, where highly deformed quartz-rich phyllites and metaconglomerates crop out and are overlain by low-grade marbles (Schneider et al., 2018). On Amorgos, Rosenbaum et al. (2007), describe a sequence of blueschist-facies metabasites followed by Triassic to Eocene Marbles.

Triantafillis et al. (1986) and Van Hinsbergen & Boekhout (2009) describe Permo-Carboniferous anchimetamorphic phyllites and quartzites with minor carbonates within the Dikeos window on Kos, into which the Kos monzonite intruded around 12 Ma (Altherr et al. 1976; Kalt et al. 1998). The permo-carboniferous is separated from the thick-bedded to massive Mesozoic carbonates by a brittle fault zone. Interesting fact is the occurrence of boudinage within the foliation plane, isoclinally folded thin-bedded quartzites and the development of a crenulation cleavage. The age of folding can only be constrained between the time of rock deposition and the monzonite intrusion. Kalt et al. 1998 indicate that peak metamorphic conditions of the permo-carboniferous metapelites was at 1.5-2.5 kbar (5-7.5 km depth).

Regarding the deformation history of the earlier described sequence (Temenia, Panormos, Emporios and Marina Units) the deformation phases are described at various degrees of detail for each of the islands of the Dodecanese and Aegean. Roche et al. (2018) document polyphase deformation with one prominent fold axis around 040/30 highlighted within the Temenia Unit on Leros. The Metabasite Unit an Amorgos shows isoclinal folds affected by sub-horizontal folds creating a crenulation cleavage and overprinted by a last folding stage of open folds (Rosenbaum et al., 2007). Within the pre-Alpidic rocks in the Dodecanese (Panormos & Emporios Unit of Franz et al., 2005), four distinct phases can be delineated: (1) quartz mobilisates termed D1, (2) isoclinal folding with a penetrative schistosity regarded as D2, (3) refolding of the isoclinal folds, designated D3, and (4) refolding of the previous structures by open and closed, cylindrical folds with fold axes trending NE-SW. While phases 1 to 3 are regarded as pre-Alpidic, the phase 4 falls into the alpine orogenic phase (Franz et al., 2005). Similar deformation events were observed on Kalymnos during the current work. However, the timing of the deformation phase 4 might be earlier than the alpine orogenic phase. In any case it is linked to the thrusting of the Quartz-Mica Schist Unit onto the Metaconglomerate Unit along a sub-horizontal thrust. This thrust is not folded and thus post-dates the open, cylindrical folds.

The overview of the lithostratigraphic columns starts with the lithostratigraphic column on the Island of Leros, to the north of Kalymnos (Fig. 99), followed by the currently developed lithostratigraphic column from Kalymnos and then the N-S row closes with the column of Kos. The findings on Leros are mainly described in Franz et al. (2005), Franz & Okrusch (1992) and Katagas (1980). The lithostratigraphic column of Kos is compiled from Triantafillis et al. (1986) and Van Hinsbergen & Boekhout (2009) and citations therein.

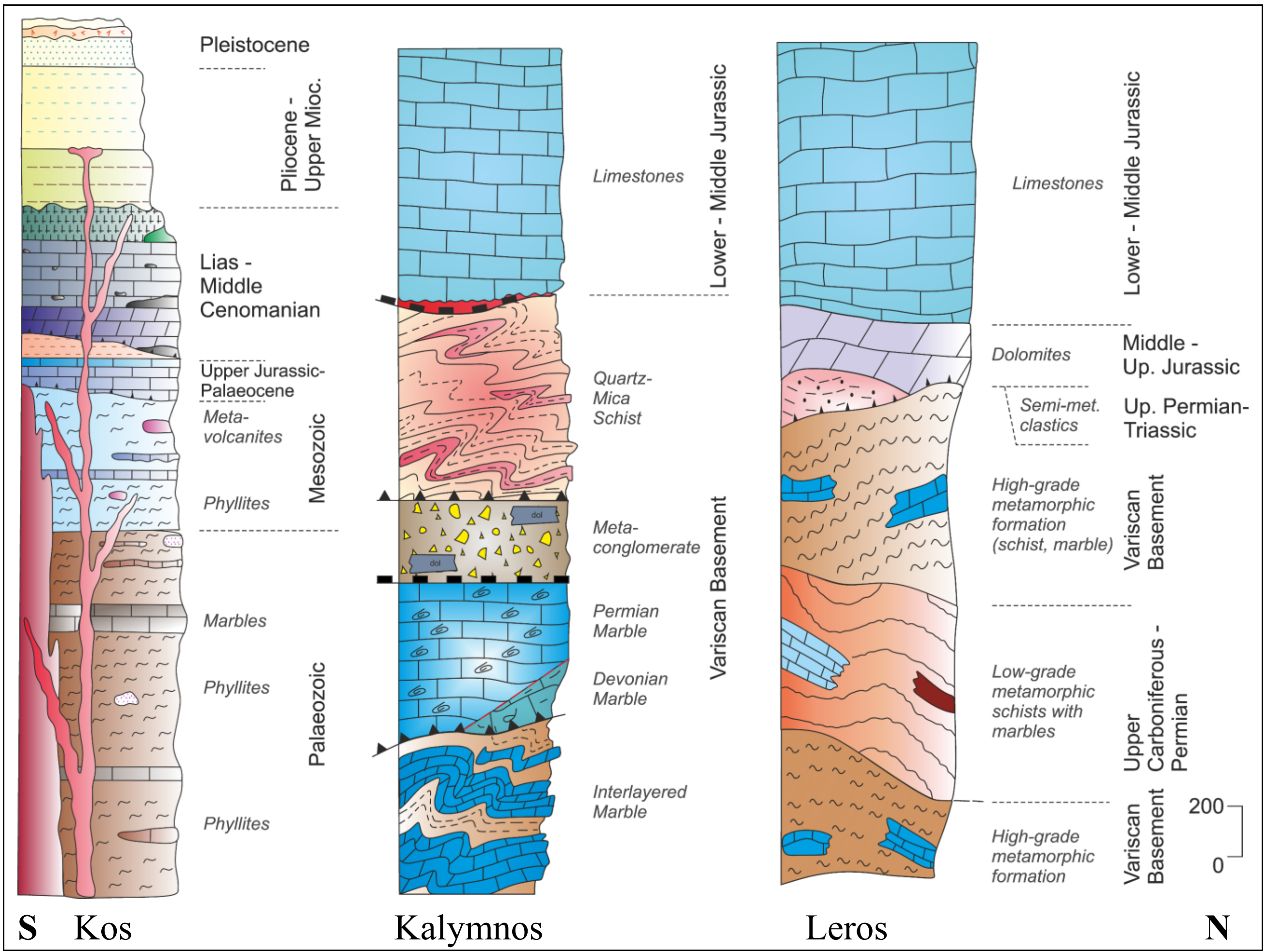

Fig. 99: Lithostratigraphic columns of the Islands of Kos, Kalymnos and Leros compiled after data from the current study, Franz et al. (2005), Franz & Okrusch (1992), Katagas (1980), Triantafillis et al. (1986), Van Hinsbergen & Boekhout (2009) and citations therein. The scale is approximate.

As a second correlation overview, Table 4 presents the findings from literature for a wider area from Santorini to the Menderes Massif.

W		E	NW			SE	W E
Crete	Santorini	Amorgos	Arki	Lipsi	Leros	Kalymnos	S Anatolide belt
Zulauf et al. (2007)	Schneider et al. (2018)	Rosenbaum et al. (2007)	Franz & Okrusch (1992)	Franz et al. (2005)	Franz et al. (2005), Roche et al. (2018)	Current study, Franz&Okrusch (1992), Dürr etal.(1978)	Arslan et al. (2013), Jolivet et al. (2004)
		Flysch Unit	Sarmatian Limestones		Neogene		Karabörtlen Flysch
	Triassic Limestones	Triassic to Eocene Marbles Isoclinal folding		?	Marina Unit Mesozoic Limestones Verrucano		Lycian Nappes HP/LT Gereme Limestone, Karaova Fm.
Chamezí C. (Crystalline Complex)	? Phyllites 25-18Ma	Mica-Schist, Quartzite		?	Emporios Unit Schists 230-320Ma	Q.Mica-Schist 196-243Ma	Menderes cover Dilek nappe?
Myrsini C., Kalavros C. 330Ma 270Ma			Basal Conglomerate	? Amphibolite, Gneiss 201-207Ma	Panormos Unit	Amphibolite 346Ma	
		Metacongl.		Metaconglomerate			
		Metabasite HP/MT	Temenia Unit HP/LT	HP/LT?	Interlayered-Permian Mrb. HP/LT	HP/LT?	Menderes Cover, Selimiye nappe

Tab. 4: Correlation scheme of tectonic units from the Western Aegean to the South Anatolide belt based on the classification into four main units in the Dodecanese (current study; Dürr et al., 1978; Franz & Okrusch, 1992). The equivalents of the Temenia, Panormos, Emporios and Marina Units are suggested based on data from literature, mainly on the papers mentioned at the top of each column. First, always the unit name is mentioned. If there is no clear unit name, the lithology is described. Below the unit/lithology, the cooling age or grade of metamorphism is indicated.

As a conclusion, the current study supports the finding from Franz et al. (2005) that the slices of crystalline rocks found at present separated across the Aegean (Santorini, Crete, Amorgos) and in the Dodecanese (Lipsi, Leros, Kalymnos) probably belong to one, formerly continuous Variscan basement complex.

The slice of pre-Alpine basement rocks on Kalymnos (Amphibolite and Quartz-Mica Schist Units) is probably more correlatable with units from the Menderes Cover, supporting a north- and westward thrusting of the Lycian Nappes onto the Menderes Massif and the Dodecanese Islands.

Several mylonitic zones with top to the SSE shear sense are mentioned on the Dodecanese Islands, but in different positions in the nappe-stack. On Arki, the mylonitic zone is probably deeper than on Kalymnos (current study; Franz & Okrusch, 1992). This indicates a possible continuous, alpine, top to the SSE deformation zone cutting through the nappe stack.

7 Conclusions

Based on ten days of fieldwork, sampling and analysis, a geologic map of the study area, the Kefala Peninsula was created. The pre-Alpidic Units of Kalymnos can be separated into a nappe-stack of six units: (1) Interlayered Marble Unit, (2) Devonian Marble Unit, (3) Permian Marble Unit, (4) Metaconglomerate Unit, (5) Quartz-Mica Schist Unit and (5) Amphibolite-Gneiss Unit. These units correlate well with the Temenia, Panormos, Emporios and Marina Units mentioned in earlier literature.

The geochronologic data show $^{40}Ar/^{39}Ar$ white mica cooling ages to below 400°C from the Quartz –Mica Schist and the Amphibolite-Gneiss Unit ranging from 196 ± 2 Ma in the North to 346 ± 6 Ma in the South. The geochronologic data show a continuous northward younging.

(U-Th)/He cooling ages yield 27.6 ± 1.4 Ma in the N and 27.7 ± 2.8 Ma in the South, indicating a simultaneous cooling of the northern and southern area below 183°C.

The carbonatic sequence on the Kefala Peninsula (Interlayered -, Devonian - and Permian Marble Units) was dated using the fossil content showing Devonian and Permian ages, which are reflected in the naming of the units.

The pre-Alpidic rocks on Kalymnos derive from Minoan Terranes that were then subjected to Variscan Epidote-Amphibolite facies metamorphosis and show an Alpine Greenschist facies overprint. Peak metamorphic conditions of the Variscan metamorphosis are about 500°C and 3 kbar.

The carbonatic sequence is cut by a transpressional Alpine mylonitic shear zone with top to SSW shear sense. In the mylonitic shear zone, boudinaged calcite veins are ptygmatically folded during the last, transpressional deformation phase.

The slices of pre-Alpidic rocks that are at present found in isolated outcrops throughout the Aegean, previously formed a continuous Variscan basement complex.

The pre-Alpidic rocks on Kalymnos can be correlated to units from the Menderes cover, which supports a north and westward thrusting of the Lycian nappes onto the Menderes Massif and the Dodecanese.

EBSD data of the sample from the mylonitic shear zone show no differences between the correlated, uncorrelated and expected misorientation angle distributions and thus no indication of inherited microstructures. Only at small angles some deviations can be observed, which points to grain boundary sliding as predominant deformation mechanism.

The ODF plots from EBSD measurements show clearly visible girdle arrangements which together with the overall similar misorientation angle distributions indicate that the mylonitic shear zone is in a beginning stage and was subject to a homogenous, simple shear stress field.

The mylonitic shear zone on Kalymnos formed in post-Variscan times and is correlatable to other mylonitic shear zones on neighboring islands, which cut through the units at different lithostratigraphic levels.

8 Appendix

8.1 Structural map

8.2 ^{40}Ar-^{39}Ar Geochronology data

8.3 (U-Th)/He Geochronology data

8.4 List of samples

9 References

Acharyya K.S. 2018. Regional Tectonism and Gondwana Stratigraphy. In: Acharyya S., Bhattacharyya S. & Mukhopadhyay S. (eds): Tectonic Setting and Gondwana Basin Architecture in the Indian Shield. Elsevier, Amsterdam, 137 pp.

Altherr R., Keller J. & Kott K. 1976. Der jungtertiäre Monzonit von Kos und sein Kontakthof (Ägäis, Griechenland). Bulletin de la Société Géologique de France, **18**, 403-412.

Anavasi 2014. Kalymnos. Hiking Map 1:25 000. ISBN: 978-960-8195-94-3

Angelier J., Lybéris N., Le Pichon X., Barrier E. & Huchon P. 1982. The tectonic development of the hellenic arc and the sea of Crete: a synthesis. *Tectonophysics*, **86**, 159-196.

Arslan A., Güngör T., Erdoğan B. & Passchier C.W. 2013. Tectonic transport directions of the Lycian nappes in southwest Turkey constrained by kinematic indicators. Journal of Asian Earth Sciences, **64**, 198-209.

Aubouin J. 1959. Contribution à l´étude géologique de la Grece septentrional: les confins de L`Epire et de la Thessalie. *Annales Geologiques des Pays Helleniques*, **9**, 1-484.

Banga G. 1982. A major crustal shear-zone in the Greek Islands Ios and Sikinos. *Unpublished Msc Thesis, University of Utrecht, The Netherlands.*

Bernoulli D., Graciansky P.C. & Monod O. 1974. The extension of the Lycian Nappes (SW Turkey) into the Southeastern Aegean Islands. Eclogae Geologicae Helveticae, **67**(1), 39-90.

Besang C., Eckhardt F.J., Harre W., Kreuzer H & Müller P. 1976.Geol. Jb. in press.

Bestmann M., Kunze K. & Matthews A. 2000. Evolution of a calcite marble shear zone complex on Thassos Island, Greece: microstructural and textural fabrics and their kinematic significance. Journal of Structural Geology, **22**, 1789-1807.

Bestmann M. & Prior D.J. 2003. Intragranular dynamic recrystallization in naturally deformed calcite marble: diffusion accommodated grain boundary sliding as a result of subgrain rotation recrystallization. Journal of Structural Geology, **25**, 1597-1613.

Bizon G., Bonneau M., Leboulenger P., Matesco S. & Thiebault F. 1976. Sur la signification et l'extension des "massifs cristallins externes" en Péloponnèse méridional et dans l'Arc égéen. Bulletin de la Société géologique de France, 18, 337-345.

Blenkinsop T.G. & Treloar P.J. 1995. Geometry, classification and kinematics of S-C fabrics. Journal of Structural Geology, **17**, 397-408.

Bonneau M. 1973. Sur les affinités ioniennes des "calcaires en plaquettes" epimetamorphiques de la Crète, le charriage de la série de Gavrovo-Tripolitza et la structure de L'arc égéen. CR Acad Sci Paris, **277**, 2453-2456.

Bonneau M. 1984. Correlation of the Hellenides Nappes in the south-east Aegean and their tectonic reconstruction. In: Dixon J.E., Robertson. A.H.F. (eds): The geological evolution of the eastern Mediterranean. Geological Society, London, Special Publication, **17**, 517-527.

Brinkmann R. 1967. Die Südflanke des Menderes-Massivs bei Milas-Bodrum und Oeren. Ege Universitesi Fen Fakultesi Uni Raportar, Serisi **43**, 1-12.

Brinkmann R. 1971. Das kristalline Grundgebirge von Anatolien. Geologische Rundschau, **60**, 886-899.

Brumm A., Jensen G.M., van den Bergh G.D., Morwood M.J., Kurniawan I., Aziz F. & Storey M. 2010. Hominins on Flores, Indonesia, by one million years ago. Nature, **464**, 748-752.

Brunn J.H., Dumont J.F., Graciansky P.C.de, Gutnic M., Juteau T., Marcoux J., Monod O. & Poisson A. 1971. Outline of the geology of the western Taurides. In: Campbell A.S. (ed): Geology and history of Turkey: Tripoli, Libya. Petroleum Exploration Society of Lybia, 225-255.

Bunge H.J. 1982. Texture Analysis in Materials Science: Mathematical Models. Butterworths, London.

Bushmin S.A. & Glebovitsky V.A. 2008. Scheme of Mineral Facies of Metamorphic Rocks. Geology of Ore Deposits, **50**(8), 659-669.

Chatzaras V., Xypolias P. & Doutsos T. 2006. Exhumation of high-pressure rocks under continuous compression: A working hypothesis for the southern Hellenides (central Crete, Greece). Geological Magazine **143**(6), pp. 859-876.

Christodoulou G. 1966. About the geology of Astypalaia island. Scientific yearbook: issued by the Faculty of Natural and Mathematical Sciences [Επί της γεωλογίας της νήσου Αστυπάλαιας. Επιστημονική Επετηρίς: εκδιδόμενη υπό της Σχολής των Φυσικών και Μαθηματικών Επιστημών. – (ΑΠΘ)], **10**, 169-180.

Christodoulou G. 1969. Observations of the geology of Kalymnos island (Dodecanese) and the ages of the lithologies of which it consists. Ann. Geol. Des Pays Helleniques, Athenes, **21**, 307-319,

Christodoulou G. 1970. Some remarks on the geology of Kalymnos island (Dodecanes) and the age of its formations. Ann. geol Pays Héllen., (I), **21**, 307-319.

Deino A.L. 2001. User's manual for Mass Spec v. 5.02. Berkeley Geochronology Center Special Publication 1a, 119 p.

Dennis A.J. & Secor D.T. 1987. A model for the development of crenulations in shear zones with applications from the southern Appalachian Piedmont. Journal of Structural Geology, **9**, 809-817.

Dercourt J., Zonenshain L.P., Ricou L.E., Kazmin V.G., Le Pichon X., Knipper A.L., Grandjacquet C., Sbortshikov I.M., Geyssant J., Lepvrier C., Pechersky D.H., Boulin J., Sibuet J.C., Savostin L.A., Sorokhtin O., Westphal M., Bazhenov M.L., Lauer J.P. & Biju-Duval B. 1986. Geological Evolution of the Tethys Belt from the Atlantic to the Pamirs since the Lias. Tectonophysics, **123**, 241-315.

Dercourt J., Ricou L.E. & Vrielynck B. (eds) 1993. Atlas Tethys Palaeoenvironmental Maps. Gauthier-Villars, Paris, p. 307, 14 maps.

Desio A. 1925. Sulla costituzione geologica di alcune isole minori del Dodecaneso. Rend. R. Accad. Lincei, Roma, ser. 6a, **vol. I**, 1 sem., fasc. II, 680-681.

Desio A. 1931. Le isole Italiene dell Egeo. Mem. Descr. Carta Geol. Ital., Roma, 24, 534 p.

Dounas A., Kakavas N. & Tasios N. 1972. Hydrogeological research of Kalymnos Island. Hydrologic and Hydrogeologic Research, 6, I.G.M.E, Athens.

Dounas A., Kakavas N. & Tasios N. 1983. Map of Kalymnos Island, Greece, scale 1:50.000, IGME.

Dilek Y. 2006. Collision tectonics of the Mediterranean region: Causes and consequences. Geological Society of America, Special Paper 409.

Dürr S. 1975. Habil. Schr. Geol. Jahrb. (B), Marburg, 105p.

Dürr S., Altherr R., Keller J., Okrusch M. & Seidel E. 1978. The Median Aegean Belt: Stratigraphy, Structure, Metamorphism. In: Closs H., Roeder D. & Schmidt K. (eds.): Alps, Apennines, Hellenides; Geodynamic Investigations along Geotraverses by an International Group of Geoscientists. E. Schweizerbart´sche Verlagsbuchhandlung, Stuttgart, Pp. 455-474.

Edwards M.A. & Grasemann B. 2009. Mediterranean snapshots of accelerated slab retreat: Subduction instability in stalled continental collision. Geological Society London Special Publications, **311**(1), 155-192.

Eren Y. 2001. Polyphase Alpine deformation at the northern edge of the Menderes-Taurus block, North Konya, Central Turkey. Journal of Asian Earth Sciences, **19**, 737-749.

Fassoulas C., Rahl J.M., Ague J. & Henderson K. 2004. Contact metamorphism in pelitic rocks on the island of Kos. Bulletin of the Geological Society of Greece, **36**, 1626-1635.

Ferrill D.A., Morris A.P., Evans M.A., Burkhardd M., Groshong Jr.R.H. & Onasch C.M. 2004. Calcite twin morphology: a low-temperature deformation geothermometer. Journal of Structural Geology Acta, **26**, 1521-1529.

Fleuty M.J. 1964. The description of folds. Proc. Geol. Assoc., **sta**, 461-492.

Finger F. & Steyrer H. P. 1990. I-type granitoids as indicators of a late Paleozoic convergent ocean/continent margin along the southern flank of the Central European Variscan Orogen. Geology, **18**, 1207-1210.

Fokin P.A., Nikishin A.M. & Ziegler A.M. 2001. Peri-Uralian and Peri-Paleo-Tethyan rift systems of the East European Craton. In: Ziegler P.A., Cavazza W., Robertson A.H.F. & Crasquinsoleau S. (eds): PeriTethys Memoir 6: Peritethyan Rift/Wrench Basins and Passive Margins, IGCP 369. Mémoires da Muséum National d'Histoire Naturelle, **186**, 347–368.

Forster M.A. & Lister G.S. 2016. $^{40}Ar/^{39}Ar$ geochronology and the diffusion of ^{39}Ar in phengite-muscovite intergrowths during step-heating experiments in vacuo. In: Jourdan F., Mark D.F. & Verati C. (eds) 2014: Advances in $^{40}Ar/^{39}Ar$ Dating: from Archaeology to Planetary Sciences. Geological Society, London, Special Publications, **378**, 117-135.

Fossen H. 2010. Structural Geology. Cambridge University Press, 547 p.

Franz L. 1991. Geologische, geochemische und petrologische Untersuchungen an prealpidischen Metamorphiten der Insel Kreta und des Dodekanes (Griechenland). Diss naturwiss, Bayer. Univer. Würzburg, 76-81.

Franz L. 1992. Die polymetamorphe Entwicklung des Altkristallins auf Kreta und im Dodekanes (Griechenland): Eine geologische, geochemische und petrologische Bestandsaufnahme, Stuttgart (Enke), 389p.

Franz L. & Okrusch M. 1992. Aragonite-bearing blueschists on Arki island, Dodekanese, Greece. – Eur. J. Miner., **4**, 527–537.

Franz L., Okrusch M., Seidel E. & Kreuzer H. 2005. Polymetamorphic evolution of pre-Alpidic basement relics in the external Hellenides, Greece. Neues Jahrbuch für Mineralogie - Abhandlungen, **181**(2), 147-172.

Fusseis F. & Grasemann B. 2002. Animation of refold structures. In: (Ed.) Andy Bobyarchick, Visualization, Teaching and Learning in Structural Geology, Journal of the Virtual Explorer, Electronic Edition, ISSN 1441-8142, Vol. 9, paper 1, doi:10.3809/jvirtex.2002.00059

Garfunkel Z. 1998. Constrains on the origin and history of the Eastern Mediterranean basin. Tectonophysics, **298**, 5-35.

Gerolimatos I., Mauridou, F.E.K. & Stauropoulos A. 1993. Polymetamorphic and geodynamic evolution of formations at Leros island (Dodecanese). Geological Society of Greece Structural Geology Commission 29-30/5/93.

Giannopoulos G. 2006. "Δωδεκάνησος, η γένεση ενός ονόματος και η αντιμετώπισή του από τους Ιταλούς" [Dodecanese, the genesis of a name and the Italian approach]. Ἑῷα καὶ Ἑσπέρια (in Greek). **6**. 275–296. doi:10.12681/eoaesperia.78. ISSN 2241-7540.

Gould S.J. & Calloway C.B. 1980. Clams and brachiopods – ships that pass in the night. Paleobiology, **6**(4), 383-396.

Graciansky P. de 1972. Recherches géologiques dans le Taurus lycien. Thèse Fac. Sci. Université Paris-Sud (Orsay) 896, 762 p.

Gradstein F.M., Ogg J.G., Schmitz K. & Ogg G. 2012. The Geologic Time Scale 2012. Elsevier Publishing Company, Amsterdam.

Halamski A.T. & Baliński A. 2013. Middle Devonian Brachiopods from the Southern Maïder (Eastern Anti-Atlas, Morocco). Annales Societatis Geologorum Poloniae, **83**, 243-307.

Hirth G. & Tullis J. 1992. Dislocation creep regimes in quartz aggregates. Journal of Structural Geology, **14**, 145-159.

Jacobshagen V. 1986. Geologie von Griechenland. Gebrüder Borntraeger, Berlin, 363 p.

Jarvis A., Reuter H.I., Nelson A. & Guevara E. 2008. Hole-filled seamless SRTM data V4, International Centre for Tropical Agriculture (CIAT), available from http://srtm.csi.cgiar.org.

Jin J. & Copper P. 2000. Late Ordovician and Early Silurian pentamerid brachiopods from Anticosti Island, Quebec, Canada. Palaeontographica Canadiana, 18. 140 p.

Jolivet L., Rimmelé G., Oberhänsli R., Goffé B. & Candan O. 2004. Correlation of syn-orogenic tectonic and metamorphic events in the Cyclades, the Lycian nappes and the Menderes massif. Geodynamic implications. Bulletin Societé Géologique de France, **175**(3), 217-238.

Jolivet L. & Brun J.P. 2010. Cenozoic geodynamic evolution of the Aegean. International Journal of Earth Sciences, **99**, 109–138.

Kalaitzidis St., Siavalas G., Skarpeli N., Araujo C. V. & Christanis K. 2010. Late Cretaceous coal overlying Karstic bauxite deposits in the Parnassus-Ghiona Unit, Central Greece: Coal characteristics and depositional environment. International Journal of Coal Geology, **81**(4), pp. 211-226.

Kalt A., Altherr R. & Ludwig T. 1998. Contact metamorphism in pelitic rocks on the island of Kos (Greece, Eastern Aegean Sea): a test for the Na-in-cordierite thermometer. Journal of Petrology, **39**, 663–688.

Kahler F. 1987. Fusuliniden-Faunen auf Chios, Kalymnos und Kos in der Ägäis. – Mitteilungen der Österreichischen Geologischen Gesellschaft, **80**, 287-322.

Karakitsios V. 1995. The Influence of Preexisting Structure and Halokinesis on Organic Matter Preservation and Thrust system Evolution in the Ionian Basin, Northwest Greece. AAPG Bulletin, **79**(7), 960-980.

Katagas C. & Sapountzis E. 1977a. Petrochemistry of metasedimentary rocks from Leros island (Greece) and its effects on the appearance of chloritoid staurolite and kyanite. Neues Jahrb. Mineral. Abh., **129**, 100-112.

Katagas C. & Sapountzis E. 1977b. Petrochemistry of low and medium grade metamorphic rocks from Leros island, Greece. Tschermaks Mineral Petrogr Mitt, **24**, 39-55.

Katagas C.G. 1980. Metamorphic Zones and Physical Conditions of Metamorphism in Leros Island, Greece. Contrib. Mineral. Petrol., **73**, 389-402.

Kellett D. & Joyce N. 2014. Analytical details of the single- and multicollection $^{40}Ar/^{39}Ar$ measurements for conventional step-heating and total-fusion age calculation using the Nu Noblesse at the Geological Survey of Canada.Geological Survey of Canada, Technical Note 8, 27 pp.

Kleber W., Bautsch H.J., Bohm J. & Klimm D. 2010. Einführung in die Kristallographie. Oldenbourg Verlag München, 19. Auflage, 469 pp. ISBN 978-3-486-59075-3

Kopp K.O. & Ott E. 1977. Spezialkartierungen im Umkreis neuer Fossilfunde in Trypali und Tripolitza-Kalken Westkretas. Neues Jahrbuch für Geologie und Paläontologie, Monatshefte, 217-238.

Krahl J., Richter D., Forster O., Kozur H. & Hall R. 1988. Zur Stellung der Talea Ori im Bau des kretischen Deckenstapels (Griechenland). Zeitschrift der Deutschen Geologischen Gesellschaft, **149**, 191-227.

Lister G.S., Banga G. & Feenstra A. 1984. Metamorphic core complex of Cordilleran type in the Cyclades, Aegean Sea, Greece, *Geology*, **12**, 221-225.

Llyod G.E, Farmer A.B. & Mainprice D. 1997. Misorientation analysis and the formation and orientation of subgrain and grain boundaries. Tectonophysics, **279**, 55-78.

Mackintosh P.W. & Robertson A.H.F. 2012. Late Devonian–Late Triassic sedimentary development of the central Taurides, S Turkey: Implications for the northern margin of Gondwana. Gondwana Research, **21**(4), 1089-1114.

Mahon K. 1996. The new "York" regression; application of an improved statistical method to geochemistry. International Geology Review, **38**, 293–303.

Mariani E., Brodie K.H. & Rutter E.H. 2006. Experimental deformation of muscovite shear zones at high temperatures under hydrothermal conditions and the strength of phyllosilicate-bearing faults in nature. Journal of Structural Geology, **28**(9), 1569-1587.

McClay K.R. 1991. Glossary of thrust tectonics terms. In: McClay K.R. (ed) Thrust tectonics: London, Chapman & Hall, p. 419-433.

McClelland W.C. (eds): Circum-Arctic Structural Events: Tectonic Evolution of the Arctic Margins and Trans-Arctic Links with Adjacent Orogens. Geological Society of America Special Paper 541, Chapter 8, https://doi.org/10.1130/2018.2541(08).

McClusky S., Reilinger R., Mahmoud S., Ben Sari D. & Tealeb A. 2003. GPS constraints on Africa (Nubia) and Arabia plate motions. Geophysical Journal International, **155**, 126-138.

Mottequin B., Brice D. & Legrand-Blain M. 2014. Biostratigraphic significance of brachiopods near the Devonian-Carboniferous boundary. Geological Magazine, **151**(2), 216-228.

Murawski H. & Meyer W. 2004. Geologisches Wörterbuch. Elsevier, München, 262pp.

Okay A.I. & Tuysuz O. 1999. Tethyan sutures of northern Turkey. In: Durand B., Jolivet L., Horvath F. & Séranne M. (eds.): The Mediterranean Basins: tertiary Extension within the Alpine Orogen. Geological Society London, Special Publications, **156**, 475-515.

Papanikolaou D. 2015. Geology of Greece, 307 p.

Passchier C.W. 1991. Geometric constraints on the development of shear bands in rocks. Geol Mijnb, **70**, 203-211.

Passchier C.W. & Trouw R.A.J. 2005. Microtectonics. Springer Berlin Heidelberg, 365pp.

Pe-Piper G. 1998. The nature if Triassic extension-related magmatism in Greece: Evidence from Nd and Pb isotope geochemistry. Geological Magazine, **135**(3), 331-348.

Pe-Piper G. & Piper D.J.W. 2002. The igneous rocks of Greece - The anatomy of an orogen. Berlin, Gebrüder Bornträger, 316 p.

Philipson A. 1959. Das Ägäische Meer und seine Inseln. In: Kirsten E. (ed): Die griechischen Landschaften IV. Frankfurt.

Pomoni – Papaioannou F., Karakitsios V., Kamberis E. & Marnelis F. 2004. Chevron-type halite and nodular anhydrite in the Triassic subsurface evaporates of the Ionian zone (western Greece). Bulletin of the Geological Society of Greece, vol.**36**, Proceedings of the 10th International Congress, Thessaloniki.

Ramsay 1950. https://www.see.leeds.ac.uk/structure/folds/polyphase/ramsay1.htm

Reiners P.W. 2005. Zircon (U-Th)/He Thermochronometry. Reviews in Mineralogy & Geochemistry, **58**, 151-179.

Renne P.R., Swisher C.C., Deino A.L., Karner D.B., Owens T.L. & DePaolo D.J. 1998. Intercalibration of standards, absolute ages and uncertainties in $^{40}Ar/^{39}Ar$ dating. Chemical Geology, **145**, 117-152.

Renz C. 1940. Die Tektonik der griechischen Gebirge. *Pragmatica Akademia Athena*, **8**, 1-171.

Robertson A.H.F. 1997. Correlation and tectonic significance of Mesozoic ophiolites in the Dinarides, Albanides and Hellenides. Przeglad Geologiczny, **45**(10), 1099-1100.

Robertson A.H.F., Clift P.D., Degnan P.J. & Jones G. 1991. Palaeogeographical and palaeotectonic evolution of the eastern Mediterranean Neotethys Palaeoceanography, Palaeoclimatology and Palaeoecology **87**, 289-343.

Robertson A.H.F., Dixon J.E., Brown S., Collins A., Morris A., Pickett E., Sharp I. & Ustaömer T. 1996. Alternative tectonic models for the Late Palaeozoic-Early tertiary development of Tethys in the Eastern Mediterranean region. In: Morris A. & Tarling D.H (eds): Palaeomagnetism and Tectonics of the Mediterranean Region. Geological Society, London, Special Publications, **105**, 239-263.

Robertson A.H.F. & Pickett E.A. 2000. Palaeozoic-Tertiary Tethyan evolution of melanges, rift and passive margin units in the Karaburun Peninsula (western Turkey) and Chios Island (Greece). In: Bozkurt E., Winchester J.A. & Piper J.D.A. (eds.): Tectonics and Magmatism in Turkey and the Surrounding Area. Geological Society, London, Special Publications, **173**, 43-82.

Robertson A.H.F. 2006. Sedimentary evidence form the south Mediterranean region (Sicily, Crete, Peloponnes, Evia) used to test alternative models for the regional tectonic setting of Tethys during Late Palaeozoic-Early Mesozoic time. In: Robertson A.H.F. & Mountrakis D. (eds): Tectonic Development of the Eastern Mediterranean Region. Geological Society, London, Special Publication, **260**, 91-154.

Roche V., Conand C., Jolivet L. & Augier R. 2018. Tectonic evolution of Leros Island (Dodecanese, Greece) and correlations between the Aegean Domain and the Menderes Massif. Journal of the Geological Society, **1**, 836-849.

Rosenbaum G., Ring U. & Kühn A. 2007. Tectonometamorphic evolution of high-pressure rocks from the island of Amorgos (Central Aegean, Greece). Journal of the Geological Society, London, **164**, 425-438.

Ross, C.A., Ross, J.R.P. & Brenckle, P.L. 1997: Late Paleozoic Foraminifer, their biostratigraphy, evolution, and paleoecology and the mid-Carboniferous boundary. – Cushman Foundation for Foraminiferal Research, Special Publication **36**: 1-170.

Royden L.H. 1993: The tectonic expression slab pull at continental convergent boundaries. Tectonics, **12**(2), 303-325.

Schneider D.A., Grasemann B., Lion A., Soukis K. & Draganits E. 2018. Geodynamic significance of the Santorini Detachment System (Cyclades, Greece). Terra Nova, **30**, 414-422.

Schneider D.A., Faehnrich K., Majka J. & Manecki M. 2019. $^{40}Ar/^{39}Ar$ geochronologic evidence of Eurekan deformation within the West Spitsbergen Fold and Thrust Belt. In: Piepjohn K., Strauss J.V., Reinhardt L. & McClelland W.C. (eds): Circum-Arctic Structural Events: Tectonic Evolution of the Arctic Margins and Trans-Arctic Links with Adjacent Orogens, Special Paper of the Geological Society of America, 541.

Schuchert C. & Cooper G.A. 1931. Synopsis of the brachiopod genera of the suborders Orthoidea and Pentameroidea, with notes on the Telotremata. American Journal of Science, **20**, pp. 241-251.

Şengör A.M.C., Yilmaz Y. & Sungurlu O. 1984. Tectonics of the Mediterranean Cimmerides: nature and evolution of the western termination of Palaeo-Tethys. – In: Robertson A.H.F. & Dixon J.E. (eds): Tectonic Evolution of the Eastern Mediterranean. Geological Society London, Special Publication, **17**, 77–112.

Spaletti L.A., Limarino C.O. & Geuna S. 2010. The Late Palaeozoic of Western Gondwana: New insights from South American records. Geologica Acta, **8**(4), 341-347.

Stampfli G. & Pillevuit A. 1993. An alternative Permo-Triassic reconstruction of the kinematics of the Tethyan realm. In: Dercourt J., Ricou L.E. & Vrielinck B. (eds): Atlas Tethys Palaeoenvironmental Maps. Explanatory Notes. Gauthier-Villars, 55-62.

Stampfli G.M., von Raumer J. & Borel G.D. 2002. The Palaeozoic evolution of pre-Variscan terranes: from peri-Gondwana to the Variscan collision. In: Martinez-Catalan J.R., Hatcher R.D., Arenas R. & Diaz Garcia F. (eds): Variscan Appalachian Dynamics: The Building of the Upper Paleozoic Basement. Geological Society of America, Special Papers, **364**, 263-280.

Stampfli G.M. & Kozur H.W. 2006. Europe from the Variscan to the Alpine Cycles. - In: Gee D.G., Stephenson R.A. (ed). European Lithosphere Dynamics. Geological Society, London, Memoirs, **32**, 57-82.

Sengör A.M.C. & Hsü K.J. 1984. The Cimmerides of Eastern Asia: History of the Eastern end of Paleo-Tethys. Memoires de Societe Geologique de France, **47**, 139-167.

Steiger R.H. & Jäger E. 1977. Subcommission on geochronology: convention on the use of decay constants in geo- and cosmochronology. Earth and Planetary Science Letters, **36**, 359–362.

Thorbecke G. 1987. Zur Zonengliederung der ägäischen Helleniden und westlichen Tauriden. – Mitteilungen der Gesellschaft der Geologie- und Bergbaustudenten Österreichs **SH 2**, 1-161.

Triantafillis M., Mavrides A., Tsaila-Monopoli S., Skourtsi-Koroneou V., Ioakim C., Karantassi S., Kanaki-Mavridou F., Petridou-Nazou, Mettos A., Tsalahouri I., Foundou C., Hadjopoulou-Zarkadi A. & Ganotis G. 1986. Geological Map Eastern Kos Sheet 1:50 000. IGME.

Triantafillis M. & Karfakis I. 1994. Bulletin of the Geological Society of Greece, **30**(2), 123-134, Proceedings of the 7th Congress, Thessaloniki, May 1994.

Van Hinsbergen D.J.J. & Boekhout F. 2009. Neogene brittle detachment faulting on Kos (E Greece): implications for a southern break-away fault of the Menderes metamorphic core complex (western Turkey). In: Van Hinsbergen D.J.J., Edwards M.A. & Govers R. (eds): Collision and Collapse at the Africa-Arabia-Eurasia Subduction Zone. The Geological Society, London, Special Publications, **311**, 311-320.

Vavassis I., De Bono A., Stampfli G.M., Giorgis D., Valloton A. & Amelin Y. 2000. U-Pb and Ar-Ar geochronological data from the Pelagonian basement in Evia (Greece): Geodynamic implications for the evolution of Paleotethys. Schweizerische Mineralogische und Petrographische Mitteilungen, **80**, 21-43.

Wachendorf H. & Gralla P. 1983: Korrelation der präneogenen Serien im NE-Dodekanes (Griechenland). Zeitschrift der deutschen Geologischen Gesellschaft, **34**, 95-117.

Wheeler J., Prior D.J., Jiang Z., Spiess R. & Trimby P.W. 2001. Misorientation analysis and the formation and orientation of subgrain and grain boundaries. Contributions to Mineralogy and Petrology, **141**, 109-124.

Wilson J.L. 1975. Carbonate Facies in Geologic History. Springer-Verlag, Berlin, Heidelberg, New York, 471pp.

Wooler D.A., Smith A.G. & White N. 1992. Measuring lithospheric stretching on Tethyan passive margins. Journal of the Geological Society, **149**(4), 517-532.

Wortel M.J.R. & Spakman W. 2000. Subduction and Slab Detachment in the Mediterranean-Carpathian Region. *Science's Compass Review Geophysics*, **290**, 1910-1917.

Zanchi A., Garzanti E., Larghi C., Angiolini L. & Gaetani M. 2003. The Variscan orogeny in Chios (Greece): Carboniferous accretion along a Palaeotethyan active margin. Terra Nova, **15**, 213-223.

Ziegler P.A. & Stampfli G.M. 2001. Late Paleozoic-Early Mesozoic plate boundary reorganisation: Collapse of the Variscan orogen and opening of Neotethys. In: Cassinis R. (ed): The Continental Permian of the Southern Alps and Sardinia (Italy) Regional Reports and General Correlations. Annali Museo Civico Science Naturali, Brescia, **25**, 17-34.

Zulauf G., Romano S.S., Dörr W. & Fiala J. 2007. Crete and the Minoan terranes: age constraints from U-Pb dating of detrital zircons. In: Linnemann U., Nance R.D., Kraft P. & Zulauf G. (eds): The evolution of the Rheic Ocean: from Avalonian-Cadomian active margin to Alleghenian-Variscan Collision. – Geol. Soc. America, Spec. Pap., **423**, 401–411.

Zulauf G., Klein T., Kowalczyk G., Krahl J. & Romano S. 2008. The Mirsini Syncline of eastern Crete, Greece: a key area for understanding pre-Alpine and Alpine orogeny in the eastern Mediterranean. Zeitschrift der Deutschen Gesellschaft für Geowissenschaften, **159**(3), 399-414.

APPENDIX 8.1

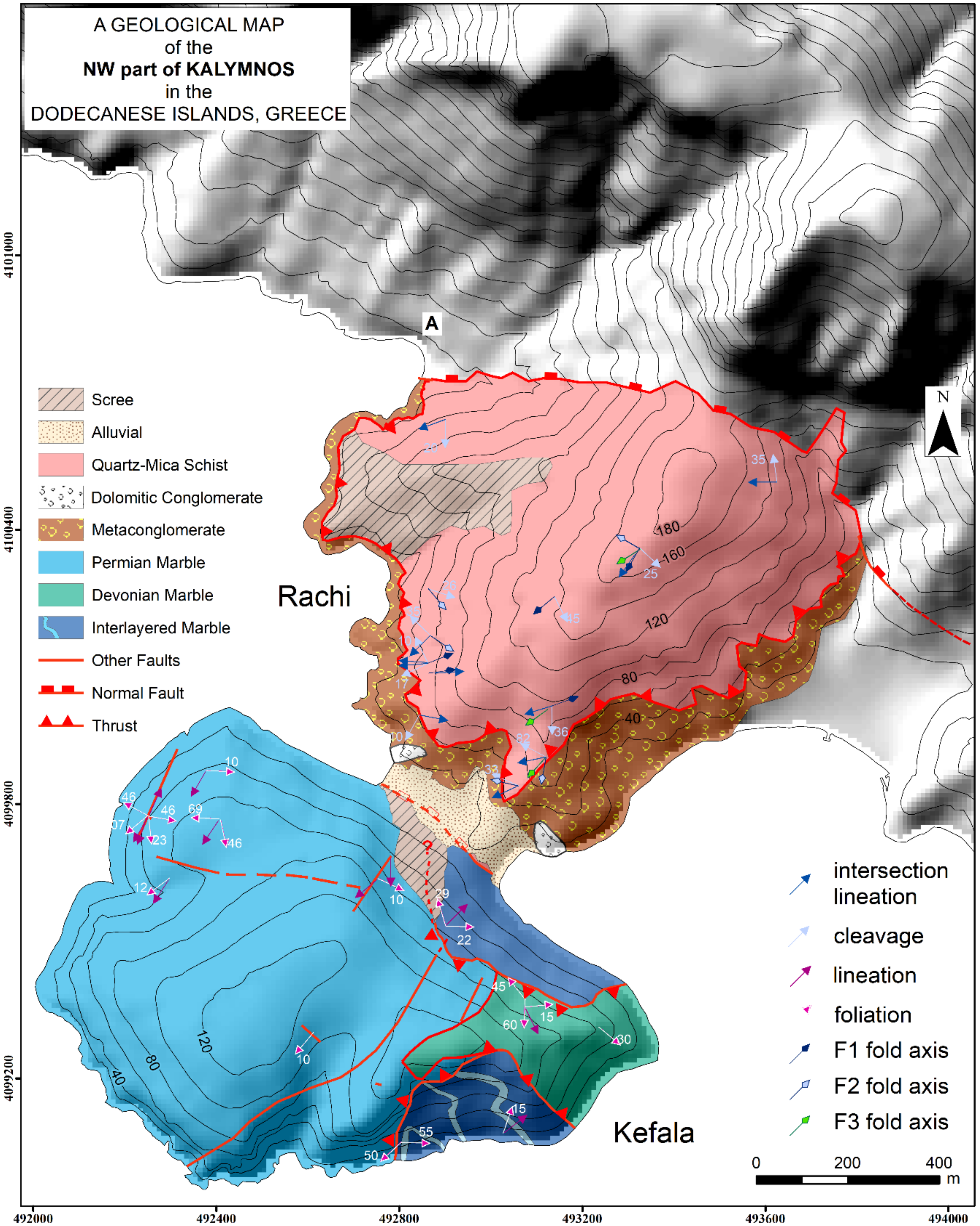

A GEOLOGICAL MAP
of the
NW part of KALYMNOS
in the
DODECANESE ISLANDS, GREECE
A
Scree
Alluvial
Quartz-Mica Schist
Dolomitic Conglomerate
Metaconglomerate
Permian Marble
Devonian Marble
Interlayered Marble
Other Faults
Normal Fault
Thrust
Rachi
Kefala
N
intersection lineation
cleavage
lineation
foliation
F1 fold axis
F2 fold axis
F3 fold axis
0
200
400
m
180
160
120
80
40
4101000
4100400
4099800
4099200
492000
492400
492800
493200
493600
494000

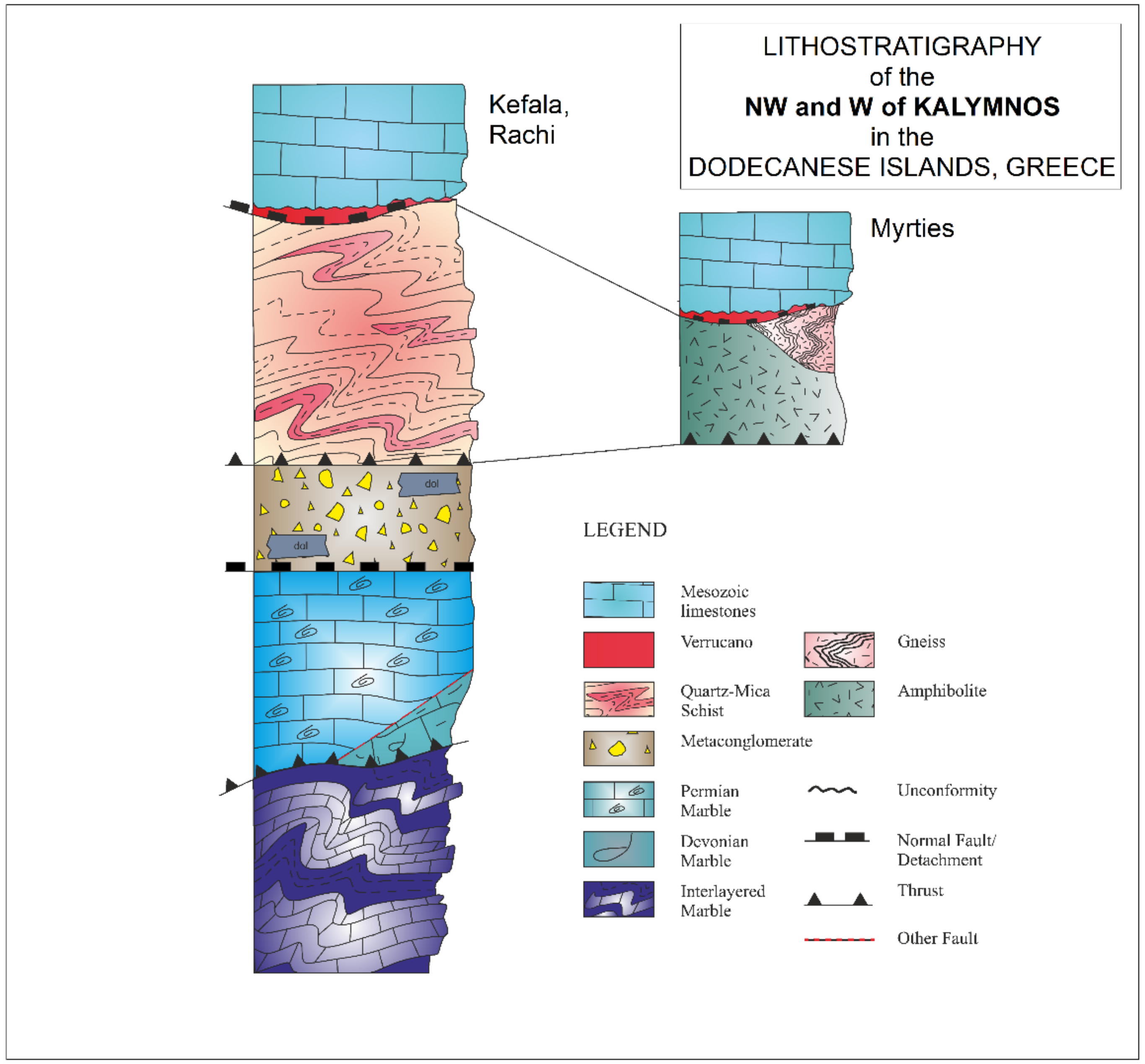

LITHOSTRATIGRAPHY
of the
NW and W of KALYMNOS
in the
DODECANESE ISLANDS, GREECE
Kefala, Rachi
Myrties
LEGEND
Mesozoic limestones
Verrucano
Gneiss
Quartz-Mica Schist
Amphibolite
Metaconglomerate
Permian Marble
Unconformity
Devonian Marble
Normal Fault/ Detachment
Interlayered Marble
Thrust
Other Fault

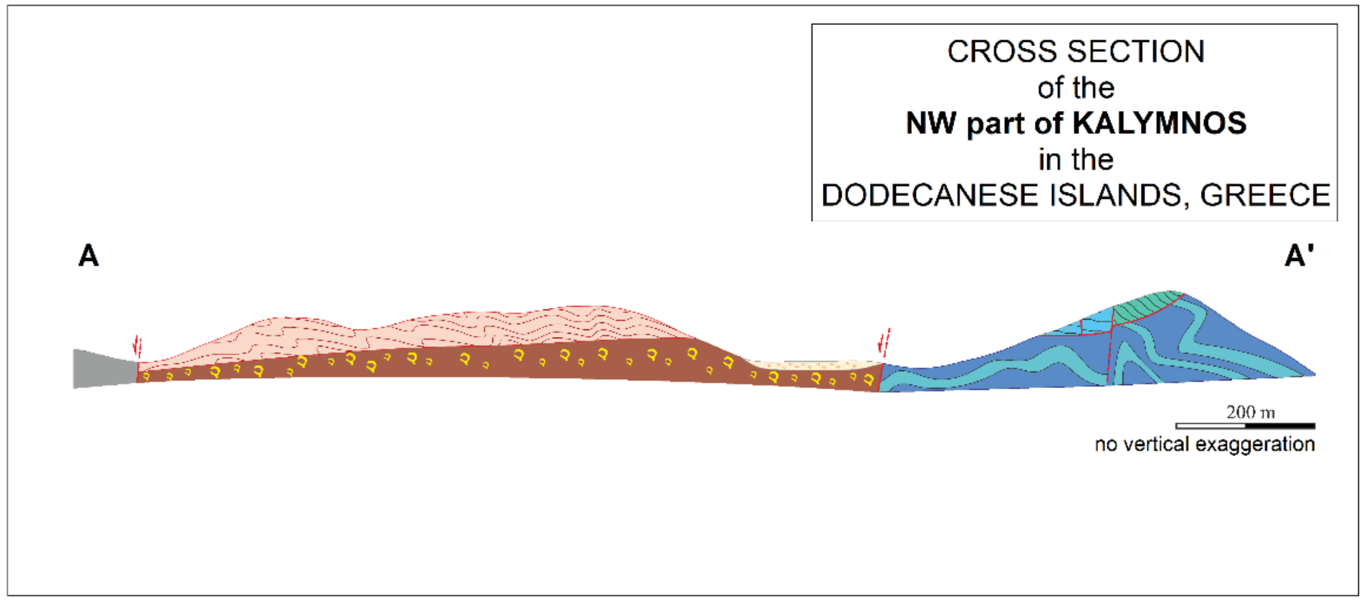

CROSS SECTION
of the
NW part of KALYMNOS
in the
DODECANESE ISLANDS, GREECE
A
A'
200 m
no vertical exaggeration

APPENDIX 8.2. $^{40}Ar/^{39}AR$ isotopic data for white mica, Kalymnos, Greece

Sample*	Watts	^{40}Ar	±1s	^{39}Ar	±1s	^{38}Ar	±1s	^{37}Ar	±1s	^{36}Ar	±1s	^{39}Ar Mol†	Ca/K	±1s	Cl/K	±1s	$^{37}Ar/^{39}Ar$	±1s	$^{38}Ar/^{39}Ar$	±1s	$^{40}Ar/^{39}Ar$	±1s	$^{40}Ar^{*}/^{39}Ar$	±1s	%$^{40}Ar^{*}$	Age†† (Ma)	±1s
KA014002 (J: 3.530x10^{-3} ± 0.020)																											
A	0.25	1799173.00	979.79	31259.66	91.87	390.36	10.27	13.24	21.29	0.00	0.00	0.110	0.000830	0.0013	0.012627	0.000000	0.0004	0.0007	0.0125	0.0003	57.556	0.1720	±58.094	0.2008	100.9	336.54	1.06
B*	0.30	176873.60	76.26	2964.13	11.49	36.87	1.63	0.00	0.00	0.00	0.00	0.010	0.000000	0.0000	0.010557	0.000000	0.0000	0.0000	0.0124	0.0006	59.671	0.2327	±59.732	0.3046	100.1	**345.17**	**1.60**
C*	0.35	23545.84	56.11	392.64	4.26	7.32	1.24	0.00	0.00	3.69	2.11	0.001	0.000000	0.0000	0.036644	0.000002	0.0000	0.0000	0.0187	0.0032	59.969	0.6659	±57.152	1.7258	95.3	**331.56**	**9.15**
D*	0.40	47499.05	52.65	804.66	4.14	13.20	1.36	2.08	4.28	1.56	2.01	0.003	0.005065	0.0104	0.031651	0.000001	0.0026	0.0053	0.0164	0.0017	59.030	0.3104	±58.450	0.8077	99.0	**338.42**	**4.26**
E*	0.45	42681.19	50.38	737.26	7.99	7.68	1.44	0.00	0.00	0.00	0.00	0.003	0.000000	0.0000	0.000000	0.000000	0.0000	0.0000	0.0104	0.0020	57.892	0.6310	±58.296	1.0039	100.7	**337.61**	**5.30**
F*	0.50	85834.83	65.49	1452.37	7.99	20.73	1.44	0.00	0.00	6.07	2.32	0.005	0.000000	0.0000	0.016532	0.000001	0.0000	0.0000	0.0143	0.0010	59.100	0.3282	±57.849	0.5745	97.9	**335.25**	**3.04**
G*	0.55	163542.20	79.61	2776.06	12.63	39.08	2.08	0.00	0.00	4.84	2.00	0.010	0.000000	0.0000	0.018087	0.000000	0.0000	0.0000	0.0141	0.0008	58.912	0.2695	±58.388	0.3427	99.1	**338.09**	**1.81**
H*	0.60	223971.80	99.18	3716.69	10.12	43.84	1.86	0.00	0.00	2.12	1.89	0.013	0.000000	0.0000	0.005861	0.000000	0.0000	0.0000	0.0118	0.0005	60.261	0.1662	±60.088	0.2247	99.7	**347.04**	**1.18**
I*	0.65	291251.40	110.28	4840.43	11.37	56.81	1.76	3.47	3.91	4.25	2.20	0.017	0.001406	0.0016	0.005163	0.000000	0.0007	0.0008	0.0117	0.0004	60.171	0.1432	±59.906	0.1970	99.6	**346.09**	**1.04**
J*	0.70	311234.10	164.43	5161.25	16.40	64.72	1.77	0.00	0.00	0.00	0.00	0.018	0.000000	0.0000	0.011706	0.000000	0.0000	0.0000	0.0125	0.0003	60.302	0.1942	±60.512	0.2529	100.4	**349.27**	**1.33**
K*	0.75	345539.90	119.41	5707.41	13.88	73.51	1.89	0.00	0.00	2.41	1.98	0.020	0.000000	0.0000	0.012457	0.000000	0.0000	0.0000	0.0129	0.0003	60.542	0.1488	±60.413	0.1811	99.8	**348.75**	**0.95**
L*	0.80	245511.00	126.90	4036.06	12.63	50.87	1.65	0.00	0.00	0.00	0.00	0.014	0.000000	0.0000	0.011898	0.000000	0.0000	0.0000	0.0126	0.0004	60.829	0.1929	±60.988	0.2468	100.3	**351.77**	**1.29**
M*	0.90	117072.60	58.86	1956.07	7.87	24.15	1.74	0.00	0.00	0.00	0.00	0.007	0.000000	0.0000	0.010855	0.000000	0.0000	0.0000	0.0123	0.0009	59.851	0.2425	±60.141	0.4229	100.5	**347.32**	**2.22**
N*	1.10	83859.45	65.47	1413.90	6.72	13.90	1.45	2.46	4.59	1.50	2.27	0.005	0.003417	0.0064	0.000000	0.000000	0.0017	0.0032	0.0098	0.0010	59.311	0.2856	±58.990	0.5568	99.5	**341.27**	**2.93**
O*	1.50	86576.54	67.89	1446.20	7.70	21.36	1.43	6.02	5.06	5.21	2.58	0.005	0.008154	0.0069	0.020113	0.000001	0.0042	0.0035	0.0148	0.0010	59.865	0.3223	±58.787	0.6189	98.2	**340.20**	**3.26**
P*	3.50	127707.10	76.42	2167.13	9.69	26.15	1.57	6.80	4.59	0.39	1.98	0.008	0.006155	0.0041	0.007894	0.000000	0.0031	0.0021	0.0121	0.0007	58.929	0.2658	±58.873	0.3811	99.9	**340.65**	**2.01**
Q*	6.00	81043.91	59.14	1326.17	5.46	17.83	1.64	0.00	0.00	2.72	2.14	0.005	0.000000	0.0000	0.013997	0.000001	0.0000	0.0000	0.0134	0.0012	61.111	0.2555	±60.497	0.5447	99.0	**349.19**	**2.86**
																										Tg: 342 ± 4 Ma	
KA014002 (J: 3.530x10^{-3} ± 0.020)																										**Tp: 346 ± 6 Ma**	
A	0.20	12691.06	51.95	387.25	3.85	10.71	1.36	25.66	5.10	20.41	2.60	0.001	0.129884	0.0258	0.041678	0.000003	0.0663	0.0132	0.0277	0.0035	32.772	0.3527	±17.038	2.0140	52.0	105.37	12.10
B	0.25	29132.35	63.98	626.10	4.60	15.26	1.54	7.05	4.81	10.60	3.13	0.002	0.022061	0.0151	0.062184	0.000002	0.0113	0.0077	0.0244	0.0025	46.530	0.3566	±41.474	1.5267	89.1	246.50	8.48
C	0.30	31389.72	57.71	591.18	6.99	4.64	1.42	0.00	0.00	3.45	3.04	0.002	0.000000	0.0000	0.000000	0.000000	0.0000	0.0000	0.0078	0.0024	53.096	0.6350	±51.352	1.6516	96.7	300.55	8.90
D	0.35	44702.40	49.54	802.17	6.50	11.80	1.23	8.75	5.33	1.68	2.15	0.003	0.021386	0.0130	0.021472	0.000001	0.0109	0.0066	0.0147	0.0015	55.727	0.4556	±55.100	0.9192	98.9	320.65	4.90
E	0.40	190501.90	189.88	3364.87	16.45	42.22	2.01	10.88	6.16	9.83	2.59	0.012	0.006337	0.0036	0.007682	0.000000	0.0032	0.0018	0.0125	0.0006	56.615	0.2825	±55.740	0.3608	98.5	324.05	1.92
F*	0.45	439683.60	239.93	7534.87	25.28	87.60	2.14	10.93	6.28	0.00	0.00	0.027	0.002844	0.0016	0.005706	0.000000	0.0015	0.0008	0.0116	0.0003	58.353	0.1983	±58.408	0.2321	100.1	**338.20**	1.23
G*	0.50	613924.40	315.28	10108.36	27.79	126.41	2.29	2.98	6.28	4.87	1.94	0.036	0.000577	0.0012	0.010170	0.000000	0.0003	0.0006	0.0125	0.0002	60.734	0.1698	±60.588	0.1789	99.8	**349.67**	0.94
H*	0.55	207244.30	124.82	3368.21	11.28	40.06	1.64	0.00	0.00	1.72	1.94	0.012	0.000000	0.0000	0.006502	0.000000	0.0000	0.0000	0.0119	0.0005	61.529	0.2094	±61.374	0.2706	99.8	**353.79**	1.42
I*	0.60	79573.45	51.47	1337.30	6.76	15.35	1.38	3.39	6.28	0.00	0.00	0.005	0.004973	0.0092	0.007859	0.000001	0.0025	0.0047	0.0115	0.0010	59.503	0.3031	±60.370	0.5309	101.5	**348.53**	2.79
J*	0.65	27972.33	45.30	490.37	4.21	3.93	1.30	0.00	0.00	0.03	1.84	0.002	0.000000	0.0000	0.000000	0.000000	0.0000	0.0000	0.0080	0.0027	57.044	0.4978	±57.022	1.2269	100.0	**330.87**	6.50
K*	0.70	9817.74	46.39	183.42	2.45	1.89	1.23	0.00	0.00	0.00	0.00	0.001	0.000000	0.0000	0.016082	0.000006	0.0000	0.0000	0.0103	0.0067	53.526	0.7596	±58.457	3.2600	109.2	**338.46**	17.21
L*	0.75	14247.00	44.22	253.08	3.37	3.91	1.25	0.00	0.00	0.00	0.00	0.001	0.000000	0.0000	0.035871	0.000005	0.0000	0.0000	0.0154	0.0050	56.294	0.7696	±58.350	2.5338	103.7	**337.89**	13.38
M*	0.80	11470.99	36.88	204.52	2.64	0.00	0.00	3.99	4.81	0.00	0.00	0.001	0.038241	0.0461	0.000000	0.000000	0.0195	0.0235	0.0000	0.0000	56.087	0.7453	±60.787	2.7139	108.4	**350.72**	14.23
N*	0.90	102632.80	93.46	1735.63	8.47	18.17	1.51	0.38	5.28	0.40	1.68	0.006	0.000431	0.0060	0.000000	0.000000	0.0002	0.0030	0.0105	0.0009	59.133	0.2937	±59.061	0.4117	99.9	**341.64**	2.17
O*	1.10	111766.90	56.74	1827.31	6.85	18.65	1.19	1.46	5.56	0.90	1.98	0.006	0.001565	0.0060	0.000000	0.000000	0.0008	0.0030	0.0102	0.0007	61.165	0.2312	±61.014	0.3969	99.8	**351.91**	2.08
P*	1.50	54259.94	56.74	895.75	10.73	6.58	1.33	4.74	6.22	0.00	0.00	0.003	0.010373	0.0136	0.000000	0.000000	0.0053	0.0069	0.0073	0.0015	60.575	0.7286	±60.777	0.9614	100.3	**350.67**	5.04
Q*	3.50	29108.94	35.17	497.63	4.03	6.94	1.36	6.41	4.20	1.21	1.78	0.002	0.025235	0.0165	0.016594	0.000002	0.0129	0.0084	0.0140	0.0027	58.496	0.4787	±57.771	1.1655	98.8	**334.83**	6.17
R	6.00	5132.57	28.94	81.56	2.25	2.37	1.39	11.24	5.75	1.63	1.98	0.000	0.270211	0.1383	0.086398	0.000014	0.1379	0.0706	0.0290	0.0171	62.926	1.7682	±56.969	7.4203	90.5	330.58	39.34
																										Tg: 338 ± 4 Ma	
																										Tp: 350 ± 7 Ma	

Sample*	Watts	^{40}Ar	±1s	^{39}Ar	±1s	^{38}Ar	±1s	^{37}Ar	±1s	^{36}Ar	±1s	^{39}Ar Mol†	Ca/K	±1s	Cl/K	±1s	^{37}Ar/^{39}Ar	±1s	^{38}Ar/^{39}Ar	±1s	^{40}Ar/^{39}Ar	±1s	^{40}Ar*/^{39}Ar	±1s	%^{40}Ar*	Age†† (Ma)	±1s
KA014003 (J: 3.526x10^{-3} ± 0.020)																											
A	0.25	63162.00	57.94	5852.98	15.13	123.89	2.71	51.08	4.59	145.12	3.44	0.021	0.017104	0.0015	0.034357	0.000000	0.0087	0.0008	0.0212	0.0005	10.791	0.0296	± 3.387	0.1760	31.4	21.42	1.11
B	0.30	26349.42	50.77	2001.59	8.72	33.76	1.85	6.51	3.84	36.42	2.16	0.007	0.006372	0.0038	0.016223	0.000000	0.0033	0.0019	0.0169	0.0009	13.164	0.0627	± 7.730	0.3244	58.7	48.52	2.01
C	0.35	57007.62	152.02	2796.89	17.64	48.64	1.86	28.52	4.11	37.67	3.29	0.010	0.019989	0.0029	0.024619	0.000000	0.0102	0.0015	0.0174	0.0007	20.383	0.1396	±16.359	0.3698	80.3	101.18	2.22
D	0.40	90005.89	99.40	3687.66	11.38	60.47	2.26	17.15	4.34	40.50	2.72	0.013	0.009117	0.0023	0.021516	0.000000	0.0047	0.0012	0.0164	0.0006	24.407	0.0800	±21.126	0.2310	86.6	129.63	1.37
E	0.45	68643.14	67.87	2481.62	10.25	31.72	2.01	8.27	4.40	14.42	1.97	0.009	0.006531	0.0035	0.005854	0.000000	0.0033	0.0018	0.0128	0.0008	27.661	0.1175	±25.924	0.2611	93.7	157.81	1.52
F	0.50	207361.10	99.40	6369.37	15.14	83.26	2.05	20.15	4.32	16.75	1.97	0.022	0.006200	0.0013	0.011123	0.000000	0.0032	0.0007	0.0131	0.0003	32.556	0.0790	±31.768	0.1203	97.6	191.56	0.69
G*	0.55	9912573.00	9527.65	242049.00	1250.96	2920.50	50.42	431.03	102.80	68.91	53.96	0.853	0.003490	0.0008	0.007781	0.000000	0.0018	0.0004	0.0121	0.0002	40.953	0.2153	±40.865	0.2249	99.8	**242.87**	**1.25**
H	0.60	449736.30	240.59	11372.21	20.16	137.50	3.01	5.63	4.24	20.84	2.49	0.040	0.000971	0.0007	0.006197	0.000000	0.0005	0.0004	0.0121	0.0003	39.547	0.0732	±38.997	0.0975	98.6	232.45	0.55
I	0.65	261531.20	178.15	6696.78	25.20	81.64	2.02	12.86	4.55	20.41	2.13	0.024	0.003763	0.0013	0.005431	0.000000	0.0019	0.0007	0.0122	0.0003	39.053	0.1493	±38.141	0.1742	97.7	227.65	0.98
J	0.70	191721.80	128.54	4774.44	15.13	60.43	1.56	7.75	4.84	12.36	2.68	0.017	0.003182	0.0020	0.008710	0.000000	0.0016	0.0010	0.0127	0.0003	40.156	0.1301	±39.380	0.2108	98.1	234.59	1.18
K	0.75	164775.50	75.35	4119.93	11.12	57.03	1.76	7.51	4.76	0.00	0.00	0.015	0.003572	0.0023	0.018767	0.000000	0.0018	0.0012	0.0138	0.0004	39.995	0.1095	±40.029	0.1783	100.1	238.21	0.99
L	0.80	139914.90	103.30	3394.66	13.88	44.41	1.65	3.11	5.07	0.00	0.00	0.012	0.001795	0.0029	0.014339	0.000000	0.0009	0.0015	0.0131	0.0005	41.216	0.1713	±41.270	0.2763	100.1	245.11	1.53
M	0.90	237223.00	91.07	5791.51	21.43	70.63	1.90	6.95	4.30	3.36	2.25	0.020	0.002353	0.0015	0.008223	0.000000	0.0012	0.0007	0.0122	0.0003	40.960	0.1524	±40.784	0.1910	99.6	242.42	1.06
N	1.10	712154.90	265.73	16234.84	21.44	206.92	2.77	6.96	4.51	4.43	1.99	0.057	0.000841	0.0005	0.011825	0.000000	0.0004	0.0003	0.0127	0.0002	43.866	0.0602	±43.781	0.0704	99.8	259.01	0.39
O	1.50	565097.70	203.22	12833.19	21.44	159.57	2.82	0.00	0.00	3.55	1.88	0.045	0.000000	0.0000	0.009975	0.000000	0.0000	0.0000	0.0124	0.0002	44.034	0.0753	±43.948	0.0870	99.8	259.93	0.48
P	3.50	320457.80	118.92	7290.84	13.90	93.26	2.40	0.00	0.00	4.22	1.88	0.026	0.000000	0.0000	0.011758	0.000000	0.0000	0.0000	0.0128	0.0003	43.953	0.0854	±43.778	0.1147	99.6	258.99	0.63
Q	6.00	23965.42	54.93	505.88	3.96	7.57	1.37	0.46	4.47	9.40	2.64	0.002	0.001795	0.0173	0.004494	0.000002	0.0009	0.0088	0.0150	0.0027	47.374	0.3868	±41.821	1.5973	88.3	248.17	8.86
																										Tg: 235 ± 3 Ma	
KA014003 (J: 3.526x10^{-3} ± 0.020)																										**Tp: 243 ± 3 Ma**	
A	0.25	29457.26	55.09	3205.41	8.23	57.98	1.58	0.00	0.00	33.97	2.10	0.011	0.000000	0.0000	0.031971	0.000001	0.0000	0.0000	0.0181	0.0005	9.190	0.0292	± 6.023	0.1966	65.6	37.92	1.22
B	0.30	45379.28	62.33	2512.39	7.85	31.27	1.46	8.45	10.71	12.59	2.16	0.009	0.006590	0.0084	0.004752	0.000001	0.0034	0.0043	0.0124	0.0006	18.062	0.0616	±16.563	0.2633	91.7	102.41	1.58
C	0.33	50714.90	60.05	2224.01	5.34	26.83	1.32	21.31	9.19	4.16	2.07	0.008	0.018784	0.0081	0.005998	0.000001	0.0096	0.0041	0.0121	0.0006	22.803	0.0611	±22.242	0.2840	97.6	136.22	1.68
D	0.36	37645.18	50.08	1569.85	5.09	20.55	1.26	23.95	10.66	0.00	0.00	0.006	0.029904	0.0133	0.014645	0.000001	0.0153	0.0068	0.0131	0.0008	23.980	0.0841	±24.104	0.3860	100.5	147.17	2.26
E	0.40	42420.61	44.82	1651.28	9.86	21.99	1.31	0.00	0.00	0.00	0.00	0.006	0.000000	0.0000	0.015884	0.000001	0.0000	0.0000	0.0133	0.0008	25.689	0.1557	±25.787	0.4057	100.4	157.01	2.37
F	0.45	204430.80	83.15	6392.46	17.67	78.13	1.91	27.14	8.87	17.58	1.80	0.023	0.008320	0.0027	0.005956	0.000000	0.0042	0.0014	0.0122	0.0003	31.980	0.0893	±31.156	0.1211	97.4	188.06	0.69
G	0.50	103545.80	68.90	3228.36	6.88	42.12	1.38	26.05	10.05	3.49	2.51	0.011	0.015817	0.0061	0.012720	0.000001	0.0081	0.0031	0.0130	0.0004	32.074	0.0716	±31.749	0.2428	99.0	191.45	1.39
H	0.53	115258.70	85.56	3552.91	8.12	43.91	1.41	21.40	11.03	5.91	2.18	0.013	0.011806	0.0061	0.007982	0.000001	0.0060	0.0031	0.0124	0.0004	32.441	0.0780	±31.942	0.1991	98.5	192.55	1.14
I	0.56	61924.43	62.31	1966.12	6.31	23.98	1.29	0.00	0.00	3.32	1.84	0.007	0.000000	0.0000	0.006976	0.000001	0.0000	0.0000	0.0122	0.0007	31.496	0.1059	±30.989	0.2979	98.4	187.10	1.71
J	0.60	58314.18	59.97	1827.63	5.69	25.06	1.16	26.01	10.50	3.51	2.03	0.006	0.027898	0.0113	0.015732	0.000001	0.0142	0.0057	0.0137	0.0006	31.907	0.1047	±31.333	0.3472	98.2	189.07	1.99
K	0.65	85246.19	81.37	2791.59	6.68	37.16	1.38	26.78	10.96	12.12	1.84	0.010	0.018802	0.0077	0.010640	0.000001	0.0096	0.0039	0.0133	0.0005	30.537	0.0787	±29.238	0.2111	95.8	177.03	1.22
L	0.70	63567.22	67.01	2008.44	5.94	24.19	1.40	0.00	0.00	4.63	2.03	0.007	0.000000	0.0000	0.005392	0.000001	0.0000	0.0000	0.0120	0.0007	31.650	0.0994	±30.958	0.3176	97.8	186.92	1.82
M	0.75	61263.53	47.41	1860.13	5.87	23.80	1.44	24.55	9.27	1.42	2.01	0.007	0.025873	0.0098	0.011555	0.000001	0.0132	0.0050	0.0128	0.0008	32.935	0.1070	±32.705	0.3395	99.3	196.91	1.94
N	0.80	93205.88	57.35	2664.18	6.62	32.26	1.54	4.11	10.42	0.00	0.00	0.009	0.003025	0.0077	0.010044	0.000001	0.0015	0.0039	0.0121	0.0006	34.985	0.0895	±35.431	0.3183	101.3	212.39	1.80
O*	0.90	45083.20	55.09	1204.14	7.24	18.00	1.12	7.44	9.71	0.00	0.00	0.004	0.012103	0.0158	0.029970	0.000002	0.0062	0.0081	0.0149	0.0009	37.440	0.2297	±38.714	0.5110	103.4	**230.86**	**2.86**
P*	1.10	63619.46	58.92	1668.55	5.97	17.62	1.27	0.00	0.00	3.41	1.84	0.006	0.000000	0.0000	0.000000	0.000000	0.0000	0.0000	0.0106	0.0008	38.129	0.1409	±37.513	0.3581	98.4	**224.13**	**2.01**
Q*	1.50	65613.60	60.05	1696.41	5.59	23.80	1.44	0.00	0.00	4.75	1.85	0.006	0.000000	0.0000	0.016627	0.000001	0.0000	0.0000	0.0140	0.0008	38.678	0.1324	±37.836	0.3497	97.8	**225.95**	**1.96**
R*	3.50	28531.13	55.55	649.96	5.47	11.55	1.12	0.00	0.00	13.68	1.95	0.002	0.000000	0.0000	0.018413	0.000003	0.0000	0.0000	0.0178	0.0017	43.897	0.3791	±37.611	0.9522	85.7	**224.68**	**5.35**
S	6.00	4824.78	37.99	92.52	2.75	4.94	1.09	0.00	0.00	3.35	1.76	0.000	0.000000	0.0000	0.212834	0.000024	0.0000	0.0000	0.0534	0.0119	52.150	1.6036	±41.304	5.8182	79.2	245.30	32.31
																										Tg: 174 ± 2 Ma	
																										Tp: 226 ± 3 Ma	

Sample*	Watts	^{40}Ar	±1s	^{39}Ar	±1s	^{38}Ar	±1s	^{37}Ar	±1s	^{36}Ar	±1s	^{39}Ar Mol†	Ca/K	±1s	Cl/K	±1s	$^{37}Ar/^{39}Ar$	±1s	$^{38}Ar/^{39}Ar$	±1s	$^{40}Ar/^{39}Ar$	±1s	$^{40}Ar^{*}/^{39}Ar$	±1s	%$^{40}Ar^{*}$	Age†† (Ma)	±1s
KA014004 (J: 3.524×10^{-3} ± 0.020)																											
A	0.25	47848.13	59.24	2815.07	11.41	40.34	1.73	0.00	0.00	12.33	1.45	0.010	0.000000	0.0000	0.016624	0.000001	0.0000	0.0000	0.0143	0.0006	16.997	0.0721	±15.686	0.1677	92.3	97.06	1.01
B	0.30	38101.26	54.56	1706.40	6.19	24.97	1.39	0.34	10.41	0.23	1.76	0.006	0.000389	0.0120	0.023183	0.000001	0.0002	0.0061	0.0146	0.0008	22.328	0.0870	±22.285	0.3193	99.8	136.38	1.88
C	0.33	131468.10	74.76	4801.57	10.41	62.88	1.54	0.00	0.00	0.00	0.00	0.017	0.000000	0.0000	0.014402	0.000000	0.0000	0.0000	0.0131	0.0003	27.380	0.0614	±27.430	0.1438	100.2	166.45	0.83
D	0.36	37190.73	59.60	1181.94	4.94	18.66	1.23	11.49	10.28	10.40	2.81	0.004	0.019061	0.0171	0.020350	0.000002	0.0097	0.0087	0.0158	0.0010	31.466	0.1407	±28.838	0.7221	91.7	174.60	4.17
E	0.40	424361.20	215.13	11454.99	20.19	150.95	2.25	6.07	9.02	11.51	2.37	0.040	0.001039	0.0015	0.013569	0.000000	0.0005	0.0008	0.0132	0.0002	37.046	0.0680	±36.743	0.0915	99.2	219.65	0.51
F*	0.45	79313.75	56.11	1957.72	5.92	23.17	1.57	0.00	0.00	2.08	2.21	0.007	0.000000	0.0000	0.005557	0.000001	0.0000	0.0000	0.0118	0.0008	40.513	0.1258	±40.193	0.3595	99.2	**238.96**	**2.00**
G*	0.50	45770.15	65.49	1113.88	4.45	17.94	1.32	0.00	0.00	0.00	0.00	0.004	0.000000	0.0000	0.032406	0.000002	0.0000	0.0000	0.0161	0.0012	41.091	0.1743	±41.184	0.7708	100.2	**244.47**	**4.28**
H*	0.53	43924.81	61.52	1080.72	4.35	12.18	1.20	0.00	0.00	0.00	0.00	0.004	0.000000	0.0000	0.003636	0.000002	0.0000	0.0000	0.0113	0.0011	40.644	0.1732	±40.708	0.6551	100.2	**241.83**	**3.64**
I*	0.56	27357.25	54.65	678.44	3.86	7.03	1.17	0.00	0.00	5.98	2.14	0.002	0.000000	0.0000	0.000000	0.000000	0.0000	0.0000	0.0104	0.0017	40.324	0.2429	±37.683	0.9676	93.5	**224.93**	**5.43**
J*	0.60	38149.47	53.52	954.38	3.86	10.70	1.32	8.85	10.88	0.00	0.00	0.003	0.018169	0.0223	0.004851	0.000002	0.0093	0.0114	0.0112	0.0014	39.973	0.1709	±40.453	0.8459	101.2	**240.41**	**4.71**
K*	0.65	46768.67	66.56	1154.23	3.99	13.90	1.10	0.00	0.00	0.00	0.00	0.004	0.000000	0.0000	0.011092	0.000002	0.0000	0.0000	0.0120	0.0010	40.519	0.1516	±41.353	0.4989	102.1	**245.41**	**2.77**
L*	0.70	6977.79	40.19	170.30	2.30	0.00	0.00	13.35	10.11	0.00	0.00	0.001	0.153675	0.1164	0.000000	0.000000	0.0784	0.0594	0.0000	0.0000	40.975	0.6010	±55.558	4.0329	135.6	**322.55**	**21.44**
M*	0.75	3117.28	42.19	71.18	1.84	0.00	0.00	0.00	0.00	0.00	0.00	0.000	0.000000	0.0000	0.000000	0.000000	0.0000	0.0000	0.0000	0.0000	43.791	1.2757	±63.869	6.8934	145.9	**366.20**	**35.77**
N*	0.80	16565.41	51.76	414.32	3.26	4.27	1.12	1.94	12.14	0.00	0.00	0.001	0.009168	0.0574	0.004451	0.000006	0.0047	0.0293	0.0103	0.0027	39.982	0.3382	±41.808	1.3627	104.6	**247.93**	**7.55**
O*	0.90	31038.88	52.29	741.56	4.42	7.57	1.24	0.00	0.00	5.36	2.21	0.003	0.000000	0.0000	0.000000	0.000000	0.0000	0.0000	0.0102	0.0017	41.856	0.2594	±39.692	0.9223	94.8	**236.17**	**5.14**
P*	1.10	23433.93	33.03	546.23	3.94	5.91	1.08	0.00	0.00	1.42	2.55	0.002	0.000000	0.0000	0.000000	0.000000	0.0000	0.0000	0.0108	0.0020	42.901	0.3150	±42.118	1.4271	98.2	**249.65**	**7.90**
Q	1.50	12253.49	44.12	284.23	2.52	4.18	1.13	0.00	0.00	7.39	2.29	0.001	0.000000	0.0000	0.000000	0.000000	0.0000	0.0000	0.0147	0.0040	43.111	0.4127	±35.340	2.4353	82.0	211.73	13.77
R	3.50	4226.20	35.17	93.44	1.87	1.60	1.11	0.00	0.00	7.12	2.13	0.000	0.000000	0.0000	0.000000	0.000000	0.0000	0.0000	0.0171	0.0118	45.229	0.9803	±22.484	6.8318	49.7	137.55	40.24
S	6.00	454.82	44.04	5.31	1.32	3.63	1.15	13.70	9.90	0.00	0.00	0.000	5.057340	3.8673	5.016464	0.000396	2.5803	1.9731	0.6829	0.2760	85.672	22.9056	±361.654	128.81	421.4	1482.41	360.02
																										Tg: 201 ± 2 Ma Tp: 241 ± 12 Ma	
KA014014 (J: 3.520×10^{-3} ± 0.020)																											
A	0.25	117369.20	65.16	6031.73	12.65	92.86	2.10	6.43	4.28	87.18	3.49	0.021	0.002088	0.0014	0.011684	0.000000	0.0011	0.0007	0.0154	0.0003	19.459	0.0422	±15.140	0.1761	77.8	93.67	1.06
B	0.30	350838.00	152.51	13013.47	27.72	182.16	3.42	13.66	4.77	84.72	2.66	0.046	0.002057	0.0007	0.012278	0.000000	0.0010	0.0004	0.0140	0.0003	26.960	0.0586	±25.013	0.0819	92.8	152.23	0.48
C	0.35	766044.60	302.85	22610.95	47.86	299.07	3.95	22.41	5.09	91.78	2.46	0.080	0.001942	0.0004	0.010446	0.000000	0.0010	0.0002	0.0132	0.0002	33.879	0.0730	±32.665	0.0776	96.4	196.34	0.44
D	0.40	265544.70	94.26	7344.43	16.39	89.72	2.50	0.00	0.00	30.71	2.22	0.026	0.000000	0.0000	0.004314	0.000000	0.0000	0.0000	0.0122	0.0003	36.156	0.0817	±34.905	0.1200	96.5	209.06	0.68
E	0.45	284115.60	128.54	7688.90	23.95	97.02	2.48	12.60	4.63	31.70	2.16	0.027	0.003211	0.0012	0.006764	0.000000	0.0016	0.0006	0.0126	0.0003	36.951	0.1163	±35.718	0.1403	96.7	213.65	0.79
F	0.50	327776.00	122.38	8371.44	12.63	107.88	2.61	6.32	5.52	16.05	2.37	0.030	0.001479	0.0013	0.010826	0.000000	0.0008	0.0007	0.0129	0.0003	39.154	0.0609	±38.579	0.1036	98.5	229.72	0.58
G	0.55	78765.27	83.46	2014.92	7.49	22.93	1.72	0.00	0.00	4.61	1.85	0.007	0.000000	0.0000	0.001470	0.000000	0.0000	0.0000	0.0114	0.0009	39.091	0.1512	±38.405	0.3116	98.3	228.74	1.74
H	0.60	90471.79	61.19	2311.19	7.87	30.44	1.73	1.67	4.63	5.53	2.26	0.008	0.001416	0.0039	0.011965	0.000000	0.0007	0.0020	0.0132	0.0007	39.145	0.1359	±38.428	0.3205	98.2	228.87	1.79
I	0.65	90957.08	72.43	2269.68	8.74	26.89	1.37	13.07	4.17	0.96	1.98	0.008	0.011286	0.0036	0.006332	0.000000	0.0058	0.0018	0.0118	0.0006	40.075	0.1576	±39.946	0.3045	99.7	237.34	1.70
J	0.70	215631.60	120.94	5252.31	13.89	64.84	1.98	12.86	4.18	5.87	1.98	0.019	0.004799	0.0016	0.008512	0.000000	0.0024	0.0008	0.0123	0.0004	41.055	0.1110	±40.718	0.1577	99.2	241.64	0.88
K	0.75	23.79	45.29	3.30	1.48	0.02	1.14	16.00	4.57	0.00	0.00	0.000	9.491633	5.0491	0.000000	0.000000	4.8427	2.5761	0.0070	0.3465	7.200	14.0815	±11.072	197.26	153.3	68.97	1205.6
L	0.80	580.83	33.08	10.12	1.63	0.00	0.00	0.00	0.00	0.00	0.00	0.000	0.000000	0.0000	0.000000	0.000000	0.0000	0.0000	0.0000	0.0000	57.402	9.8115	±283.116	94.62	493.4	1247.37	300.96
M	0.90	7579.89	47.01	180.21	2.90	2.37	1.32	0.62	5.23	1.96	1.94	0.001	0.006701	0.0569	0.002350	0.000006	0.0034	0.0290	0.0132	0.0073	42.060	0.7256	±38.803	3.2918	92.3	230.97	18.39
N	1.10	41160.63	51.15	1035.21	10.61	10.06	1.35	0.00	0.00	0.00	0.00	0.004	0.000000	0.0000	0.000000	0.000000	0.0000	0.0000	0.0097	0.0013	39.761	0.4106	±40.605	0.7733	102.1	241.01	4.30
O	1.50	32117.71	55.43	768.44	4.24	10.17	1.17	0.00	0.00	3.08	1.94	0.003	0.000000	0.0000	0.010529	0.000001	0.0000	0.0000	0.0132	0.0015	41.796	0.2418	±40.595	0.7911	97.1	240.96	4.40
P	3.50	34800.44	58.35	815.97	4.91	16.89	1.50	5.59	4.32	6.60	2.01	0.003	0.013419	0.0104	0.050269	0.000001	0.0068	0.0053	0.0207	0.0018	42.649	0.2664	±40.230	0.7768	94.3	238.93	4.32
Q	6.00	4123.98	42.65	90.19	1.97	4.54	1.46	2.74	4.44	3.89	2.31	0.000	0.059516	0.0964	0.186956	0.000010	0.0304	0.0492	0.0504	0.0162	45.724	1.1062	±32.842	7.6932	71.8	197.35	43.79
																										Tg: 196 ± 2 Ma	

Sample*	Watts	^{40}Ar	±1s	^{39}Ar	±1s	^{38}Ar	±1s	^{37}Ar	±1s	^{36}Ar	±1s	^{39}Ar Mol†	Ca/K	±1s	Cl/K	±1s	$^{37}Ar/^{39}Ar$	±1s	$^{38}Ar/^{39}Ar$	±1s	$^{40}Ar/^{39}Ar$	±1s	$^{40}Ar^{*}/^{39}Ar$	±1s	%$^{40}Ar^{*}$	Age†† (Ma)	±1s
KA014014 (J: 3.520x10^{-3} ± 0.020)																											
A	0.25	17819.22	52.20	1150.15	5.23	23.90	1.27	13.94	10.70	39.13	2.04	0.004	0.023764	0.0182	0.021764	0.000002	0.0121	0.0093	0.0208	0.0011	15.493	0.0838	± 5.333	0.5328	34.4	33.55	3.32
B	0.30	131206.70	71.20	5756.40	8.98	80.96	1.72	5.96	10.35	69.95	2.27	0.020	0.002030	0.0035	0.006367	0.000000	0.0010	0.0018	0.0141	0.0003	22.793	0.0377	±19.162	0.1221	84.1	117.76	0.73
C	0.33	13488.92	50.17	485.36	3.99	9.19	1.13	37.78	10.15	2.48	2.78	0.002	0.152567	0.0410	0.043091	0.000004	0.0778	0.0209	0.0189	0.0023	27.791	0.2507	±26.273	1.7267	94.5	159.57	10.04
D	0.36	289591.50	140.54	8466.50	10.61	120.81	2.09	46.79	9.54	75.54	2.53	0.030	0.010832	0.0022	0.011191	0.000000	0.0055	0.0011	0.0143	0.0002	34.204	0.0460	±31.538	0.0991	92.2	189.92	0.57
E	0.40	30258.39	50.17	866.60	4.61	11.03	1.24	7.94	9.89	9.75	2.14	0.003	0.017954	0.0224	0.000000	0.000000	0.0092	0.0114	0.0127	0.0014	34.916	0.1945	±31.555	0.7578	90.4	190.01	4.33
F	0.45	170887.90	74.47	4582.18	8.48	56.33	1.69	19.73	9.39	22.72	2.23	0.016	0.008441	0.0040	0.003902	0.000000	0.0043	0.0020	0.0123	0.0004	37.294	0.0709	±35.811	0.1607	96.0	214.18	0.91
G	0.50	169515.80	98.40	4435.05	8.97	57.76	1.65	6.99	9.87	21.99	1.92	0.016	0.003090	0.0044	0.008232	0.000000	0.0016	0.0022	0.0130	0.0004	38.222	0.0804	±36.739	0.1508	96.1	219.40	0.85
H	0.53	121357.10	78.96	3042.39	7.46	36.46	1.47	3.69	10.05	16.61	1.82	0.011	0.002378	0.0065	0.001502	0.000001	0.0012	0.0033	0.0120	0.0005	39.889	0.1012	±38.256	0.2037	95.9	227.91	1.14
I	0.56	20103.53	43.15	491.90	3.10	3.90	1.17	7.43	11.11	0.45	1.90	0.002	0.029614	0.0443	0.000000	0.000000	0.0151	0.0226	0.0079	0.0024	40.869	0.2719	±40.594	1.1820	99.3	240.95	6.57
J	0.60	23234.15	39.59	566.20	3.25	2.17	1.15	0.00	0.00	1.18	1.79	0.002	0.000000	0.0000	0.000000	0.000000	0.0000	0.0000	0.0038	0.0020	41.036	0.2455	±40.410	0.9740	98.5	239.93	5.41
K	0.65	41893.91	41.47	931.95	4.23	12.51	1.19	0.00	0.00	9.97	2.87	0.003	0.000000	0.0000	0.004215	0.000002	0.0000	0.0000	0.0134	0.0013	44.953	0.2089	±41.756	0.9391	92.9	247.39	5.20
L	0.70	27760.34	53.84	656.89	3.62	3.78	1.25	0.00	0.00	1.24	1.78	0.002	0.000000	0.0000	0.000000	0.000000	0.0000	0.0000	0.0058	0.0019	42.260	0.2466	±41.694	0.8465	98.7	247.05	4.69
M	0.75	13499.37	41.47	310.63	2.64	4.13	1.23	33.76	10.63	1.00	2.19	0.001	0.213029	0.0671	0.011748	0.000007	0.1087	0.0342	0.0133	0.0040	43.458	0.3928	±42.505	2.1427	97.8	251.54	11.84
N	0.80	6371.90	36.98	145.95	1.91	4.50	1.02	1.56	10.19	0.00	0.00	0.001	0.020948	0.1368	0.142087	0.000014	0.0107	0.0698	0.0308	0.0070	43.659	0.6258	±49.743	3.5629	113.9	291.08	19.25
O	0.90	18935.70	48.59	438.25	2.63	7.70	1.23	4.10	11.20	0.00	0.00	0.002	0.018348	0.0501	0.043898	0.000005	0.0094	0.0256	0.0176	0.0028	43.207	0.2817	±44.056	1.1365	102.0	260.08	6.25
P	1.10	55790.32	42.09	1277.35	4.35	19.45	1.24	21.70	11.15	5.64	1.60	0.005	0.033298	0.0171	0.021935	0.000002	0.0170	0.0087	0.0152	0.0010	43.677	0.1522	±42.358	0.4029	97.0	250.72	2.23
Q	1.50	49928.62	56.51	1141.47	5.09	17.29	1.43	4.39	9.70	13.29	1.85	0.004	0.007533	0.0167	0.013380	0.000002	0.0038	0.0085	0.0152	0.0013	43.741	0.2011	±40.261	0.5186	92.1	239.10	2.88
R	3.50	24943.29	42.09	438.28	3.47	12.33	1.35	11.53	9.27	26.43	1.95	0.002	0.051580	0.0414	0.035915	0.000004	0.0263	0.0211	0.0281	0.0031	56.911	0.4608	±38.910	1.3658	68.4	231.57	7.63
S	6.00	9445.25	40.00	121.25	1.89	5.87	1.29	0.00	0.00	29.98	1.85	0.000	0.000000	0.0000	0.000000	0.000000	0.0000	0.0000	0.0484	0.0106	77.899	1.2608	± 4.054	4.5736	5.2	25.56	28.63
																										Tg: 193 ± 2 Ma	
KA014026 (J: 3.520x10^{-3} ± 0.020)																											
A	0.25	373859.90	239.59	7302.84	15.15	249.83	4.33	54.69	5.40	733.6	5.97	0.026	0.014679	0.0015	0.027132	0.000000	0.0075	0.0007	0.0342	0.0006	51.194	0.1112	±21.202	0.2501	41.4	129.66	1.48
B	0.30	253030.80	164.25	5955.00	18.92	78.69	2.19	24.15	4.77	35.40	2.53	0.021	0.007950	0.0016	0.008261	0.000000	0.0041	0.0008	0.0132	0.0004	42.491	0.1378	±40.713	0.1834	95.8	241.28	1.02
C	0.35	410606.50	152.80	8349.43	16.40	104.28	2.46	13.34	4.66	40.69	2.60	0.029	0.003131	0.0011	0.005163	0.000000	0.0016	0.0006	0.0125	0.0003	49.178	0.0983	±47.720	0.1333	97.0	279.73	0.72
D	0.40	2370536.0	1285.86	45431.33	171.49	532.84	13.98	59.06	21.44	0.00	0.00	0.160	0.002548	0.0009	0.007750	0.000000	0.0013	0.0005	0.0117	0.0003	52.178	0.1990	±52.617	0.2123	100.8	306.12	1.14
E*	0.45	3006752.0	1102.23	56771.34	98.00	696.60	9.86	80.76	19.70	0.00	0.00	0.200	0.002788	0.0007	0.010194	0.000000	0.0014	0.0003	0.0123	0.0002	52.962	0.0935	±53.195	0.1032	100.4	**309.22**	0.55
F*	0.50	380287.70	190.61	7125.70	17.66	92.16	2.18	28.16	4.64	5.59	1.85	0.025	0.007747	0.0013	0.012370	0.000000	0.0040	0.0007	0.0129	0.0003	53.369	0.1350	±53.132	0.1551	99.6	**308.88**	0.83
G*	0.55	400282.00	140.89	7439.39	13.90	89.13	2.30	33.59	5.08	11.18	1.85	0.026	0.008850	0.0013	0.005917	0.000000	0.0045	0.0007	0.0120	0.0003	53.806	0.1023	±53.355	0.1257	99.2	**310.07**	0.67
H*	0.60	535805.60	215.58	9876.54	17.66	128.08	2.81	44.60	5.38	15.67	1.95	0.035	0.008850	0.0011	0.011676	0.000000	0.0045	0.0005	0.0130	0.0003	54.250	0.0995	±53.774	0.1149	99.1	**312.31**	0.61
I*	0.65	695058.50	240.59	12902.30	18.92	161.30	2.35	55.50	4.81	21.89	1.95	0.045	0.008431	0.0007	0.008786	0.000000	0.0043	0.0004	0.0125	0.0002	53.871	0.0812	±53.362	0.0923	99.1	**310.11**	0.49
J	0.70	800024.80	416.17	14743.22	22.71	191.85	2.35	51.91	4.88	14.48	2.37	0.052	0.006901	0.0006	0.012617	0.000000	0.0035	0.0003	0.0130	0.0002	54.264	0.0882	±53.968	0.1001	99.5	313.34	0.53
K	0.75	710765.00	315.70	13092.51	20.20	161.62	2.67	44.71	5.81	15.61	1.76	0.046	0.006693	0.0009	0.008417	0.000000	0.0034	0.0004	0.0123	0.0002	54.288	0.0872	±53.929	0.0955	99.3	313.14	0.51
L	0.80	502150.20	165.55	9171.26	27.74	116.99	2.52	35.89	5.18	6.96	2.05	0.032	0.007669	0.0011	0.011346	0.000000	0.0039	0.0006	0.0128	0.0003	54.753	0.1666	±54.523	0.1788	99.6	316.30	0.95
M	0.90	352458.30	227.39	6403.83	13.93	73.32	1.82	9.24	4.74	2.20	2.81	0.023	0.002829	0.0014	0.004061	0.000000	0.0014	0.0007	0.0114	0.0003	55.039	0.1249	±54.933	0.1808	99.8	318.48	0.96
N	1.10	509080.20	189.78	8991.23	16.44	116.59	2.22	19.94	5.70	9.82	2.25	0.032	0.004346	0.0012	0.012222	0.000000	0.0022	0.0006	0.0130	0.0002	56.620	0.1057	±56.291	0.1290	99.4	325.68	0.68
O	1.50	375116.30	164.75	6645.62	15.19	81.06	1.96	7.39	4.83	0.00	0.00	0.023	0.002179	0.0014	0.009770	0.000000	0.0011	0.0007	0.0122	0.0003	56.446	0.1313	±56.680	0.2013	100.4	327.74	1.06
P	3.50	237696.30	98.78	4167.97	12.56	49.21	1.70	28.25	4.84	3.45	1.85	0.015	0.013284	0.0023	0.005634	0.000000	0.0068	0.0012	0.0118	0.0004	57.029	0.1734	±56.780	0.2176	99.6	328.27	1.15
Q	6.00	6812.50	32.56	79.98	2.13	3.15	1.05	0.00	0.00	2.44	2.11	0.000	0.000000	0.0000	0.135738	0.000011	0.0000	0.0000	0.0393	0.0132	85.178	2.3078	±76.072	8.1327	89.3	427.46	40.69
																										Tg: 303 ± 3 Ma	
																										Tp: 309 ± 3 Ma	

Sample*	Watts	^{40}Ar	±1s	^{39}Ar	±1s	^{38}Ar	±1s	^{37}Ar	±1s	^{36}Ar	±1s	^{39}Ar Mol†	Ca/K	±1s	Cl/K	±1s	^{37}Ar/^{39}Ar	±1s	^{38}Ar/^{39}Ar	±1s	^{40}Ar/^{39}Ar	±1s	^{40}Ar*/^{39}Ar	±1s	%^{40}Ar*	Age†† (Ma)	±1s
KA014026 (J: 3.515x10^{-3} ± 0.020)																											
A	0.25	242997.70	89.85	4510.63	8.34	66.27	1.78	13.77	10.44	52.42	2.15	0.016	0.005985	0.0045	0.010678	0.000000	0.0031	0.0023	0.0147	0.0004	53.872	0.1016	±50.400	0.1716	93.6	294.22	0.92
B	0.30	247004.50	123.41	4451.41	8.60	54.23	1.70	9.40	10.35	12.11	2.67	0.016	0.004139	0.0046	0.005746	0.000000	0.0021	0.0023	0.0122	0.0004	55.489	0.1107	±54.674	0.2098	98.5	317.10	1.12
C*	0.32	110007.60	74.80	1998.08	7.22	25.14	1.35	0.00	0.00	7.11	1.94	0.007	0.000000	0.0000	0.007182	0.000001	0.0000	0.0000	0.0126	0.0007	55.057	0.2024	±53.990	0.3516	98.1	**313.46**	1.87
D*	0.36	12410.97	41.19	229.65	3.48	3.44	0.99	0.00	0.00	2.06	1.73	0.001	0.000000	0.0000	0.015374	0.000009	0.0000	0.0000	0.0150	0.0043	54.043	0.8386	±51.361	2.3887	95.0	**299.39**	12.83
E*	0.40	18122.23	53.27	340.72	2.88	3.50	1.15	0.00	0.00	2.50	1.59	0.001	0.000000	0.0000	0.000000	0.000000	0.0000	0.0000	0.0103	0.0034	53.188	0.4763	±50.995	1.4689	95.9	**297.42**	7.90
F*	0.45	38303.05	59.83	654.20	4.98	8.53	1.23	11.29	9.59	0.00	0.00	0.002	0.033812	0.0287	0.016624	0.000003	0.0173	0.0147	0.0130	0.0019	58.549	0.4547	±59.289	0.9371	101.3	**341.48**	4.92
G*	0.50	27447.51	106.96	483.65	5.60	6.29	1.24	31.01	10.32	1.06	2.33	0.002	0.125650	0.0419	0.011219	0.000004	0.0641	0.0214	0.0130	0.0026	56.751	0.6932	±56.105	1.5964	98.9	**324.69**	8.45
H*	0.53	20260.51	50.10	357.65	3.00	3.72	1.23	5.39	8.90	0.00	0.00	0.001	0.029545	0.0488	0.003117	0.000005	0.0151	0.0249	0.0104	0.0035	56.648	0.4959	±57.940	1.4172	102.3	**334.39**	7.47
I*	0.56	12258.02	45.43	234.21	2.46	3.39	1.14	0.15	10.47	0.00	0.00	0.001	0.001217	0.0876	0.029021	0.000009	0.0006	0.0447	0.0145	0.0049	52.337	0.5820	±54.098	2.8736	103.4	**314.04**	15.31
J*	0.60	147453.00	90.59	2703.83	7.16	37.75	1.39	19.56	9.88	2.02	2.21	0.010	0.014182	0.0072	0.018504	0.000001	0.0072	0.0037	0.0140	0.0005	54.535	0.1482	±54.310	0.2852	99.6	**315.16**	1.52
K*	0.65	54964.64	58.06	1025.27	6.78	13.89	1.14	30.76	10.77	0.00	0.00	0.004	0.058805	0.0206	0.021531	0.000002	0.0300	0.0105	0.0135	0.0011	53.610	0.3592	±54.856	0.7116	102.3	**318.07**	3.78
L*	0.70	14682.93	46.55	270.30	4.21	4.03	1.08	10.94	10.50	0.00	0.00	0.001	0.079327	0.0762	0.025488	0.000008	0.0405	0.0389	0.0149	0.0040	54.322	0.8628	±54.475	2.5999	100.3	**316.04**	13.84
M*	0.75	9481.88	44.97	178.25	1.90	2.01	1.17	9.57	10.78	2.54	1.63	0.001	0.105191	0.1185	0.000000	0.000000	0.0537	0.0605	0.0113	0.0065	53.194	0.6210	±48.941	2.7994	92.0	**286.35**	15.15
N*	0.80	6999.44	40.53	121.43	1.90	1.58	1.09	3.73	10.42	2.93	1.72	0.000	0.060166	0.1682	0.000000	0.000000	0.0307	0.0858	0.0130	0.0089	57.640	0.9623	±50.443	4.3184	87.5	**294.45**	23.26
O*	0.90	25367.90	41.63	455.19	3.11	5.03	1.29	10.84	10.98	2.44	1.57	0.002	0.046681	0.0473	0.000000	0.000000	0.0238	0.0241	0.0111	0.0028	55.731	0.3911	±54.130	1.1009	97.1	**314.21**	5.86
P*	1.10	18476.22	41.04	324.29	4.67	1.61	1.06	22.02	8.72	1.24	2.03	0.001	0.133066	0.0527	0.000000	0.000000	0.0679	0.0269	0.0050	0.0033	56.974	0.8297	±55.839	2.0385	98.0	**323.29**	10.81
Q*	1.50	20088.04	36.00	330.49	3.22	6.26	1.16	0.00	0.00	7.65	2.37	0.001	0.000000	0.0000	0.023017	0.000006	0.0000	0.0000	0.0189	0.0035	60.782	0.6017	±53.865	2.2039	88.6	**312.79**	11.75
R*	3.50	29855.81	55.36	494.55	4.18	8.39	1.10	0.00	0.00	8.06	2.37	0.002	0.000000	0.0000	0.018954	0.000004	0.0000	0.0000	0.0170	0.0022	60.370	0.5223	±55.496	1.5072	91.9	**321.47**	8.00
S*	6.00	19900.22	43.15	353.70	2.63	6.19	1.24	0.00	0.00	4.58	2.28	0.001	0.000000	0.0000	0.025894	0.000006	0.0000	0.0000	0.0175	0.0035	56.264	0.4365	±52.393	1.9684	93.1	**304.93**	10.54
																										Tg: 309 ± 4 Ma	
																										Tp: 314 ± 4 Ma	

* heating increment used in calculation of plateau or preferred age

† x10^{-14}

†† Tg: total gas age; Tp: plateau age

APPENDIX 8.3 (U-Th)/He data, Kalymnos, Greece

Full Sample Name	length 1 (mm)	width 1 (mm)	length 2 (mm)	width 2 (mm)	2X Term	Dim Mass (mg)	rs (mm)	4He (nmol/g)	±	U (ppm)	±	Th (ppm)	±	eU	4He (ncc)	±	U (ng)	±	Th (ng)	±	Th/U	Raw Date (Ma)	±	Ft	± (%)	Corrected Date (Ma)	Full Unc. (Ma)	Analytic Unc. (Ma)
KA004_Zr1	172.6	94.5	170.5	108.2	y	8.16	58.76	14.022	0.013	98.56	0.09	68.07	0.99	114.6	2.563	0.002	0.8039	0.013	0.5552	0.008	0.691	22.65	0.31	0.801	7.0	28.27	2.02	0.31
KA004_Zr2	227.4	118.2	227.6	116.6	y	6.52	69.98	42.355	0.049	332.17	0.38	150.88	2.33	367.6	6.187	0.007	2.1648	0.046	0.9833	0.015	0.454	21.33	0.40	0.764	7.0	27.91	2.02	0.40
KA004_Zr3	188.3	103.1	188.4	98.6	y	3.98	59.66	36.039	0.044	291.80	0.36	150.34	4.12	327.1	3.216	0.004	1.1618	0.022	0.5986	0.016	0.515	20.40	0.34	0.727	7.0	28.07	2.02	0.34
KA004_Zr4	231.8	102.4	236.7	100.0	n	11.15	62.30	10.735	0.012	87.92	2.83	36.21	1.18	96.4	2.684	0.003	0.9806	0.032	0.4039	0.019	0.412	20.62	0.59	0.823	7.0	25.04	0.59	1.89
KA004_Zr5	240.5	124.8	245.4	127.0	y	17.91	74.84	24.518	0.014	168.74	5.25	42.53	1.33	178.7	9.840	0.006	3.0214	0.094	0.7614	0.020	0.252	25.40	0.72	0.843	7.0	30.13	0.72	2.28
KA004_Zr6	230.8	122.0	232.2	94.7	y	12.44	65.81	20.344	0.023	165.11	2.78	35.55	0.60	173.5	5.671	0.006	2.0534	0.035	0.4422	0.016	0.215	21.73	0.34	0.823	7.0	26.40	0.34	1.89
KA004_Zr7	251.3	140.1	246.7	135.3	y	21.95	81.07	62.096	0.055	391.04	8.05	358.51	7.43	475.3	30.547	0.027	8.5825	0.177	7.8684	0.320	0.917	24.17	0.43	0.853	7.0	28.34	0.43	2.05
KA004_Zr8	246.0	127.5	250.3	135.8	y	19.98	77.89	14.347	0.008	106.81	2.02	25.91	0.49	112.9	6.425	0.004	2.1339	0.040	0.5177	0.015	0.243	23.54	0.41	0.849	7.0	27.72	0.41	2.00
KA026_zr1	268.4	127.5	271.8	130.8	y	20.95	78.08	13.988	0.013	106.34	2.50	32.27	0.76	113.9	6.567	0.006	2.2274	0.052	0.6759	0.010	0.303	22.74	0.48	0.849	7.0	26.78	1.96	0.48
KA026_zr2	337.4	78.1	332.7	104.2	y	12.68	60.23	27.224	0.024	200.14	4.74	71.52	1.71	216.9	7.737	0.007	2.5376	0.060	0.9068	0.019	0.357	23.24	0.49	0.807	7.0	28.79	2.11	0.49
KA026_zr3	313.0	119.8	316.4	111.0	y	19.46	73.08	30.198	0.026	176.59	2.80	64.79	1.03	191.8	13.171	0.011	3.4364	0.054	1.2608	0.025	0.367	29.14	0.42	0.839	7.0	34.72	2.48	0.42
KA026_zr4	231.8	102.4	236.7	100.0	n	11.15	62.30	10.735	0.012	35.35	0.68	55.67	1.08	48.4	2.684	0.003	0.3943	0.008	0.6209	0.009	1.575	40.92	0.58	0.820	7.0	49.90	3.56	0.58
KA026_zr5	240.5	124.8	245.4	127.0	y	17.91	74.84	24.518	0.014	103.46	2.68	35.18	0.92	111.7	9.840	0.006	1.8525	0.048	0.6300	0.014	0.340	40.57	0.94	0.843	7.0	48.14	3.55	0.94
KA026_zr6	230.8	122.0	232.2	94.7	y	12.44	65.81	20.344	0.023	68.51	1.33	12.61	0.25	71.5	5.671	0.006	0.8520	0.017	0.1568	0.002	0.184	52.59	0.95	0.823	7.0	63.89	4.62	0.95
KA026_zr7	251.3	140.1	246.7	135.3	y	21.95	81.07	62.096	0.055	29.42	0.86	18.97	0.56	33.9	30.547	0.027	0.6458	0.019	0.4164	0.004	0.645	330.46	8.18	0.853	7.0	387.22	28.75	8.18
KA026_zr8	246.0	127.5	250.3	135.8	y	19.98	77.89	14.347	0.008	38.56	0.54	36.42	0.52	47.1	6.425	0.004	0.7703	0.011	0.7277	0.018	0.945	56.18	0.68	0.847	7.0	66.34	4.71	0.68

Fish Canyon Tuff zircons run in conjunction with these samples yielded an average date of 26 ± 1 Ma (n=7)

Full Sample Name	Notes
KA004_Zr1	euh/ slight rounding, incls, little chip
KA004_Zr2	slight irregular shape, little grungy, incl
KA004_Zr3	euh/ slight rounding, incls,
KA004_Zr4	euh, broken end, incls, clear
KA004_Zr5	euh/ slight rounding, incls, pinkish
KA004_Zr6	euh/ slight rounding, chipped, inc, pinkish
KA004_Zr7	euh, dirty, incls, pink
KA004_Zr8	euh/ slightly worn, incls, clear
KA026_zr1	euh, clear incls, pink
KA026_zr2	euh, elongate, clear, sml incls, pinkish
KA026_zr3	euh/ slight roundinf, dirty, incls, pinkish
KA026_zr4	euh, broken end, incls, clear
KA026_zr5	euh/ slight rounding, incls, pinkish
KA026_zr6	euh/ slight rounding, chipped, inc, pinkish
KA026_zr7	euh, dirty, incls, pink
KA026_zr8	euh/ slightly worn, incls, clear

Appendix 8.4: "Samples"

NAME	GPS point	Lithology	Fol.	Lin.	Comment	Pol.	Dat.	Thickness
KA014001	5: 0238515/4182721	amph.	-		MYRTIES	Y	N	*Normal*
KA014002	11: 0493796/4092800	Q-M Schist		024/25	MYRTIES	Y	Y	*Normal*
KA014003	17: 0493134/4100014	Q-M Schist	179/36	253/08	RACHI	Y	Y	*Normal*
KA014004	21: 0493326/4100361	Q-M Schist	133/25	210/03	RACHI	Y	Y	*Normal*
KA014005	´´	-	-	-	-	-	-	
KA014006	23: 0493634/4100512	Mr		200/05	KEFALA kato pleura	N	N	*Normal*
KA014007	-	-	-	-				
KA014008	29: 0492378/4099874	C-M schist	093/10	210/05	KEFALA	N	N	*Normal*
KA014009	32: 0492299/4099638	Mr FOS			KEFALA	N	N	*Normal*
KA014010	36: 0492755/4099638		115/10	180/10	KEFALA	Y	N	*Normal*
KA014011	37: 0492902/4099534	QTZ ins ant		048/20	KEFALA	N	N	*Normal*
KA014012	´´	Mr FOS	020/45		KEFALA	N	N	***Thicker***
KA014013	41: 0493236/4099313	Mr	123/87		KEFALA L UNIT	N	N	*Normal*
KA014014	46: 0492902/4100642	M schist		236/03	RACHI	Y	Y	*Normal*
KA014015	48: 0493028/4099081	Mt sld stone	019/15		KEFALA L UNIT	N	N	*Normal*
KA014016	52: 0492738/4099088	Mr			SC KEFALA	Y	N	*Normal*
KA014017	-	Tlk fol congl	311/57		RACHI	Y	N	*Normal*
KA014018	-							
KA014019	58: 0492800/4099893	Mr Dol	230/75		ALEXIS	N	N	*Normal*
KA014020	59: 0492801/4099893	Mc Schist		311/05	RACHI	Y	N	*Normal*
KA014021	67: 0493005/4099820	Congl-Dl-Mr	310/82		RACHI	N	N	*Normal*
KA014022	72: 0493178/4099800	Mr FOS	113/80		KEFALA	N	N	***Thicker***
KA014023	73: 0492571/4099811	Mr FOS	189/15		KEFALA	N	N	***Thicker***
KA014024	74: 0492267/4099734	Mr FOS	301/14		KEFALA	N	N	***Thicker***
KA014025	75: 0492269/4099725	Mr FOS	124/13		KEFALA	N	N	***Thicker***
KA014026	76: 0494612/409951	Mc Schist	082/22	028/01	EMPORIOS	Y	Y	*Normal*

*Normal = 30 μm

*Thicker= 50 -60 μm

Kalymnos Sept.
2014